

UNICA

UNIVERSITÀ
DEGLI STUDI
DI CAGLIARI

Ph.D. DEGREE IN
Physics

Cycle XXXVIII

TITLE OF THE Ph.D. THESIS

Studies of charmonia production ratios as a function of the centrality in PbPb collisions at LHCb

Scientific Disciplinary Sector(s)

FIS/01

Ph.D. Student:	Camilla De Angelis
Supervisor	Prof. Giulia Manca
Co-Supervisor	Dr. Pasquale Di Nezza

Final exam. Academic Year 2024/2025
Thesis defence session: February 2026



Università degli Studi di Cagliari

Doctoral Thesis, cycle XXXVIII

Studies of charmonia production ratios as a function of the centrality in PbPb collisions at LHCb

---

Candidate:
Camilla De Angelis

Advisors:
Prof. Giulia Manca
Dr. Pasquale Di Nezza

A thesis submitted in fulfillment of the requirements for the degree at the

Dipartimento di Fisica
Università degli Studi di Cagliari,
Cagliari, Italy

Academic Year 2024/2025

Declaration of Authorship

I, Camilla De Angelis, declare that this doctoral thesis titled, "Studies of charmonia production ratios as a function of the centrality in PbPb collisions at LHCb " and the work presented in it are my own. I confirm that:

- Where I have consulted the published work of others, this is always clearly attributed.
- Where I have quoted from the work of others, the source is always given. Except for such quotations, this thesis is entirely my own work.
- I have acknowledged all main sources of help.
- Where the thesis is based on work done by myself jointly with others, I have made clear exactly what was done by others and what I have contributed myself.

Signed:

Date: December 8, 2025

Abstract

Università degli studi di Cagliari
Dipartimento di Fisica

Doctor of Physics

Studies of charmonia production ratios as a function of the centrality in PbPb collisions at LHCb

by Camilla De Angelis

The dissociation of quarkonium states with different binding energies produced in heavy-ion collisions is a powerful probe for investigating the formation and properties of an intriguing state of matter called Quark-Gluon Plasma. Through these bound states of heavy quarks it is possible to study the hot and dense medium created in ultrarelativistic nuclear collisions, tackling phenomena like colour screening and recombination, which play a significant role in their suppression and regeneration.
This thesis presents the first measurement of the prompt production ratio of two charmonium states at forward rapidity as a function of event activity in PbPb collisions. The ratio of production cross-sections of $\psi(2S)$ and J/ψ mesons times the ratio of their branching fractions into the dimuon final state is measured as a function of event activity using data collected by the LHCb detector at CERN, at both $\sqrt{s_{\mathrm{NN}}} = 5.02$ TeV and $\sqrt{s_{\mathrm{NN}}} = 5.36$ TeV in Run 2 and Run 3, respectively. The measured ratio is compared to the latest theory predictions and to other measurements in literature.

Contents

Declaration of Authorship **iii**

Abstract **v**

Introduction **xi**

1 Theory **1**
1.1 Standard Model . . . 1
1.2 Quantum Chromodynamics . . . 3
1.2.1 Colour confinement and asymptotic freedom . . . 3
1.2.2 Chiral symmetry and spontaneous symmetry breaking . . . 5
1.3 Quarkonium states . . . 5
1.3.1 Quarkonium production and decay . . . 6
1.4 Quark-Gluon Plasma . . . 8
1.4.1 Cold Nuclear Matter effects . . . 9
1.5 Heavy-ion collisions . . . 11
1.5.1 Geometry of the heavy-ion collisions . . . 12
1.5.2 Nuclear modification factor . . . 14
1.5.3 Experimental signatures of the QGP . . . 14
1.5.4 Quarkonia suppression as a tool to study QGP . . . 16
1.5.5 Heavy-ion facilities . . . 18
1.6 $Q\bar{Q}$ production: experimental results . . . 18
1.6.1 $Q\bar{Q}$ production in pp collisions . . . 19
1.6.2 $Q\bar{Q}$ production in pA collisions . . . 20
1.6.3 $Q\bar{Q}$ production in AA collisions . . . 21
1.6.3.1 $\psi(2S)$ over J/ψ production ratio in AA collisions . . . 22

2 The LHCb Experiment **27**
2.1 The Large Hadron Collider . . . 27
2.2 The LHCb Detector . . . 31
2.2.1 Dipole Magnet . . . 33
2.2.2 Tracking System . . . 33
2.2.2.1 VErtex LOcator . . . 34
2.2.2.2 Tracker Turicensis (TT) . . . 36

2.2.2.3 T stations . . . 37
2.2.3 Particle Identification System . . . 37
2.2.3.1 The Ring Imaging Cherenkov Detectors . . . 38
2.2.3.2 The Calorimeter System . . . 40
2.2.3.3 The Muon System . . . 41
2.2.4 The System for Measuring Overlap with Gas (SMOG) . . . 42
2.2.5 The trigger system . . . 44
2.2.5.1 L0 trigger . . . 45
2.2.5.2 High Level trigger . . . 46
2.2.6 Event processing . . . 47
2.2.6.1 Track reconstruction . . . 47
2.2.6.2 Particle identification . . . 48
2.2.7 Data processing framework . . . 49
2.2.8 LHCb simulation . . . 50
2.2.9 Heavy-ion Run 2 data collected at LHCb . . . 51
2.3 The LHCb Upgrade I . . . 53
2.3.1 Tracking System - Upgrade I . . . 54
2.3.1.1 VELO - Upgrade I . . . 54
2.3.1.2 Upstream Tracker (UT) . . . 58
2.3.1.3 Scintillating Fibre (SciFi) . . . 59
2.3.2 Particle Identification System - Upgrade I . . . 60
2.3.3 The trigger system - Upgrade I . . . 61
2.3.4 SMOG Upgrade: SMOG2 . . . 63
2.3.5 Improved performance in Run 3 heavy-ion collisions . . . 64

3 Measurement of $\psi(2S)/J/\psi$ in PbPb collisions at $\sqrt{s_{\mathrm{NN}}} = 5.02$ TeV (Run 2 Analysis) 67
3.1 Analysis strategy . . . 67
3.2 Data and simulation samples . . . 68
3.2.1 Data and data taking conditions . . . 68
3.2.1.1 Trigger selection . . . 68
3.2.1.2 Selection in the "stripping" stage . . . 69
3.2.2 Simulation . . . 69
3.3 Sample selection . . . 70
3.3.1 Global event selection . . . 70
3.3.2 J/ψ and $\psi(2S)$ candidate selection . . . 71
3.3.2.1 Prompt candidate selection . . . 72
3.4 Centrality measurement . . . 74
3.4.1 Basic strategy . . . 74
3.4.2 Glauber model and fit results . . . 75
3.4.3 Centrality bins for this analysis . . . 77

3.5 Signal yields extraction . . . 77
3.6 Efficiencies determination . . . 80
3.6.1 Truth-matching efficiency . . . 81
3.6.2 MC weighting . . . 84
3.6.3 Acceptance efficiency . . . 85
3.6.4 Reconstruction and selection efficiency . . . 88
3.6.5 MuonID efficiency . . . 90
3.6.6 Trigger efficiency . . . 97
3.6.7 Total efficiency . . . 99
3.7 Systematic uncertainties . . . 101
3.7.1 Fit model . . . 101
3.7.1.1 Signal model . . . 101
3.7.1.2 Background model . . . 102
3.7.1.3 Same-sign dimuon fit cross-check . . . 103
3.7.2 Prompt candidate selection . . . 104
3.7.3 Efficiency estimation . . . 104
3.7.3.1 MC sample size limitation . . . 104
3.7.3.2 MC reweighting . . . 104
3.7.3.3 MuonID efficiency . . . 105
3.7.3.4 Trigger efficiency . . . 107
3.7.4 Summary of systematic uncertanties . . . 108
3.8 Results . . . 108

4 Measurement of $\psi(2S)/J/\psi$ in PbPb collisions at $\sqrt{s_{\mathrm{NN}}} = 5.36$ TeV (Run 3 Analysis) 113
4.1 Analysis strategy . . . 113
4.2 Data and simulation samples . . . 114
4.2.1 Data and data-taking conditions . . . 114
4.2.1.1 Trigger selection . . . 114
4.2.2 Simulation . . . 114
4.3 Sample selection . . . 114
4.3.1 Global event selection . . . 115
4.3.2 J/ψ and $\psi(2S)$ candidate selection . . . 115
4.4 Centrality determination . . . 117
4.4.1 Methodology . . . 117
4.4.2 Centrality classes and current binning . . . 119
4.5 Signal yield extraction . . . 120
4.6 Efficiencies determination . . . 122
4.6.1 MC reweighting . . . 122
4.6.2 Acceptance efficiency . . . 123
4.6.3 Reconstruction and selection efficiency . . . 125

4.6.4 Muon identification efficiency . . . 128
4.6.5 Trigger efficiency . . . 131
4.6.6 Total efficiency . . . 132
4.7 Preliminary Results . . . 134

Conclusions **139**

A Run 2 Analysis **141**
A.1 Simulation fit results . . . 141
A.2 Charmonium–Muon p_{T} Correlation . . . 142
A.3 Tag&Probe PID Efficiency Cross-Check . . . 143
A.4 Alternative signal fit model . . . 145
A.5 Alternative background fit model . . . 145

B Run 3 Analysis **147**
B.1 Simulation fit results . . . 147
B.2 Fit results for the Muon Efficiency with Tag&Probe . . . 148

C Transverse polarization measurement of Λ hyperons in pNe collisions at $\sqrt{s_{\mathrm{NN}}} = 68.4$ GeV **157**
C.1 Introduction . . . 157
C.2 The LHCb detector . . . 158
C.3 Data sample and analysis strategy . . . 159
C.4 Simulation and efficiencies . . . 160
C.5 Results and systematic uncertainties . . . 161
C.6 Conclusions . . . 165

Bibliography **167**

Introduction

The Standard Model (SM) of particle physics provides a remarkably successful framework for describing the fundamental constituents of matter and their interactions [1]. It incorporates the electromagnetic, weak, and strong forces, three of the four known fundamental interactions, into a self-consistent quantum field theory. Within this framework, quarks and leptons, the elementary building blocks of matter, interact via the exchange of gauge bosons: photons for electromagnetism, $W^{\pm}$ and Z^0 bosons for the weak force, gluons for the strong force, and the Higgs boson, which provides mass to the elementary particles through the Higgs mechanism. The strong interaction, described by the theory of Quantum Chromodynamics (QCD), governs the dynamics of quarks and gluons, confined inside the hadrons. QCD exhibits a rich phenomenology across a wide range of energy scales. At high momentum transfer, the running of the strong coupling constant makes the theory perturbative. In contrast, at lower energies, QCD becomes nonperturbative, giving rise to complex phenomena such as hadronisation and the formation of bound states like mesons and baryons. One of the most intriguing predictions of QCD is the existence of a deconfined phase of quarks and gluons at extreme temperatures and energy densities: the Quark-Gluon Plasma (QGP) [2].

This state of matter is believed to have existed shortly after the Big Bang and can now be recreated in heavy-nuclei collisions at high-energy accelerators such as the Large Hadron Collider (LHC) [3] at CERN. The experimental study of the QGP relies on identifying sensitive probes of its properties. Among these, heavy quarkonium states, bound states of charm–anticharm or bottom–antibottom pairs, play an important role. Their formation and survival in the medium are influenced by colour screening [4], dissociation, and regeneration processes [5], offering insight into the QGP formation, temperature and dynamical evolution. The differential suppression patterns of different charmonium states, such as the ground state J/ψ and the first excited state $\psi(2S)$, are especially relevant due to their differing binding energies and production mechanisms.

The thesis is devoted to the study of charmonium production in heavy-ion collisions at LHCb, focusing on the $\psi(2S)/J/\psi$ production ratio as a probe of the QGP. Its main objective is to measure the ratio in PbPb collisions at $\sqrt{s_{\mathrm{NN}}} = 5.02$ TeV in the forward rapidity region using data collected during Run 2, and at $\sqrt{s_{\mathrm{NN}}} = 5.36$ TeV in Run 3. The results are interpreted in terms of suppression and regeneration mechanisms in

the QGP.

The thesis is organised as follows. Chapter 1 describes the theoretical framework, including a general overview of the Standard Model, the fundamentals of QCD, and the main properties of the Quark–Gluon Plasma. The production and suppression of heavy quarkonium in high-energy nuclear collisions are also discussed, along with the role of the $\psi(2S)/J/\psi$ ratio as an experimental observable sensitive to QGP effects. Chapter 2 describes the LHCb experiment in detail, focusing on the detector subsystems most relevant for the analysis of dimuon final states in the heavy-ion environment. The performance of the tracking, particle identification, and trigger systems is also illustrated for the Run 2 configuration. In addition, the upgraded Run 3 detector is presented, highlighting the major improvements introduced for high-luminosity operation, and explaining the improvements achieved for the heavy-ion sector. A dedicated section (2.3.1.1) is also included on the new vertex locator detector, with a focus on studies I performed during its commissioning phase. Chapter 3 presents the analysis performed on the 2018 (Run 2) PbPb dataset. It includes the selection of signal candidates, the extraction of signal yields via dimuon invariant mass fits, and the evaluation of efficiencies using simulation and data-driven techniques. The treatment of systematic uncertainties affecting the cross-section ratio measurement is also described before showing the results obtained. Finally, Chapter 4 discusses the preliminary results of the ratio measurement using data from Run 3 of the LHC. With the upgraded LHCb detector and improved data-taking conditions, the new dataset provides an opportunity to enhance the precision and scope of the measurement. In particular, since the accessible centrality range is significantly extended, a more comprehensive exploration of collision dynamics across different event classes is allowed. The reconstruction, selection strategies, trigger performance, and preliminary yield studies, are documented in this chapter.

In addition to the primary focus on quarkonium production in nucleus–nucleus collisions, part of the research work carried out during this PhD has been devoted to the study of spin-dependent phenomena in fixed-target collisions. In particular, a measurement of the transverse polarisation of Λ hyperons produced in proton–neon (pNe) collisions at $\sqrt{s_{\mathrm{NN}}} = 68.4$ GeV was performed using data collected with the fixed-target (SMOG [6]) system at LHCb. The analysis is motivated by the growing interest in transverse-momentum-dependent (TMD) parton distribution functions, and it probes spin-orbit correlations in the fragmentation process in a novel kinematic regime [7, 8, 9]. The results, which represent the first measurement of Λ polarisation in a fixed-target configuration at the LHC energies, have been published in a peer-reviewed journal and are included in the thesis as an appendix (see Appendix C). Although the physics goals are distinct from the heavy-ion analysis discussed in the main chapters, this complementary work reflects the broader scope of the LHCb experiment and the diversity of topics addressed during the doctoral research.

Chapter 1

Theory

One of the main goals of modern physics is to understand the fundamental constituents of matter and the forces that govern their interactions. The Standard Model (SM) of particle physics is the theoretical framework that currently provides the most accurate and comprehensive description of these phenomena. In this chapter, the structure and key components of the Standard Model are explained, with a particular focus on the strong interaction and the theory that describes it: Quantum Chromodynamics (QCD). This opens the way to study extreme QCD phenomena like the formation of the Quark-Gluon Plasma (QGP), which can be investigated using heavy-nuclei collisions. The suppression of $q\bar{q}$ bound states, called quarkonia, is one of the signatures of QGP formation and constitutes the main focus of the analyses presented in this thesis.

1.1 Standard Model

The Standard Model describes all known elementary particles and three of the four fundamental forces in nature: electromagnetic, weak, and strong, within the framework of quantum field theory. Developed over the second half of the twentieth century, the SM has been remarkably successful in explaining a wide range of experimental results, culminating in the discovery of the Higgs boson in 2012.

The SM incorporates the Glashow-Weinberg-Salam (GWS) model, which unifies the electromagnetic and weak forces into the electroweak interaction, and Quantum Chromodynamics, which describes the strong interaction. The three interactions are embedded in a gauge symmetry structure given by $SU(3)_C \times SU(2)_L \times U(1)_Y$, corresponding to the strong, weak, and electromagnetic forces, respectively. Each of these gauge symmetries is associated with a set of force carriers [1]:

- 8 massless gluons (g) for the strong interaction,
- 3 massive bosons ($W^{\pm}$ and Z^0) for the weak interaction,
- 1 massless photon (γ) for the electromagnetic interaction.

Elementary particles (Fig. 1.1) are classified, according to their spin, into fermions, with semi-integer spin, and bosons, with integer spin, which include the interaction mediator particles and the Higgs boson. Fermions can be divided into leptons and quarks: the first interact only via the electroweak interaction, while the latter also via the strong force. Leptons and quarks, the main constituents of matter, are arranged in three families and particles in the same family have different masses.

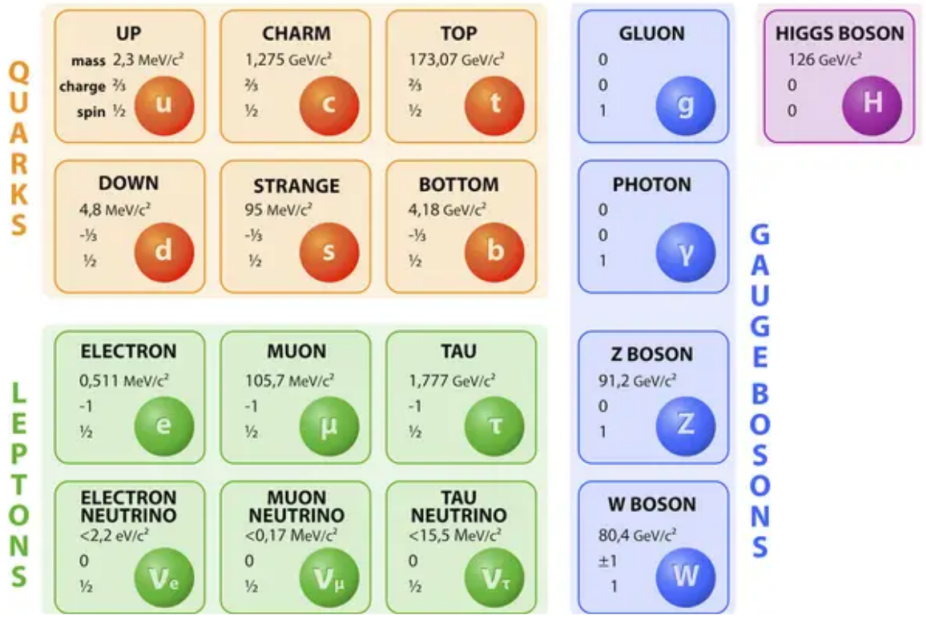


FIGURE 1.1: Elementary particles of the Standard Model, with their mass, charge and spin.

Although the SM is an established theory confirmed by decades of experiments, to date it still has a few inconsistencies and limitations. For example it does not explain:

- The existence of dark matter and dark energy (96% of the matter in the universe is "dark");
- The excess of baryons over antibaryons in the universe (the SM contains a mechanism to explain this, the CP violation, however it predicts a baryon-antibaryon asymmetry that is ten orders of magnitude smaller than needed to explain such excess);
- The origin of the neutrino (ν) masses;
- The inclusion of gravity, which is the fourth fundamental interaction governing the universe.

Moreover, the Standard Model is not able to answer some fundamental questions regarding the QCD, the theory that describes the strong interaction among quarks,

mediated by gluons, on which the focus of this thesis is posed. A number of Beyond the Standard Model (BSM) theories have been proposed to expand the SM into a more universal theory which would accommodate solutions to these problems, but none has been experimentally confirmed at present.

1.2 Quantum Chromodynamics

Quantum Chromodynamics is the quantum field theory that describes the strong interaction, one of the four fundamental forces of nature. It is a non-abelian gauge theory based on the $SU(3)_C$ symmetry group, where the subscript C stands for *colour*, the charge associated with the strong force. QCD governs the dynamics of quarks and gluons, the fundamental constituents of hadronic matter.

The QCD Lagrangian is given by:

$$\mathcal{L}_{\text{QCD}} = \sum_{f=1}^{N_f} \bar{q}_f (i\gamma^\mu D_\mu - m_f) q_f - \frac{1}{4} G^a_{\mu\nu} G^{a\mu\nu}, \tag{1.1}$$

where q_f represents the quark field of flavour f with mass m_f, and $D_\mu = \partial_\mu - i\alpha_s T^a A^a_\mu$ is the covariant derivative, with α_s the strong coupling constant, A^a_μ the gluon fields, and T^a the generators of the $SU(3)$ group. The gluon field strength tensor $G^a_{\mu\nu}$ is defined as:

$$G^a_{\mu\nu} = \partial_\mu A^a_\nu - \partial_\nu A^a_\mu + \alpha_s f^{abc} A^b_\mu A^c_\nu, \tag{1.2}$$

where f^{abc} are the structure constants of $SU(3)$. QCD predicts the existence of eight massless gluons corresponding to the eight generators of the colour group. Unlike the photons in Quantum Electrodynamics (QED), gluons carry colour charge and can interact with each other. This self-interaction is a fundamental property of non-Abelian gauge theories, responsible for key phenomena such as confinement and asymptotic freedom, described below.

1.2.1 Colour confinement and asymptotic freedom

Quarks carry one of three colour charges (red r, green g, or blue b), while antiquarks carry the corresponding anticolour ($\bar{r}$, $\bar{g}$, $\bar{b}$). Observable particles must be colour-neutral, a condition known as colour confinement. To satisfy this requirement, quarks must combine in such a way that their colour charges cancel out, forming colour-singlet states, allowing the formation of hadrons, the observable particles in nature composed of quarks. The two main classes of hadrons are mesons, consisting of a quark and an antiquark ($q\bar{q}$), and (anti)baryons, composed of three quarks ($\bar{q}\bar{q}\bar{q}$)qqq. In both cases, the combination of colour charges results in an overall neutral (white) colour state, making the particle colourless and so consistent with confinement.

One of the most remarkable properties of QCD is its energy dependence, encapsulated in the concept of the running coupling constant. The strength of the strong interaction decreases with increasing energy scale (or decreasing distance), a phenomenon known as asymptotic freedom. At sufficiently high energies, quarks and gluons interact weakly and can be treated perturbatively. Conversely, at low energies, the coupling becomes large and non-perturbative effects dominate, leading to the phenomenon of colour confinement, which prevents the observation of free quarks or gluons.

The one-loop expression for the running of the strong coupling constant α_s is:

$$\alpha_s(Q^2) = \frac{\alpha_s(Q_0^2)}{1 + \alpha_s(Q_0^2)\frac{11N_c - 2N_f}{12\pi}\log\left(\frac{Q^2}{Q_0^2}\right)}, \tag{1.3}$$

where $N_c = 3$ is the number of colours and $N_f = 3$ is the number of quark flavours. This expression shows (Fig. 1.2) that α_s decreases logarithmically with increasing momentum transfer Q^2. At low Q^2, the coupling grows large, marking the breakdown of perturbation theory and the onset of confinement.

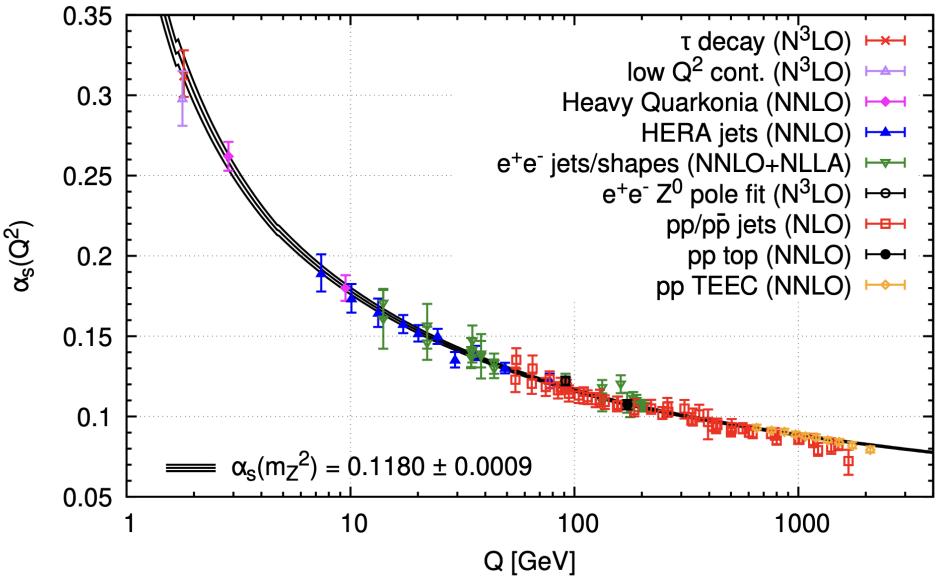


FIGURE 1.2: Summary of different measurements of the running constant of the strong interaction as a function of the energy scale Q [10].

However, in the high-energy regime where asymptotic freedom dominates, quarks and gluons behave as quasi-free particles. This opens the possibility to study a deconfined phase of strongly interacting matter, where quarks and gluons are no longer bound inside hadrons. As will be discussed in Sec. 1.4 and 1.5, such conditions can be achieved in high-energy heavy-nuclei collisions, potentially leading to the formation of the Quark-Gluon Plasma.

1.2.2 Chiral symmetry and spontaneous symmetry breaking

Another important feature of QCD is that, in the limit of vanishing quark masses, its Lagrangian exhibits a global chiral symmetry: $SU(N_f)_L \times SU(N_f)_R$. However, this symmetry is spontaneously broken in the QCD vacuum, leading to the formation of a non-zero quark condensate $\langle \bar{q}q \rangle \neq 0$. This spontaneous symmetry breaking gives rise to (pseudo-)Goldstone bosons, which are identified with the lightest pseudoscalar mesons (*e.g.*, pions).

Chiral symmetry breaking is a crucial mechanism in hadronic physics, as it explains why hadrons acquire masses that are much larger than the sum of the bare quark masses. It also plays an important role in the behaviour of QCD matter under extreme conditions, such as high temperature or baryon density, where chiral symmetry is expected to be (partially) restored and confinement may be lifted, leading to the formation of the Quark-Gluon Plasma. For the lightest quark flavours (up, down, and to a good approximation strange) the restoration of chiral symmetry at high temperature is considered nearly complete, since their masses are small compared to the QCD scale $\Lambda_{\mathrm{QCD}} \sim 200$ MeV/c^2 [11, 12].

1.3 Quarkonium states

An important class of hadronic bound states, especially for the content of the thesis, is represented by quarkonia, mesons composed of a heavy quark and its corresponding antiquark ($Q\bar{Q}$), where Q denotes either a charm (c) or a bottom (b) quark. Quarkonium systems provide a unique testing ground for QCD in both perturbative and non-perturbative regimes: the heavy-quark mass sets a hard scale that allows perturbative calculations of the production processes, while the subsequent binding into hadronic states requires a proper description of long-distance dynamics. Among the various quarkonium families, two are especially relevant:

- **Charmonium ($c\bar{c}$)**: including the s-wave ground state J/ψ, the excited $\psi(2S)$, as well as p-wave χ_c and η_c states.
- **Bottomonium ($b\bar{b}$)**: including the s-wave ground state $\Upsilon(1S)$, the excited $\Upsilon(2S)$ and $\Upsilon(3S)$, together with p-wave χ_b and η_b states.

Quarkonia are identified by the spectroscopic notation $n\,^{2S+1}L_J$, where n is the radial quantum number, S is the total spin, L is the orbital angular momentum, and J is the total angular momentum. The parity (P) and charge-conjugation (C) quantum numbers are given by:

$$P = (-1)^{L+1}, \qquad C = (-1)^{L+S}. \tag{1.4}$$

A summary of the most relevant quarkonium states, together with their quantum numbers and masses, is provided in Tab. 1.1.

TABLE 1.1: Main quarkonium states with their quantum numbers and masses [13].

State	Family	J^{PC}	Mass [MeV/c^2]
$J/\psi(1S)$	$c\bar{c}$	1^{--}	3097
$\psi(2S)$	$c\bar{c}$	1^{--}	3686
$\chi_{c0}(1P)$	$c\bar{c}$	0^{++}	3415
$\chi_{c1}(1P)$	$c\bar{c}$	1^{++}	3511
$\chi_{c2}(1P)$	$c\bar{c}$	2^{++}	3556
$\Upsilon(1S)$	$b\bar{b}$	1^{--}	9460
$\Upsilon(2S)$	$b\bar{b}$	1^{--}	10023
$\Upsilon(3S)$	$b\bar{b}$	1^{--}	10355
$\chi_{b1}(1P)$	$b\bar{b}$	1^{++}	9892

1.3.1 Quarkonium production and decay

In high-energy proton-proton (pp) collisions, $Q\bar{Q}$ production is regulated by perturbative QCD processes. The dominant production mechanism is gluon-gluon fusion, given the high gluon density at high energies, together with the $Q\bar{Q}$ annihilation as shown in Fig 1.3.

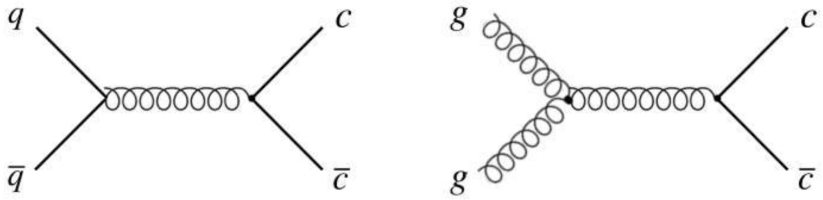


FIGURE 1.3: Feynman diagrams of the main $c\bar{c}$ production mechanisms at Leading Order (LO): quark annihilation (left) and gluon fusion (right).

Once the heavy-quark pair is produced, it can either hadronise into open heavy-flavour mesons or form a quarkonium bound state.

Several theoretical models describe the formation of quarkonium states, explained below:

- **Colour Singlet Model (CSM)**: Assumes that the $Q\bar{Q}$ pair is produced in a colour-singlet state with the same quantum numbers as the final quarkonium. The hadronisation is then described by a wavefunction at the origin. While simple and predictive, it underestimates cross-sections at high transverse momentum (p_{T}) [14].

- **Colour Octet Mechanism (COM)**: It allows the $Q\bar{Q}$ pair to be initially produced in a colour-octet state, which subsequently neutralises its colour via soft gluon emission. This improves the agreement with data, especially at high p_T, but introduces non-perturbative long-distance matrix elements (LDMEs) that must be extracted from data [15, 16].

- **Non-Relativistic QCD (NRQCD)**: A rigorous effective field theory that systematically separates short-distance perturbative processes from long-distance non-perturbative dynamics. It includes both singlet and octet contributions and has become the standard framework to study quarkonium production [17]. It provides a satisfactory description of the data so far but fails in reproducing simultaneously the experimental results of observables as cross-section and polarisation in a wide kinematic range.

Once produced, quarkonium states evolve and eventually decay through different channels. The pattern of these decays is governed by the interplay of strong, electromagnetic, and weak interactions [18].

For quarkonium above the open heavy-flavour threshold, the dominant decay modes are strong decays into open-flavour mesons. For states below threshold, the main decay mechanisms include annihilation into leptons or hadrons, as well as radiative transitions to lower quarkonium states:

- **Strong decays** into open charm or open beauty mesons such as $\psi(3770) \to D\bar{D}$ or $\Upsilon(4S) \to B\bar{B}$, resulting in large decay widths. These channels provide a valuable probe of α_s at the quarkonium mass scale and of non-perturbative QCD dynamics.

- **Electromagnetic decays** which occur when the $Q\bar{Q}$ pair annihilates into a virtual photon that subsequently materialises as a lepton pair. For instance, the dileptonic channels $J/\psi,\ \psi(2S) \to e^+e^-,\ \mu^+\mu^-$ and $\Upsilon(nS) \to e^+e^-,\ \mu^+\mu^-$ play a central role in quarkonium studies.

- **Radiative transitions** between quarkonium states, such as $\chi_{cJ} \to J/\psi + \gamma$ or $\psi(2S) \to \chi_{cJ} + \gamma$, play an important role in mapping out the quarkonium spectrum.

In the context of this thesis, special emphasis is placed on the J/ψ and $\psi(2S)$ states. While their dominant decay modes are hadronic, the dilepton channels are the most relevant for experimental studies. Despite their relatively small branching fractions, $\mathcal{B}(J/\psi \to \mu^+\mu^-) \simeq 5.9\%$ and $\mathcal{B}(\psi(2S) \to \mu^+\mu^-) \simeq 0.8\%$ [13], these decays provide exceptionally clean signatures in a hadronic environment, as leptons are unaffected by the strong interaction and can be efficiently reconstructed experimentally.

Consequently, dilepton decays, specifically into dimuons, constitute the *golden* channel for experimental analyses, especially in heavy-nuclei collisions, where hadronic decays are overwhelmed by background.

From an experimental point of view, the observed quarkonium sample consists of three components. *Prompt direct* mesons are produced directly in the primary interaction. *Prompt indirect* mesons originate from the decays of heavier quarkonia, such as $\chi_c \to J/\psi\,\gamma$, which occur essentially at the primary vertex and do not exhibit a measurable displacement. Finally, *nonprompt* (or from-b) mesons arise from the weak decays of longer-lived hadrons containing a b quark, *e.g.*, $B \to J/\psi + X$, where X denotes additional hadrons. The nonprompt charmonia can be experimentally distinguished from the prompt component thanks to their displaced decay vertices, a consequence of the relatively long b-hadron lifetime ($\tau_B \sim 1.5$ ps). In high-energy pp collisions, nonprompt decays typically contribute 10–20% of the inclusive charmonium yield [19, 20].

1.4 Quark-Gluon Plasma

Quarkonium states are very sensitive to the surrounding medium, making them directly connected to the study of deconfined matter. Quantum Chromodynamics predicts that, under extreme conditions of temperature and baryon density, hadronic matter undergoes a transition to a new state where quarks and gluons are no longer confined within hadrons, known as the Quark-Gluon Plasma. It is characterised by deconfinement and the (partial) restoration of chiral symmetry. In the medium, the relevant degrees of freedom are the colour-charged quarks and gluons, rather than colour-neutral hadrons.

The QCD phase diagram (Fig. 1.4) summarises the expected phases of strongly interacting matter in the plane of temperature T and baryon chemical potential μ_B. At low temperature and μ_B, ordinary hadronic matter is stable. However, as the temperature increases (or, alternatively, as μ_B increases at low T), a transition to the QGP is expected to occur.

From a theoretical point of view, lattice QCD simulations at vanishing baryon chemical potential ($\mu_B \sim 0$), relevant for early-universe conditions and high-energy heavy-nuclei collisions, indicate that the transition is a smooth crossover rather than a sharp phase transition [22]. The crossover is expected to occur at a pseudo-critical temperature of $T_c \sim 155$ MeV [23]. At higher values of μ_B, which are more relevant for the physics of neutron stars and collisions at lower energies, model calculations suggest the presence of a first-order phase transition and a hypothetical critical endpoint, although its precise location remains experimentally unconfirmed [24, 25].

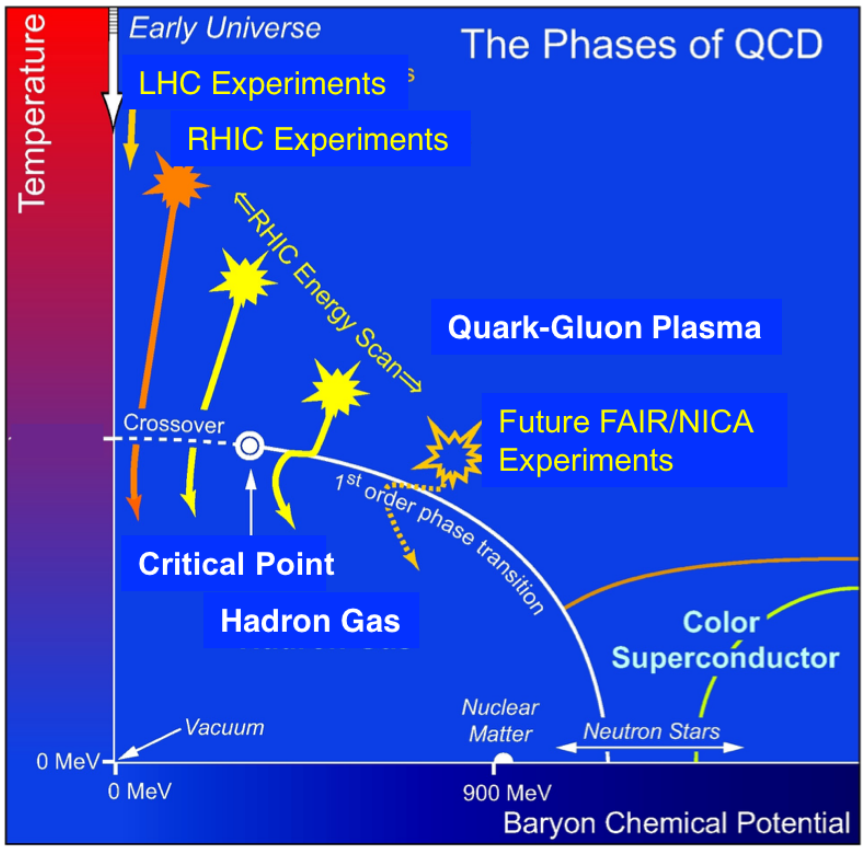


FIGURE 1.4: Phase diagram of the hadronic matter [21].

1.4.1 Cold Nuclear Matter effects

Before discussing the signatures and tools used to study the properties of the QGP, it is important to consider the so-called Cold Nuclear Matter (CNM) effects. Listed below, these effects arise from the nuclear environment itself, independently of any deconfined medium, and play a crucial role in QGP studies. They can indeed mimic or mask genuine QGP-induced modifications and must therefore be carefully understood and subtracted in order to clearly establish the QGP formation.

- **Nuclear Parton Distribution Functions (nPDFs)**: Parton distributions inside nuclei differ from those in free protons, which affects the initial-state parton flux in nuclear collisions. Similarly to the PDFs measured in proton–proton collisions, nPDFs describe the probability to find a parton carrying a given fraction of the nucleon's momentum at a certain energy scale. Their precise knowledge is crucial, as they can be modified in different regions of phase space by various nuclear effects, illustrated in Fig. 1.5:

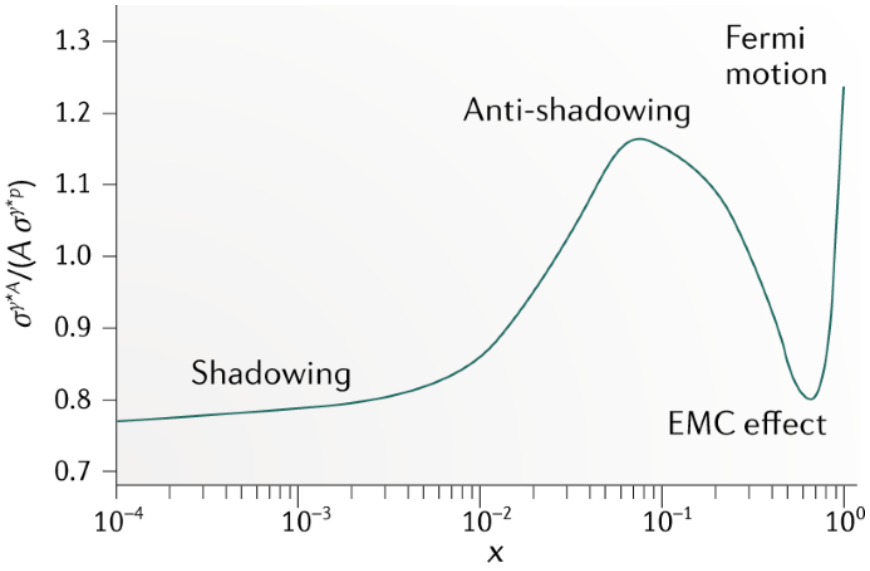


FIGURE 1.5: Schematic behaviour of the nPDFs effects as a function of Bjorken-x for a fixed Q^2.

Shadowing: at low Bjorken-x (the fraction of the nucleon momentum carried by a parton), gluon densities are reduced in nuclei compared to free protons, suppressing $Q\bar{Q}$ production.

Anti-shadowing: in the intermediate x region (~ 0.1), gluon densities can be enhanced, possibly increasing $Q\bar{Q}$ yields.

EMC effect: at high Bjorken-x, parton distributions are suppressed in bound nucleons due to modifications of nucleon structure in the nuclear medium.

Fermi motion: at very high $x \to 1$, the nucleon's momentum distribution inside the nucleus introduces a broadening of the parton kinematics, possibly affecting production rates.

nPDFs, such as EPPS16 [26] or nCTEQ15 [27], are used to model shadowing or anti-shadowing effects on the initial gluon densities.

- **Gluon Saturation:** at very small x, the continuous growth of the gluon density measured [28], shown in Fig. 1.6, may lead to gluon saturation effects, depending on Q^2 and Bjorken-x. This saturation at low-x would limit quarkonium production resulting in suppressed yields.

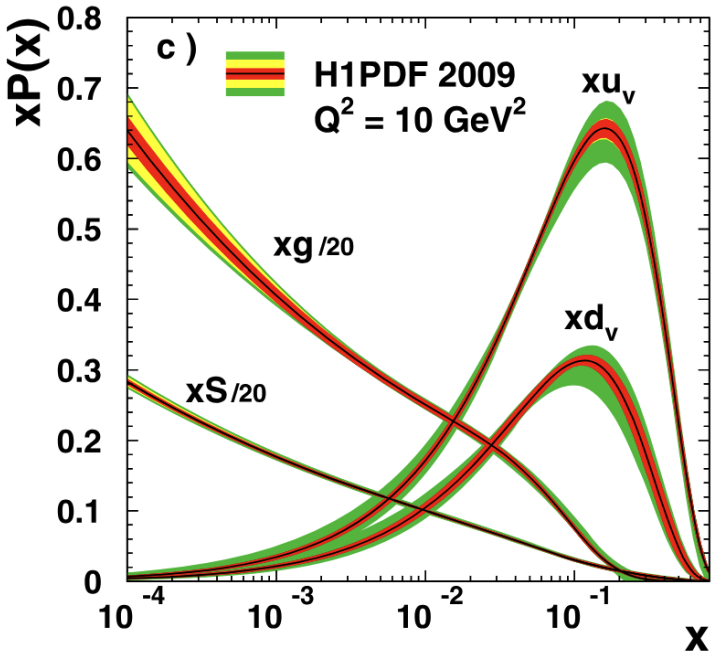


FIGURE 1.6: Evolution of the gluon, sea quark, and valence quark distributions at $Q^2 = 10$ GeV$^2/c^2$ [28].

- **Coherent Parton Energy Loss:** initial-state partons can lose energy through gluon radiation while traversing the nucleus. The coherent parton energy loss, as modelled in the framework of Arleo and Peigné [29], can lead to a suppression of the final-state $Q\bar{Q}$ yield, especially at forward rapidity, without invoking a thermalised medium.

Having introduced the QGP together with the CNM effects that can influence its signals, the next step is to consider the tools used to recreate and study this hot and dense state of matter in the laboratory: the heavy-ion collisions.

1.5 Heavy-ion collisions

Ultra-relativistic heavy-ion collisions provide the only known method to create and study the Quark-Gluon Plasma in laboratory. When two heavy nuclei (such as Pb or Au) collide at high energies, a large amount of energy is deposited in a small volume, leading to the formation of an extremely hot and dense medium where quarks and gluons can become deconfined.

The space-time evolution of the system produced in a heavy-ion collision, represented in Fig. 1.7, is typically described using a hydrodynamic picture, with distinct stages. A simplified framework to describe this evolution was proposed by Bjorken [30], assuming longitudinal boost invariance near midrapidity. The initial collision produces

a highly excited system in which partons undergo hard scatterings and gluon radiation. Shortly after the collision (within $\sim$ 0.1-1 fm/c), the system evolves toward a locally thermalized state: this marks the formation of the QGP phase.

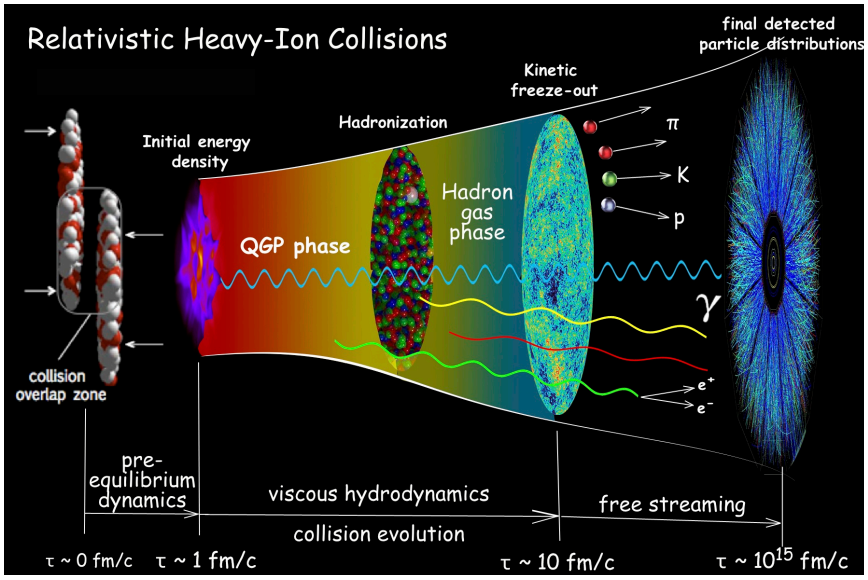


FIGURE 1.7: Space-time evolution of a heavy-ion collision with QGP formation.

As the system expands and cools down, it reaches the critical temperature $T_c \sim 155$ MeV [23], below which quarks and gluons hadronise into colour-neutral hadrons. This stage is known as the chemical freeze-out, where inelastic collisions stop and the relative abundances of particle species are fixed. The system continues to expand until it reaches the so-called kinetic freeze-out, where elastic scatterings also stop and the momentum distributions of the final-state hadrons are fixed.

Understanding the full space-time evolution of the QGP requires a combination of theoretical modelling and experimental input. While the general picture describes a deconfined phase followed by hadronisation and freeze-out, the properties of the medium, such as its temperature, viscosity, and opacity, must be inferred indirectly. Accordingly, a variety of experimental observables have been developed, each providing complementary insights into different stages and aspects of the QGP.

1.5.1 Geometry of the heavy-ion collisions

The outcome of a heavy-ion collision is strongly influenced by the initial geometry of the interacting nuclei. The key parameter characterising the geometry is the *impact parameter* b, defined as the transverse distance between the centres of the two colliding nuclei at closest approach, as shown in the top panel of Fig. 1.8. The value of b determines the *centrality* of the collision, which quantifies the degree of overlap

between the two nuclei. Depending on the value of the impact parameter, heavy-ion collisions are typically classified into three categories:

- **Peripheral collisions** ($b \sim R$, with R the nuclear radius) have a small overlap area, resulting in low initial energy density and a small QGP volume. They are illustrated in the bottom left panel of Fig. 1.8. If $b > R$, the nuclei do not touch but interact exchanging a photon in what are called Ultra-Peripheral Collisions (UPCs).
- **Non-Central collisions** ($0 < b < R$) produce an asymmetric, almond-shaped overlap region. The spatial anisotropy in the initial geometry leads to anisotropic pressure gradients in the medium, which drive collective flow phenomena such as elliptic flow. They are illustrated in the bottom central panel of Fig. 1.8.
- **Central collisions** ($b \sim 0$) correspond to nearly head-on impacts, producing a large, approximately circular overlap region. They generate the highest energy densities and temperatures, creating a hot QGP. They are illustrated in the bottom right panel of Fig. 1.8.

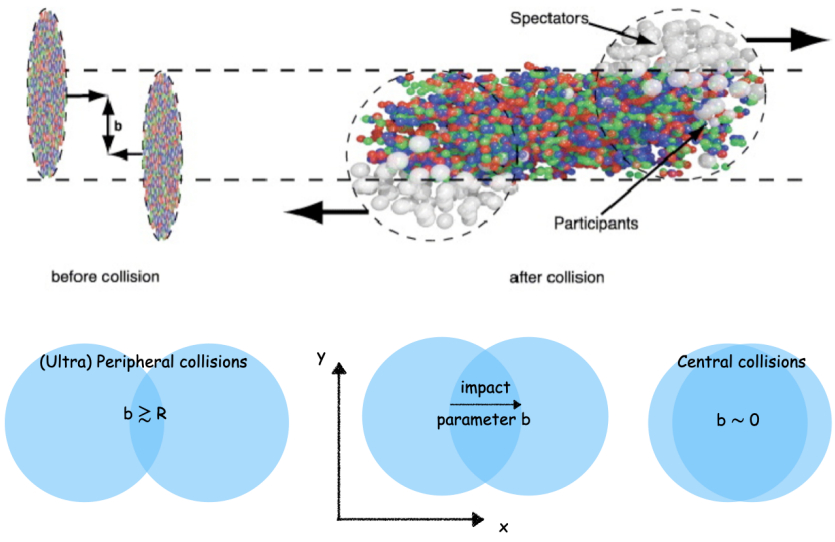


FIGURE 1.8: Illustration of a heavy-ion collision, showing (top) the impact parameter b, the separation of spectators and participants, and (bottom) the classification of collisions by centrality in the transverse plane. The colliding beams travel along the z axis, perpendicular to the plane of the figure.

The centrality classes are usually expressed as percentiles of the total hadronic cross-section and are experimentally estimated either by measuring the multiplicity of produced particles, which correlates with the number of participants N_{part}, or by detecting spectator nucleons that do not interact, typically with dedicated detectors

usually placed away from the interaction point very close to the beam. A phenomenological approach based on Glauber models [31] is used to characterise the geometry of the collisions. Here, the nucleons trajectories are treated as straight lines and the nucleon-nucleon collisions are assumed independent.

The number of binary nucleon-nucleon collisions N_{coll} is also an important quantity derived from this geometry. More details on the experimental determination of the centrality classes are presented in Sec. 3.4.

The collision geometry affects many important features of the medium, including its size, but also its lifetime, temperature profile, and density gradients. Such parameters influence the production, propagation, and behaviour of probes used to study it, such as jets and quarkonia, and thus impact the observed experimental signatures of the QGP. By studying collisions across different centralities, experiments can map out how QGP properties evolve with the initial conditions, allowing for stringent tests of theoretical models of QGP formation and evolution.

1.5.2 Nuclear modification factor

One of the key observables used to quantify the effects of the QGP medium on particle production in heavy-ion collisions is the so-called *nuclear modification factor*. It allows a quantitative comparison between different collision systems and energies, and it is defined as

$$R_{AA}(p_T, y) = \frac{1}{\langle N_{\text{coll}} \rangle} \frac{d^2N^{AA}/dp_T dy}{d^2N^{pp}/dp_T dy}, \tag{1.5}$$

The nuclear modification factor compares particle production in nucleus-nucleus (AA) collisions with that in pp, scaled by the number of binary nucleon-nucleon interactions $\langle N_{\text{coll}} \rangle$. If AA collisions were a simple superposition of independent pp collisions, then R_{AA} would be equal to 1. Values smaller than unity indicate suppression, while values larger than unity correspond to an enhancement, both highlighting medium effects.

A related quantity is the nuclear modification factor in proton-nucleus (pA) collisions,

$$R_{pA}(p_T, y) = \frac{1}{\langle N_{\text{coll}} \rangle} \frac{d^2N^{pA}/dp_T dy}{d^2N^{pp}/dp_T dy}, \tag{1.6}$$

which is used to isolate the CNM effects.

1.5.3 Experimental signatures of the QGP

Several experimental observables listed below serve as probes of the QGP, each sensitive to different properties of the medium.

- **Jet quenching:** high p_{T} partons produced in the early stages of the collision lose energy as they traverse the QGP through gluon radiation and collisions with

the medium. It results in a suppression of high-p_T hadrons and jets in heavy-ion collisions relative to pp ones. The suppression is quantified using the nuclear modification factor as a function of the transverse momentum $R_{AA}(p_T)$. Jet quenching is a key signature of the dense colour-charged medium and provides information about its opacity and transport properties [32].

- **Particle flow:** in non-central heavy-ion collisions, the almond-shaped overlap region between the nuclei leads to anisotropic pressure gradients, which are translated into momentum anisotropies through the collective hydrodynamic expansion of the medium. As a result, more particles are emitted in-plane (along the short axis of the overlap region) than out-of-plane, as shown in Fig. 1.9.

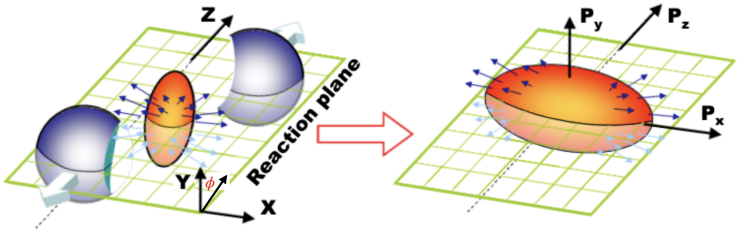


FIGURE 1.9: Schematic illustration of the almond-shaped overlap region in a non-central heavy-ion collision.

The azimuthal distribution of produced particles with respect to the reaction plane can be expressed as a Fourier expansion:

$$\frac{dN}{d\phi} \propto 1 + 2v_1\cos(\phi) + 2v_2\cos(2\phi) + 2v_3\cos(3\phi) + \ldots, \tag{1.7}$$

where ϕ is the azimuthal angle. The coefficients v_n describe different flow components: v_1 (directed flow) reflects the sideward deflection of matter at forward rapidities, v_2 (elliptic flow) arises from the almond-shaped geometry and is the clearest signature of QGP collectivity, while v_3 (triangular flow) originates mainly from initial-state fluctuations.

- **Strangeness enhancement:** in the QGP phase, the high temperature and energy density lower the threshold for strange quark production, allowing strange quarks to be produced more abundantly and rapidly than in hadronic matter. This results in an enhanced yield of strange and multi-strange hadrons (*e.g.*, K, Λ, Ξ, Ω) in heavy-ion collisions compared to baseline pp or pA collisions. Strangeness enhancement is one of the historically proposed signatures of QGP formation [33], as it reflects the thermal and partonic nature of the medium. The effect is particularly pronounced for multi-strange baryons, which are rare in purely hadronic interactions. Recent measurements also show that this enhancement exhibits a smooth dependence on event multiplicity, hinting

that similar mechanisms could possibly play a role even in small systems as pA collisions.

- **Quarkonium suppression:** $Q\bar{Q}$ states are sensitive to the colour screening effect in the deconfined medium [4]. In the QGP, the binding potential between the heavy quark and antiquark is screened by the surrounding colour charges, leading to dissociation of the bound state. Such phenomenon serves as a powerful probe of the QGP temperature and its properties. In addition to suppression, quarkonium production can be influenced by recombination of uncorrelated heavy-quark pairs in the later stages of the medium evolution, which can partially balance suppression effects [34]. The recombination is expected to be more significant at high energies due to the abundant heavy-quark production. A much more detailed discussion of quarkonium suppression and recombination is provided in Sec. 1.5.4.

The observables just illustrated, when combined, provide a comprehensive picture of the QGP properties, from its formation, initial temperature and energy density to its collective behaviour and partonic interactions.

1.5.4 Quarkonia suppression as a tool to study QGP

Quarkonium states, owing to their large masses and short formation times, are produced in the earliest stages of the collision and thus traverse the entire evolution of the QGP, making them powerful probes of the medium. The idea that quarkonium suppression could signal the formation of a deconfined medium was first proposed by T. Matsui and H. Satz, who argued that the colour potential binding the heavy quark and antiquark is screened in the QGP, in analogy with Debye screening in electrodynamics [4]. This mechanism prevents the formation of bound states and leads to a suppression of quarkonium yields, the strength of which depends on the binding energy of the state. In particular, excited states such as the $\psi(2S)$ are expected to dissolve at lower temperatures than the more tightly bound J/ψ, giving rise to a sequential suppression pattern.

Experimentally, quarkonium production in AA collisions is compared to that in pp and pA systems, which provide the necessary baselines. The suppression is quantified through the nuclear modification factor defined in Sec. 1.5.2, allowing the separation of hot-medium effects from CNM or other initial-state effects. Early measurements indeed indicated a suppression of J/ψ production in PbPb collisions [35, 36], but the interpretation was complicated by additional mechanisms, such as final-state interactions with co-moving particles, which can also reduce the observed yield [37].

It has since become clear that suppression alone does not provide the full picture. At high-collision energies, where the total charm cross-section is large, recombination processes become relevant: uncorrelated c and $\bar{c}$ quarks produced in the medium can

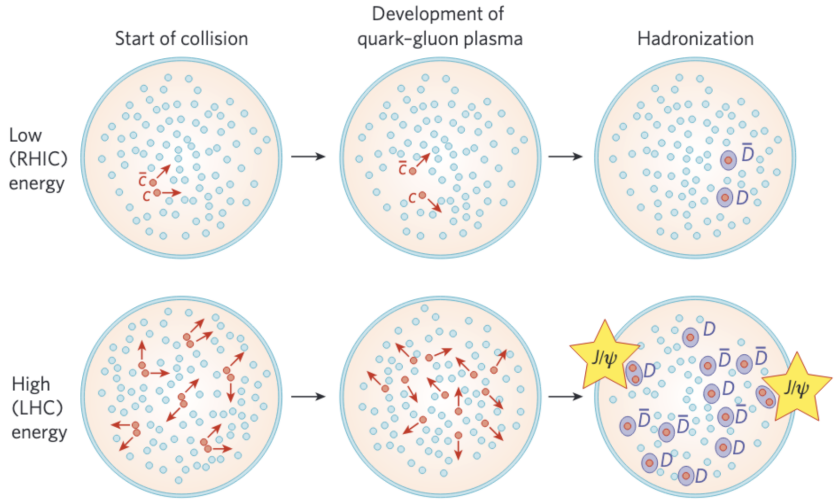


FIGURE 1.10: Low energies: the only $c\bar{c}$ pair created (red dots) is screened by QGP and the single (anti)-charm, paired with any other quark, hadronises into a D meson (purple circles). High energies: many $c\bar{c}$ pairs produced, at hadronisation c and $\bar{c}$ quarks from different original pairs may combine to form a charmonium (yellow stars) [5]

.

recombine into a bound charmonium state either inside the QGP or at the hadronisation stage [38, 39]. The contribution from regeneration is expected to be most significant at low transverse momentum and in central collisions, while at lower energies, where the number of charm quarks is smaller, suppression dominates. The interplay between suppression and regeneration is illustrated in Fig. 1.10.

Several models try to explain the relative contribution of the screening and recombination while describing the charmonia production in PbPb collisions, such as:

- **Transport Model**: it treats quarkonium production as a dynamic interplay between suppression and regeneration within the QGP. The evolution of the quarkonium phase-space distribution is governed by rate equations that include both dissociation and recombination terms, coupled to a realistic hydrodynamic evolution of the medium. The regeneration component increases with the total charm cross-section, becoming significant at high energies. This model can describe both time-dependent suppression and late-stage regeneration [40, 41].

- **Statistical Hadronisation Model (SHM)**: it assumes all charm quarks to thermalise in the QGP, and quarkonia are formed at chemical freeze-out through statistical coalescence of independently produced c and $\bar{c}$ quarks. No bound states are assumed to survive in the deconfined phase; instead, yields are entirely determined by statistical weights at hadronisation. The model naturally explains the increase of charmonium production at high energies and predicts a strong centrality and system-size dependence of the quarkonium yield [42].

- **Co-mover Interaction Model (CIM)**: it attributes the suppression of quarkonia to interactions with the dense medium of co-moving particles produced in the collision, without invoking the formation of a deconfined QGP. Both dissociation (via final-state interactions) and regeneration (through inverse processes) are considered in the hadronic phase. The amount of suppression depends on the density of co-movers and their interaction cross-sections with quarkonia. CIM provides an alternative to QGP-based suppression, especially in small or peripheral systems [43, 37].

A sensitive observable is the $\psi(2S)/J/\psi$ production ratio, since the different binding energies and regeneration probabilities of the two states provide a powerful discriminator between competing scenarios. The measurement of this ratio in large collision systems is the main focus of this thesis.

1.5.5 Heavy-ion facilities

The investigation of the QGP relies on collisions of heavy nuclei at dedicated high-energy facilities. The Large Hadron Collider (LHC) at CERN and the Relativistic Heavy Ion Collider (RHIC) at Brookhaven National Laboratory are the two main machines where such collisions are studied.

At RHIC, gold nuclei (Au+Au) are collided at centre-of-mass energies up to $\sqrt{s_{\mathrm{NN}}}$ = 200 GeV, allowing the creation of a hot and dense medium with temperatures above the predicted QCD critical temperature. The LHC, operating at much higher energies, reaches $\sqrt{s_{\mathrm{NN}}} = 5$ TeV for lead-lead (Pb+Pb) collisions, producing even higher energy densities and extending the study of QGP phenomena to new kinematic regimes.

Several experiments are specifically designed to measure heavy-ion observables at these facilities. At RHIC, STAR and PHENIX provide precise measurements of collective flow, strangeness production, and quarkonium yields, while at the LHC, ALICE focuses on soft probes and low-momentum observables, and ATLAS, CMS, and LHCb extend the reach to high-momentum probes, jets, and forward rapidity measurements.

Together, the measurements performed by these experiments offer a comprehensive view of the QGP, allowing the study of the signatures explained above. The experimental infrastructure provides the essential foundation for the investigations presented in the following section.

1.6 $Q\bar{Q}$ production: experimental results

Quarkonium states provide a powerful probe of the strong interaction and the properties of QCD matter. Their production and suppression patterns have been extensively studied across different collision systems, from pp interactions, which provide a baseline, to pA and AA collisions, where cold and hot nuclear matter effects modify their

yields. In the following sections some of the most recent measurement of quarkonium production in these systems are presented, focusing on J/ψ and $\psi(2S)$ results, culminating in the discussion of their production ratio.

1.6.1 $Q\bar{Q}$ production in pp collisions

Experimentally, all major LHC and RHIC experiments have extensively measured quarkonia production in pp collisions at various centre-of-mass energies ranging between 200 GeV and 13 TeV, partially agreeing with the theoretical model predictions [44, 45, 46]. Such measurements are important to both disentangle the different theoretical models, and serve as a crucial baseline for interpreting heavy-ion results.

Moreover, recently measurements in pp collisions at high-multiplicity show signatures of QGP formation also in small systems, as shown in Fig. 1.11, where the ratio of $\psi(2S)$ and J/ψ is observed to decrease at high-multiplicity for the prompt contribution, a possible effect of QGP presence [47]. It suggests that QGP-like features may emerge even in the absence of a large-volume medium, providing a novel testing ground for the understanding of QCD matter under extreme conditions.

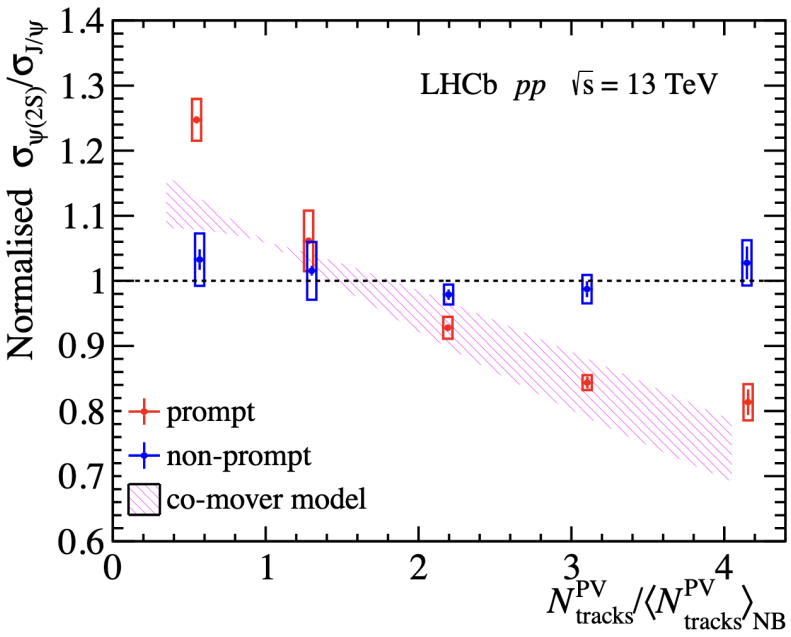


FIGURE 1.11: Normalised production ratio of $\psi(2S)$ over J/ψ measured by LHCb as a function of the multiplicity of the event [47]. Prompt (red circles) contribution show a decreasing trend with respect to the nonpront (blue circles) one, in agreement with the co-mover model [37], which could be QGP-like behaviour in small systems.

1.6.2 $Q\bar{Q}$ production in pA collisions

Proton-nucleus collisions provide an essential reference to isolate CNM effects from the hot nuclear matter one. Since no QGP is expected to form in these collisions, modifications in quarkonium production reflect initial- and final-state nuclear effects unrelated to deconfinement.

At the LHC, pPb runs at $\sqrt{s_{\rm NN}} = 5.02$ and 8.16 TeV have provided extensive data on J/ψ and $\psi(2S)$ production [48, 49]. While J/ψ suppression can often be described by CNM effects, the $\psi(2S)$ shows stronger suppression in some cases [50], especially at backward rapidity, that suggests the presence of final-state interactions even in the absence of a QGP, possibly related to the interaction with co-moving hadrons.

An example of this behaviour is observed by LHCb in forward pPb collisions [51]. In Fig. 1.12, a clear suppression of the prompt $\psi(2S)/J/\psi$ production ratio at forward rapidity (pPb collisions) is observed, while in the opposite direction (Pbp collisions) there is a stronger suppression of the charmonia excited state with respect to the ground state, but with a flatter behaviour, in better agreement with ALICE PbPb results [52].

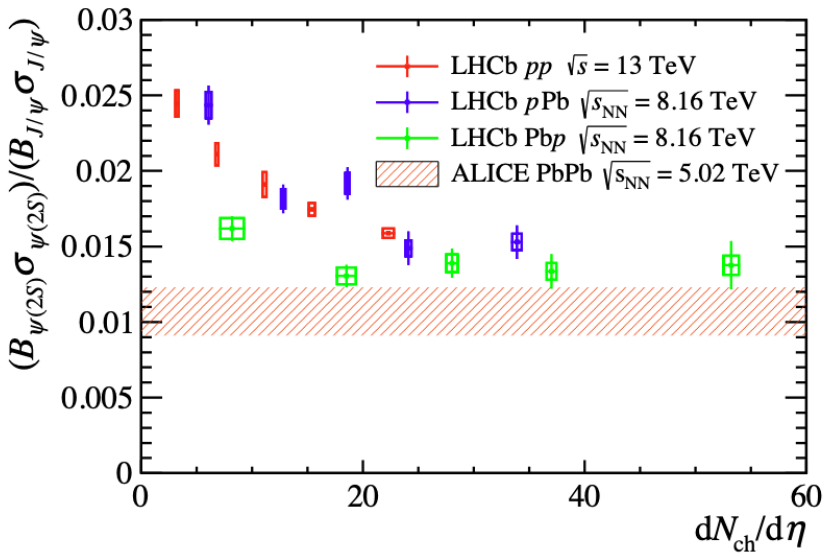


FIGURE 1.12: Production ratio of $\psi(2S)/J/\psi$ measured by LHCb as a function of the multiplicity of the event. Red circles: pp, blue circles: pPb, green circles: Pbp, similar shape as ALICE PbPb results (red band) [52].

At RHIC, d-Au collisions at $\sqrt{s_{\rm NN}} = 200$ GeV also show rapidity-dependent modifications, generally consistent with CNM expectations but also hinting at possible final-state effects [53].

1.6.3 $Q\bar{Q}$ production in AA collisions

Many measurements are present in the literature, aiming to disentangle the different production and suppression mechanisms in AA collisions. At the LHC, the ALICE [54] collaboration measured the J/ψ nuclear modification factor R_{AA} in PbPb collisions at $\sqrt{s_{\rm NN}} = 5.02$ TeV. As shown in Fig. 1.13, a strong suppression is observed, depending on centrality (left) and transverse momentum (right). Such measurements are broadly consistent with theoretical models incorporating both suppression and regeneration mechanisms. The increase of R_{AA} at low p_T in central collisions supports the presence of recombination, as described by transport and statistical hadronisation models.

Similarly, the ATLAS [55] and CMS [56] collaborations have reported measurements of the R_{AA} for inclusive J/ψ production in PbPb collisions at the same energy. The results are consistent across the different experiments, providing complementary insights into the suppression mechanisms in heavy-ion collisions.

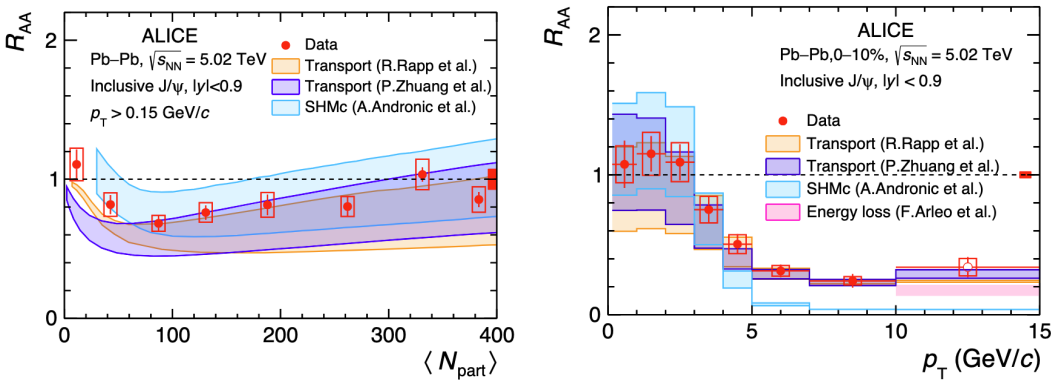


FIGURE 1.13: Inclusive J/ψ R_{AA} at mid-rapidity measured by ALICE [54], as a function of the number of participating nucleons integrated over $p_{\rm T}$ (left), and as a function of $p_{\rm T}$ for central collisions (right).

At RHIC energies $\sqrt{s_{\rm NN}} = 200$ GeV, the STAR [57] and PHENIX [58] collaborations also measured J/ψ suppression in Au-Au collisions. The results show significant suppression in central collisions, with STAR observing a $p_{\rm T}$-dependent suppression and PHENIX reporting a stronger suppression at forward rapidity, interpreted in terms of both hot medium effects and interactions with co-moving particles in the late stages of the collision.

Despite the substantial progresses made through these measurements and model developments, a complete understanding of quarkonium production and suppression in heavy-ion collisions remains elusive. Additional observables are therefore essential to further disentangle the underlying mechanisms. Among these, the study of the $\psi(2S)/J/\psi$ production ratio provides a powerful tool to probe the interplay between suppression and regeneration as explained in the next section.

1.6.3.1 $\psi(2S)$ over J/ψ production ratio in AA collisions

The study of the ratio

$$\frac{N_{\psi(2S)}}{N_{J/\psi}} \tag{1.8}$$

provides an interesting probe of quarkonium suppression and regeneration mechanisms in the QGP. Since the $\psi(2S)$ is a more weakly bound state compared to the J/ψ (binding energy ~ 0.05 GeV vs. ~ 0.64 GeV, see Fig. 1.14), it is expected to dissociate at lower temperatures.

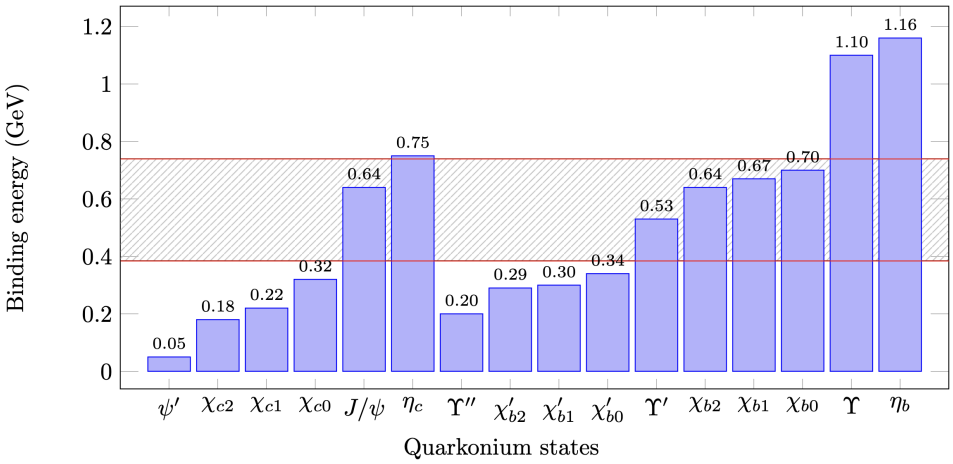


FIGURE 1.14: Representation of the binding energies of different quarkonia states compiled using the known values [59], compared to the peak QGP temperature estimated from thermal photon yields [60].

Therefore, a stronger suppression of $\psi(2S)$ relative to J/ψ is generally expected in a QGP scenario, and the ratio serves as a sensitive observable to sequential melting. Moreover, due to its longer formation time and larger size, the $\psi(2S)$ is more sensitive to the later stages of the medium evolution and to final-state effects such as interactions with co-moving hadrons [37]. This makes the $\psi(2S)$ excited charmonia state a very interesting probe to disentangle QGP suppression from hadronic phase effects.

Experimental results are needed to disentangle between the different scenarios. Measurements at the LHC and RHIC have revealed interesting features. ALICE recently measured the $\psi(2S)/J/\psi$ ratio in PbPb collisions at $\sqrt{s_{\rm NN}} = 5.02$ TeV at forward rapidity ($2.5 < y < 4$). They observed that $\psi(2S)$ is suppressed by a factor of about 2 relative to J/ψ, with patterns varying across centrality and $p_{\rm T}$, and with results consistent with both transport and statistical hadronisation models [52].

Figure 1.15, represents their result as a function of the centrality of the collisions compared with previous NA50 results [61] and theoretical calculation based on SHMc [62] and TAMU model [41].

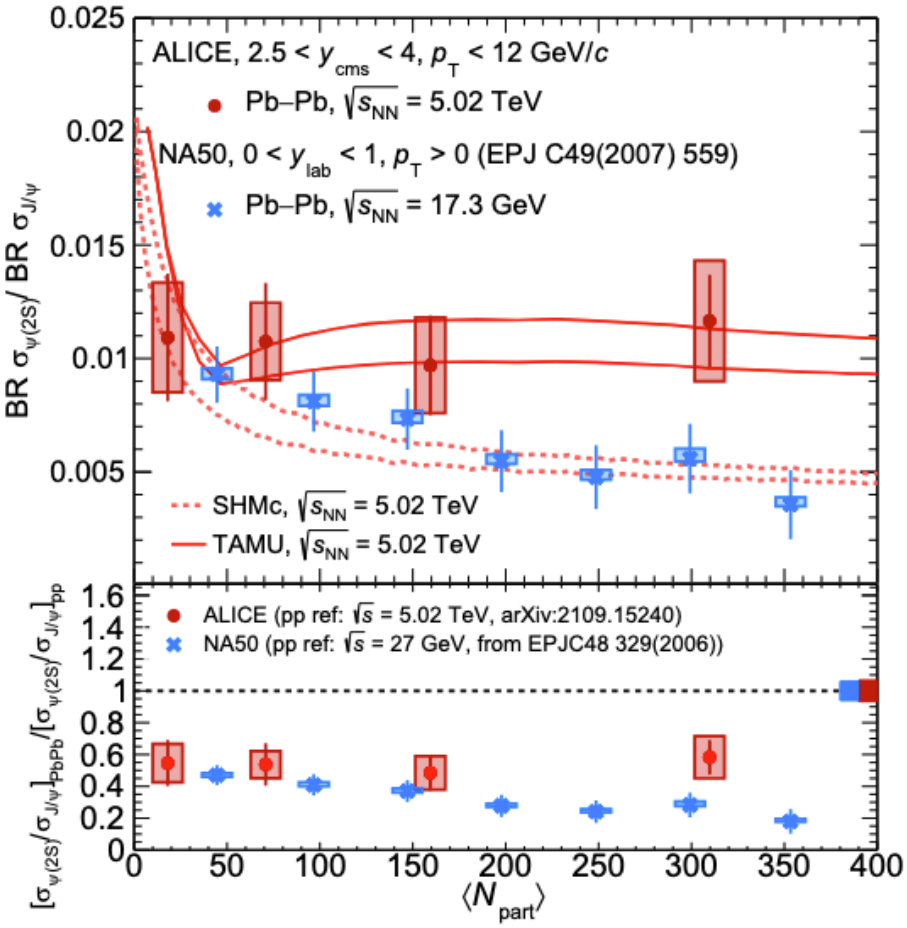


FIGURE 1.15: Ratio of the $\psi(2S)$ to J/ψ inclusive production cross-section as a function of the number of participating nuclei, measured by ALICE [52]

CMS measured the double ratio $((\psi(2S)/J/\psi)_{\mathrm{PbPb}}/(\psi(2S)/J/\psi)_{pp})$ at mid-rapidity for $\sqrt{s_{\mathrm{NN}}} = 2.76$ and 5.02 TeV. They observed that the $\psi(2S)$ can be more suppressed than the J/ψ at high p_{T}, as expected from its weaker binding, but also less suppressed in certain kinematic regions, particularly at low p_{T} and forward rapidity in central PbPb collisions [63], see Fig. 1.16.

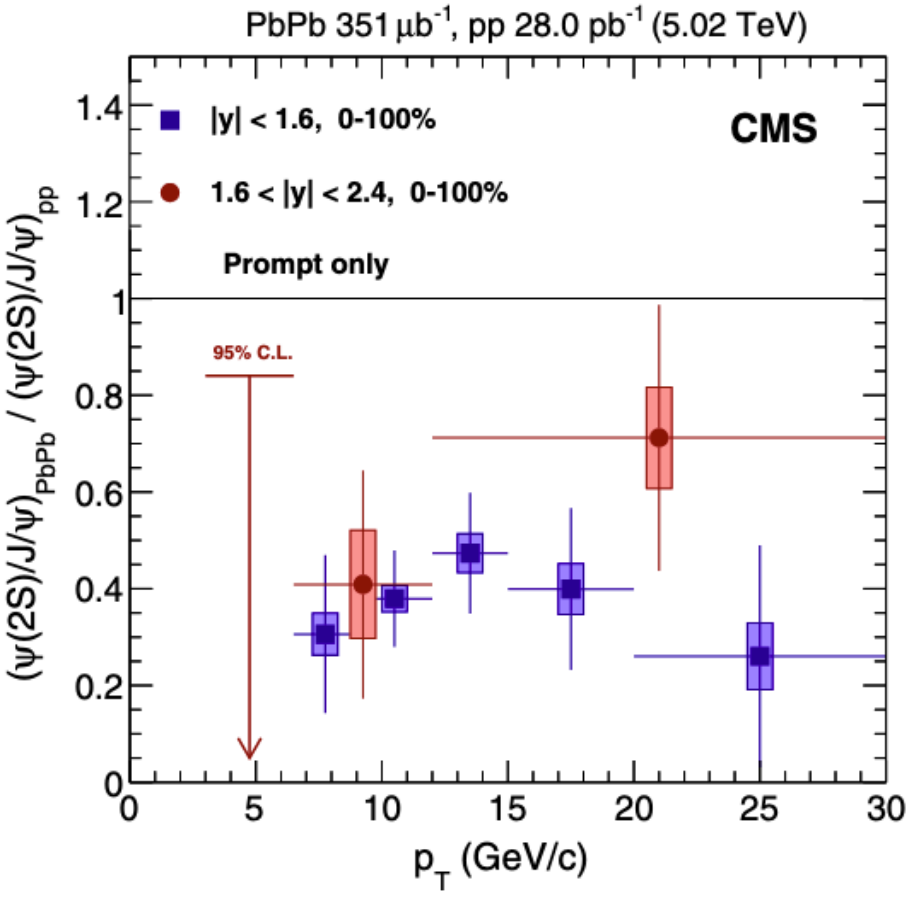


FIGURE 1.16: Double ratio of the $\psi(2S)$ to J/ψ prompt production cross-section as a function of the transverse momentum in two rapidity intervals, measured by CMS [63]

At RHIC energies $\sqrt{s_{\mathrm{NN}}} = 200$ GeV, measurements are more limited due to lower statistics. PHENIX and STAR have reported results in smaller datasets, consistently showing enhanced suppression of $\psi(2S)$ compared to J/ψ of about a factor 2, at backward rapidity and in central collisions, as visible in the double ratio reported in Fig. 1.17. These results indicate the importance of final-state interactions such as dissociation and co-mover absorption [64] and demonstrate a clear hierarchy in suppression. However they are currently constrained by limited rapidity and transverse momentum coverage, especially in the low-p_{T}, forward-rapidity region. Model comparisons show that while some transport and co-mover models can reproduce the observed double ratios qualitatively [65, 37], significant theoretical uncertainties remain, especially regarding the treatment of $\psi(2S)$ regeneration and late-stage interactions.

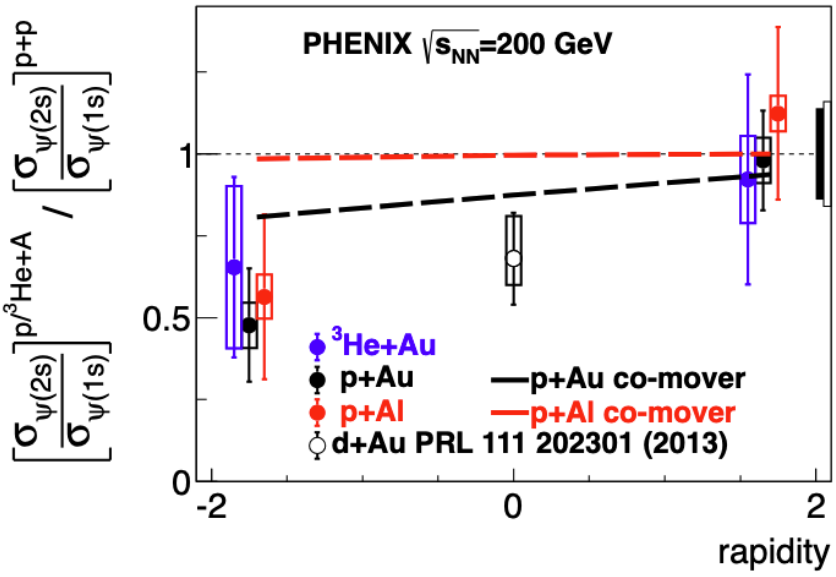


FIGURE 1.17: Double ratio of the $\psi(2S)$ to J/ψ production cross-section as a function of the rapidity in different collision systems, measured by PHENIX [64]

More experimental results are needed, but the measurement of the $\psi(2S)/J/\psi$ production ratio is challenging due to the lower branching ratio of $\psi(2S)$ to muon pairs, and the smaller production cross-section of the $\psi(2S)$ with respect to J/ψ. In this context the LHCb detector can bring unique contributions, as for instance it is the first experiment able to disentangle between prompt and nonprompt contribution (by removing the from-b component of the decaying charmonia) at forward rapidities ($2.0 < y < 4.5$), and to go to very low p_{T}, such as 300 MeV/c, as discussed in the analysis chapter (Chap. 3). Finally, the preliminary Run 3 analysis presented here is based on a much larger statistical sample, with an higher reach in centrality coverage (Chap. 4). The results shown are achievable thanks to the capabilities of the LHCb detector which is explained in details in Chap. 2.

Chapter 2

The LHCb Experiment

The Large Hadron Collider beauty (LHCb) experiment [66] is one of the four main experiments operating at the Large Hadron Collider (LHC) at CERN, the European Organization for Nuclear Research in Geneva, Switzerland.

Originally conceived to perform high-precision studies of the decays and properties of hadrons containing b and c quarks, LHCb has then evolved into a more versatile experiment with a broader physics programme. This includes important contributions to heavy-ion physics through dedicated proton-lead and lead-lead runs, as well as the development of a unique Fixed-Target programme enabled by the SMOG system [67]. The most important features of the experiment lie in its exceptional vertexing, tracking, and particle identification capabilities, in a unique kinematic coverage optimised for b and c physics.

This chapter presents the LHCb detector with a focus on its performance in heavy-ion collisions, first during LHC Run 2 and then in its upgraded configuration for Run 3 data-taking.

2.1 The Large Hadron Collider

The Large Hadron Collider is the world's largest and most powerful particle accelerator [68], that pushes protons or nuclei beams near the speed of light. Built at the European Organization for Nuclear Research (CERN), it was constructed between 1998 and 2008 through an international collaboration involving over 10 000 scientists, hundreds of universities and laboratories, and more than 100 countries. The LHC is located at an average depth of 100 m beneath the French-Swiss border, and consists of a 27 km ring of superconducting magnets with a complex system of accelerating structures to boost the energy of particles along their trajectory.

The LHC was designed to enable high-energy hadronic collisions to test predictions of the Standard Model and probe physics beyond it. Such goals include precision measurements of the Higgs boson properties, searches for new particles such as supersymmetric particles or dark matter candidates, and testing the nuclear matter under extreme conditions through heavy-ion collisions.

Proton beams were first collided at a centre-of-mass energy of $\sqrt{s} = 7$ TeV in 2010. During the first run of data-taking (Run 1), the energy was increased to 8 TeV in 2012, while in the second run (Run 2) (2015–2018) it reached 13 TeV. After a long shutdown for machine upgrades (LS2) from 2019 to 2022, the last data taking campaign (Run 3) began with proton beams of 6.8 TeV each, colliding at a $\sqrt{s}$ of 13.6 TeV.

Heavy-ion collisions have also been an integral part of the LHC programme since Run 1, typically taking place during dedicated periods of about three weeks at the end of each pp data-taking year. The first PbPb collisions were delivered in 2010 and 2011 at a centre-of-mass energy per nucleon $\sqrt{s_{\mathrm{NN}}}$ of 2.76 TeV, followed in 2013 by the first pPb run at $\sqrt{s_{\mathrm{NN}}} = 5.02$ TeV. Run 2 extended this programme with PbPb collisions at $\sqrt{s_{\mathrm{NN}}} = 5.02$ TeV in both 2015 and 2018, as well as a pPb run at $\sqrt{s_{\mathrm{NN}}} = 8.16$ TeV in 2016. In Run 3, the PbPb centre-of-mass energy per nucleon pair was further increased to $\sqrt{s_{\mathrm{NN}}} = 5.36$ TeV, marking a new record for heavy-ion collisions. The list of the main data taking periods and the corresponding centre-of-mass energies are available in Tab. 2.1.

TABLE 2.1: Summary of the main LHC running periods and corresponding collision systems and energies.

Run period	**Years**	**Collision system**	**Centre-of-mass energy**
Run 1	2010–2012	pp	7–8 TeV
		PbPb	2.76 TeV
		pPb (Pbp)	5.02 TeV (2013)
Run 2	2015–2018	pp	13 TeV
		PbPb	5.02 TeV (2015, 2018)
		pPb (Pbp)	8.16 TeV (2016)
Run 3	2022–2026 (ongoing)	pp	13.6 TeV
		PbPb	5.36 TeV

In addition to the standard collision systems, the LHC periodically included short dedicated data-taking periods with lighter ions, such as in Run 3 proton-oxygen, oxygen-oxygen, and neon-neon collisions. Although the special runs span only a few days each, they provide valuable input for characterising small collision systems and benchmarking theoretical models relevant for cosmic ray physics and the initial stages of Quark-Gluon Plasma formation. The current Run 3 is expected to last until 2026, after which further upgrades will prepare the accelerator for the High-Luminosity LHC (HL-LHC) phase [69].

The LHC is the final stage of CERN's accelerator complex shown in Fig. 2.1. Protons extracted from hydrogen molecules through an electric field, are initially accelerated using a series of smaller machines: a linear accelerator (LINAC), the Proton Synchrotron (PS), and the Super Proton Synchrotron (SPS). For ion beams, instead,

lead ions are first produced by heating a lead source and undergo an intermediate acceleration in the Low Energy Ion Ring (LEIR) and then follow the same acceleration steps as the proton beams. The particles are then injected into the LHC, where they are brought to their final energy within approximately 20 minutes.

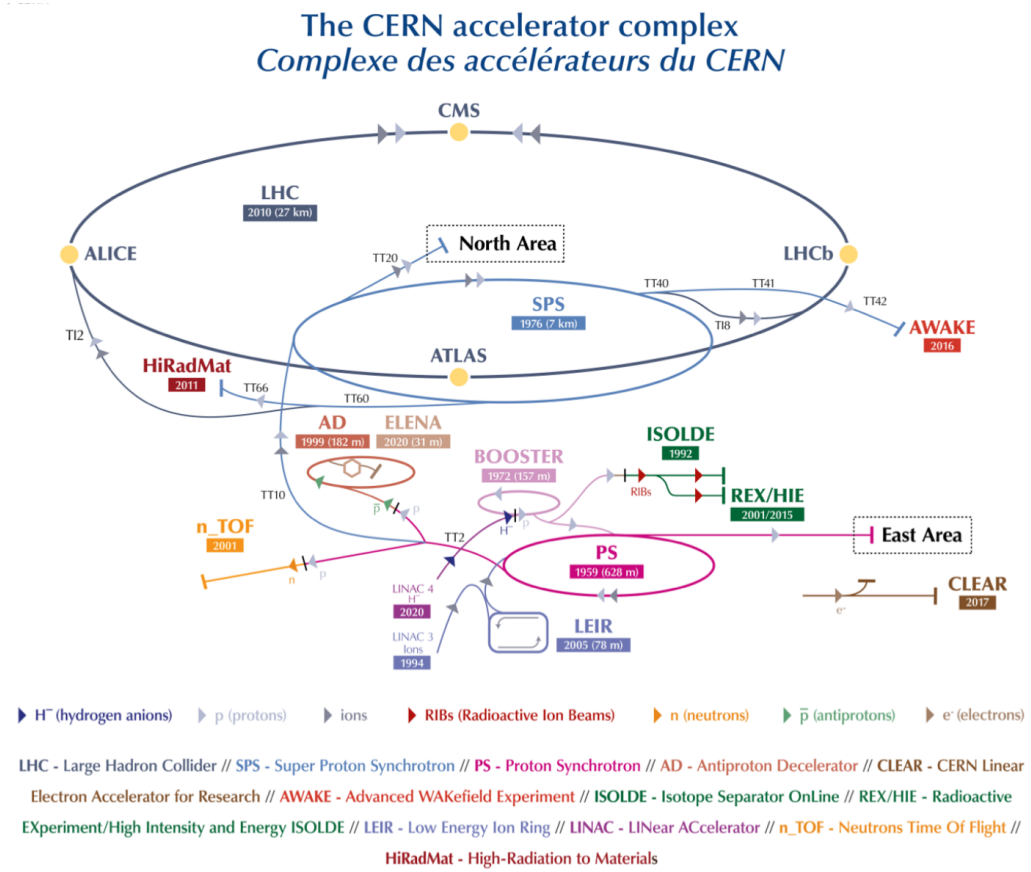


FIGURE 2.1: The CERN accelerator complex [70].

Inside the LHC, the two beams travel in opposite directions in separate beam pipes kept under ultra-high vacuum. They are guided by 1232 superconducting dipole magnets (producing fields up to 8T) and focused by 392 quadrupole magnets. These magnets operate at a temperature of 1.85K, maintained using liquid helium, which is necessary to achieve superconductivity and ensure zero electrical resistance. The acceleration is provided by superconducting radiofrequency (RF) cavities operating at 400 MHz, delivering a total of 16MV per turn.

The beams are structured into bunches of protons or lead nuclei, each separated by 25, 50, or 75 ns [71]. To quantify the number of collisions provided by a particle accelerator, the instantaneous luminosity variable $\mathcal{L}_i$ is used. This represents the number of projectiles crossing each other per unit of surface and time and it depends on the beam properties, following the definition:

$$\mathcal{L}_i = f_{\text{coll}} \frac{n_1 n_2}{4\pi\sigma_x\sigma_y}, \tag{2.1}$$

where f_{coll} is the collision frequency, n_1 and n_2 are the number of particles per bunch, and σ_x, σ_y are the transverse beam dimensions, assuming a Gaussian profile.

Since the LHC outperformed, the goal instantaneous luminosities designated for Run 2 have been surpassed in later years [72]. In pp collisions, instantaneous luminosities as high as $2 \times 10^{34}\,\text{cm}^{-2}\text{s}^{-1}$ were achieved during the most intense fills. Similarly, in heavy-ion running, peak luminosities reached up to $7 \times 10^{27}\,\text{cm}^{-2}\text{s}^{-1}$ for both PbPb and pPb collisions. Run 3, started in 2022, aims to further increase the delivered luminosity, and the pp peak luminosity is expected to reach up to $7.5 \times 10^{34}\,\text{cm}^{-2}\text{s}^{-1}$.

The beam-beam collisions occur at four interaction regions, as indicated in Fig. 2.1, each defined as the nominal beam crossing point at $z = 0$ along the beam axis. These correspond to the positions of the four main LHC experiments: ATLAS [73], CMS [74], ALICE [75], and LHCb [66]. Each detector was designed with a different physics goal in mind. ATLAS and CMS for precision Higgs measurements and new physics searches at the TeV scale, ALICE for the study of the Quark-Gluon Plasma in heavy-ion collisions, and LHCb for high-precision studies of b and c hadrons. However, with time the physics program has expanded such that they can now all be considered general purpose detectors.

A key element distinguishing the four detectors is their angular coverage around the interaction point. At the LHC, the coordinate system is defined such that the z-axis lies along the nominal beam direction, pointing downstream through the experiments, while the x–y plane corresponds to the plane transverse to the beams. The x-axis points radially inward from the centre of the accelerator ring, and the y-axis points vertically upward. The position of any produced particle can thus be described in spherical coordinates by its polar angle θ, measured with respect to the beam axis (z), and its azimuthal angle ϕ, measured in the transverse plane (x, y). In collider physics, it is often more convenient to use the pseudorapidity variable, defined as $\eta = -\ln\tan(\theta/2)$, which provides a natural measure of the detector acceptance. The most peculiar feature of the LHCb experiment is that it is the only one fully instrumented in the very forward pseudo-rapidity region ($2.0 < \eta < 5.0$), making it unique for several physics studies.

A schematic overview of the four LHC experiments and their pseudorapidity coverage is shown in Fig. 2.2. The specific layout and capabilities of the LHCb detector will be described in detail in the next sections.

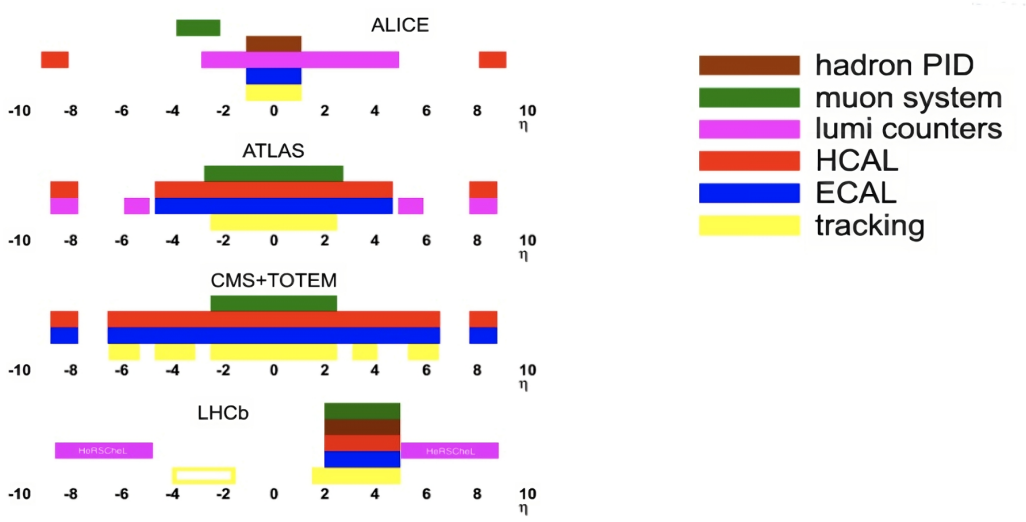


FIGURE 2.2: Pseudo-rapidity coverage of the main experiments at LHC, with the main subdetectors details.

2.2 The LHCb Detector

LHCb is one of the four main experiments at the LHC, designed primarily to search for physics beyond the Standard Model through the study of rare decays of beauty and charm hadrons and the investigation of *CP*-violating phenomena [76, 77].

To meet these objectives, LHCb was conceived as a single-arm spectrometer with forward angular coverage from approximately 10 mrad to 300 (250) mrad in the bending (non-bending) plane, corresponding to a pseudorapidity range of $2.0 < \eta < 5.0$. This geometry is motivated by the fact that, at high energies, both b and $\bar{b}$ quarks are predominantly produced in the same forward or backward cone very close to the beam direction.

Roughly 27% of the b or $\bar{b}$ quarks produced in pp collisions fall within the LHCb acceptance. This forward design therefore enables the experiment to detect a significant fraction of beauty hadrons, despite covering only about 4% of the full solid angle. A similar argument applies to charm hadrons, whose masses are of the same order of magnitude as the b quark mass and are also produced abundantly at LHC energies.

The LHCb spectrometer is located at Interaction Point 8 (IP8) of the LHC. Its layout is shown in Fig. 2.3 [78], where the z axis is aligned with the direction of the proton beams.

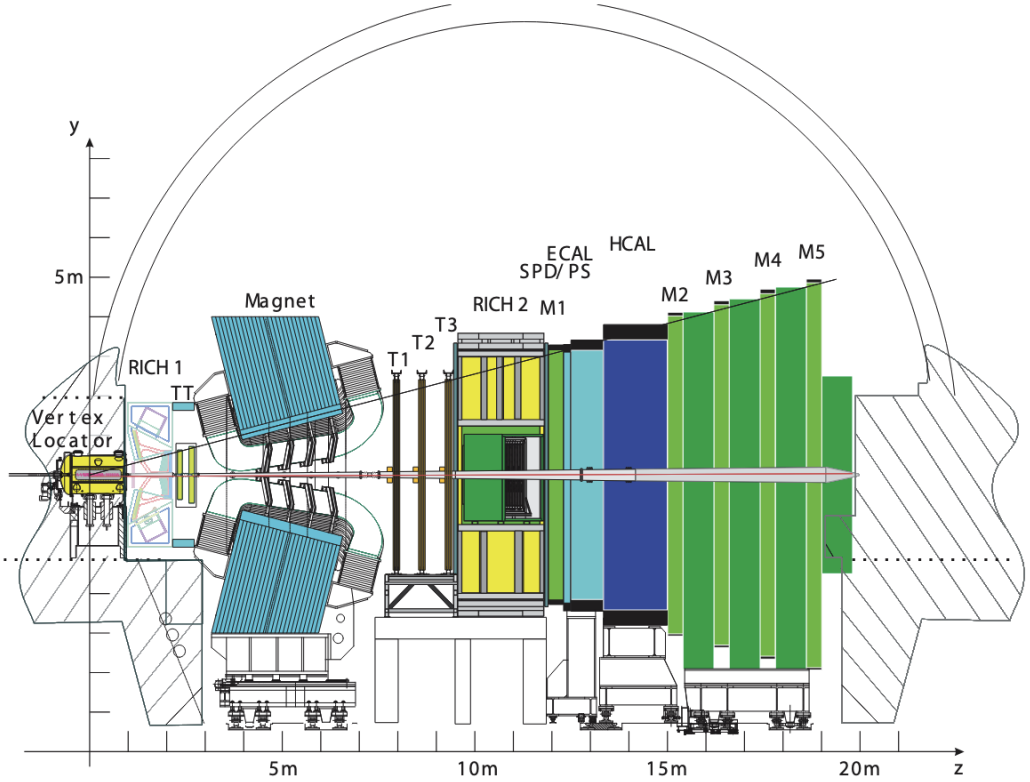


FIGURE 2.3: Side view of the LHCb detector in its Run 2 configuration [78]. The positive x axis is entering the page towards the centre of the LHC ring.

To efficiently measure the rare decay products of B mesons in an environment with high background rates, the detector must meet several critical requirements:

- High-precision (at the μm scale) measurement of the positions of primary and secondary vertices originating from B meson decays, along with excellent time resolution.
- Efficient and accurate particle identification (PID). The ability to distinguish among protons, kaons, pions, and muons over a wide momentum range, from a few GeV/c up to about 100 GeV/c, is essential for reconstructing key decay modes.
- A fast and efficient trigger system.
- Powerful online data processing capabilities to optimise data collection and real-time event reconstruction.

The detector is organised into three main subsystems: the tracking system, the particle identification system, and the trigger system. These will be described in detail in the following sections, together with the introduction of the SMOG system, which

allows LHCb to collect fixed-target interactions uniquely at the LHC energies. The description provided here refers to the Run 2 configuration of the detector, which was used in the analysis of the charmonium production ratio with the 2018 PbPb dataset, discussed in Chapter 3. During the second long shutdown (LS2, 2018 - 2021), the LHCb detector underwent a major upgrade, known as Upgrade I, which significantly enhanced its performance, including in the heavy-ion sector. The main characteristics of the upgraded detector, used to collect the 2024 PbPb data subject of the analysis presented in Chapter 4, are illustrated in Sec. 2.3.

2.2.1 Dipole Magnet

One key component of LHCb is the large magnet, crucial to bend the trajectories of the produced charged particles in order to measure their momentum. The LHCb magnet is a warm dipole, shown in Fig. 2.4 (left), which covers a forward acceptance of ±250 mrad vertically and of ±300 mrad horizontally. It consists of two trapezoidal resistive coils bent positioned at 45 degrees with respect to the z axis. Each coil is supplied with a nominal current of 5.8 kA, and the magnet provides a bending power of 4 Tm. The right panel of Fig. 2.4 shows the main component of the obtained field, B_y, for both polarities (MagUp/negative polarity, MagDown/positive polarity).

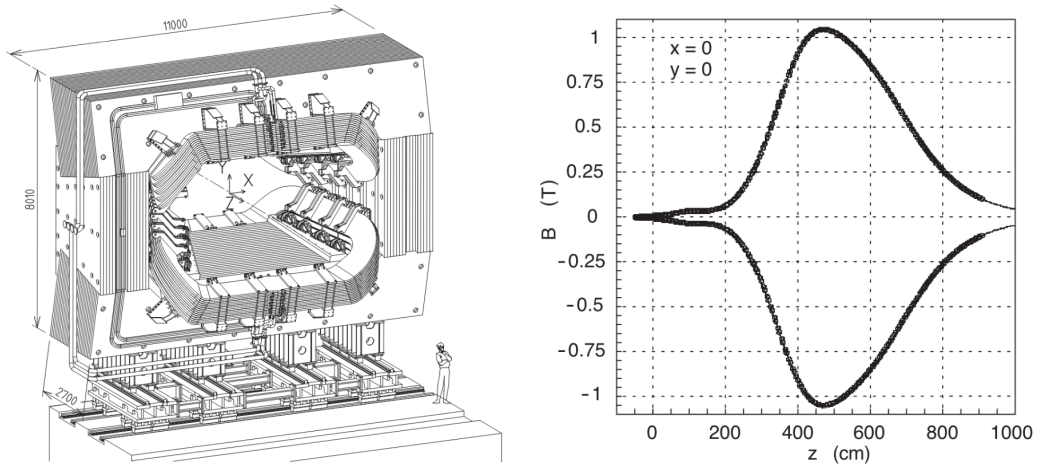


FIGURE 2.4: Perspective view of the LHCb dipole magnet (units in mm) (left). Magnetic field along z axis (right) [76].

2.2.2 Tracking System

The tracking system consists of several crucial sub-detectors: the VErtex LOcator (VELO), which is the first sub-detector surrounding the interaction region of the collisions; the Tracker Turicensis (TT), located just upstream of the magnet; and three tracking stations (T1, T2, T3) placed downstream of the magnet, as shown in Fig. 2.3.

These components work together to reconstruct the trajectories of the particles produced in the collisions. The tracking system provides a precise reconstruction of both primary and secondary vertices, as well as an accurate measurement of particle momenta.

2.2.2.1 VErtex LOcator

The VErtex LOcator (VELO) [79] is a silicon microstrip detector which surrounds the interaction region. It is composed of two retractable halves that can be opened or closed around the beam line, allowing safe operation during beam injection and optimal precision during data taking. The VELO plays a crucial role in reconstructing the positions of both the primary and secondary vertices with high accuracy.

The primary vertex (PV) corresponds to the point where the collision occurs, while secondary vertices are displaced decay points of short-lived particles such as B or D mesons. The precise reconstruction of these vertices allows the measurement of decay lengths, impact parameters, and proper decay times, which are essential for heavy-flavor physics and for identifying signals from rare decays.

The VELO consists of 21 circular silicon sensor modules per half, arranged along the beam direction. Each module provides measurements of both radial (r) and azimuthal (ϕ) coordinates. In addition, two planes located upstream of the VELO sensors form the pile-up veto system, used to identify and reject events with multiple pp interactions in the same bunch crossing, as illustrated in Fig. 2.5.

Figure 2.6 shows the geometry of an individual VELO module. A central hole allows for the passage of the beam. During beam injection, the two VELO halves are retracted to accommodate the larger transverse beam size; they are closed only when the beam reaches nominal (squeezed) conditions. To minimise the material traversed by the particles and ensure high precision tracking, the VELO sensors operate under vacuum and are placed only 8 mm from the beam axis during data taking. The proximity of this detector to the interaction point ensures an astonishing spatial resolution of about 4 μm.

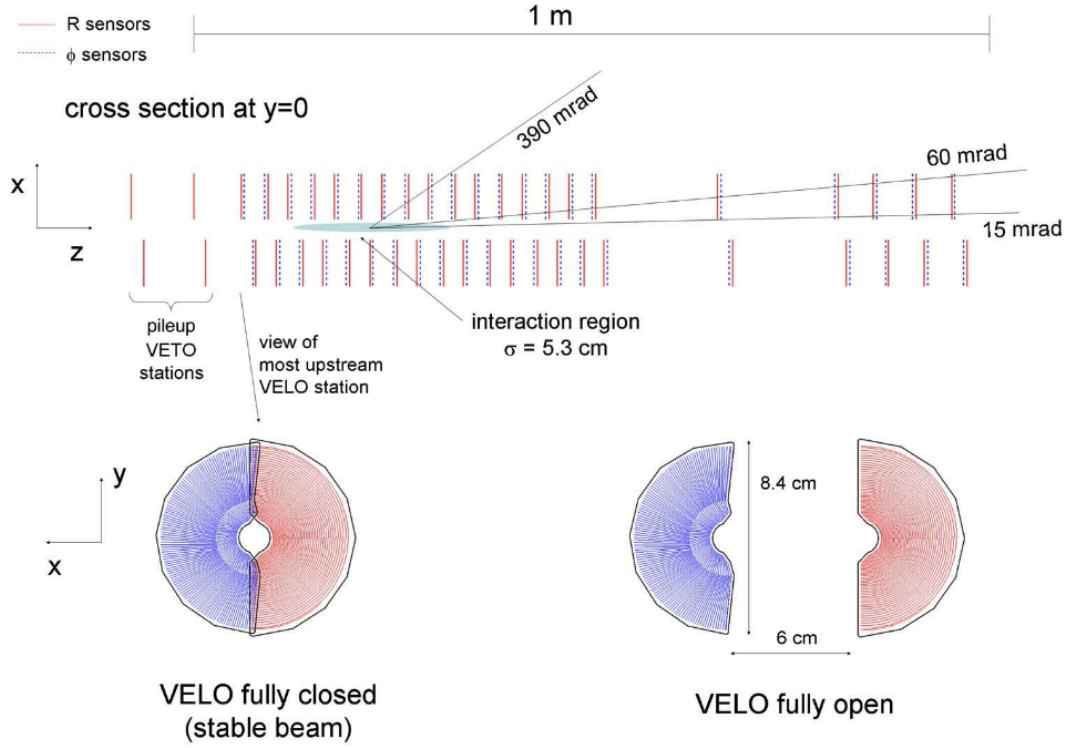


FIGURE 2.5: Cross section in the (x, z) plane of the VELO silicon sensors, at $y = 0$, with the detector in the fully closed position. The beams travel along the z axis perpendicular to the page. The front face of the first modules is illustrated in both the closed and open positions. The two pile-up veto stations are located upstream of the VELO sensors [76].

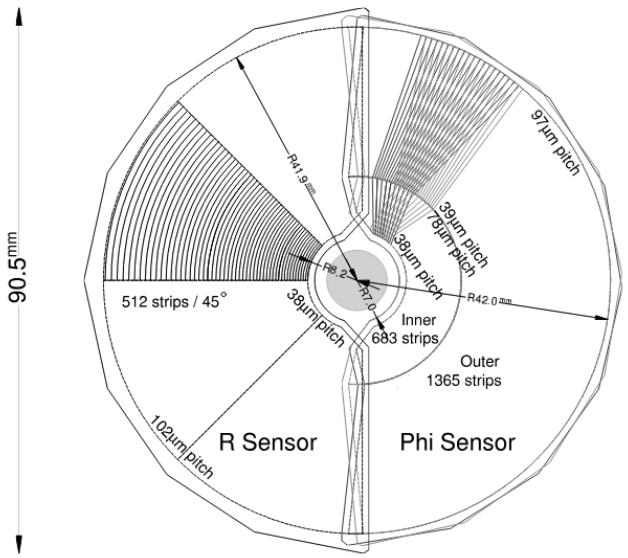


FIGURE 2.6: Sketch illustrating the $r\phi$ geometry of the VELO sensors [76].

2.2.2.2 Tracker Turicensis (TT)

The Tracker Turicensis (TT) station is another silicon detector, located downstream of the first RICH detector and in front of the LHCb magnet. Its main goal is to improve the momentum resolution for particles which traverse the whole detector. The station consists of four planar detection layers with a width and height of approximately 160 cm and 130 cm, respectively. It covers a total active area of approximately 8.4 m^2 by 143360 silicon microstrip detectors with a strip pitch of about 200 μm. The four detection layers, as shown in Fig. 2.7, are arranged with vertical strips in the first and the last layer and strips rotated by a stereo angle of $-5°$ and $+5°$ in the second and the third layer, respectively. This layout provides a precise measurement of track coordinates for momentum determination in the bending plane of the magnet, with a hit resolution of about 50 μm.

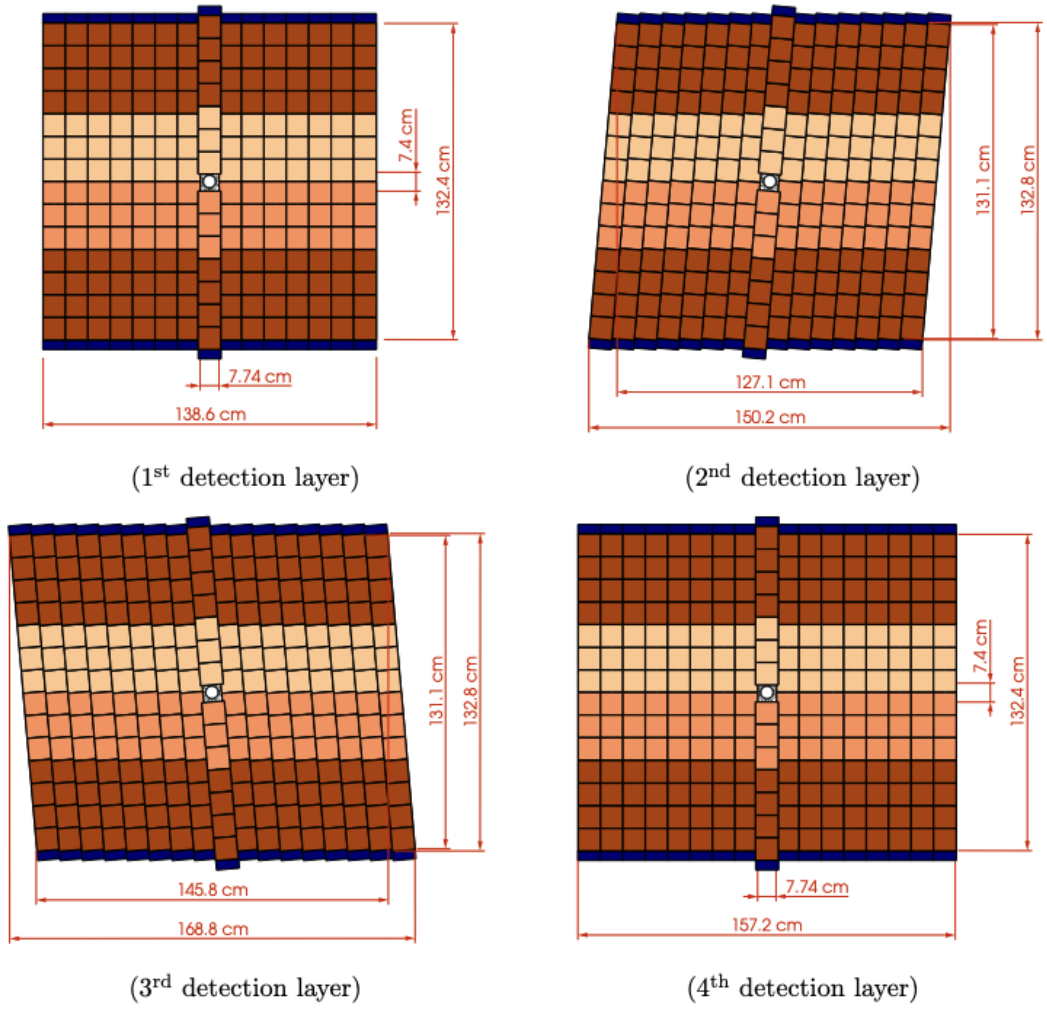


FIGURE 2.7: Layout of the four detection layers of the TT station in the xy plane [80].

2.2.2.3 T stations

The tracking stations T1, T2 and T3 are placed downstream of the magnet, before the second RICH detector. Each of the three consists of an inner region closer to the beam pipe (IT) and it is surrounded by an outer one (OT) arranged as shown in Fig. 2.8.

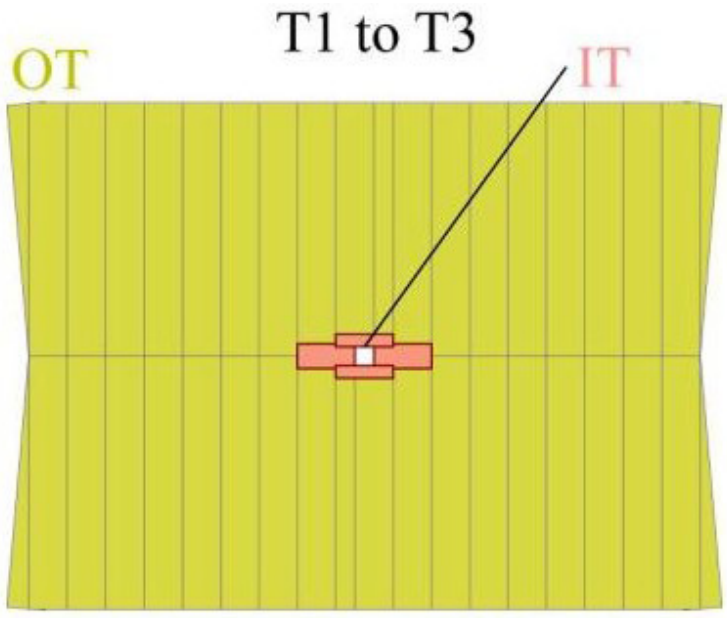


FIGURE 2.8: Layout of a T station in the xy plane.

The IT stations consist of four individual detector boxes (120 cm w $\times$ 40 cm h), arranged around the beam pipe. They have an high granularity assuring a spatial hit resolution of about 50 μm. The OT ones instead covers the majority of the detector acceptance (600 cm w $\times$ 490 cm h), with a lower granularity (spatial resolution $\sim$ 200 μm) with respect to IT being far from the beam pipe and thus dealing with lower occupancy.

2.2.3 Particle Identification System

The particle identification (PID) system is essential for determining the nature of the particles associated with reconstructed tracks. In particular, the two Ring Imaging Cherenkov detectors (RICH1 and RICH2) are fundamental for discriminating among light hadrons (protons, kaons, and pions); the electromagnetic and hadronic calorimeters (ECAL and HCAL) are used to distinguish photons and electrons; and the muon stations (M1–M5) are employed to identify muons. A brief description of each subsystem follows.

2.2.3.1 The Ring Imaging Cherenkov Detectors

The Ring Imaging Cherenkov (RICH) detectors are designed to identify charged particles by exploiting the Cherenkov effect. When a charged particle travels through a dielectric medium at a speed greater than the phase velocity of light in that medium, it emits Cherenkov radiation at a characteristic angle θ_C with respect to its trajectory. This angle depends on the particle's velocity $\beta = v/c$ and on the refractive index n of the medium, according to the relation:

$$\cos\theta_C = \frac{1}{n\beta}. \tag{2.2}$$

The RICH system measures the Cherenkov angle θ_C by reconstructing the ring of emitted photons on a dedicated photon detector plane. Since the refractive index n of the radiator material is known, the particle velocity β can be inferred from the measured angle. Combining this information with the momentum p of the track, previously determined by the tracking system, allows the mass m of the particle to be calculated via the relativistic relation:

$$\beta = \frac{p}{\sqrt{p^2 + m^2}}. \tag{2.3}$$

As a result, the RICH detectors can distinguish between different hadron species, such as pions, kaons, and protons, over a broad momentum range, as illustrated in Fig. 2.9. The unique identification capability provided by the RICH system plays a crucial role in a wide variety of LHCb analyses, particularly in flavour physics and hadron spectroscopy.

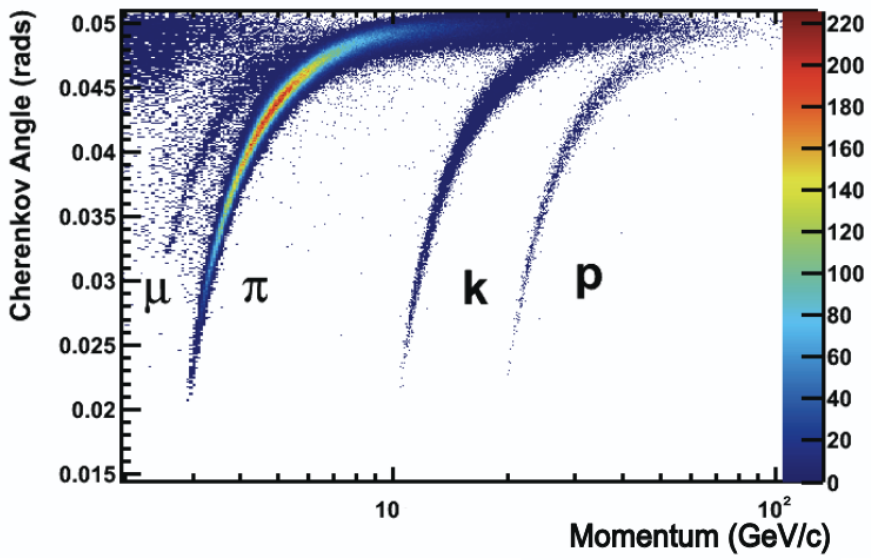


FIGURE 2.9: Reconstructed Cherenkov angle as a function of track momentum in the C_4F_{10} radiator [81].

At large polar angles, the momentum spectrum is softer, while at small polar angles it is harder. Therefore, two RICH detectors arranged as shown in Fig. 2.10 are needed to cover the full momentum and angular acceptance of the experiment.

- **RICH1** is located upstream of the LHCb dipole magnet, between the VELO and the TT. It covers the low-momentum charged particle range $\sim$ 1-60 GeV/c using aerogel and fluorobutane (C_4F_{10}) gas radiators. RICH1 spans the full LHCb angular acceptance from $\pm$25 mrad to $\pm$300 mrad (horizontal) and $\pm$250 mrad (vertical). Its average Cherenkov angle resolution is 1.65 mrad.
- **RICH2** is located downstream of the magnet, between the last tracking station and the first muon station. It has a more limited angular acceptance of approximately $\pm$15 mrad to $\pm$120 mrad (horizontal) and $\pm$100 mrad (vertical), but covers the region where high-momentum particles are typically produced. It contains a CF_4 gas radiator, providing PID capabilities from approximately 15 GeV/c to above 100 GeV/c. Its average Cherenkov angle resolution is 0.67 mrad.

In both RICH detectors, the focusing of the Cherenkov light is achieved using a system of spherical and flat mirrors, which reflect the light out of the spectrometer acceptance onto the photon detector arrays.

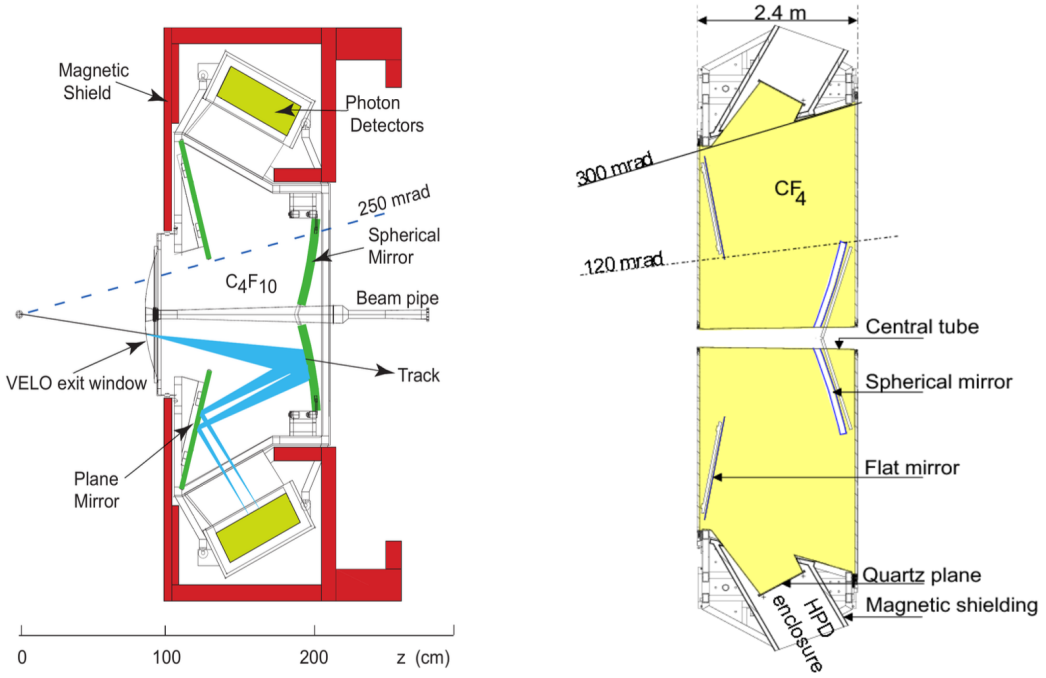


FIGURE 2.10: Layout of the RICH1 (left) and RICH2 (right) detectors [76].

2.2.3.2 The Calorimeter System

The LHCb calorimeter system provides identification of hadrons, electrons, and photons, as well as measurements of their energies and positions. It consists of four sub-detectors: a Scintillator Pad Detector (SPD), a PreShower (PS), an Electromagnetic CALorimeter (ECAL), and a Hadronic CALorimeter (HCAL), all arranged perpendicular to the beam axis, as shown in Fig. 2.11.

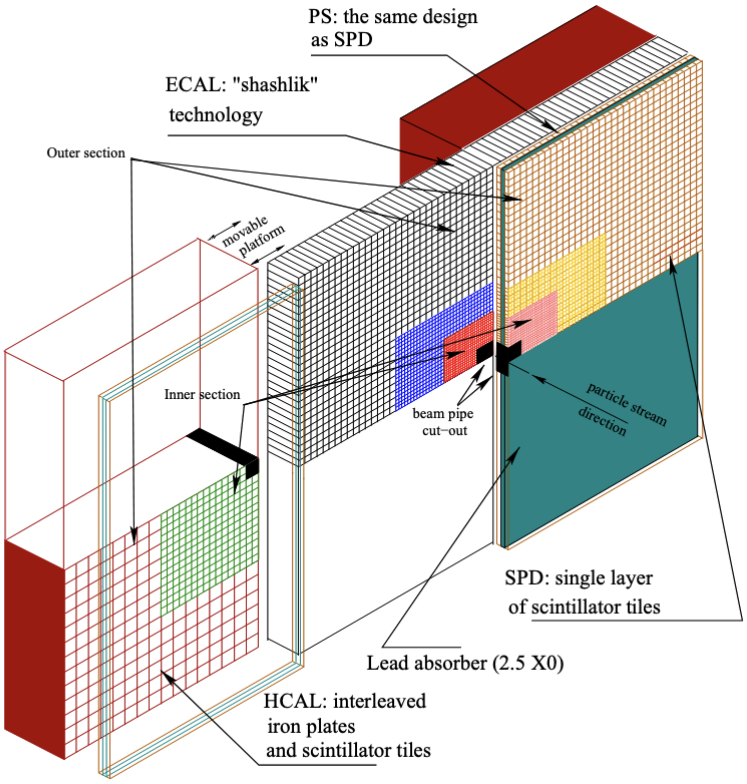


FIGURE 2.11: Layout of the calorimeter system [82].

At the LHC, the particle flux across the calorimeter surface varies by up to two orders of magnitude, with the highest densities observed in the inner region close to the beam pipe. To accommodate these variations, the calorimeters are segmented into regions with smaller cells near the beam pipe and progressively larger cells at greater radial distances. All four sub-detectors are composed of alternating layers of absorber material (lead or iron) and scintillator tiles. A brief description of each component follows.

- **SPD and PS** are located upstream of the ECAL. The PS helps to reject the high background from charged pions, while the SPD is used to identify and suppress backgrounds from high transverse energy π^0 decays. Both detectors

consist of scintillator pads separated by a lead converter corresponding to 2.5 radiation lengths.

- **ECAL** is a sampling calorimeter composed of alternating layers of scintillator and lead. It provides energy measurements for electrons and photons. Its design resolution is

$$\frac{\sigma_E}{E} = \frac{(9.0 \pm 0.5)\%}{\sqrt{E}} \oplus 0.8\%,$$

where E is in GeV. It leads to a mass resolution of approximately 65 MeV/c^2 for $B \to K^*\gamma$ decays (with a high-E_T photon) and about 75 MeV/c^2 for $B \to \rho\pi$ decays, with a π^0 mass resolution of roughly 8 MeV/c^2. The ECAL is positioned at $z = 12.5$ m from the interaction point.

- **HCAL** is also a sampling calorimeter, consisting of iron as absorber material and scintillating tiles as the active medium. Uniquely, the scintillating tiles are oriented parallel to the beam axis. The HCAL is located at $z = 13.33$ m from the interaction point and has dimensions of 8.4 m in height, 6.8 m in width, and 1.65 m in depth. Its energy resolution is

$$\frac{\sigma_E}{E} = \frac{(69 \pm 5)\%}{\sqrt{E}} \oplus (9 \pm 2)\%$$

When a particle passes through the calorimeter system, it interacts with the sub-detectors depending on its nature. Photons do not leave signals in the SPD but interact in the lead converter, producing electromagnetic showers detected in the PS and ECAL. Electrons deposit energy in all three detectors: SPD, PS, and ECAL. Hadrons, by contrast, deposit most of their energy in the HCAL.

In heavy-ion collisions, the ECAL plays a special role. By studying the total energy deposited in the electromagnetic calorimeter, it is possible to estimate the event centrality. The centrality measurement is performed using the Glauber model and will be discussed in more detail in Sec. 3.4.

2.2.3.3 The Muon System

The identification of muons is a crucial component of many analyses performed by the LHCb collaboration, as muons often appear in the final states of CP-sensitive, and very rare, B-hadrons decays. In particular, they are essential for the analysis presented in this thesis, since both charmonium states studied are reconstructed in the dimuon decay channel, as discussed in the analyses chapters 3 and 4.

The muon system consists of five rectangular stations (M1–M5) placed along the beam axis. The system covers angular acceptances of 20 (16) mrad to 306 (258) mrad in the bending (non-bending) plane, resulting in an overall acceptance of about 20% for muons originating from inclusive semileptonic b-hadron decays. Stations M2 to

M5 are located downstream of the calorimeters and are interleaved with 80 cm thick iron absorbers, which serve to filter out non-penetrating particles and select muons. Station M1, instead, is placed in front of the calorimeter system and is used to improve the transverse momentum measurement at the trigger level, as illustrated in Fig. 2.12 (left).

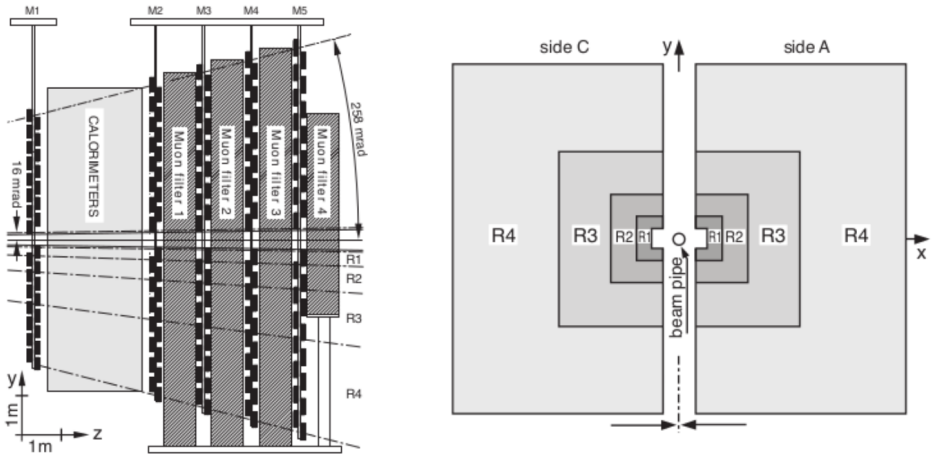


FIGURE 2.12: Side (left) and front (right) view of the muon system [76]. The beam moves in the z direction.

Stations M1 to M3 provide high spatial resolution in the x-coordinate (bending plane) and are used to define the track direction and estimate the transverse momentum of the muon with a resolution of approximately 20%. Stations M4 and M5 have lower spatial resolution and are primarily used to confirm that the particle has penetrated the full system, thus identifying it as a muon. Each station is segmented into four concentric regions (R1–R4), defined by increasing radial distance from the beam axis, as shown in Fig. 2.12 (right). The segmentation is designed such that all four regions cover approximately equal solid angles. The granularity of the chambers increases with particle density: smaller cells are used closer to the beam pipe to maintain a roughly uniform occupancy across the detector.

The muon detectors are primarily based on Multi-Wire Proportional Chamber (MWPC) technology. Due to the high particle flux in station M1, Gas Electron Multiplier (GEM) detectors are used in this region because of their superior rate capability and radiation hardness.

2.2.4 The System for Measuring Overlap with Gas (SMOG)

LHCb is the only LHC experiment capable of collecting data both in collider and fixed-target mode. This is made possible by its fixed-target system, known as SMOG (System for Measuring Overlap with Gas), originally designed to enable precise luminosity calibration of proton-proton collisions [6]. The SMOG system allows for the

controlled injection of a low flow of noble gas into the vacuum chamber of the LHCb Vertex Locator (VELO). The SMOG system enables fixed-target collisions at the LHC for the first time, allowing the study of proton-nucleus and nucleus-nucleus interactions at various centre-of-mass energies. Operational since 2015, SMOG has been involved in several data-taking campaigns using different target gases (He, Ne, Ar) and beam species (protons or lead ions) at energies ranging from 2.5 to 6.5 TeV. The gas is injected into the beam pipe near the interaction region, see Fig. 2.13, increasing the local vacuum pressure from $\sim 10^{-9}$ mbar to just above 10^{-7} mbar, still sufficiently low to avoid perturbing LHC operations. For a beam intensity of 10^{14} protons, this corresponds to a luminosity of 6×10^{29} cm^{-2}s^{-1} over a 1 meter gas column, which matches the acceptance of the VELO detector [83].

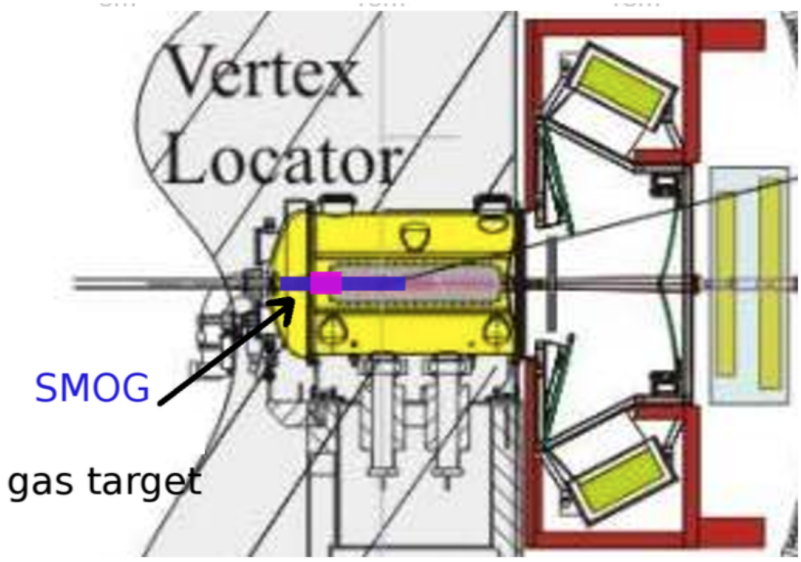


FIGURE 2.13: Zoom of the Vertex Locator region, showing the spatial extension of the internal gas target provided by the SMOG device, highlighted in dark purple [83]. The light purple square indicates the SMOG upgrade, SMOG2 [84] (discussed is Sec. 2.3.4).

During gas injection, the two vacuum ion pumps located beneath the interaction point are turned off and the nominal vacuum is typically restored within minutes once injection ceases. All the components of the SMOG gas injection system are shown in Fig. 2.14. The gas is stored in a high-pressure reservoir and then directed toward the VELO detector through a 4 m long tube at a flow rate of $3 \cdot 10^{-5}$ mbar l/s.

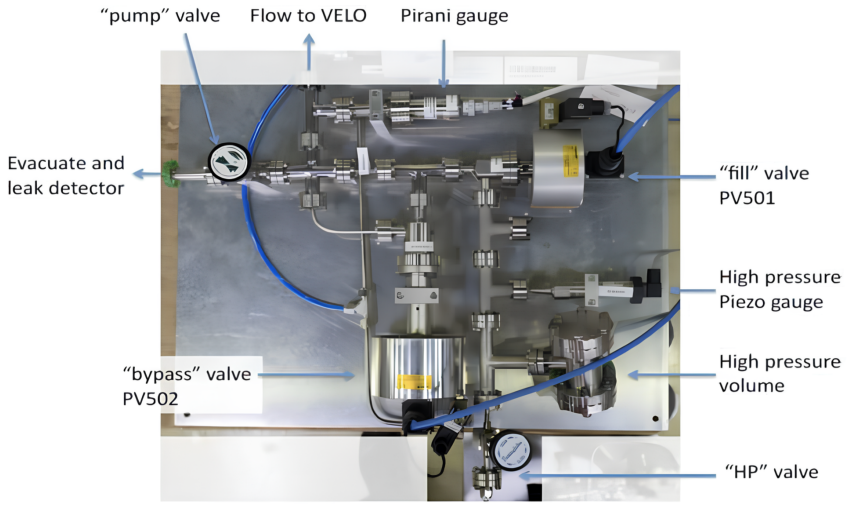


FIGURE 2.14: The SMOG gas feed system [83].

In the fixed-target configuration, proton or ion beams with per-nucleon energy E_N between 0.9 and 7 TeV deliver nucleon-nucleon collisions with centre-of-mass energies $\sqrt{s_{\mathrm{NN}}} \sim \sqrt{2E_N M_N}$, ranging from 41 to 115 GeV [83]. This configuration significantly boosts the centre-of-mass frame in the direction of the beam, resulting in the LHCb detector covering the backward rapidity region. For instance, at $\sqrt{s_{\mathrm{NN}}} = 110$ GeV, the rapidity shift is $y^* = y_{\mathrm{lab}} - 4.8$, and the detector acceptance spans $-2.77 < y^* < 0.23$, allowing access to the large-x region of the target nucleon, which is typically only reachable in collider mode at much higher momentum transfers Q^2.

The SMOG unique configuration enables a broad physics program, including studies of parton distribution functions at large $x(\to 1)$, where theoretical uncertainties remain significant. Fixed-target data also help constrain models relevant for cosmic ray physics [83]. In collisions of ion beams with heavy gases, SMOG allows access to the high-density regime of QCD, offering valuable input for the study of Quark-Gluon Plasma signatures with heavy quarks.

2.2.5 The trigger system

An efficient trigger system is essential to ensure good detector performance and high-quality data collection. It allows the selection of events containing potentially interesting physical processes from the large number produced in each bunch crossing. The bunch-crossing rate for proton-proton collisions at the LHC is 40 MHz, far too high to store all events efficiently. The LHCb trigger system is therefore designed to reduce the event rate from 40 MHz to about 12.5 kHz, a rate manageable by the online data acquisition system.

The trigger is structured in three levels: a hardware stage, the Level-0 (L0) trigger, followed by two software stages, the High-Level Trigger 1 (HLT1) and High-Level

Trigger 2 (HLT2), as illustrated in Fig. 2.15, which shows the system used during Run 2.

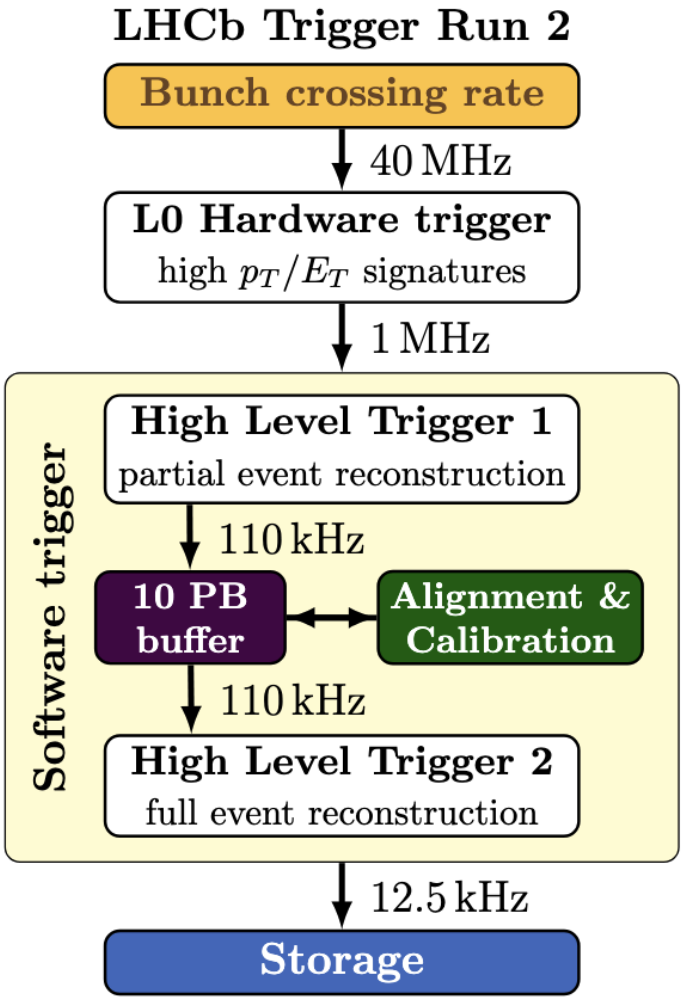


FIGURE 2.15: Overview of the LHCb trigger system [85].

2.2.5.1 L0 trigger

The hardware stage of the trigger, called L0, is responsible for rapidly reducing the 40 MHz bunch-crossing rate to 1 MHz, which corresponds to the maximum readout rate of the full detector. Due to their large mass, B mesons tend to decay into particles with high transverse momentum (p_T) and transverse energy (E_T). The L0 trigger identifies the highest E_T hadron, electron, and photon clusters in the calorimeter system, and the two highest p_T muons in the muon chambers.

The L0 calorimeter trigger uses the energy deposited in the SPD, PS, ECAL, and HCAL to make its decisions. Trigger candidates are selected based on the transverse energy deposited in 2×2 cell clusters in the ECAL and HCAL. The transverse energy

of a cluster is defined as:

$$E_T = \sum_{c=1}^{4} E_c \sin\theta_c,$$

where c is the cell index, E_c is the energy deposited in the cell, and θ_c is the angle between the z-axis and the line connecting the cell centre to the nominal pp interaction point.

Information from the SPD and PS detectors is used to distinguish between hadron (L0Hadron), photon (L0Photon), and electron (L0Electron) candidates. The L0 muon trigger searches for straight-line tracks across the five muon stations. The estimated p_T of each muon candidate is based on its trajectory, and the trigger decision is based on the two muons with the highest p_T. A trigger is issued if either the leading p_T exceeds the L0Muon threshold, or the product of the leading and subleading p_T values exceeds the L0DiMuon threshold.

To reduce event complexity and ensure fast processing in the software trigger stages, most L0 trigger lines also impose a maximum number of SPD hits after which the event is rejected.

2.2.5.2 High Level trigger

Events accepted by the L0 trigger are passed to the first stage of the software trigger, known as HLT1. At this level, the reduced event rate allows for fast and more refined (although not yet offline-quality) reconstruction and selection algorithms to be applied. Initially, primary vertices and tracks in the VELO are reconstructed. These VELO tracks are then matched to hits in the tracking stations to refine the measurement of the transverse momentum and provide a first estimate of the particle charge. A Kalman filter [86] is used to fit the tracks, taking into account effects such as multiple scattering and energy loss. The reconstructed tracks can then be used to compute several quantities, including their impact parameter with respect to the PV, the positions of possible secondary vertices, invariant masses of track combinations, and flight directions, which help in performing an initial event selection. For muon candidates, an initial matching is performed between tracks from the VELO and T-stations and hits in the muon chambers. This enables a basic selection based on the p_{T} of the muon candidates.

Events selected by HLT1 are then passed to the HLT2 stage, where a full event reconstruction is carried out using information from all detector subsystems, including the RICH detectors and calorimeters. The final output rate after HLT2 is reduced to about 12.5 kHz.

Both HLT1 and HLT2 use specific trigger algorithms that are designed in advance based on the physics goals of each data-taking period.

2.2.6 Event processing

Once the event survive the trigger, the information from the detector is stored and the full event reconstruction starts by performing the reconstruction of the track trajectories and the identification of the particle type.

2.2.6.1 Track reconstruction

The particle trajectories (tracks) are reconstructed from hits in the tracking sub-detectors: VELO, TT, IT, and OT described in Sec. 2.2.2. Five types of tracks are defined, as shown in Fig. 2.16, based on how the particles cross the LHCb tracking system.

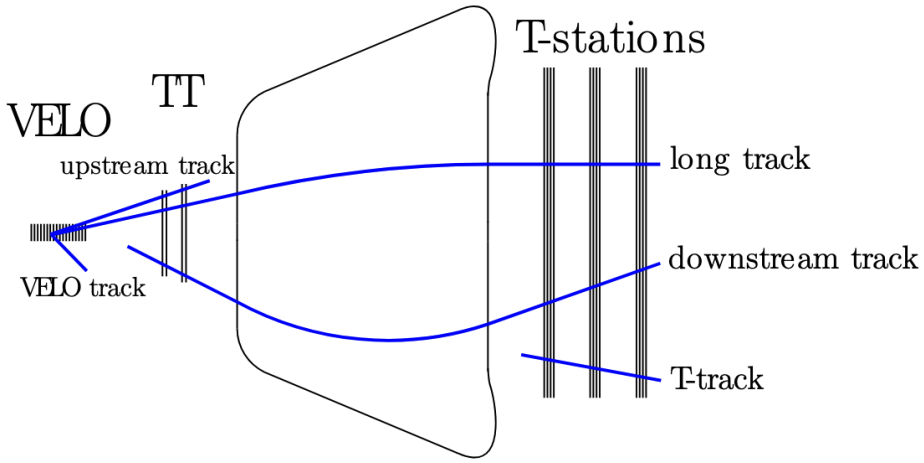


FIGURE 2.16: Sketch of the different types of tracks within LHCb. [85].

- **VELO tracks**: pass only through the VELO; used primarily for precise reconstruction of the primary vertex;
- **T tracks**: cross only the T stations;
- **Upstream tracks**: pass through the VELO and TT stations;
- **Downstream tracks**: pass through the TT and T stations;
- **Long tracks**: traverse the full tracking system; they provide the best momentum resolution and are used in most physics analyses.

Track reconstruction is carried out using several dedicated algorithms. It starts with the VELO seeding, which provides the initial track segments used by subsequent steps. The forward tracking extrapolates VELO tracks through the TT and T stations and is the main method for reconstructing long tracks. T seeding instead starts from hits in the T stations and also contributes to the reconstruction of long tracks.

The track matching algorithm combines unused VELO seeds with T seeds to find additional long tracks. The upstream tracking uses the remaining unused VELO seeds and extrapolates them to hits in the TT station to reconstruct upstream tracks. Similarly, downstream tracking starts from T seeds and matches them back to the TT station to reconstruct downstream tracks. VELO or T seeds that are not used by any of these algorithms are retained as VELO or T tracks, respectively.

2.2.6.2 Particle identification

Once the tracks are reconstructed, it is necessary to identify the corresponding particle type. The LHCb detector is particularly efficient in this task, thanks especially to its dedicated PID system described in Sec. 2.2.3. Fig. 2.17 illustrates how different particles interact as they traverse the detector.

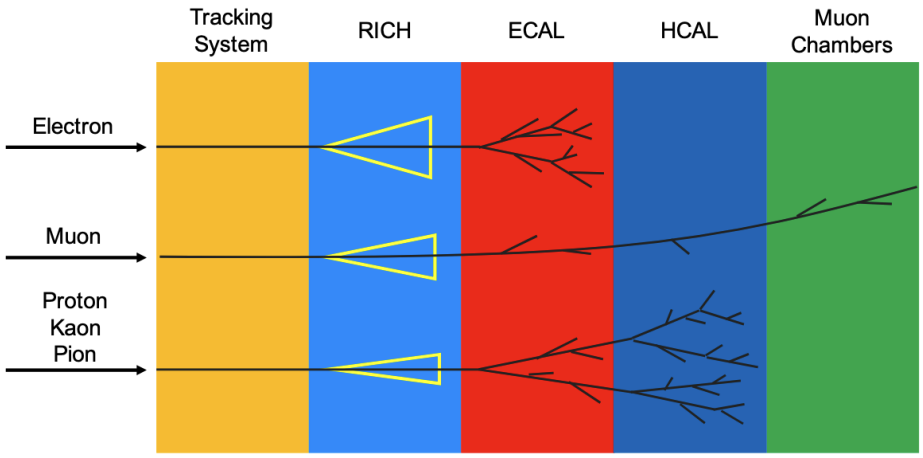


FIGURE 2.17: Illustration of the detector response for different particle types in LHCb. [87].

The thesis will concentrate on the reconstruction and identification of the muons, since the charmonia states studied in this work are reconstructed via their dimuon decay channel. Muon identification in LHCb is carried out in three main steps [88]:

- A loose binary selection of muon candidates, based on their ability to penetrate the calorimeters and iron filters. A particle leaving hits in specific muon stations, listed in Tab. 2.2 for three different momentum ranges, is selected as muon candidates through the `IsMuon` variable. This procedure provides high efficiency while keeping the misidentification rate of hadrons at the percent level.

TABLE 2.2: Muon stations required to trigger the `IsMuon` decision in different momentum ranges.

Momentum range	Muon stations
$3 < p < 6$ GeV/c	M2 and M3
$6 < p < 10$ GeV/c	M2 and M3 and (M4 or M5)
$p > 6$ GeV/c	M2 and M3 and M4 and M5

- A likelihood-based selection using the logarithm of the likelihood ratio between the muon and non-muon hypotheses, denoted as ΔLL_μ. It is computed using the pattern of hits around the extrapolated track position in the muon stations, where the extrapolation is based on tracks reconstructed with high precision in the tracking system.

- A multivariate selection, based on a classification algorithm that combines information from the tracking system, RICH detectors, calorimeters, and muon chambers. The process results in a single output variable that estimates the muon probability, known as $\texttt{ProbNN}_\mu$ [87].

The $\texttt{ProbNN}_\mu$ variable, introduced during Run 2 of LHC operations, has been shown to provide the best performance as it uses information from the entire detector to distinguish between particle types, thus is the one used in this thesis.

2.2.7 Data processing framework

The data collected by the LHCb detector, as well as simulated events, undergo a multi-stage processing chain before being used for physics analyses. After the hardware and software trigger selections, events are reconstructed to identify tracks, vertices, and particles. The reconstructed samples are then further reduced by dedicated selections, called "stripping", to extract datasets of interest, which are finally analysed to perform the physics measurements. In the case of simulated events, a comparable sequence is followed, starting from the generation of the primary collisions and particle decays, followed by the detector response simulation, reconstruction, stripping, and analysis.

This workflow is implemented within a dedicated software framework called Gaudi [89], developed for LHCb to provide a common interface between all processing steps. The main applications within this framework are:

- GAUSS [90]: the LHCb simulation framework, which interfaces event generators and decay engines, and simulates the response of the LHCb detector. The different components of Gauss are discussed in more detail in Sec. 2.2.8.

- BOOLE [91]: the application that finalises the simulation phase by reproducing the digital detector response. The output produced by BOOLE is then processed by Brunel in the same way as the data coming from the LHC collisions.

- MOORE [91]: the application responsible for defining and applying the software trigger algorithms to both real and simulated data.
- BRUNEL [92]: the LHCb application for event reconstruction, which processes both real and simulated data in the same way.
- DAVINCI [93]: the main analysis framework, which uses the reconstructed data to select events and builds the decay chains under study.

The overall data flow, from the initial collisions or event generation to the final analysis stage, is summarised in Fig. 2.18.

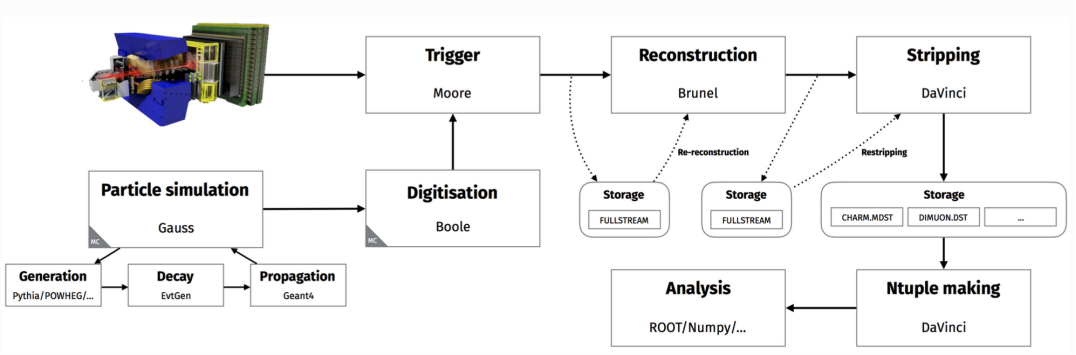


FIGURE 2.18: Illustration of the data processing flow in LHCb [94].

2.2.8 LHCb simulation

For any analysis, studying the detector response requires simulated samples that reproduce as closely as possible the physical processes observed in data. The simulation production used for the analysis presented in this thesis consists of three main stages, designed to model the production and decay of J/ψ and $\psi(2S)$ mesons in a heavy-ion environment:

- **Event generation**: The first step involves simulating the primary particle production in the collisions according to theoretical models. Parameters such as the LHC beam energy and the relevant collision configuration are provided as input. PYTHIA [95] is used as the event generator to simulate the hard scattering process leading to the signal decay. Particles are then embedded into full minimum-bias PbPb collisions generated with the EPOS event generator [96], which provides a realistic description of the underlying event. The embedding procedure is essential to reproduce the particle multiplicity and detector occupancy observed in heavy-ion collisions, which directly affect detector performance and efficiency estimation.
- **Decay simulation**: The decays of unstable particles, including the dimuon decays of the J/ψ and $\psi(2S)$, are simulated with EVTGEN [97], while final-state radiation is handled by PHOTOS [98].

- **Detector simulation**: The transport of the generated particles through the LHCb detector, along with their interactions with the detector material and the corresponding detector response, are simulated using the GEANT4 toolkit [99, 100], adapted to the LHCb environment [101].

After event generation, simulated samples undergo the same processing chain as real data. During the trigger selection, simulated events are not physically rejected but are instead marked as accepted or rejected according to the applied criteria. Moreover, the kinematic distributions of the generated particles prior to their interaction with the detector are stored separately. This procedure allows detailed studies of selection and reconstruction efficiencies, facilitating the separation of detector effects from the underlying physics processes and enabling a precise evaluation of detector-induced biases in the final analysis.

2.2.9 Heavy-ion Run 2 data collected at LHCb

The performance of the LHCb detector, originally designed for low-multiplicity environments such as proton-proton collisions, is affected by the significantly higher particle multiplicity which is created in heavy-ion collisions like PbPb, both at the hardware and software level.

From the hardware point of view, limitations arise due to the finite number of readout channels and buffer capacities of the sub-detectors. For instance, the number of clusters, *i.e.* groups of adjacent sensor hits produced by charged particles in the detector, that can be recorded in the VELO is limited by hardware constraints. As shown in Fig. 2.19, which displays the correlation between the number of VELO clusters and the energy deposited in the ECAL, the VELO reaches saturation in central PbPb collisions. The variable `nVeloClusters` corresponds to the total number of reconstructed clusters in the VELO for a given event. Since the ECAL energy deposit is correlated with the number of particles in the event, the observed saturation indicates that LHCb (in Run 2) cannot efficiently record central collisions, *i.e.* with centrality lower then 60%.

On the software side, the reconstruction algorithms face additional challenges as the detector occupancy increases. In the VELO, the high density of hits makes it more difficult to form reliable track seeds using the same algorithms developed for *pp* collisions, which reduces the efficiency of pattern recognition. In the forward tracking system, multiple VELO seeds can sometimes be associated with the same hits in the T stations arising ambiguities in linking hits to unique tracks, and resulting in the reconstruction of spurious trajectories, known as *ghost tracks*, which do not correspond to any real particle and can degrade the quality of the reconstructed event.

This effect is illustrated in Fig. 2.20, where the number of reconstructed long tracks is seen to saturate and even decrease at high VELO occupancy, highlighting the limitations of the reconstruction software algorithm under such conditions.

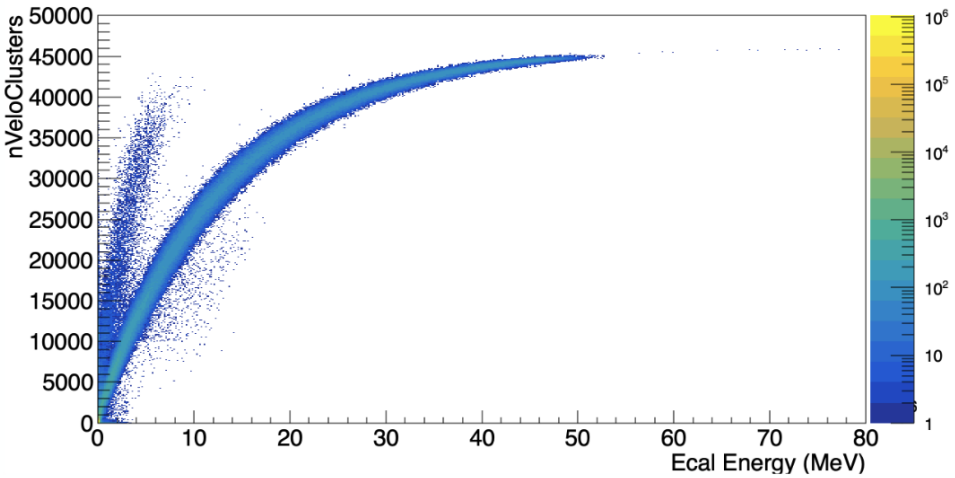


FIGURE 2.19: Number of VELO clusters as a function of the energy deposit in ECAL for Run 2 PbPb collisions recorded by LHCb.

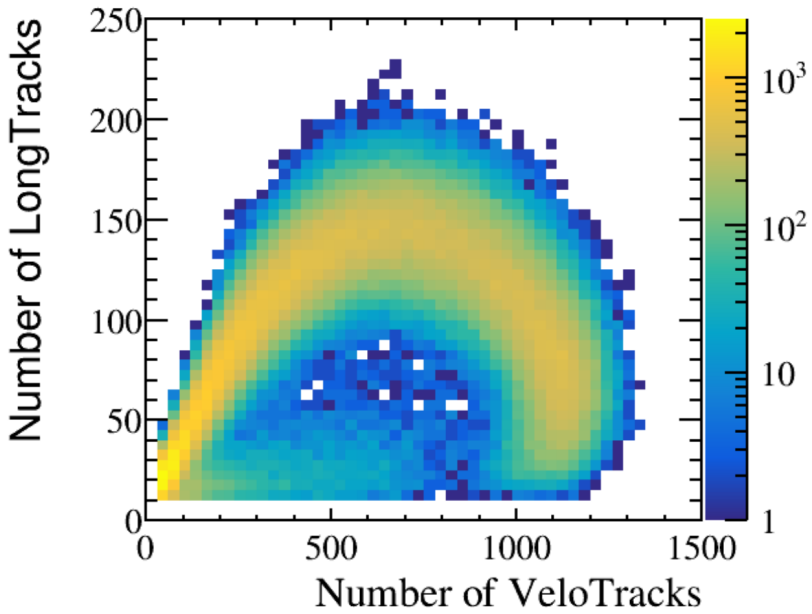


FIGURE 2.20: Number of Long tracks as a function of the VELO tracks for Run 2 PbPb collisions recorded by LHCb.

Due to these limitations, the data-taking strategy during the 2018 PbPb run focused on non-central collisions, with a restriction to centralities above 60%, where the overall particle multiplicity is lower and the reconstruction remains efficient. As already mentioned, during the LHC Long Shutdown 2, LHCb underwent major upgrades, which significantly enhanced its capabilities also for heavy-ion data taking, as discussed at the end of the next section 2.3.5.

2.3 The LHCb Upgrade I

Although the LHCb detector was primarily designed for precision measurements in heavy-flavor physics, during Run 1 and 2 the experiment demonstrated excellent capabilities in many other sectors, including electroweak, heavy-ion, and beyond the Standard Model physics. For this reason, LHCb Upgrade I (LHCb UI), installed during LS2, was conceived with the idea to expand the scope of the experiment to become a general purpose one in the forward region.

On the operational side, LHCb was designed to take data at a maximum instantaneous luminosity of $\mathcal{L} = 2 \times 10^{32}\,\mathrm{cm}^{-2}\mathrm{s}^{-1}$, in order to keep the average number of visible primary pp interactions ("pile-up") close to unity. However, the detector successfully ran for most of Run 1 and 2 at $\mathcal{L} = 4 \times 10^{32}\,\mathrm{cm}^{-2}\mathrm{s}^{-1}$, showing its ability to perform and deliver excellent physics results even at higher luminosities and with pile-up levels greater than originally foreseen. Albeit LHCb outperformed its original design, also providing high-quality data sets across different collision systems, many key physics observables, especially in the flavour sector, remain statistically limited. Increasing statistics is crucial, particularly for channels involving fully hadronic final states. However, the original detector configuration posed a limitation in this regard, primarily due to the maximum output rate allowed by the first trigger stage (L0).

Based on these considerations, the Upgrade I was designed to operate at a nominal instantaneous luminosity of $\mathcal{L} = 2\times10^{33}\,\mathrm{cm}^{-2}\mathrm{s}^{-1}$ and to collect events at the full LHC bunch crossing rate of 40 MHz. Events are filtered by a fully software-based trigger that reconstructs them in real time at a visible interaction rate of around 30 MHz. By increasing the instantaneous luminosity by a factor of five and improving trigger efficiencies for most decay modes by up to a factor of two [102], annual yields for many channels are expected to increase by an order of magnitude. The new trigger strategy, together with the increased luminosity and pile-up, required a complete redesign of the LHCb detector and its readout electronics. The upgraded system now accommodates higher event multiplicities thanks to increased granularity, a key feature for improved performance in heavy-ion collisions.

The LHCb UI detector is shown in Fig. 2.21, highlighting the new tracking system, redesigned RICH optics, and largely replaced readout electronics. The M1 muon station, along with the SPD and PS detectors, have been removed due to their inability to handle the increased occupancy. The following sections provide an overview of the upgraded LHCb detector, focusing on the newly introduced subdetectors as well as the redesigned trigger system. Conversely, the strategies for track reconstruction, particle identification, and simulation remain largely unchanged from the previous configuration already described, and will therefore not be revisited here.

Also, a brief description is also included of a technical contribution I gave related to the upgraded VELO detector.

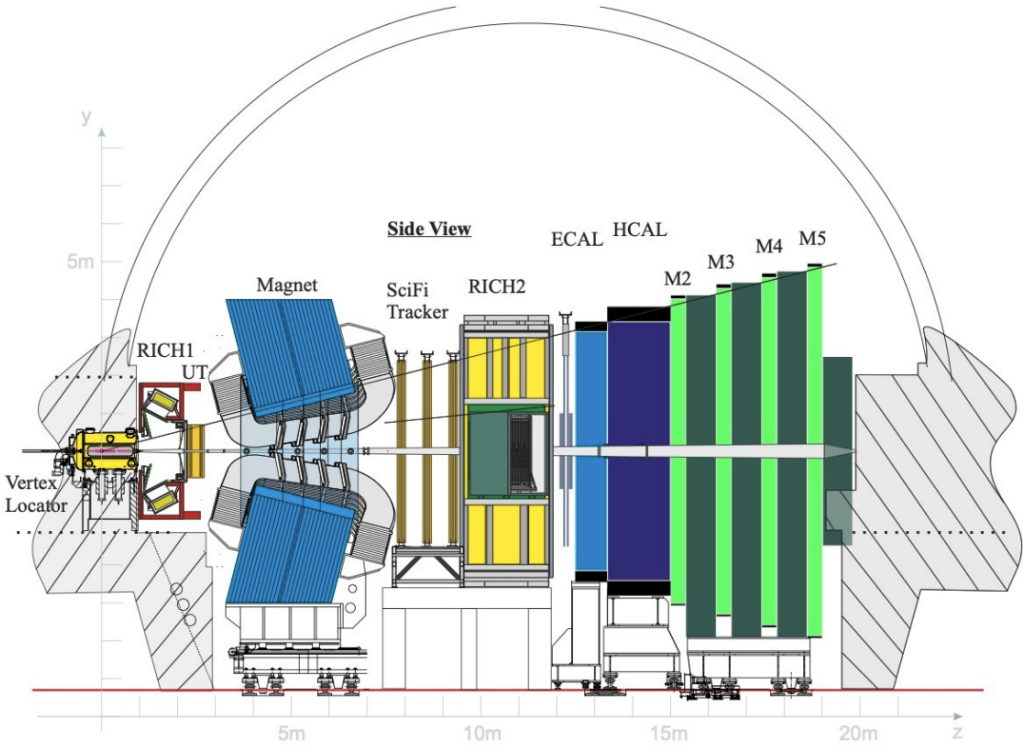


FIGURE 2.21: Layout of the upgraded LHCb detector [103].

2.3.1 Tracking System - Upgrade I

The overall geometry of the tracking system remains unchanged, but all its components have been fully redesigned. The new VELO now features pixel sensors instead of strips, significantly enhancing spatial resolution and granularity. The TT and main tracker have been replaced by the Upstream Tracker (UT), a silicon-strip detector, and the Scintillating Fibre (SciFi) tracker, which uses bundles of scintillating fibres to detect charged particles and will be discussed below.

A specific technical contribution to the operation of the new VELO detector is briefly outlined in the following Sec. 2.3.1.1.

2.3.1.1 VELO - Upgrade I

The overall layout of the detector is maintained, with modules mounted on two independent retractable halves to safeguard them during non-stable beam conditions. Nonetheless, both the spatial configuration and the module design have been updated [104]. The upgraded VELO is a hybrid pixel detector capable of operating at a 40 MHz readout rate and designed for a luminosity of $2 \times 10^{33}\,\mathrm{cm}^{-2}\mathrm{s}^{-1}$. The upgrade delivers a significant improvement in tracking speed and spatial resolution compared to the previous version, even in high-occupancy environments, thanks to the finer

pixel granularity and a reduced distance of just 5.1 mm between the LHC beam line and the first active pixel layer.

The detector consists of two halves (referred to as the A and C sides), each containing an array of 26 L-shaped silicon pixel modules (see Fig. 2.22), covering a sensitive area of 14.08×14.08 mm^2 per module. Each module integrates complex front-end electronics, including the VeloPix ASICs, which are responsible for handling the high data throughput from the collisions.

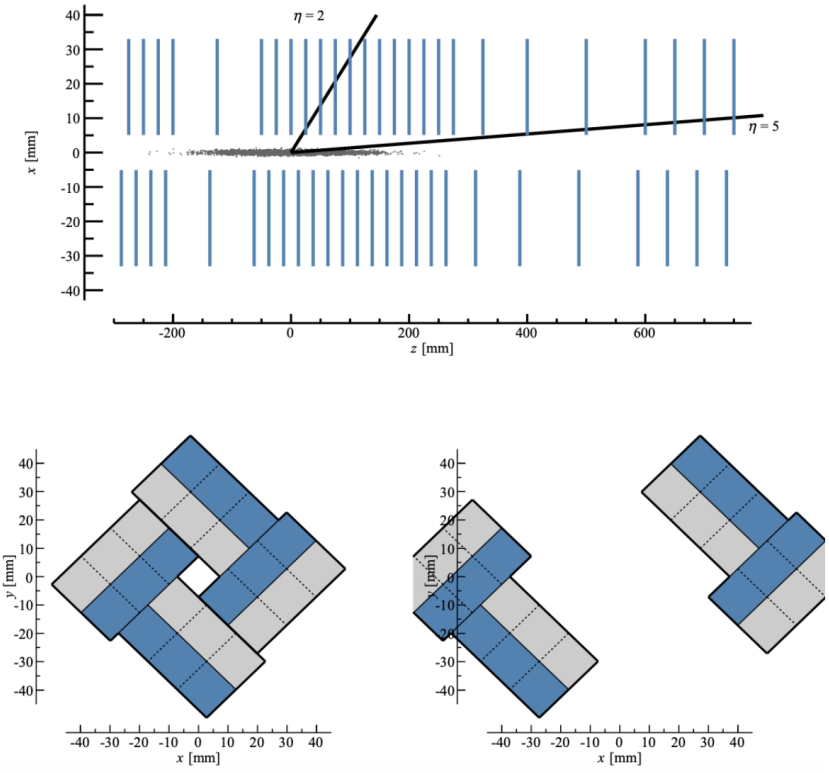


FIGURE 2.22: Layout of the upgraded VELO. Top: schematic cross section at y = 0, together with illustrations of the z-extent of the luminous region and the nominal LHCb acceptance. Bottom: schematic layout in the (x, y) plane (left: VELO closed, right: VELO fully open) [104].

To ensure that the temperature of these sensors remains within safe limits for the detector, alarm panels had to be developed, as illustrated in Fig. 2.23.

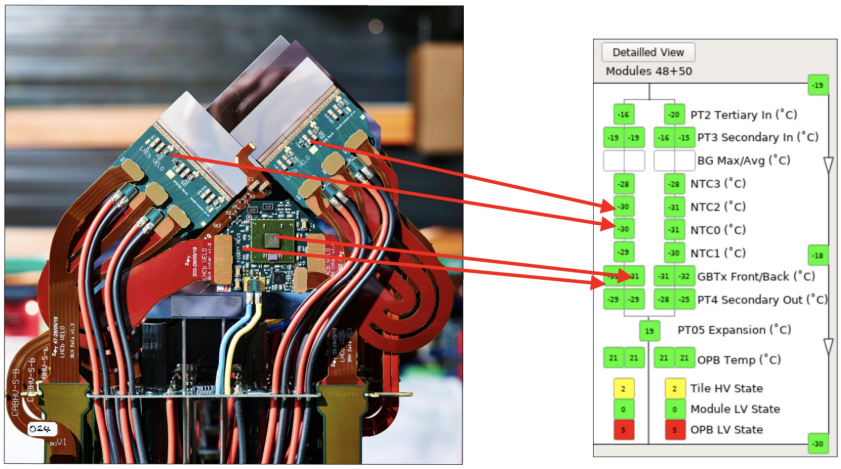


FIGURE 2.23: Detail of a VELO module (left) and the correspondent temperature sensors in the expert control panel (right).

In fact, each VELO module is equipped with multiple temperature sensors essential for monitoring and maintaining the thermal stability of the detector. In particular, four NTC (Negative Temperature Coefficient) sensors are located on the hybrid circuits, two on the GBTx (GigaBit Transceiver) boards responsible for data transmission and two on the Opto-Power Boards (OPB), which contribute to the thermal management of the optoelectronic components. In addition to these, eleven PT100 (Platinum resistance thermometer) sensors are installed throughout the VELO structure. These include sensors placed on the RF-foil, the module support base, and key locations near the vacuum enclosure, in order to provide accurate monitoring of the global thermal environment. To guarantee the safe operation of the VELO detector in Run 3 conditions, operating in vacuum at approximately $-30°C$ and very close to the LHC beam pipe, a reliable alarm system is essential. Such a system must provide visual alerts by continuously monitoring temperature inputs and promptly signaling any abnormal or potentially dangerous temperature readings. This safeguards the detector hardware and the overall experiment from damage or malfunction.

Building on these requirements, togheter with a colleague I developed the alarm panels for both the NTC and PT100 sensors, using the WinCC-OA software [105], widely adopted within the LHCb control systems. The panels are integrated into the expert control interface, accessible during data-taking and detector operation, allowing VELO experts to monitor all critical temperature sensors efficiently.

The previous (Run 2) alarm interface allowed only two alarm thresholds to be set at the higher temperature range, and all sensor alarms could be activated or deactivated only collectively. On the contrary, the new panels developed provide enhanced flexibility by enabling individual configuration and control of each sensor's alarm separately. As shown in Fig. 2.24 for NTC and in Fig. 2.25 for PT100, the control panel for the alarms allows up to six configurable alert limits, both for low

and high temperature ranges, and provides dedicated buttons for each sensor type.

Each sensor in every module on both VELO detector halves (A and C sides) can be monitored and controlled independently.

The interface displays the sensor data in tabular form, where experts can easily activate or deactivate alarms for individual sensors, adjust alarm thresholds interactively, and monitor live sensor readings. The table columns include sensor identifiers, descriptive names, activation status, and alarm limits for fatal, error, and warning levels, both at low and high temperature extremes shown in Fig. 2.24 and 2.25.

To facilitate rapid diagnosis of potential problems, the panels use a colour-coded scheme to indicate the status of each sensor reading: green signals normal operating conditions, yellow warns of cautionary levels, orange indicates errors that may degrade module performance, and red flags fatal conditions that could cause severe damage. Alternating cell shading improves readability, and separate views are available for each sensor category, as well as a consolidated module-wise overview for quick identification of problematic units, as shown in Fig. 2.26 for NTC and in Fig. 2.27 for PT100.



FIGURE 2.24: Picture of the setting alarm panel for the NTC sensors.

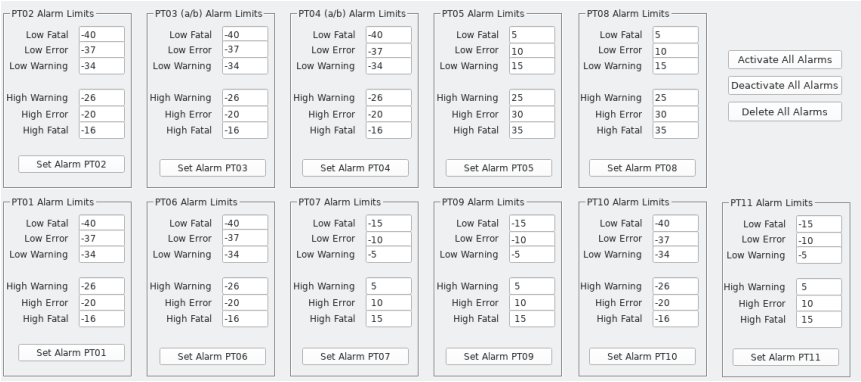


FIGURE 2.25: Picture of the setting alarm panel for the PT100 sensors.

At the time of writing, both the NTC and PT100 alarm panels have been fully implemented, thoroughly tested, and successfully integrated into the VELO operational framework. They are actively used by the VELO crew during data-taking to ensure

the detector's safe and stable functioning throughout Run 3. This implementation represents a significant improvement in the detector's safety infrastructure, reducing the risk of hardware damage due to thermal anomalies and enhancing the overall reliability of the VELO detector.

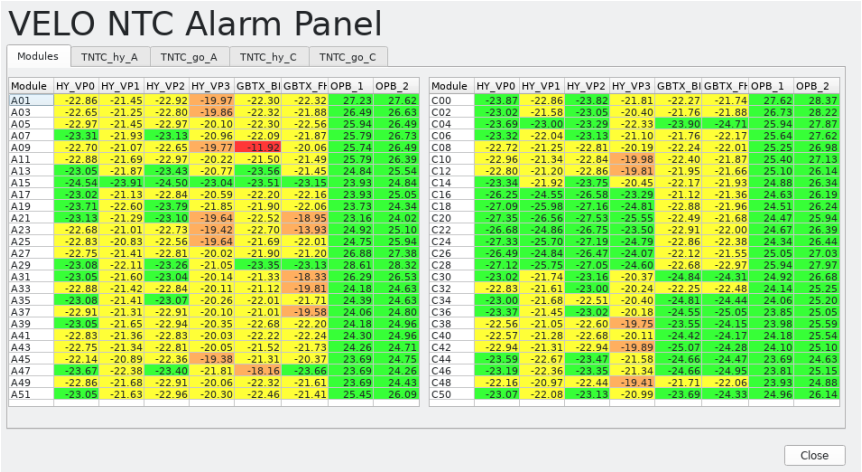


FIGURE 2.26: Picture of the monitoring alarm panel for the NTC sensors.

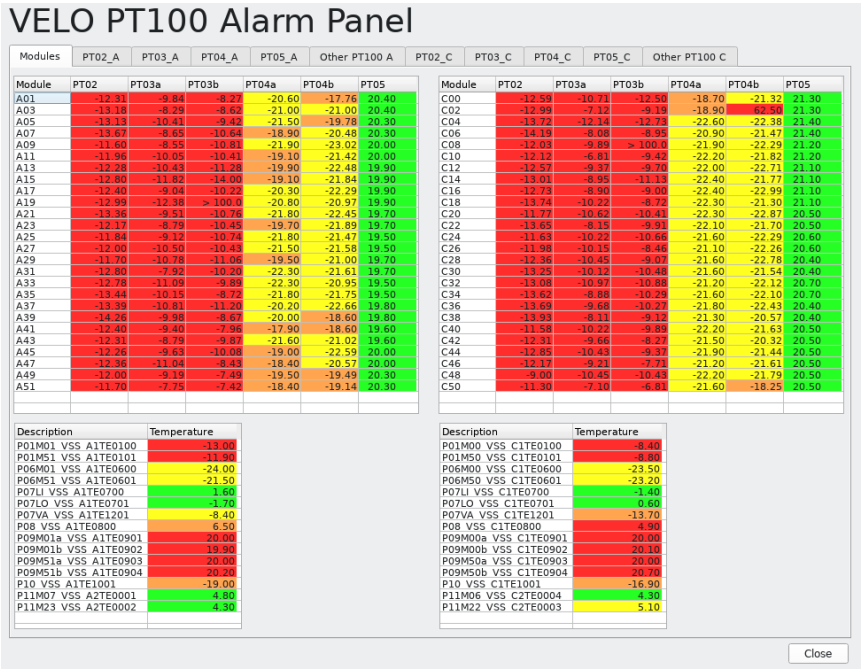


FIGURE 2.27: Picture of the monitoring alarm panel for the PT100 sensors.

2.3.1.2 Upstream Tracker (UT)

To replace the TT station, the Upstream Tracker (UT) detector [106] has been developed and installed upstream the magnet. Its structure is similar to the previous

tracking station, consisting of four layers of silicon microstrip detectors, as illustrated in Fig. 2.28. The UT is positioned approximately 7 cm closer to the LHC beam line than the former TT station, thereby improving track reconstruction efficiency in the innermost region and achieving full geometrical coverage within the nominal LHCb acceptance. To cope with the increased particle flux and occupancy expected during Run 3, the strip pitch has been reduced in the inner regions to 93.5 μm, providing enhanced granularity and better resistance to radiation damage. In the outer regions, where occupancy is lower, the strip pitch remains at 187.5 μm.

Thanks to these design improvements, the overall momentum resolution achieved by the UT has improved by approximately 10-20% relative to the previous system, contributing to better vertexing and downstream tracking performance.

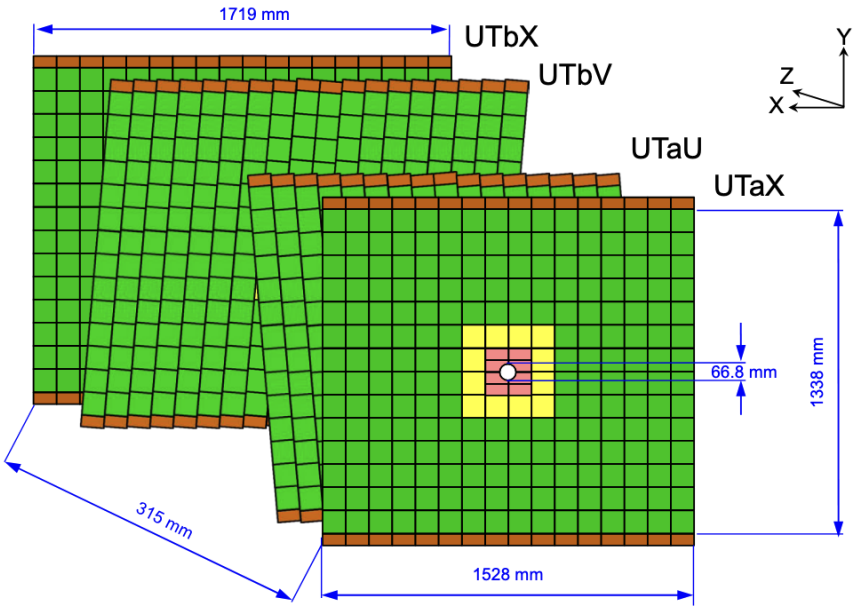


FIGURE 2.28: Layout of the four stations composing the UT detector [106].

2.3.1.3 Scintillating Fibre (SciFi)

Downstream of the magnet, the Scintillating Fibre (SciFi) tracker [106] has been installed to replace the three T stations of the original tracking system. Designed to deal with the higher detector occupancies expected in Run 3, particularly during heavy-ion runs, the SciFi detector offers significantly better performance than the previous Outer Tracker (OT), which used gaseous detection technology.

As illustrated in Fig. 2.29, the SciFi detector consists of three stations, each composed of four detection layers. Every layer is made up of 96 mats of scintillating fibres, each mat measuring 2.4 m in length and composed of fibres with a diameter of 250 μm. The mats are grouped into 12 modules per layer. At the end of each

module, 16 Silicon Photomultipliers (SiPMs) collect the light emitted by the fibres when traversed by charged particles.

The SiPMs are operated at a temperature of $-40°C$ to reduce thermal noise and mitigate radiation damage, ensuring stable long-term performance. The detector achieves a hit resolution better than 100 μm over a total active area of approximately 340 m^2, making it one of the largest and most precise silicon-free tracking systems in high-energy physics.

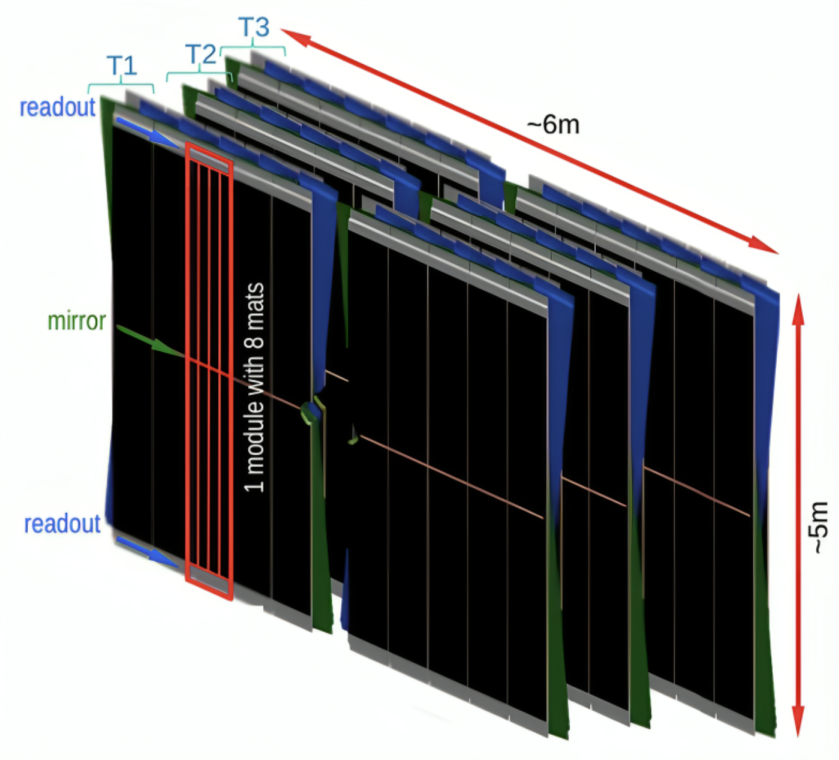


FIGURE 2.29: Layout of the SciFi detector.

2.3.2 Particle Identification System - Upgrade I

The previous PID system included the two RICH detectors, the calorimeter system, and the muon stations. In the upgraded configuration, the Preshower and Scintillating Pad Detector of the calorimeter system have been removed, together with the first muon station. These components were originally designed to provide prompt information to the L0 hardware trigger, which has been eliminated in the upgraded detector.

Aside from this, the overall structure of the PID system has remained unchanged [107]. The most significant improvements concern the RICH detectors. The original Hybrid PhotoDetectors (HPDs), which featured integrated 1 MHz readout electronics, have been replaced with multi-anode photomultiplier tubes (MaPMTs) capable of handling

the increased data rates required by the upgraded readout system. In addition, the optical system of RICH1 has been redesigned to reduce the high hit occupancy observed in the central region during Run 2. In particular, the focal lengths of the spherical mirrors were increased from 2.7 m to 3.7 m, effectively halving the hit density in the most affected areas.

The layout of the calorimeter and muon systems has remained unchanged, but the readout electronics have been upgraded to support the 40 MHz readout rate of the new system. At the same time, the gain of the photomultiplier tubes used to read the calorimeter cells has been reduced by a factor of five, mitigating the risk of rapid ageing due to the higher luminosity conditions of Run 3.

2.3.3 The trigger system - Upgrade I

One of the most important updates introduced in the LHCb upgrade for Run 3 concerns the trigger system, which has undergone a complete redesign. The most notable change from the Run 1 and 2 architecture is the removal of the hardware L0 trigger. As already explained, in the previous design, the L0 system was a hardware-level decision-making layer, operating at the LHC bunch crossing rate of 40 MHz and based primarily on information from the calorimeter and muon systems. It aimed to reduce the input event rate to 1 MHz, suitable for processing by the software-based high-level triggers (HLT1 and HLT2).

However, the L0 trigger introduced significant limitations, particularly for hadronic final states and heavy-ion collisions, where event topologies are complex and calorimeter-based decisions may not be optimal. For Run 3 it was decided to move to a fully software-based trigger system, reading out the entire detector at the full LHC bunch crossing rate. The new trigger system, performs real-time processing of all events using two consecutive software-based stages: HLT1 and HLT2, as shown in Fig 2.30. The entire detector is read out for every event, and both stages are executed on a dedicated high-performance computing farm [102].

The first level, HLT1, is designed to perform a fast partial reconstruction of charged particles using VELO and tracking stations upstream and downstream of the magnet. Its purpose is to reduce the event rate from 30-40 MHz down to about 1 MHz. The HLT1 reconstruction includes fast tracking, vertexing, and basic selections on track impact parameters, momenta, and event multiplicities. It also selects displaced vertices, which are particularly useful for identifying b- and c-hadron decays. The HLT1 trigger is executed using the Allen framework [108], a highly optimised GPU-based software environment suited for real-time event reconstruction.

The second stage, HLT2, provides full offline-quality reconstruction of the events that pass HLT1. It runs complex and highly selective trigger lines based on decay topologies, particle identification, and global event characteristics. Thanks to

the usage of the Turbo stream [102], the HLT2 output includes reconstructed candidates and high-level variables, enabling physics analyses to be performed directly on trigger-output data without requiring reprocessing. This approach dramatically reduces storage requirements and turnaround time for analyses.

A large disk buffer is placed between these two stages to hold the data while the real-time alignment and calibration is being performed.

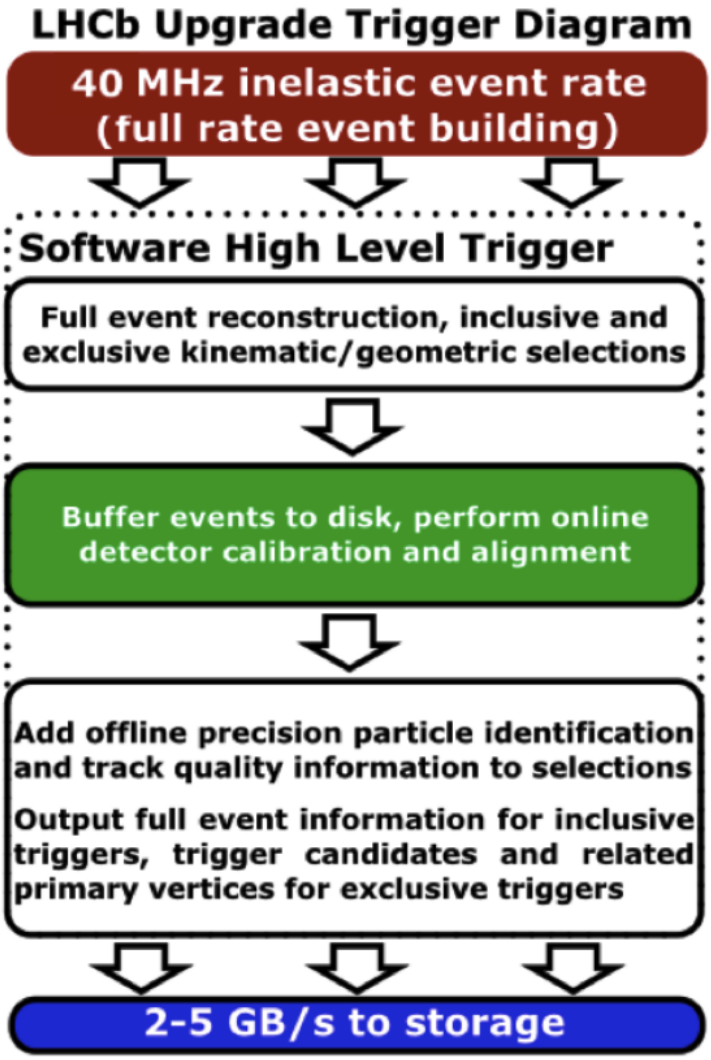


FIGURE 2.30: Overview of the LHCb trigger system in Run 3 [109].

The removal of the L0 hardware trigger and the shift to a fully software-based trigger pipeline mark a major step forward in the LHCb data acquisition and real-time analysis capabilities. This change allows for more inclusive and flexible event selection, improved efficiency for a broader range of physics channels, and better integration with real-time calibration and alignment strategies [102, 108].

2.3.4 SMOG Upgrade: SMOG2

During Run 2, the original SMOG system enabled the injection of noble gases into the LHCb vacuum chamber, allowing for the first fixed-target measurements at the LHC. However, the system faced several limitations, including low and diffuse gas density due to the open beam pipe, a single gas reservoir preventing target switching, and no direct control or measurement of the gas pressure near the interaction point.

For Run 3, a dedicated fixed-target system called SMOG2 [110] was installed (Fig. 2.31, left). It consists of an open-ended, thin-walled aluminium storage cell (20 cm long, 1 cm in diameter, 200 μm thick), located from 34 to 54 cm upstream of the nominal LHCb interaction point. The cell, is integrated upstream of the VELO and optimised to operate within the constrained space. It features Wake Field Suppressors to ensure electrical continuity and is coated with a low Secondary Electron Yield film to mitigate electron cloud effects, all while minimising additional material in the LHC beamline.

Gas is injected into the storage cell via a new Gas Feed System (GFS) (Fig. 2.31, right), which includes multiple reservoirs and allows precise regulation of the gas flow and direct measurement of areal density inside the cell. The system enables rapid switching between target species (*e.g.*, H_2, D_2, He, Ne, Ar), and significantly increases the luminosity for fixed-target physics by up to two orders of magnitude compared to SMOG.

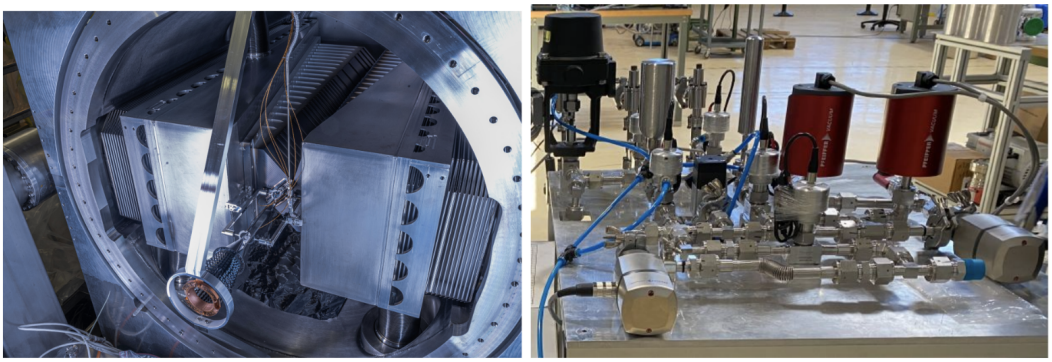


FIGURE 2.31: Picture of the SMOG2 cell (left) and gas feed system (right) [111].

The enhanced capabilities of SMOG2 open new opportunities for a broad fixed-target physics programme. These include studies of cold nuclear matter effects, and even the possible formation of a QGP when using heavier noble gases such as kripton or xenon. Other topics of interest include nuclear parton distribution functions at high Bjorken-x, charm and baryon production, and photon-induced processes in ultra-peripheral collisions. The use of hydrogen gas provides an essential baseline, and the increased data rates will also benefit cosmic ray measurements and contribute to a

better understanding of antiproton production and the muon puzzle in atmospheric showers.

2.3.5 Improved performance in Run 3 heavy-ion collisions

Thanks to the substantial detector and software upgrades implemented during LS2, the LHCb experiment has significantly improved its capabilities for heavy-ion data taking in Run 3. The upgraded tracking system, the removal of the hardware L0 trigger, and the fully software-based reconstruction pipeline have enabled efficient operation even in high-occupancy environments, allowing the experiment to collect PbPb collisions at much higher centralities than in Run 2.

As shown in Ref. [112], already with the first sample of PbPb collisions collected in November 2023 at $\sqrt{s_{\mathrm{NN}}} = 5.36$ TeV, the detector no longer exhibits saturation effects in the number of VELO clusters or SciFi tracks at high occupancy. Fig. 2.32 for example demonstrates a linear correlation between the number of SciFi clusters and the energy deposited in the ECAL up to high-multiplicity events, same is shown for the number of VELO clusters in Fig. 2.33, with no signs of hardware saturation contrary to what observed in Fig. 2.19, indicating robust tracking performance even in central PbPb collisions.

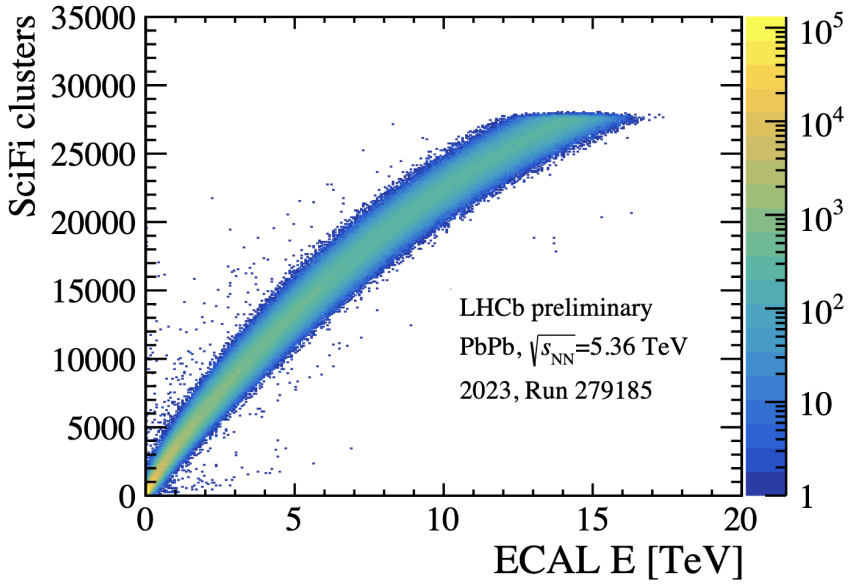


FIGURE 2.32: Correlation between the total energy collected in the ECAL and the number of clusters in the SciFi tracker for PbPb collision events [112].

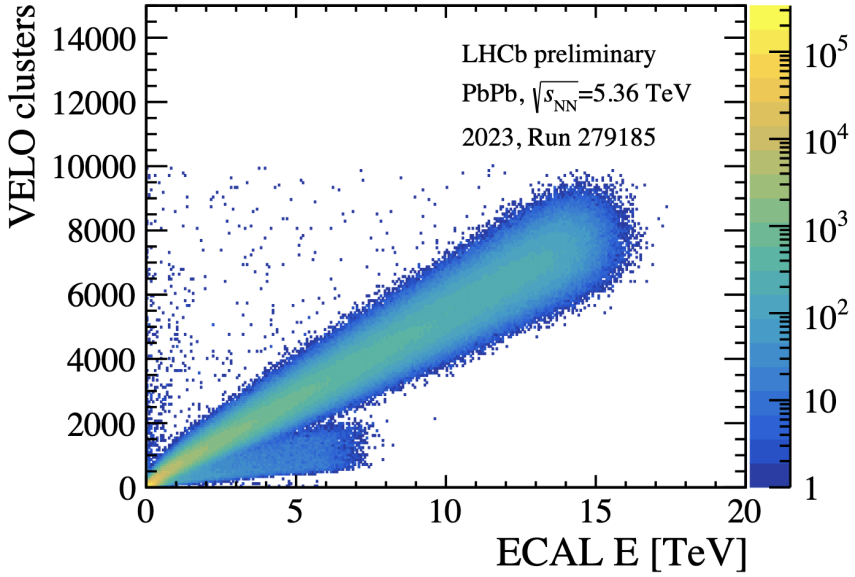


FIGURE 2.33: Correlation between the total energy collected in the ECAL and the number of clusters in the VELO for PbPb events. The main population correspond to PbPb collisions, while the smaller population spanning at lower VELO clusters values corresponds to PbAr collisions collected simultaneously thanks to SMOG2. [112].

These improvements allow the experiment to reach centralities down to 40%, greatly enhancing the accessible phase space for heavy-ion physics studies, as depicted in Fig. 2.34

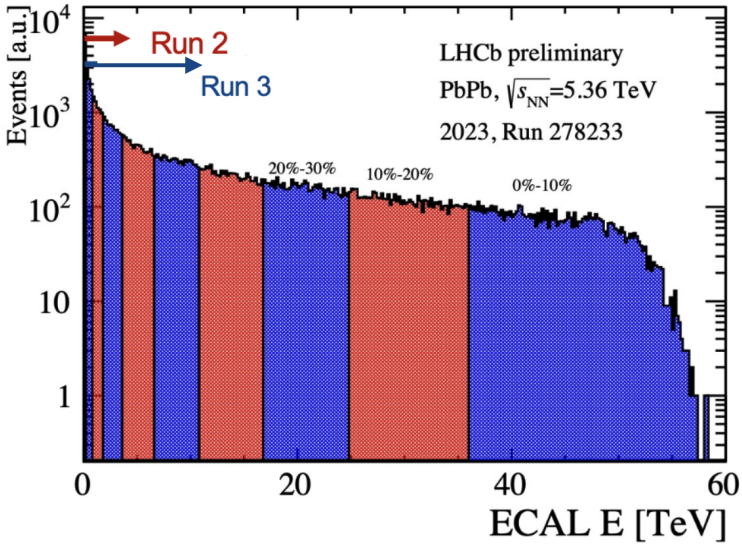


FIGURE 2.34: Distribution of the total energy collected in the ECAL for PbPb collision events divided in event activity classes, highlighting the lower centrality classes reachable in Run 3 [112].

In addition, the overall tracking efficiency has improved thanks to the upgraded

pattern recognition algorithms and increased granularity of the new detector elements. Combined with the high luminosity delivered in Run 3, these features enable LHCb to collect large statistics of central PbPb collisions with excellent tracking and PID performance, marking a major step forward in the experiment's capability to probe the Quark-Gluon Plasma and other heavy-ion observables in the forward region. The sample collected during the 2024 ion run is indeed used to reproduce the charmonium ratio analysis down to 40% centrality, as discussed in Chap. 4.

Chapter 3

Measurement of $\psi(2S)/J/\psi$ in PbPb collisions at $\sqrt{s_{\rm NN}} = 5.02$ TeV (Run 2 Analysis)

In this chapter, the ratio of $\psi(2S)$ to J/ψ mesons decaying into two muons is studied as a function of the event centrality, using the 2018 PbPb collision data collected at $\sqrt{s_{\rm NN}} = 5.02$ TeV by the LHCb detector, during the Run 2 data taking period. The analysis strategy is presented in Sec. 3.1, along with a description of the data sample in Sec. 3.2 and of the selection applied in Sec. 3.3. Before detailing the extraction of the charmonium yields in Sec. 3.5, a brief explanation of the centrality intervals determination is reported in Sec. 3.4. Then the correction of the raw yields by detector efficiencies is discussed in Sec. 3.6, and the evaluation of systematic uncertainties is reported in Sec. 3.7. Finally, the results and outlook are presented in Sec. 3.8.

3.1 Analysis strategy

The goal of this analysis is to measure the ratio of promptly produced $\psi(2S)$ to J/ψ mesons as a function of the centrality of reconstructed PbPb events, in order to explore the QGP formation and its properties. Charmonium candidates are reconstructed through their decay into pairs of oppositely charged muons. The corresponding signal yields are extracted by performing an unbinned maximum-likelihood fit to the dimuon invariant mass distribution. The raw yields are then corrected for detector effects using efficiency corrections derived from simulation and data-driven methods.

The quantity measured in this analysis is the ratio ($\mathcal{R}$) of cross-sections (σ), multiplied by their branching fractions ($\mathcal{B}$), of the two charmonium states:

$$\mathcal{R}(\psi(2S)/J/\psi) = \frac{\sigma(\psi(2S))}{\sigma(J/\psi)} \cdot \frac{\mathcal{B}(\psi(2S) \to \mu^+\mu^-)}{\mathcal{B}(J/\psi \to \mu^+\mu^-)} = \frac{N(\psi(2S))}{N(J/\psi)} \cdot \frac{\varepsilon_{\rm tot}(J/\psi)}{\varepsilon_{\rm tot}(\psi(2S))}, \quad (3.1)$$

where N and $\varepsilon_{\rm tot}$ denote the signal yields (see Sec. 3.5) and total efficiencies (see Sec. 3.6), respectively. The ratio is multiplied by the known branching fractions of

the two states, $\mathcal{B}(J/\psi \to \mu^+\mu^-) = (5.961 \pm 0.033)\%$ and $\mathcal{B}(\psi(2S) \to \mu^+\mu^-) = (8.0 \pm 0.6) \times 10^{-3}$ [13], in order to avoid introducing a large systematic uncertainty associated with the poorly known $\psi(2S)$ branching ratio.

The results are presented as a function of the average number of participating nucleons $\langle N_{\text{part}} \rangle$, extracted from the centrality value, which is estimated using the energy deposited in the ECAL as discussed in Sec. 3.4, and chose because it allows to compare with previous measurements and theoretical predictions.

3.2 Data and simulation samples

This section presents the details of the data and simulation samples used for the analysis.

3.2.1 Data and data taking conditions

The LHCb detector recorded PbPb collisions at $\sqrt{s_{\text{NN}}} = 5.02$ TeV during November and December 2018. The integrated luminosity of the collected sample corresponds to $(228 \pm 10)\ \mu\text{b}^{-1}$, with an uncertainty of 4.4% [113].

A data quality check was performed by requiring all sub-detectors to be fully operational and each period of continuous data taking (referred to as a "run") to last longer than 10 minutes.

Several L0-trigger configurations were used during data-taking, followed by different HLT selections depending on the L0 trigger decision. The details of the trigger strategy used in this analysis are outlined in the following.

3.2.1.1 Trigger selection

The analysis goal is to measure the ratio of $\psi(2S)$ over J/ψ yield as a function of the centrality of the PbPb event. Unfortunately, as explained in Sec. 2.2.9, it is not possible to access the centrality region below 60%, which corresponds to approximately 10 000 `nVeloClusters` [114], due to detector occupancy limitations, see Fig. 2.19. To target the remaining region of interest (centrality: 60–100%), three dedicated lines of the first High-Level Trigger (HLT1) are employed:

- A first signal line selects events with `nVeloClusters` $<$ 6000 and at least one muon track with a transverse momentum greater than 400 MeV/c;
- A second signal line, corresponding to a minimum-bias selection, targets all events with `nVeloClusters` between 6000 and 10 000;
- A same-sign line selects pairs of muons with the same charge. This sample is used to better describe the combinatorial background and to perform systematic studies, as discussed in Sec. 3.7.1.3.

Since the first line also requires a muon hardware trigger, which imposes a minimum transverse momentum threshold of 400 MeV/c, for consistency, the same selection is applied to the sample selected by the other lines. Finally, there is no event rejection at the HLT2 level.

3.2.1.2 Selection in the "stripping" stage

After the trigger, in the first stage of the offline data processing, called "stripping", the J/ψ and $\psi(2S)$ candidates are selected by a dedicated stripping line, which collects about 285 M events. The selection criteria are listed in Tab. 3.1.

The quality of the dimuon vertex is evaluated through the vertex-fit χ^2 per degree of freedom (`VFASPF(VCHI2/VDOF)`), which must be smaller than 25 to reject poorly fitted vertices. Each muon track is required to have a transverse momentum p_{T} greater than 700 MeV/c. The individual track quality is further constrained by the track-fit χ^2 per degree of freedom (`TRCHI2DOF`), which is required to be below three. Finally, the dimuon invariant mass $m_{\mu^+\mu^-}$ is restricted to lie within the range 2900–4000 MeV/c^2, covering the J/ψ and $\psi(2S)$ resonances region, or above 7500 MeV/c^2, to collect high-mass dimuon candidates useful for background and efficiency studies.

Table 3.1: Selection criteria for the stripping line used.

Selection variable	**Selection value**
DiMuon vertex χ^2/ndf	`VFASPF(VCHI2/VDOF)<25`
Muon p_{T}	$p_{\mathrm{T}} > 700$ MeV/c
Track χ^2	`TRCHI2DOF` < 3
Dimuon mass (MeV/c^2)	$(2900 < m_{\mu^+\mu^-} < 4000)$ or $(m_{\mu^+\mu^-} > 7500)$

3.2.2 Simulation

The details of the simulation samples are listed in Tab. 3.2. As explained in Sec. 2.2.8, the generator used to produce the J/ψ and $\psi(2S)$ mesons is Pythia [95] embedded into minimum-bias PbPb events generated by Epos [96].

Table 3.2: Simulation samples used for the analysis.

Decay	**Generator**	**Number of events**
$J/\psi \rightarrow \mu^+\mu^-$	EPOS/PYTHIA	4025741
$\psi(2S) \rightarrow \mu^+\mu^-$	EPOS/PYTHIA	2002538

The same selection of the trigger and stripping applied to the data is also applied on the simulation sample.

3.3 Sample selection

Once the sample has been filtered by the trigger and subsequently by the stripping selection, additional sets of selection criteria are applied to enhance the signal yield relative to the background. These selection steps are grouped into two categories. First, global event cuts are applied (Sec. 3.3.1) to reject generic events that are not relevant for this analysis. Then, a set of requirements on both kinematic and Particle Identification (PID) variables is imposed to increase the purity of the charmonium candidates (Sec. 3.3.2). Among these, a particularly important selection is applied to retain only mesons that are promptly produced in the collision, as described in Sec. 3.3.2.1.

Since the two signal samples are very similar, identical selection criteria are applied to both resonances, in exactly the same way for real and simulated data.

3.3.1 Global event selection

A selection on the global characteristics of the event (GECs) is applied to remove background as events produced in electromagnetic and fixed-target interactions, not part of this study. The GECs are listed in Table 3.3.

Usually GEC selections act on the activity of the event. For this analysis, since photoproduced ψ mesons typically have very low transverse momentum and generate little activity in the event, only candidates with $p_{\mathrm{T}} > 300$ MeV/c and `nVeloClusters` > 1000 are selected. In addition, events with `nVeloClusters` $> 10\,000$ are rejected already at trigger level to avoid entering the detector saturation regime.

Since SMOG was active during the 2018 data-taking period and gas was injected in the lead-lead interaction region, the selection on the z coordinate of the primary vertex (z_{PV}), on the transverse variable $\rho = \sqrt{x_{PV}^2 + y_{PV}^2}$ and on the events with a low number on `nBackTracks` are applied to reduce the background due to lead-gas interactions. Here the variable `nBackTracks` refers to the number of reconstructed backward tracks, *i.e.* tracks with a negative pseudorapidity that traverse the VELO but do not enter the downstream tracking stations.

TABLE 3.3: GEC criteria applied to the event.

Condition	**Selection value**
photon production contamination	$p_{\mathrm{T}}(\psi) > 300\,\mathrm{MeV}/c$
UPC contamination	`nVeloClusters` > 1000
SMOG contamination	$\lvert z_{PV}\rvert < 200$ mm & $0.35 < \rho_{PV} < 0.95$ mm & `nBackTracks` > 15

The impact of these requirements is illustrated in Fig. 3.1, which shows the distribution of ρ versus $|z_{\mathrm{PV}}|$ before (left) and after (right) the GECs application.

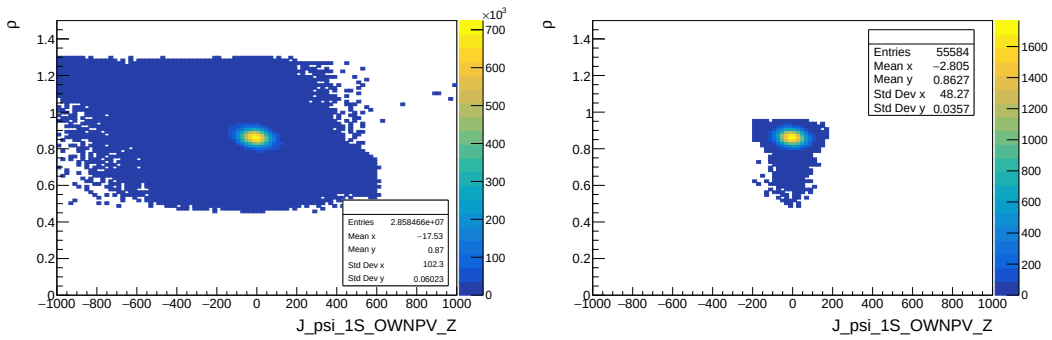


FIGURE 3.1: $\rho = \sqrt{x_{PV}^2 + y_{PV}^2}$ against $|z_{PV}|$ distribution before the selection criteria (left plot) and after (right plot).

The distribution of `nVeloClusters` versus the energy deposited in the electromagnetic calorimeter (ECAL), before and after the selection, is shown in Fig. 3.2. The SMOG contamination, visible as a secondary structure beneath the main region in the left plot, is significantly suppressed after the selection described in Tab. 3.3.

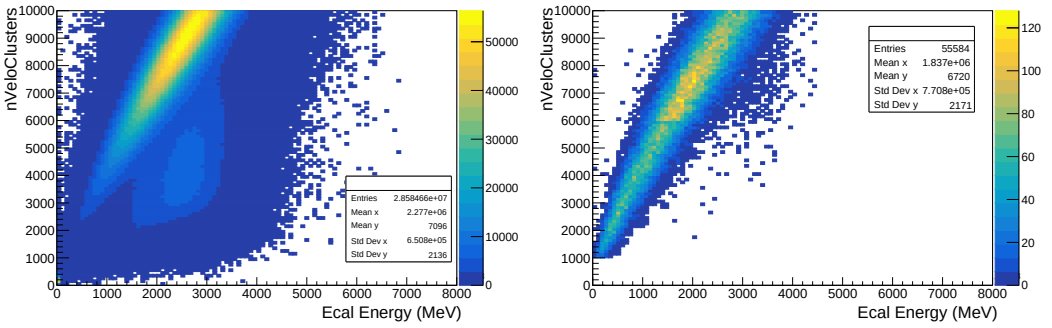


FIGURE 3.2: `nVeloClusters` against ECAL deposit energy before the selection criteria (left plot) and after (right plot).

3.3.2 J/ψ and $\psi(2S)$ candidate selection

Given the high signal purity and the limited statistics of the sample, only a minimal selection is applied to the dimuon candidates, identical for both the J/ψ and $\psi(2S)$ states. Each muon is required to have $p_{\mathrm{T}} > 900$ MeV/c. Tracks with a high probability of being incorrectly reconstructed are suppressed by requiring a track ghost probability smaller than 0.3 (`ProbGhost` < 0.3).

A particle identification requirement of `ProbNN`$\mu > 0.7$ is imposed to ensure that both tracks are genuine muons, which is a typical selection for charmonia analysis in LHCb.

Finally, the dimuon invariant mass is required to fall within the range $2900 < m_{\mu^+\mu^-} < 4000$ MeV/c^2, which includes both the J/ψ and $\psi(2S)$ resonance peaks.

To select only prompt charmonium production, a requirement is applied on the impact parameter (IP) χ^2 with respect to the primary vertex of the interaction. The

IP χ^2 quantifies how compatible a candidate is with originating from the PV, with larger values indicating a displacement from the primary interaction point. Since promptly produced J/ψ and $\psi(2S)$ mesons are expected to decay very close to the PV, while nonprompt ones (from b-hadron decays) typically exhibit larger IP values, a requirement of `log(IPCHI2)` < 3 is imposed to suppress secondary charmonium contributions. The definition of the prompt sample and its validation are discussed in Sec. 3.3.2.1. All the offline selection criteria are summarised in Table 3.4.

TABLE 3.4: Offline selection criteria applied to the dimuon candidates.

Selection variable	**Selection value**
Muon PID probability	`ProbNN`$\mu > 0.7$
Promptness requirement	`log(IP`χ^2`)` < 3
Muon transverse momentum	$p_{\mathrm{T}} > 900$ MeV/c
Dimuon invariant mass	$2900 < m_{\mu^+\mu^-} < 4000$ MeV/c^2
Track ghost probability	`ProbGhost` < 0.3

3.3.2.1 Prompt candidate selection

This analysis focuses exclusively on the prompt production ratio between the two charmonium states. The separation between prompt candidates and those originating from b-hadron decays is usually done by means of the pseudoproper time variable (t_z), defined as

$$t_z = \frac{(z_{J/\psi} - z_{PV}) \cdot M_{J/\psi}}{p_z}.$$

The canonical approach involves a two-dimensional fit to the dimuon invariant mass and the t_z distributions. In our case instead, as reported in Table 3.4, a selection based on the logarithm of the impact parameter χ^2 with respect to the primary vertex is applied: `log(IPCHI2)` < 3.

To assess the performance of this selection and estimate the residual contamination from nonprompt candidates, fits to the J/ψ pseudoproper time distribution were performed both with and without the `log(IPCHI2)` requirement. The fitting strategy follows that of previous analyses [115] and includes the following components:

- **Prompt signal:** a Dirac delta function $\delta(x)$, convolved with the sum of two Gaussian functions to account for detector resolution;
- **Nonprompt signal:** an exponential decay $f_b(x) = e^{-x/\tau}$, convolved with the same resolution model;
- **Background:** the sum of a delta function and five exponentials, convolved with two Gaussians. The shape is chosen empirically from the t_z distribution in the J/ψ mass sidebands.

The results of the fits for the J/ψ are shown in Fig. 3.3, where the left plot corresponds to the selection without the `log(IPCHI2)` requirement, and the right includes it. In the first case, the nonprompt contamination is approximately 11%, which is reduced to about 5% after applying the selection.

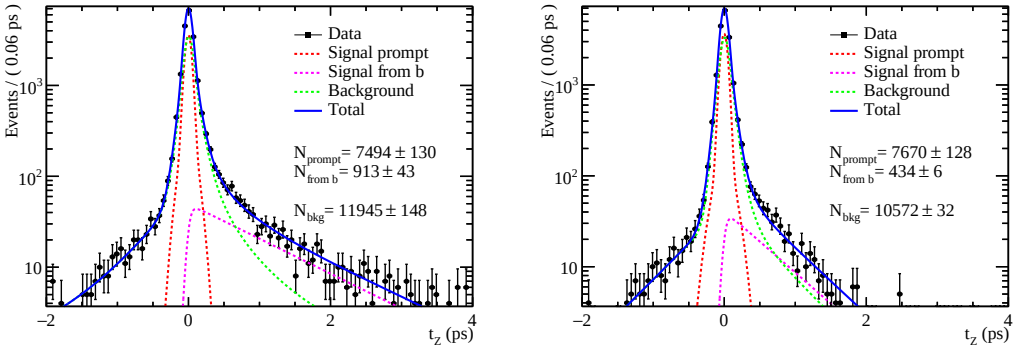


FIGURE 3.3: J/ψ pseudoproper time distribution after the selection criteria without the `log(IPCHI2)` requirement (left), with the full selection (right). Fit model overlaid.

A similar study for the $\psi(2S)$ is limited by low statistics. As shown in Fig. 3.4, on the left without the `log(IPCHI2)` selection and on the right with it, the nonprompt fraction is reduced from about 20% to approximately 8%. However, the statistical uncertainty on the fit is large. To improve precision, the muon p_{T} threshold was temporarily relaxed from 900 MeV/c to 700 MeV/c. The resulting fits, shown in Fig. 3.5, confirm the residual nonprompt contamination at ∼8% with lower statistical uncertainty.

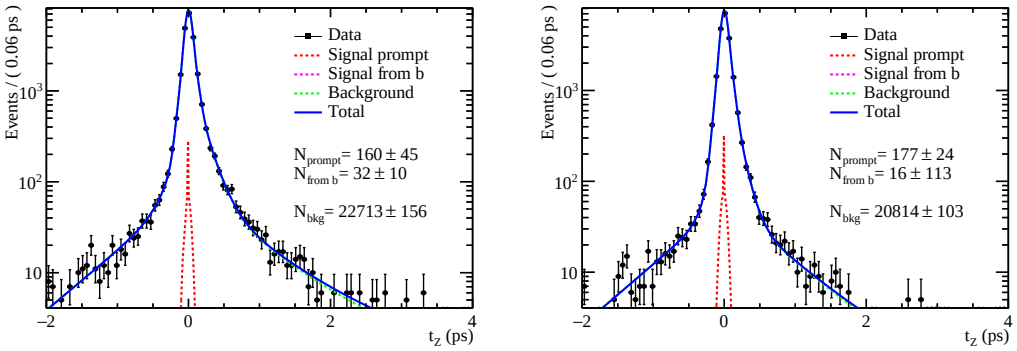


FIGURE 3.4: $\psi(2S)$ pseudoproper time distribution after the selection criteria without the `log(IPCHI2)` requirement (left), with the full selection (right), with muon p_{T} greater than 900 MeV/c. Fit model overlaid.

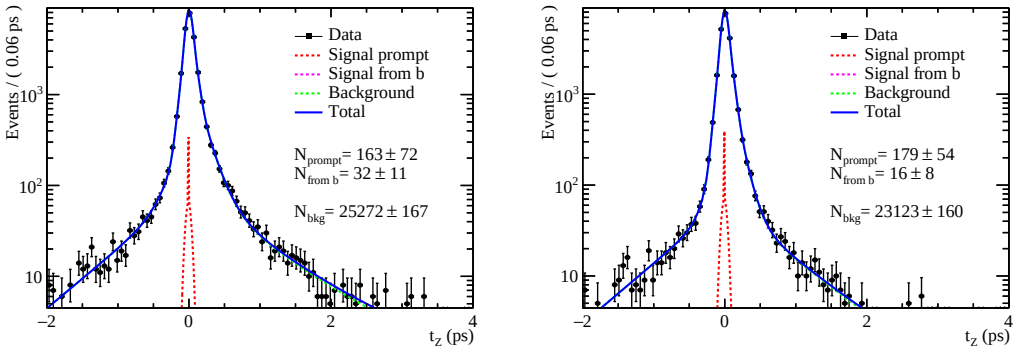


FIGURE 3.5: $\psi(2S)$ pseudoproper time distribution after the selection criteria without the `log(IPCHI2)` requirement (left), with the full selection (right), with muon p_{T} greater than 700 MeV/c. Fit model overlaid.

In summary, the residual nonprompt contamination is estimated to be approximately 5% for J/ψ and 8% for $\psi(2S)$. This effect is taken into account as a systematic uncertainty, discussed in Sec. 3.7.2.

3.4 Centrality measurement

The centrality determination for the 2018 PbPb sample, documented in Ref. [116], was performed within the LHCb collaboration. This section summarises the main concepts behind the method, along with the centrality binning scheme adopted in the analysis.

3.4.1 Basic strategy

As already mentioned in Sec. 1.5.1, centrality is a key quantity in heavy-ion collisions, reflecting the geometry of the interaction. It is related to the impact parameter b between the two nuclei, and to other geometric observables such as the average number of participating nucleons $\langle N_{\mathrm{part}} \rangle$ and the average number of binary nucleon-nucleon collisions $\langle N_{\mathrm{coll}} \rangle$ (which are not directly proportional, as a single nucleon can participate in multiple collisions). More central collisions correspond to smaller impact parameters.

Centrality classes are defined as percentiles of the inelastic hadronic PbPb cross-section $\sigma_{\mathrm{inel.}}^{\mathrm{PbPb}}$, as follows:

$$C = \frac{1}{\sigma_{inel.}^{\mathrm{PbPb}}} \int_0^b \frac{d\sigma}{db'} db', \tag{3.2}$$

where $\frac{d\sigma}{db'}$ is the differential inelastic cross-section with respect to the impact parameter b. Since b is not directly measurable, it is inferred via a correlated observable such as the multiplicity of charged particles $\langle N_{\mathrm{ch}} \rangle$, which at LHCb is approximately

proportional to the total energy E deposited in the ECAL. Centrality can then be expressed as:

$$C = \frac{1}{\sigma_{inel.}^{\mathrm{PbPb}}} \int_{E^{\mathrm{THR}}}^{\infty} \frac{d\sigma}{dE} dE, \tag{3.3}$$

where E^{THR} is the energy threshold corresponding to the chosen centrality percentile. The uncertainty in the energy threshold (*i.e.*, the ECAL bin boundaries) is evaluated by estimating the migration of events between adjacent bins due to the finite resolution in E.

3.4.2 Glauber model and fit results

To relate the ECAL energy deposit to physical quantities such as $\langle N_{\mathrm{part}} \rangle$ and $\langle N_{\mathrm{coll}} \rangle$, a fit to the ECAL energy distribution is performed using a Monte Carlo (MC) implementation of the Glauber model. This geometrical model treats PbPb collisions as an incoherent superposition of multiple binary nucleon-nucleon interactions. The fitting strategy is similar to that employed by ALICE [117].

In this framework, the number of particle-producing sources ("ancestors") is modelled as:

$$N_{anc} = f \times N_{part} + (1 - f) \times N_{coll}, \tag{3.4}$$

where f is a free parameter of the fit. An example distribution of N_{part}, N_{coll}, and N_{anc} from the MC Glauber simulation (with $f = 0.751$) is shown in Fig. 3.6.

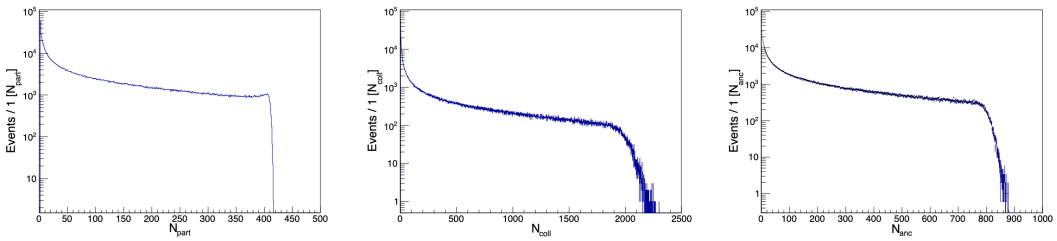


FIGURE 3.6: Distributions of N_{part}, N_{coll}, and N_{anc} from a Glauber MC simulation of 1M PbPb collisions at $\sqrt{s_{\mathrm{NN}}} = 5.02$ TeV. A value of $f = 0.751$ was used.

Each ancestor is assumed to emit particles following a negative binomial distribution (NBD):

$$P_{p,k}(n) = \frac{(n + k + 1)!}{n!(k - 1)!} p^k (1 - p)^n, \tag{3.5}$$

$$p = (\frac{\mu}{k} + 1)^{-1} \tag{3.6}$$

where k and μ are free parameters, and n is the number of particles. For each collision, N_{anc} NBDs are sampled to obtain the final multiplicity distribution. Using the known average energy per charged track in pp collisions at $\sqrt{s_{\text{NN}}} = 5.02$ TeV ($\langle E \rangle \sim 10.44$ GeV), the multiplicity distribution is translated into ECAL energy and fitted to data to extract the best-fit values of f and μ (with $k = 1.5$ fixed).

Fig. 3.7 shows the fit to data from a representative run (217730), demonstrating good agreement except at low energies, where electromagnetic background dominates.

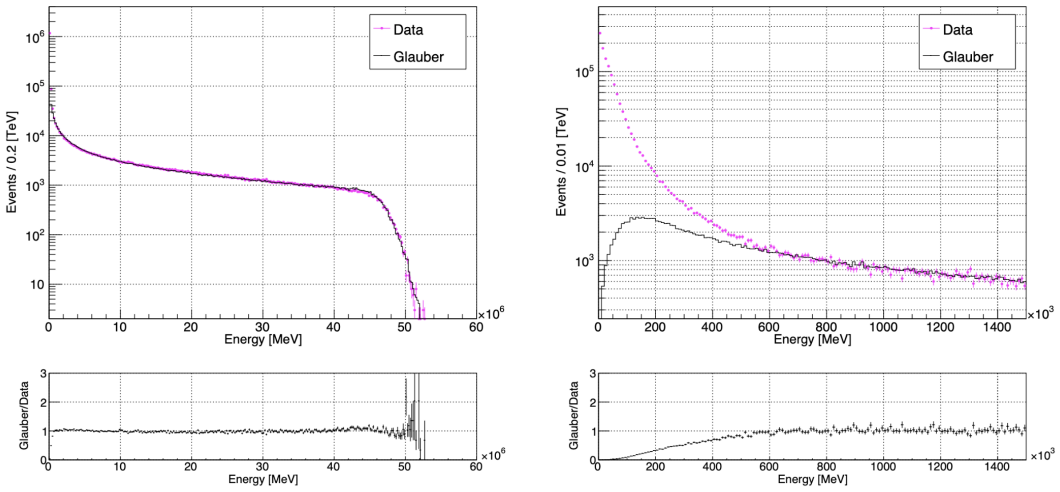


FIGURE 3.7: Top: Glauber MC fit to 2018 PbPb data as a function of ECAL energy. Bottom: data-to-fit ratio. Right: zoom at low energy values.

Once the fit is obtained, centrality intervals in ECAL energy are defined as percentiles of the Glauber distribution. For each class, the corresponding distributions of b, $\langle N_{\text{part}} \rangle$, and $\langle N_{\text{coll}} \rangle$ are obtained from the Glauber simulation. These are shown in Fig. 3.8 and summarised in Tab. 3.5.

TABLE 3.5: Centrality classes and corresponding average geometry parameters. Uncertainties are the RMS of each distribution.

percentile	ECAL limit (TeV)	$\langle b \rangle$	$\langle \text{N}_{\text{part}} \rangle$	$\langle \text{N}_{\text{coll}} \rangle$
0-10%	> 32.0	3.3 ± 1.2	357.2 ± 32.2	1570.3 ± 236.8
10-20%	32.0-21.9	6.0 ± 0.7	261.9 ± 27.1	972.5 ± 151.9
20-30%	21.9-14.6	7.8 ± 0.6	188.0 ± 21.5	593.9 ± 105.2
30-40%	14.6-9.5	9.2 ± 0.5	131.2 ± 16.9	345.5 ± 71.6
40-50%	9.5-5.7	10.5 ± 0.5	87.5 ± 13.3	187.5 ± 46.7
50-60%	5.7-3.25	11.6 ± 0.5	54.7 ± 10.0	92.6 ± 27.7
60-70%	3.25-1.7	12.6 ± 0.6	31.3 ± 7.1	41.3 ± 14.7
70-80%	1.7-0.7	13.6 ± 0.7	15.9 ± 4.8	16.4 ± 7.0
80-90%	0.7-0.3	14.6 ± 0.9	7.0 ± 2.9	5.8 ± 3.1
90-100%	< 0.3	15.4 ± 1.0	2.9 ± 1.2	1.8 ± 1.2

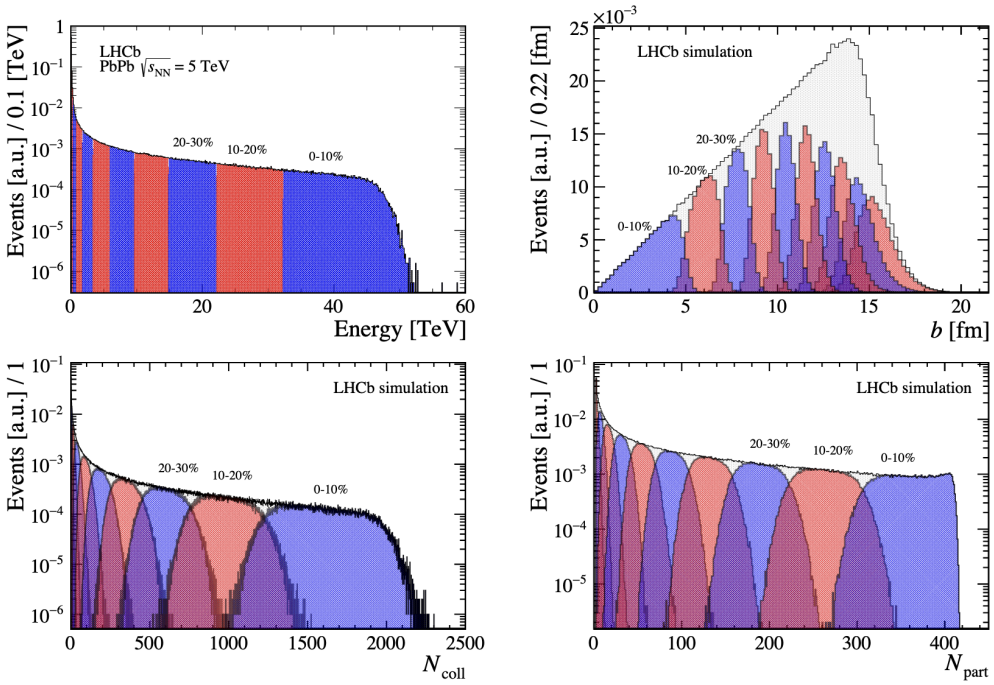


FIGURE 3.8: Top left: classification of events from PbPb data according to the defined centrality classes. Top right: impact parameter distributions. Bottom: $\langle N_{\text{coll}} \rangle$ and $\langle N_{\text{part}} \rangle$ quantities for the corresponding centrality classes.

3.4.3 Centrality bins for this analysis

In this analysis, centrality classes are defined using ECAL-based percentiles in steps of 10%. The Glauber model provides a one-to-one mapping between the ECAL energy and geometrical observables like $\langle N_{\text{part}} \rangle$, b, and the centrality on an event-by-event basis.

Since the analysis is performed in bins of centrality, the $\langle N_{part} \rangle$ dependence has been extrapolated from Tab. 3.5 and used to perform a comparison with ALICE results and the theory predictions (see Sec. 3.8), using the binning scheme in Tab. 3.6.

TABLE 3.6: Centrality and corresponding $\langle N_{part} \rangle$ bins used in this analysis.

Centrality (%)	90-100	80-90	70-80	60-70
$\langle N_{part} \rangle$	2.4-5.5	5.5-13	13-26.5	26.5-48

3.5 Signal yields extraction

This section explains the fit strategy involved to estimate the yields of J/ψ and $\psi(2S)$ candidates present in the sample, both in the integrated phase space and as a function of centrality, to be used in equation 3.1 to obtain the ratio results discussed in Sec. 3.8.

The function used to perform the unbinned extended maximum-likelihood fit to the $\mu^+\mu^-$ invariant mass distribution is composed by three terms, a Crystal Ball (CB) function [118] used to model the J/ψ signal, a Gaussian (GAUSS) used for the $\psi(2S)$ and an exponential function for the combinatorial background. The mathematical description follows:

$$f(m_{\mu^+\mu^-}) = N_{J/\psi} \cdot f_{J/\psi}(m_{\mu^+\mu^-}) + N_{\psi(2S)} \cdot f_{\psi(2S)}(m_{\mu^+\mu^-}) + N_{bkg} \cdot f_{bkg}(m_{\mu^+\mu^-}), \quad (3.7)$$

where $N_{J/\psi}$ and $N_{\psi(2S)}$ represents the J/ψ and $\psi(2S)$ yields respectively, while N_{bkg} is the number of background candidates.

- For the J/ψ signal fit function:

$$f_{J/\psi}(m_{\mu^+\mu^-}) = f_{\text{CB}}(x; \mu_{J/\psi}, \sigma_{J/\psi}, \alpha, n) = \begin{cases} \frac{\left(\frac{n}{|\alpha|}\right)^n e^{-\frac{1}{2}\alpha^2}}{\left(\frac{n}{|\alpha|} - |\alpha| - \frac{x-\mu}{\sigma}\right)^n}; & \frac{x-\mu}{\sigma} < -|\alpha| \\ e^{\left(-\frac{1}{2}\left(\frac{x-\mu}{\sigma}\right)^2\right)}; & \frac{x-\mu}{\sigma} > -|\alpha| \end{cases}$$

- while for the $\psi(2S)$ signal fit function:

$$f_{\psi(2S)}(m_{\mu^+\mu^-}) = f_{\text{GAUSS}}(x; \mu_{\psi(2S)}, \sigma_{\psi(2S)}) = \frac{1}{\sigma\sqrt{2\pi}} e^{-\frac{1}{2}\frac{(x-\mu)^2}{\sigma^2}}$$

- the combinatorial background fit function:

$$f_{bkg}(m_{\mu^+\mu^-}) = e^{\lambda \cdot m}$$

To constrain the fit and improve stability, several parameters are fixed:

- The mass difference between the $\psi(2S)$ and J/ψ peaks is fixed to the known PDG value [13]:
$$\mu_{\psi(2S)} - \mu_{J/\psi} = m^{\text{PDG}}_{\psi(2S)} - m^{\text{PDG}}_{J/\psi};$$
- The ratio $\sigma_{\psi(2S)}/\sigma_{J/\psi}$ is fixed to the value obtained from the fit to simulated signal events;
- The tail parameters (α and n) of the CB function are also fixed to the value obtained from the fit to simulated signal events;

The results of the simulation invariant mass fits in the chosen centrality intervals are shown in App. A.1.

The fit result for the full data sample is shown in Fig. 3.9, and results into 8228 ± 125 J/ψ and 197 ± 49 $\psi(2S)$ signal candidates. The invariant mass fits in

the four centrality intervals are shown in Fig. 3.10, and the extracted yields are summarised in Table 3.7. As visible, the $\psi(2S)$ signal is statistically limited, which makes the modelling of the background in the corresponding mass region more challenging. To validate the background component in the fit, an alternative method based on same-sign dimuon combinations, which do not contain true signal decays, has been implemented. The details of this validation are discussed in the dedicated section on systematic uncertainties (see Sec. 3.7.1).

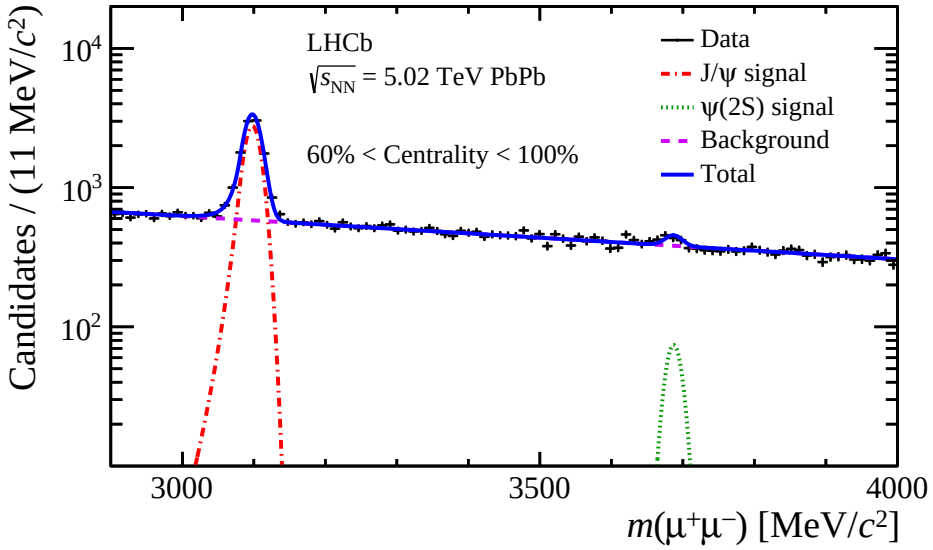


FIGURE 3.9: Dimuon invariant mass distribution for the full dataset after all selection criteria are applied, overlaid with the fit result.

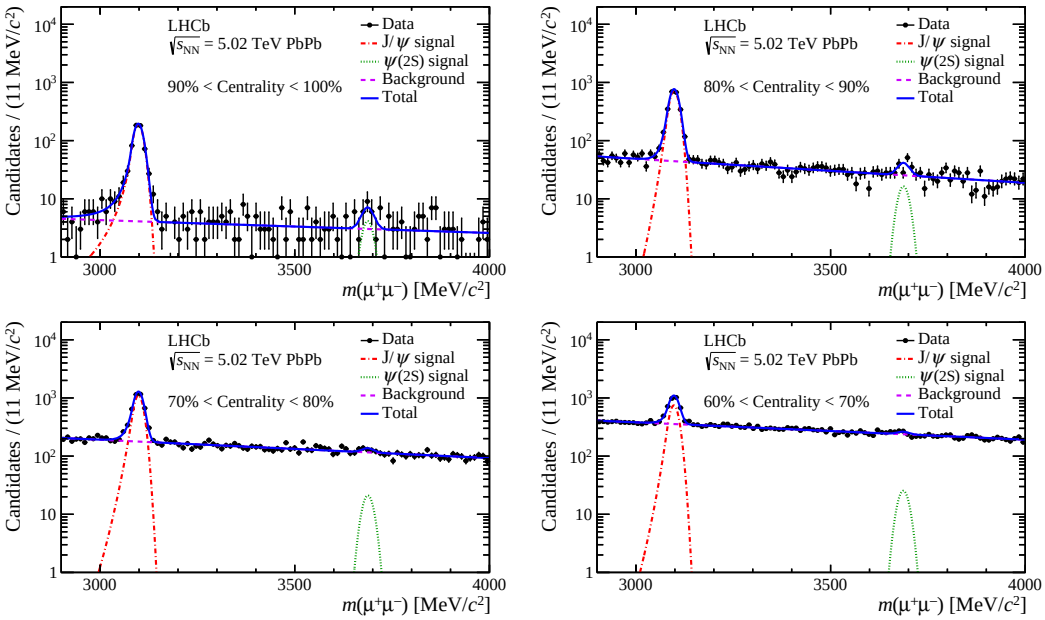


FIGURE 3.10: Dimuon invariant mass distributions in each centrality interval after selection, overlaid with fit results.

TABLE 3.7: Range for the number of participating nucleons $\langle N_{\text{part}} \rangle$ and signal yields in each centrality interval, the uncertainties are statistical only.

Centrality (%)	90–100	80–90	70–80	60–70
$\langle N_{\text{part}} \rangle$	2.4–5.5	5.5–13.0	13.0–26.5	26.5–48.0
$N(J/\psi)$	596 ± 28	2099 ± 52	3320 ± 74	2221 ± 77
$N(\psi(2S))$	13 ± 5	53 ± 14	68 ± 26	85 ± 36

3.6 Efficiencies determination

The raw signal yields extracted for J/ψ and $\psi(2S)$ are affected by several sources of inefficiency, related to the geometrical acceptance of the detector, the reconstruction and selection of the decay products, the particle identification, and the trigger response. In order to correct for these effects, the total signal efficiency ε_{tot} appearing in Eq. 3.1 is factorised as:

$$\varepsilon_{\text{tot}} = \varepsilon_{\text{acc}} \times \varepsilon_{\text{rec\&sel}} \times \varepsilon_{\text{MuonID}} \times \varepsilon_{\text{trg}} \times \frac{1}{\varepsilon_{\text{MCTruth}}}, \tag{3.8}$$

where:

- ε_{acc} accounts for the geometrical acceptance of the detector;
- $\varepsilon_{\text{rec\&sel}}$ includes the efficiency of reconstructing the tracks and applying the offline selection (described in Sec. 3.3);
- $\varepsilon_{\text{MuonID}}$ quantifies the ability of the particle identification system to correctly identify the final-state tracks as muons;
- ε_{trg} reflects the probability that an event passes the online selection;
- $\varepsilon_{\text{MCTruth}}$ is the so-called truth-matching efficiency, *i.e.* the fraction of reconstructed tracks matched to the corresponding generated particles. As this is an inefficiency, it enters the formula as a correction factor $1/\varepsilon_{\text{MCTruth}}$.

Each of these components is estimated using simulated samples (see Sec. 3.2.2), with dedicated data-driven corrections applied to improve agreement between simulation and data, as discussed in Sec. 3.6.2.

All efficiencies are evaluated not only as a function of centrality, which is the main variable of interest in the analysis, but also in bins of `nVeloClusters`, transverse momentum p_{T}, and rapidity y of the mesons, where $y = \frac{1}{2} \ln \left(\frac{E+p_z}{E-p_z} \right)$ quantifies the particle velocity along the beam axis and is invariant under Lorentz boosts in that direction. These additional variables serve as important controls for the measurement and allow for a more differential understanding of the efficiency behaviour. In each of the following sections, for every efficiency component, both the absolute efficiencies

for J/ψ and $\psi(2S)$ and their ratio are shown through dedicated plots and summary tables.

The following sections detail the computation of each efficiency term: truth-matching efficiency in Sec. 3.6.1, acceptance in Sec. 3.6.3, reconstruction and selection in Sec. 3.6.4, muon identification in Sec. 3.6.5, and trigger in Sec. 3.6.6. Each section presents figures showing the dependence of the efficiency on all four variables mentioned above, while tables summarise the values as a function of centrality only.

Finally, Sec. 3.6.7 presents the total efficiency ε_{tot} used in the ratio computation.

3.6.1 Truth-matching efficiency

The determination of the efficiencies is based on simulation samples, which are typically composed of two components. The first is the *generated* sample, in which particles are produced and decay according to the physics model used, without any detector effects or reconstruction applied. The second is the *reconstructed* sample, where the detector response is simulated and tracks are reconstructed from detector hits, following the same procedures used for real data.

A truth-matching algorithm is used to associate each reconstructed track with its corresponding generated particle. This matching is essential for identifying whether a reconstructed candidate really originates from the intended decay. In the generated simulation, only one "true" J/ψ or $\psi(2S)$ meson is produced per event. To ensure that the reconstructed candidate corresponds to this decay and to reject spurious combinations of unrelated muons, a truth-matching requirement is applied. This consists of verifying that the reconstructed muon tracks originate from the correct generated decay. The efficiency of this requirement, referred to as the truth-matching efficiency, is defined as:

$$\varepsilon_{\text{MCTruth}} \equiv \frac{J/\psi\ (\psi(2S))\text{ candidates truth matched}}{J/\psi\ (\psi(2S))\text{ reconstructed candidates in the true mass window}}, \quad (3.9)$$

where the numerator counts the number of reconstructed candidates that are successfully matched to the corresponding generated particles, and the denominator is the yield of reconstructed candidates obtained via a mass fit in simulation sample.

Figs. 3.11 and 3.12 show the efficiency as a function of centrality, `nVeloClusters`, p_{T}, and y, for J/ψ and $\psi(2S)$ respectively. Fig. 3.13 displays the ratio of the two efficiencies. The corresponding numerical values as a function of centrality are reported in Table 3.8.

As expected, the truth-matching efficiency is very high across all variables, typically above 97%, and exhibits a flat behaviour as a function of the variables considered. The ratio of the efficiencies between $\psi(2S)$ and J/ψ is consistent with unity in all regions. This indicates that the truth-matching correction has a negligible impact on

the final ratio measurement and primarily serves as a technical requirement to ensure pure candidate matching in simulation.

TABLE 3.8: Truth matching efficiency for J/ψ, $\psi(2S)$, and their ratio, as a function of centrality. The uncertainty is negligible.

	Centrality			
	$60-70\%$	$70-80\%$	$80-90\%$	$90-100\%$
$\varepsilon(J/\psi)$	97.0%	98.5%	99.4%	99.7%
$\varepsilon(\psi(2S))$	97.1%	98.6%	99.4%	99.8%
$\mathcal{R}_{\varepsilon(\psi(2S))/\varepsilon(J/\psi)}$	1.00	1.00	1.00	1.00

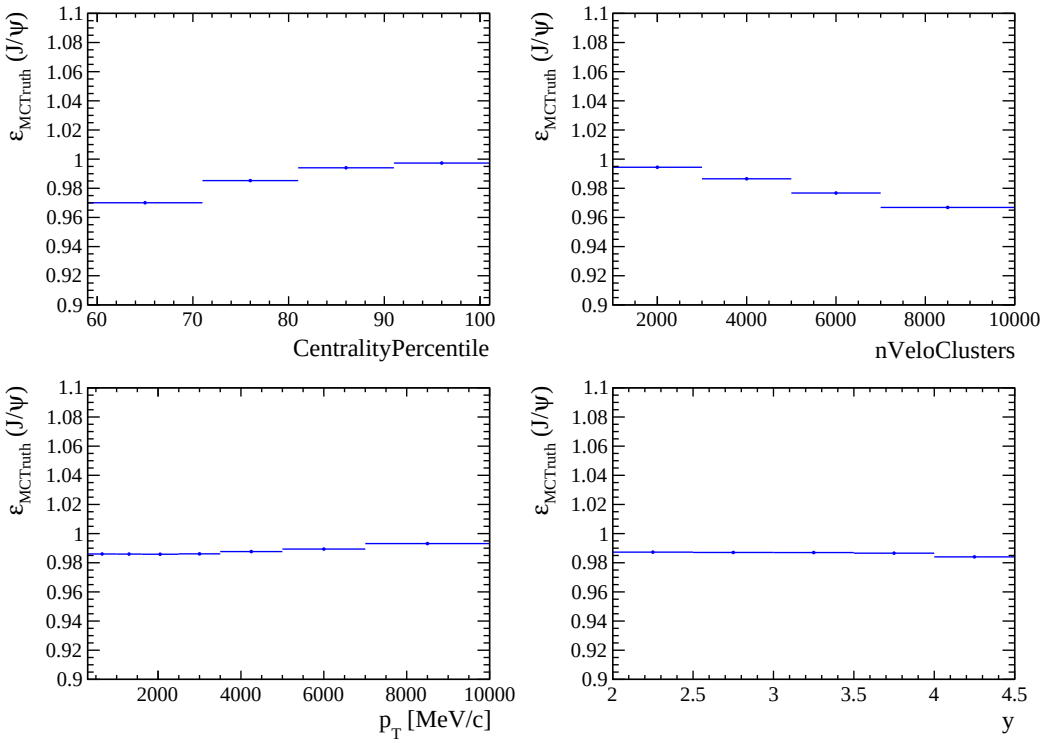


FIGURE 3.11: Truth matching efficiency $\varepsilon_{\text{MCTruth}}$ as a function of centrality (top left), `nVeloClusters` (top right), p_{T} (bottom left) and y (bottom right) for J/ψ.

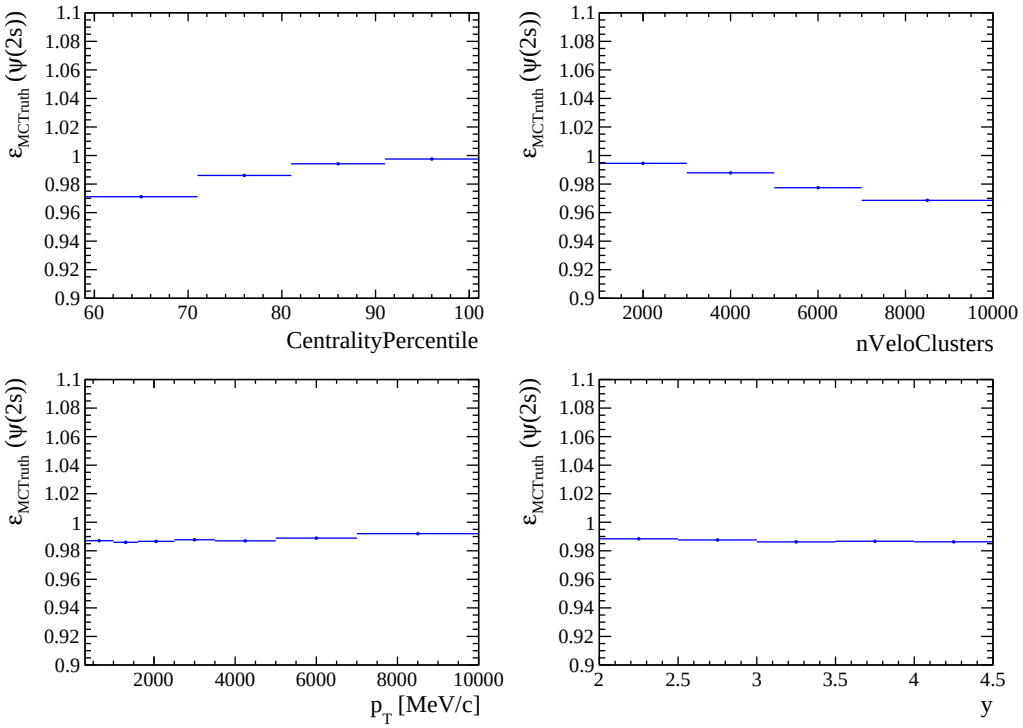


FIGURE 3.12: Truth matching efficiency $\varepsilon_{\mathrm{MCTruth}}$ as a function of centrality (top left), `nVeloClusters` (top right), p_{T} (bottom left) and y (bottom right) for $\psi(2S)$.

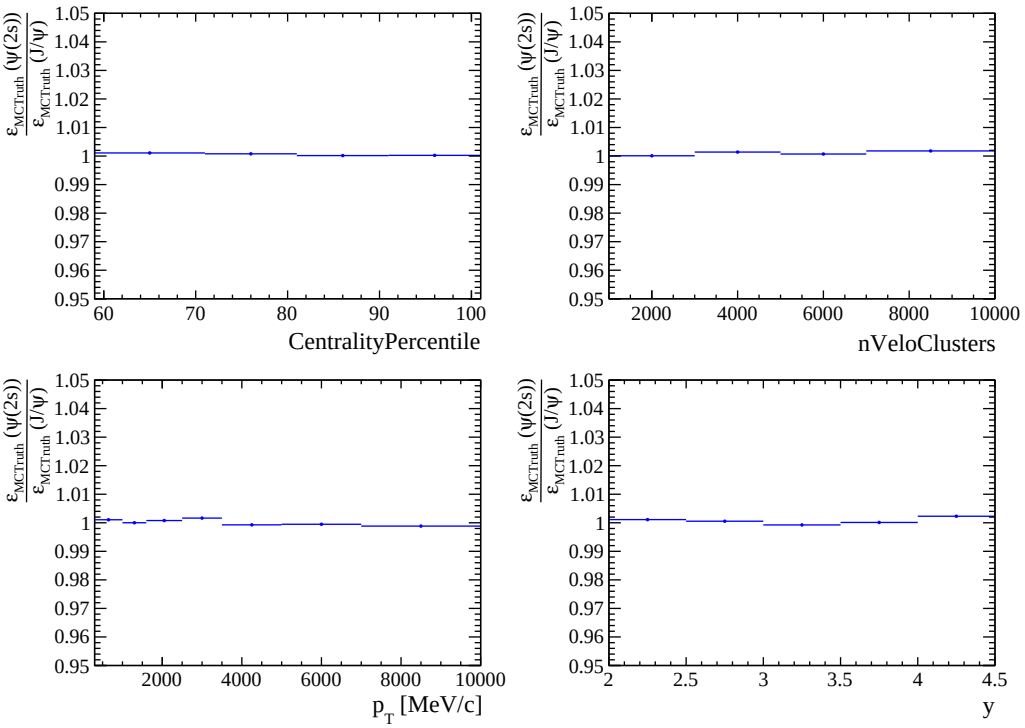


FIGURE 3.13: Truth matching efficiency $\varepsilon_{\mathrm{MCTruth}}$ ratio of $\psi(2S)$ over J/ψ as a function of centrality (top left), `nVeloClusters` (top right), p_{T} (bottom left) and y (bottom right).

3.6.2 MC weighting

As discussed in Sec. 2.2.8, the simulation samples are designed to reproduce the decay processes observed in real data. Although modern simulation techniques are highly sophisticated, differences between simulated and real data can still arise, particularly in the distributions of kinematic and event-level variables. These discrepancies must be corrected to ensure accurate efficiency estimates. A widely adopted approach for this correction is the Monte Carlo weighting technique, which consists in reweighting the simulated distributions to better match those observed in data.

Since the simulation does not include background contributions, the first step in the reweighting procedure involves unfolding the signal and background in the data. This is achieved through an extended unbinned maximum likelihood fit of the invariant mass distribution using the sPlot technique [119]. The fit provides event-by-event signal weights, known as sWeights, which once applied to the distribution of any interesting variable, statistically subtract the background contribution and isolate the signal shape.

In this analysis, the reweighting is performed with respect to two variables: one kinematic, the transverse momentum p_{T}, and one related to event multiplicity, the number of VELO clusters (`nVeloClusters`). After background subtraction in data, the reweighting factors are computed as the ratio of data to MC histograms in each bin of the chosen variable. These weights are then applied to the simulated events to improve agreement with the real data.

Due to the limited statistics available for the $\psi(2S)$ sample, the weights are computed using only the J/ψ sample, and the same weights are then applied to both states. This assumption is supported by the observed similarity between the J/ψ and $\psi(2S)$ simulation in both p_{T} and `nVeloClusters`, as shown in Fig. 3.14. The only visible difference is in the shape of the p_{T} distribution aroud the peak, but it is expected and caused by the requirement on the transverse momentum of the muons ($p_{\mathrm{T}}^{\mu} > 900$ MeV). The p_{T} distributions look indeed more similar between the two states using $p_{\mathrm{T}}^{\mu} > 700$ MeV, but this selection is not usable as in this case the $\psi(2S)$ mass peak would disappear below the combinatorial background.

So to validate this assumption, an additional study was performed: the p_{T} and `nVeloClusters` distributions of the J/ψ were reweighted to match those of the $\psi(2S)$, and new MC/data weights were computed using these modified distributions. The impact of this alternative reweighting on the final $\psi(2S)/J/\psi$ ratio was evaluated and taken into account as a systematic uncertainty, as detailed in Sec. 3.7.3.2.

The discontinuity visible in the `nVeloClusters` distribution around a value of 6000 is due to a change in the HLT1 trigger line applied during data taking.

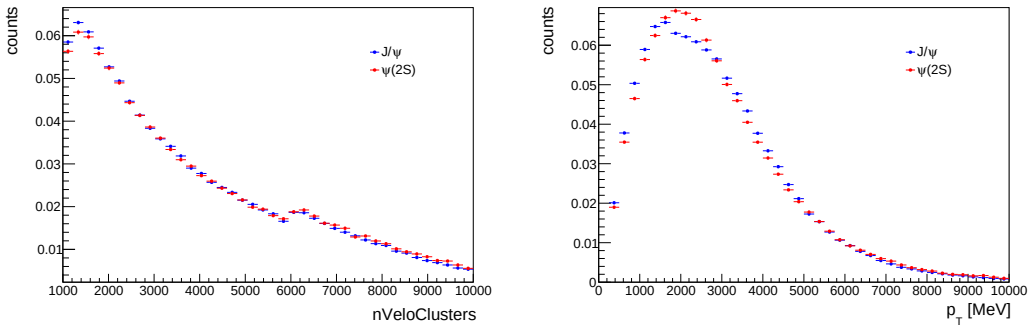


FIGURE 3.14: Comparison of normalised `nVeloClusters` (left) and p_{T} (right) distributions between J/ψ and $\psi(2S)$ simulation. The distributions are in good agreement.

The effect of the reweighting procedure is illustrated in Fig. 3.15, where the original MC, the background-subtracted data (using sWeights), and the reweighted MC distributions are compared for the two corrected variables. A clear improvement in the agreement between data and simulation is observed after applying the weights. The efficiencies in the following sections are therefore computed after the `nVeloClusters` and p_{T} weights have been applied.

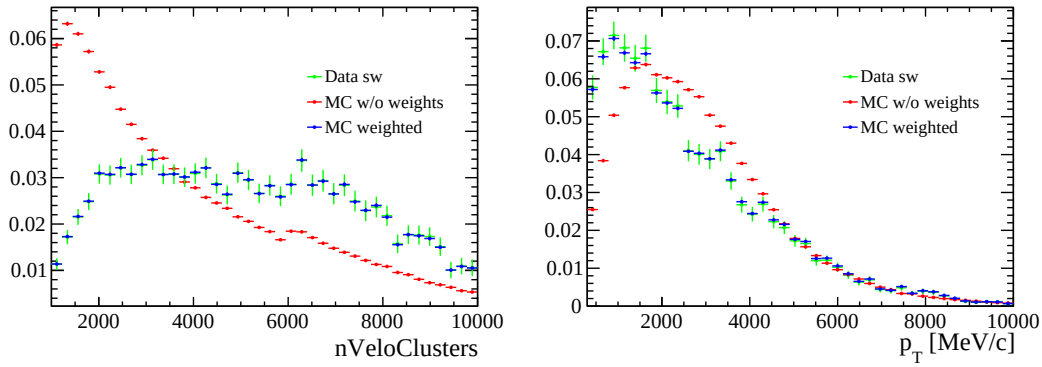


FIGURE 3.15: Comparison of `nVeloClusters` (left) and p_{T} (right) distributions in background-subtracted data (sWeights), original MC, and reweighted MC for J/ψ. The reweighting significantly improves the agreement between simulation and data.

3.6.3 Acceptance efficiency

The geometrical acceptance of the detector must be taken into account when evaluating the total efficiency. The acceptance efficiency is defined as the fraction of signal decays in which both muons from the meson decay fall within the LHCb acceptance and are geometrically reconstructible, relative to the number of decaying particles (J/ψ or $\psi(2S)$) generated within the same acceptance:

$$\varepsilon_{\mathrm{acc}} \equiv \frac{J/\psi\ (\psi(2S)) \text{ with both } \mu \text{ in the LHCb acceptance}}{\text{Generated } J/\psi\ (\psi(2S)) \text{ in the LHCb acceptance}}. \tag{3.10}$$

Here, the LHCb acceptance refers to particles within a polar angle between 10 and 400 mrad with respect to the z-axis of the detector, before the magnet.

The denominator of this efficiency is evaluated using a generator-level simulation sample produced without any geometrical acceptance requirement, *i.e.*, in the full phase space (4π). Since producing such a generator-level sample in heavy-ion mode is technically challenging, a *pp* sample containing 4 M candidates per meson species was used instead. This choice is justified because the geometrical acceptance is independent of the colliding beam species, and hence the probability for both muons to fall within the detector acceptance does not depend on whether the collision is *pp* or PbPb, as long as there is a charmonium produced.

The results of the acceptance efficiency after reweighting are shown in Fig. 3.16, and the binned values are reported in Tabs. 3.9 and 3.10, as a function of p_{T} and y. As this efficiency is purely geometrical, it is not expected to depend on event activity or centrality. Therefore, once the efficiency has been evaluated in (p_{T}, y) bins, it is also integrated to a single value and used in the total efficiency computation as a function of centrality. The integrated acceptance values are:

$$\varepsilon_{\mathrm{acc}}(J/\psi) = (84.3 \pm 0.1)\%, \qquad \varepsilon_{\mathrm{acc}}(\psi(2S)) = (83.0 \pm 0.1)\%,$$

where the uncertainties are statistical.

TABLE 3.9: Geometrical acceptance for J/ψ and $\psi(2S)$ as a function of p_{T}.

	p_{T} [GeV/c]						
	0.3−1.0	1.0−1.6	1.6−2.5	2.5−3.5	3.5−5.0	5.0−7.0	7.0−10.0
$\varepsilon(J/\psi)$	79.1%	80.1%	82.2%	85.6%	89.0%	92.4%	95.1%
$\varepsilon(\psi(2S))$	79.1%	79.1%	81.0%	83.5%	87.1%	90.5%	93.5%

TABLE 3.10: Geometrical acceptance for J/ψ and $\psi(2S)$ as a function of y.

	y				
	2.0−2.5	2.5−3.0	3.0−3.5	3.5−4.0	4.0−4.5
$\varepsilon(J/\psi)$	68.0%	87.2%	93.9%	93.2%	84.1%
$\varepsilon(\psi(2S))$	67.7%	86.9%	93.8%	92.8%	84.0%

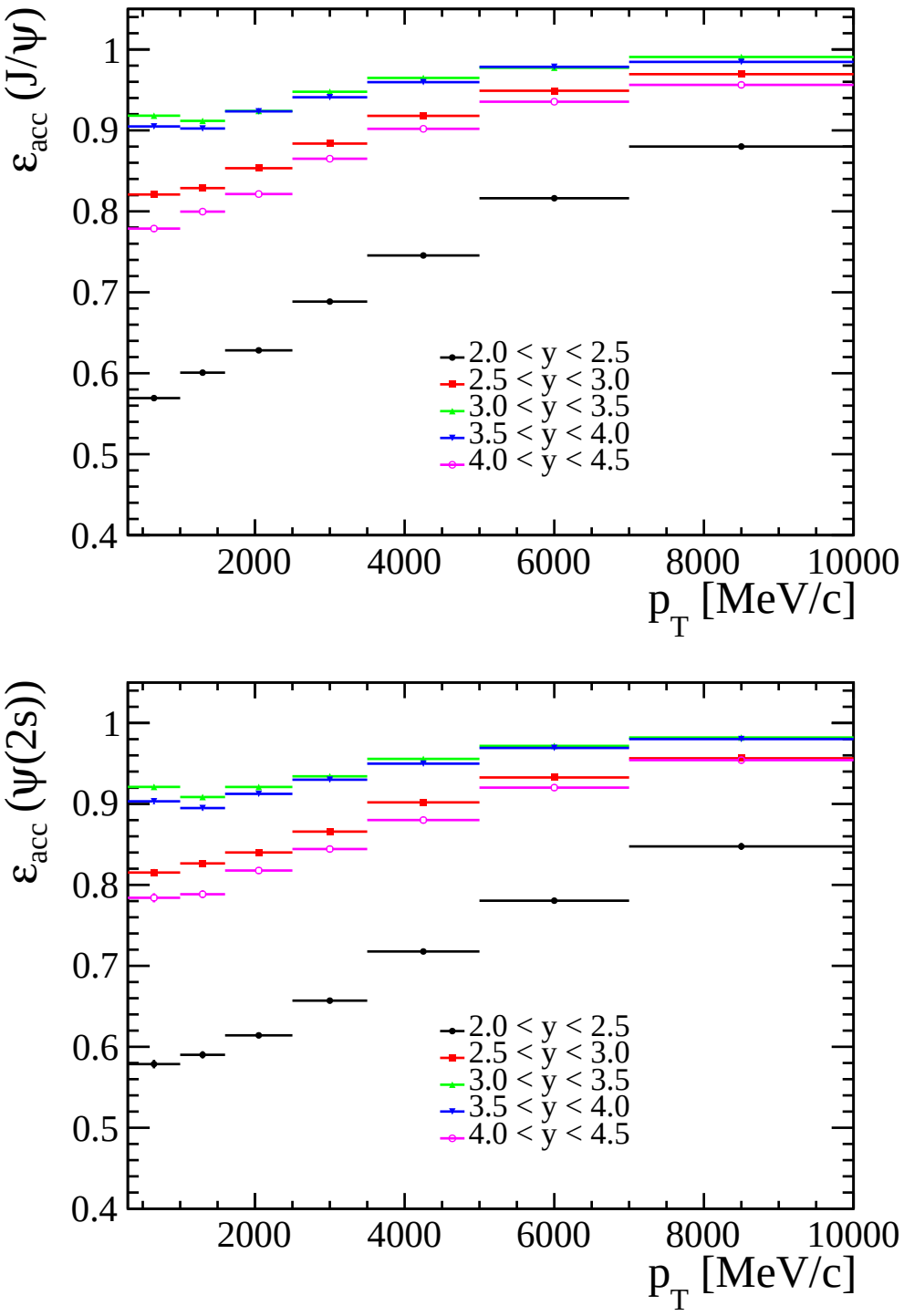


FIGURE 3.16: Geometrical acceptance $\varepsilon_{\rm acc}$ calculated using generator-level pp events as a function of $p_{\rm T}$ in bins of y, for J/ψ (top) and $\psi(2S)$ (bottom).

3.6.4 Reconstruction and selection efficiency

The reconstruction and selection efficiency quantifies the combined performance of the detector in reconstructing muon tracks and the impact of the offline selection criteria described in Sec. 3.3. It is defined as:

$$\varepsilon_{\text{rec\&sel}} \equiv \frac{J/\psi\ (\psi(2S))\text{ reconstructed and selected (without }\mu\text{ PID and trigger)}}{J/\psi\ (\psi(2S))\text{ with both }\mu\text{ in the LHCb acceptance}}. \tag{3.11}$$

As indicated in the definition, muon particle identification and trigger requirements are explicitly excluded at this stage, since these contributions are evaluated separately in Sections 3.6.5 and 3.6.6, respectively. The efficiencies, corrected by reweighting, are shown in Fig. 3.17 for the J/ψ and in Fig. 3.18 for the $\psi(2S)$, while the ratio between the two is shown in Fig. 3.19.

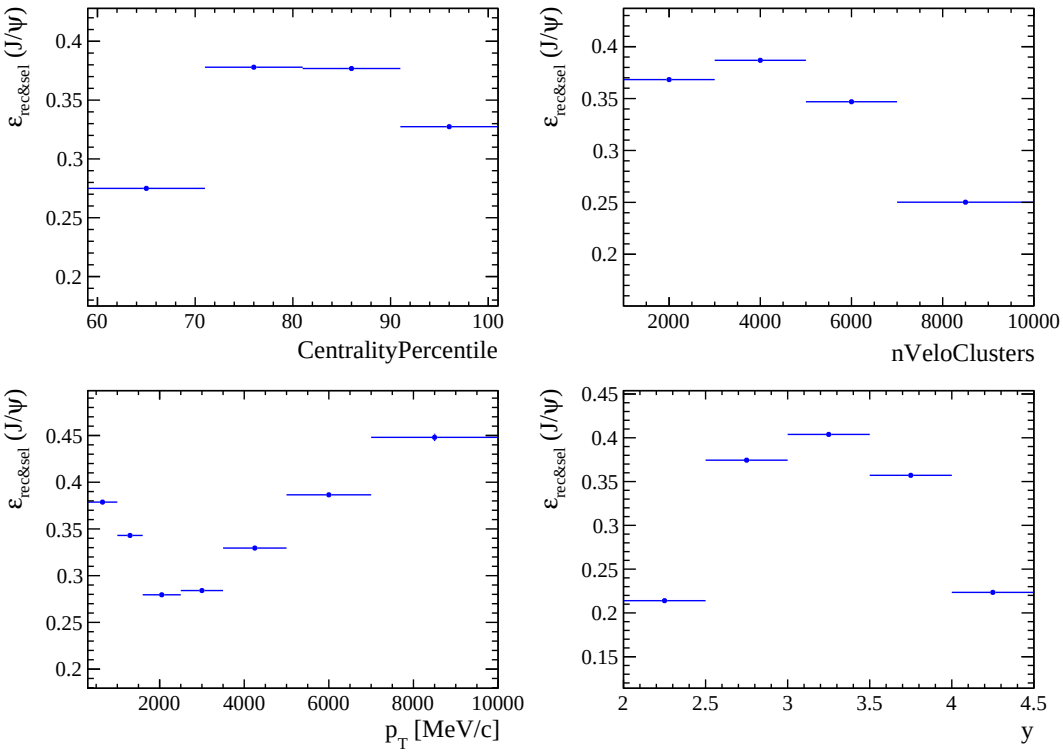


FIGURE 3.17: Reconstruction and selection efficiency $\varepsilon_{\text{rec\&sel}}$ as a function of centrality (top left), `nVeloClusters` (top right), p_{T} (bottom left), and y (bottom right) for the J/ψ.

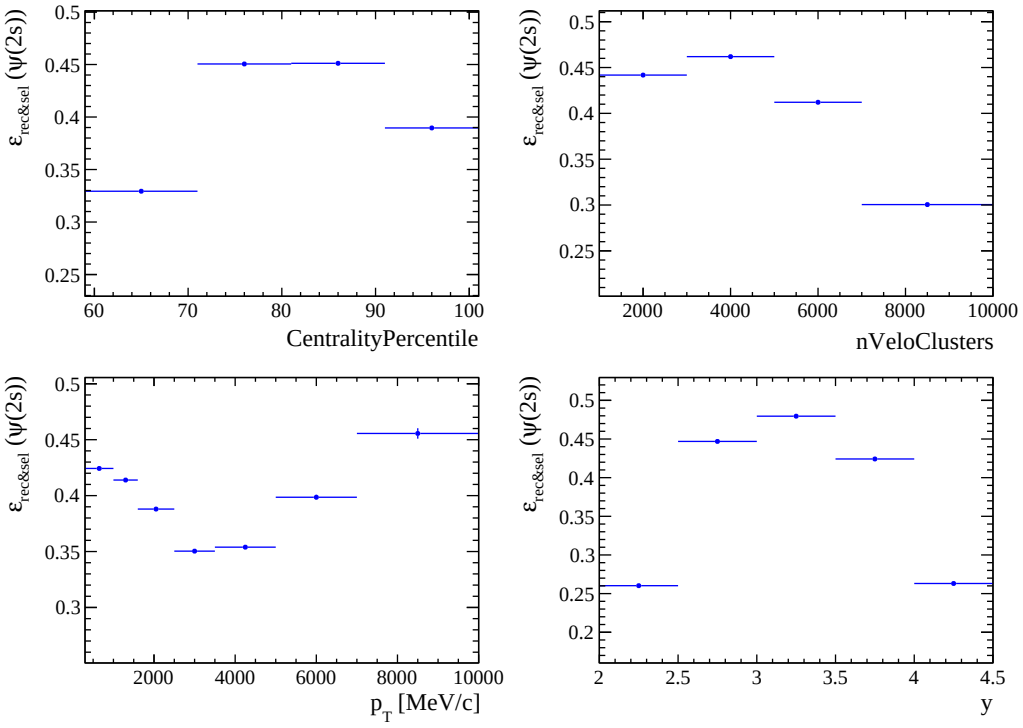


FIGURE 3.18: Reconstruction and selection efficiency $\varepsilon_{\text{rec\&sel}}$ as a function of centrality (top left), `nVeloClusters` (top right), p_{T} (bottom left), and y (bottom right) for the $\psi(2S)$.

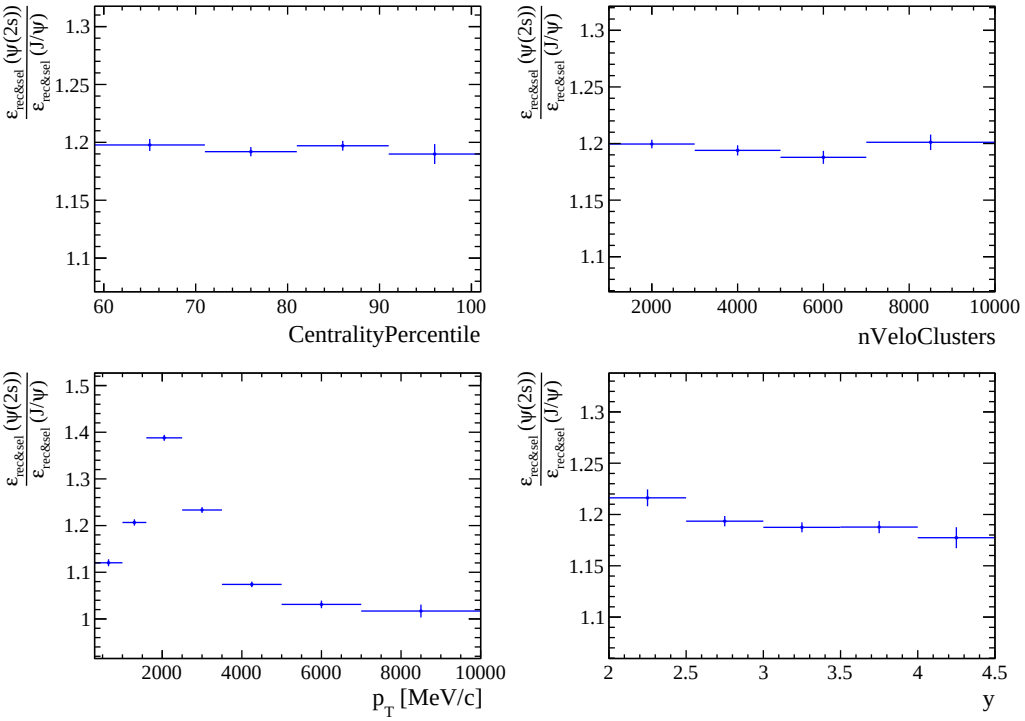


FIGURE 3.19: Ratio of the reconstruction and selection efficiencies $\varepsilon_{\text{rec\&sel}}$ $(\psi(2S))/\varepsilon_{\text{rec\&sel}}$ (J/ψ) as a function of centrality (top left), `nVeloClusters` (top right), p_{T} (bottom left), and y (bottom right).

The corresponding numerical values as a function of centrality are reported in Table 4.9.

TABLE 3.11: Reconstruction and selection efficiency for J/ψ, $\psi(2S)$, and their ratio, as a function of centrality. The uncertainty is statistical.

	Centrality			
	$60-70\%$	$70-80\%$	$80-90\%$	$90-100\%$
$\varepsilon(J/\psi)$	$(27.5 \pm 0.07)\%$	$(37.8 \pm 0.08)\%$	$(37.7 \pm 0.08)\%$	$(32.1 \pm 0.15)\%$
$\varepsilon(\psi(2S))$	$(32.9 \pm 0.11)\%$	$(45.1 \pm 0.12)\%$	$(45.1 \pm 0.12)\%$	$(39.0 \pm 0.22)\%$
$\mathcal{R}_{\varepsilon(\psi(2S))/\varepsilon(J/\psi)}$	1.198 ± 0.005	1.192 ± 0.004	1.197 ± 0.004	1.190 ± 0.009

The ratio $\varepsilon_{\text{rec\&sel}}(\psi(2S))/\varepsilon_{\text{rec\&sel}}(J/\psi)$ is found to be flat as a function of event multiplicity, remaining approximately constant around 1.2 (see, *e.g.*, the top-left and right panels of Fig. 3.19). The higher efficiencies seen for the more energetic state is consistent with expectations, as the larger mass of the $\psi(2S)$ yields more energetic decay muons, which are reconstructed with higher efficiency.

The dependence observed in the ratio as a function of p_{T} (bottom-left panel of Fig. 3.19) exhibits a characteristic peak around 2–3 GeV/c. In this p_{T} region similar to the mass of the states, one of the two muons can be produced nearly at rest in the laboratory frame, resulting in poor reconstruction efficiency. This effect is purely kinematic and is typical in the efficiency ratio between quarkonia states, already observed in other measurements [45].

3.6.5 MuonID efficiency

An essential component of the total efficiency is the one associated with the PID requirement for muons. In this analysis, muon candidates are required to satisfy `ProbNN`$\mu > 0.7$. The corresponding efficiency is defined as:

$$\varepsilon_{\text{MuonID}} \equiv \frac{J/\psi\ (\psi(2S))\text{ reconstructed and selected (with }\mu\text{ PID and without trigger)}}{J/\psi\ (\psi(2S))\text{ reconstructed and selected (without }\mu\text{ PID and trigger)}}. \tag{3.12}$$

Unlike other selection criteria included in $\varepsilon_{\text{rec\&sel}}$, the efficiency of the `ProbNN`μ requirement cannot be reliably extracted from simulation alone, as the PID response is not accurately modelled.

In LHCb, the standard approach to address this issue is the use of the `PIDCalib2` package [120]. The PIDCalib method consist in analysing data ("calibration sample") collected through custom triggers and measure the efficiency applying the Tag&Probe technique. In this method, one decay particle (the *tag*) is required to pass strict

identification criteria, ensuring a clean sample, while the other particle (the *probe*) is used to study the PID performance. By comparing the number of probe particles that pass or fail a given PID requirement, the efficiency can be directly measured from data as a function of relevant kinematic or multiplicity variables. However, no PID calibration sample is available for PbPb collisions, and given the limited statistics of the sample analysed, a dedicated Tag&Probe measurement is not feasible. To overcome this, PID efficiencies extracted from the 2018 *pp* calibration sample are employed and the single-muon efficiencies are corrected to account for the higher track multiplicity observed in PbPb events as explained below.

The PID efficiencies are initially measured as a function of (p_{T}, η, `nVeloClusters`). However, the `nVeloClusters` distribution in the *pp* calibration sample is limited to values below approximately 5000, while in PbPb collisions it extends up to 10 000, as discussed earlier. Therefore, an extrapolation procedure is implemented to estimate the efficiency in the high-multiplicity regime of PbPb events.

The following factorisation assumption is introduced:

$$\varepsilon_{\mathrm{PID}}^{\mathrm{PbPb}}\left(p_{\mathrm{T}}, \eta, \texttt{nVeloClusters}\right) = \varepsilon_{\mathrm{PID}}^{pp}\left(p_{\mathrm{T}}, \eta; \texttt{nVeloClusters} < 1000\right) \cdot f_{\mathrm{PID}}^{\mathrm{extr}}\left(p_{\mathrm{T}}, \texttt{nVeloClusters}\right), \tag{3.13}$$

where:

- $\varepsilon_{\mathrm{PID}}^{\mathrm{PbPb}}\left(p_{\mathrm{T}}, \eta, \texttt{nVeloClusters}\right)$ is the muon PID efficiency as a function of p_{T}, η and `nVeloClusters` to be evaluated;
- $\varepsilon_{\mathrm{PID}}^{pp}(p_{\mathrm{T}}, \eta; \texttt{nVeloClusters} < 1000)$ is the muon PID efficiency estimated from the 2018 *pp* calibration sample using `PIDCalib2`, evaluated in bins of p_{T} and η in the multiplicity region `nVeloClusters` < 1000;
- $f_{\mathrm{PID}}^{\mathrm{extr}}(p_{\mathrm{T}}, \texttt{nVeloClusters})$ is an extrapolation factor that accounts for the multiplicity dependence of the efficiency, it is used to estimate the value of the efficiency in the region `nVeloClusters` > 1000, and it is defined as:

$$f_{\mathrm{PID}}^{\mathrm{extr}}(p_{\mathrm{T}}, \texttt{nVeloClusters}) = \frac{\varepsilon_{\mathrm{PID}}^{\mathrm{extr}}(p_{\mathrm{T}}, \texttt{nVeloClusters} > 1000)}{\varepsilon_{\mathrm{PID}}^{pp}(p_{\mathrm{T}}, \texttt{nVeloClusters} < 1000)}. \tag{3.14}$$

This factorisation is valid under the assumption that the dependence of the PID efficiency on η and on `nVeloClusters` is uncorrelated, an hypothesis which has been verified using the available data as illustrated in Fig. 3.20.

The extrapolated efficiency $\varepsilon_{\mathrm{PID}}^{\mathrm{extr}}(p_{\mathrm{T}}, \texttt{nVeloClusters} > 1000)$ is obtained by performing a second-order polynomial fit to the *pp* calibration sample in the range $0 <$ `nVeloClusters` < 5000. The resulting fit is then extrapolated to higher multiplicities. The fit curves are shown in Fig. 3.21 as coloured lines, while the extrapolated points for `nVeloClusters` > 5000 represent the estimated efficiency beyond the calibrated region.

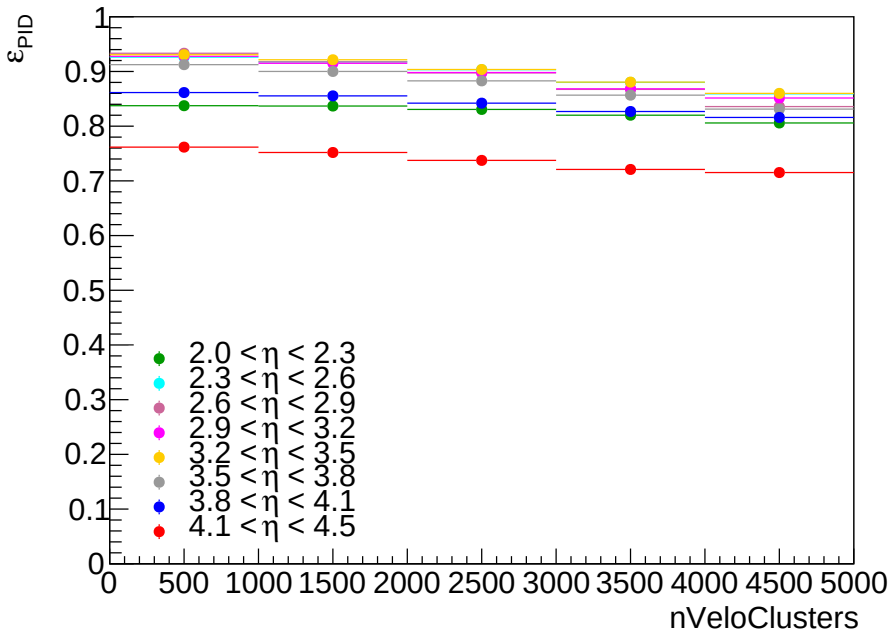


FIGURE 3.20: Muon efficiency from *pp* 2018 sample versus occupancy in different η bins.

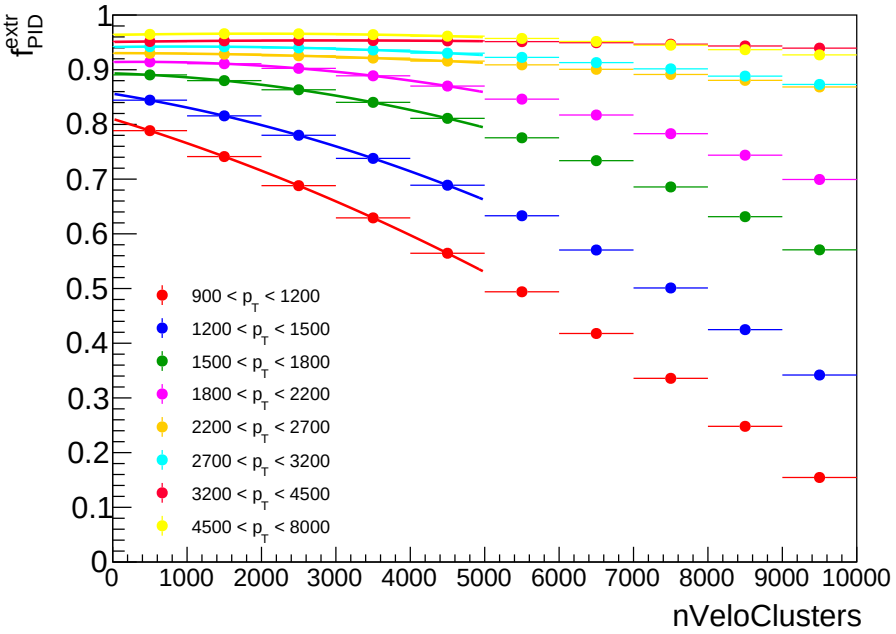


FIGURE 3.21: Muon efficiency from *pp* 2018 sample versus occupancy (up to `nVeloClusters` = 5000) in different bins of p_T indidcated in MeV/c. The fits are performed using a second-order polynomial function. The efficiency values for `nVeloClusters` > 5000 are obtained through the extrapolation explained in the text.

The correction factor f^{extr}_{PID} is then computed as described above and its values are shown in Fig. 3.22.

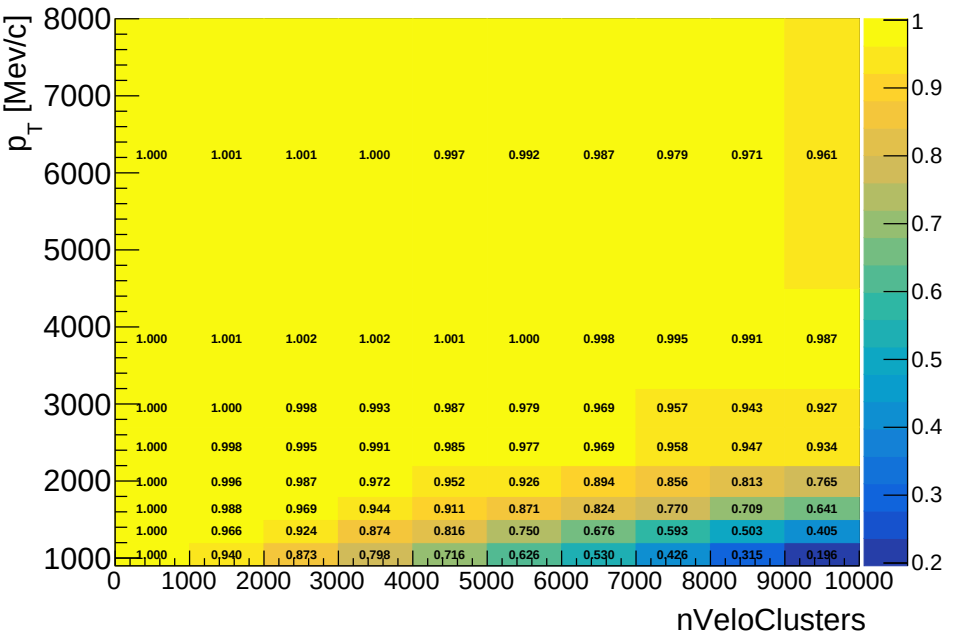


FIGURE 3.22: $f_{\mathrm{PID}}^{\mathrm{extr}}$ results in bins of p_{T} and `nVeloClusters`.

The final MuonID efficiency for J/ψ and $\psi(2S)$ is obtained, as explained in eq. 3.13, by multiplying the extrapolation correction factor $f_{\mathrm{PID}}^{\mathrm{extr}}$ with the baseline efficiency $\varepsilon_{\mathrm{PID}}^{pp}(p_{\mathrm{T}}, \eta; \texttt{nVeloClusters} < 1000)$, the latter shown in Fig. 3.23.

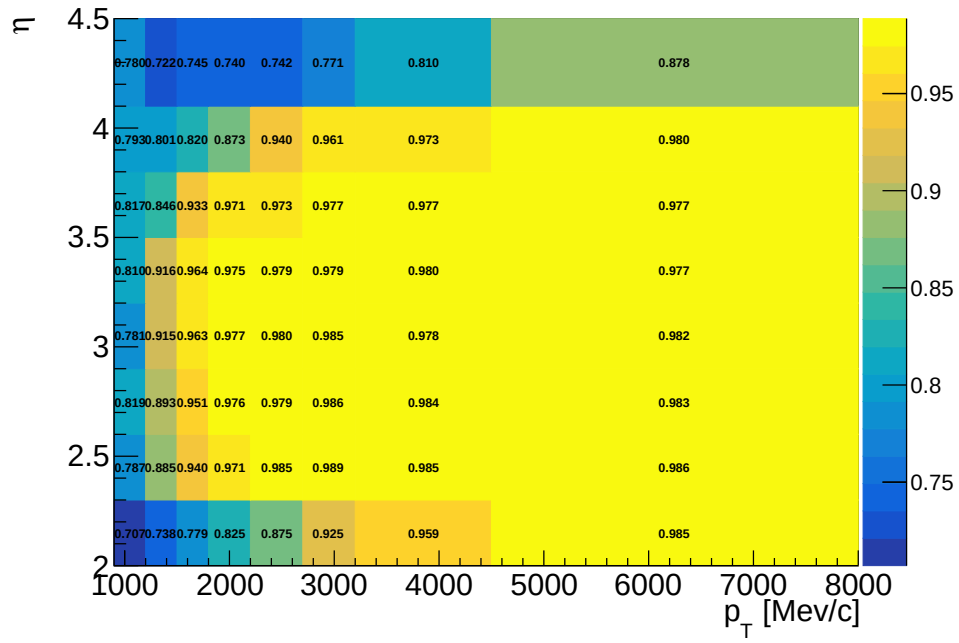


FIGURE 3.23: $\varepsilon_{\mathrm{PID}}^{pp}$ $(p_{\mathrm{T}}, \eta; \texttt{nVeloClusters} < 1000)$ results.

The resulting efficiencies are presented in Fig. 3.24 and Fig. 3.25 for J/ψ and $\psi(2S)$, respectively, and are listed in Table 3.12 as a function of the centrality. The

corresponding efficiency ratios between $\psi(2S)$ and J/ψ are shown in Fig. 3.26.

TABLE 3.12: Particle identification efficiency for J/ψ, $\psi(2S)$, and their ratio, centrality. The uncertainty is statistical.

	Centrality			
	$60-70\%$	$70-80\%$	$80-90\%$	$90-100\%$
$\varepsilon(J/\psi)$	$(44.8 \pm 0.15)\%$	$(64.0 \pm 0.15)\%$	$(74.7 \pm 0.14)\%$	$(77.9 \pm 0.15)\%$
$\varepsilon(\psi(2S))$	$(53.0 \pm 0.21)\%$	$(69.9 \pm 0.19)\%$	$(78.8 \pm 0.17)\%$	$(81.5 \pm 0.18)\%$
$\mathcal{R}_{\varepsilon(\psi(2S))/\varepsilon(J/\psi)}$	1.183 ± 0.006	1.092 ± 0.004	1.054 ± 0.003	1.046 ± 0.003

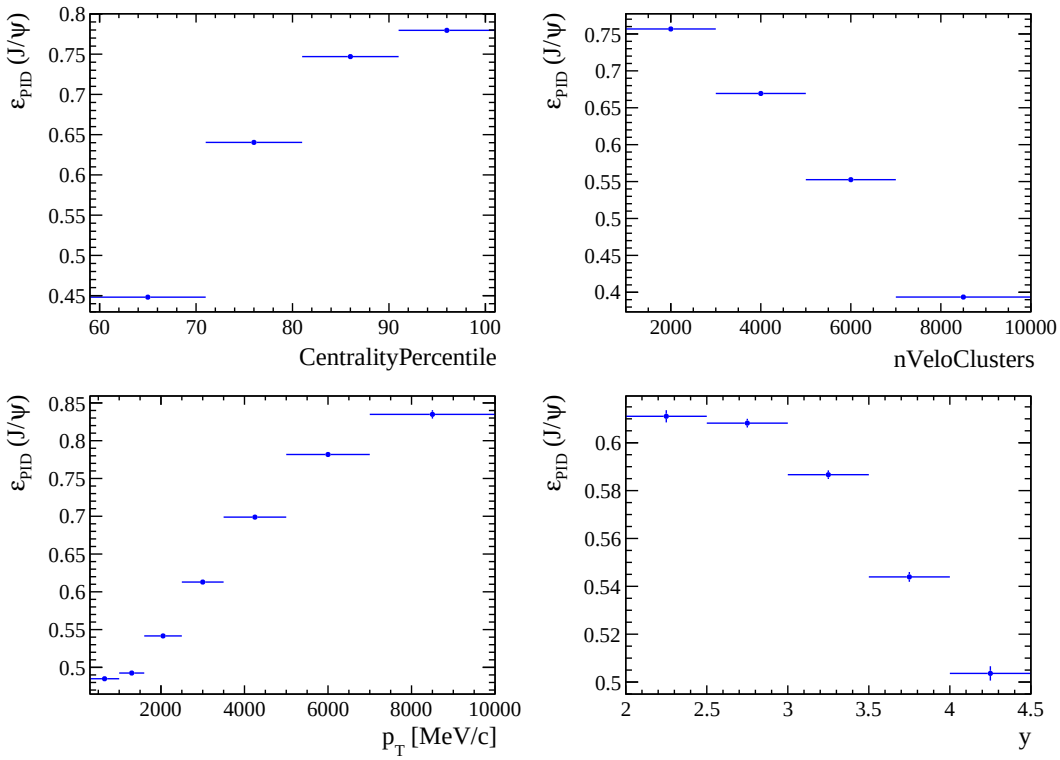


FIGURE 3.24: Particle identification efficiency $\varepsilon_{\text{MuonID}}$ as a function of centrality (top left), `nVeloClusters` (top right), p_{T} (bottom left) and y (bottom right) for J/ψ.

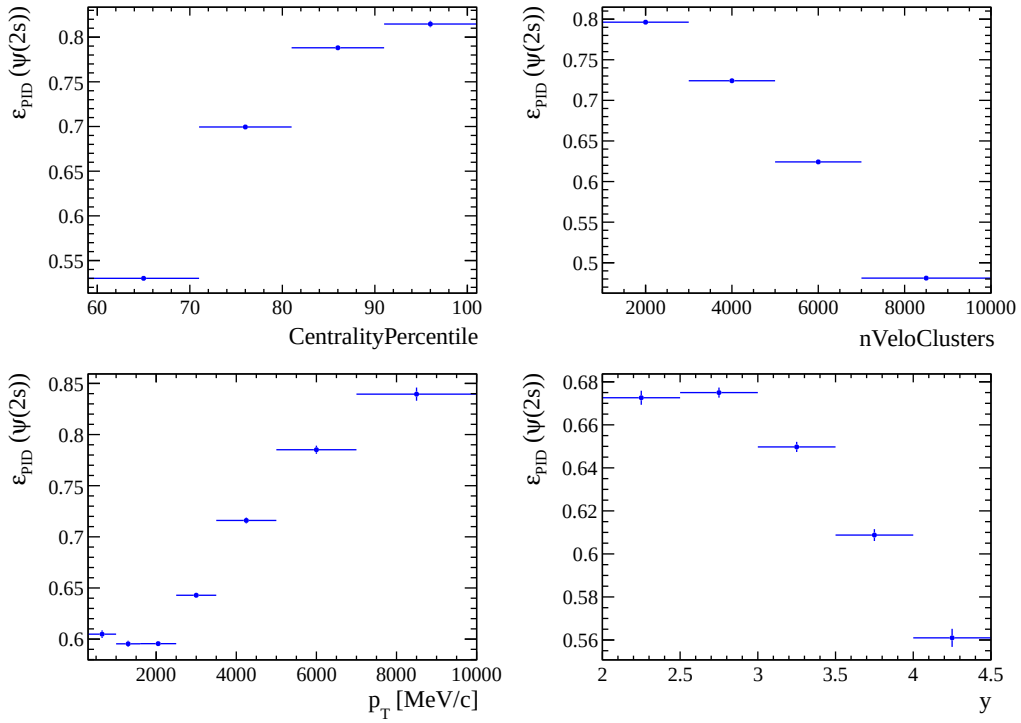


FIGURE 3.25: Particle identification efficiency $\varepsilon_{\text{MuonID}}$ as a function of centrality (top left), `nVeloClusters` (top right), p_{T} (bottom left) and y (bottom right) for $\psi(2S)$.

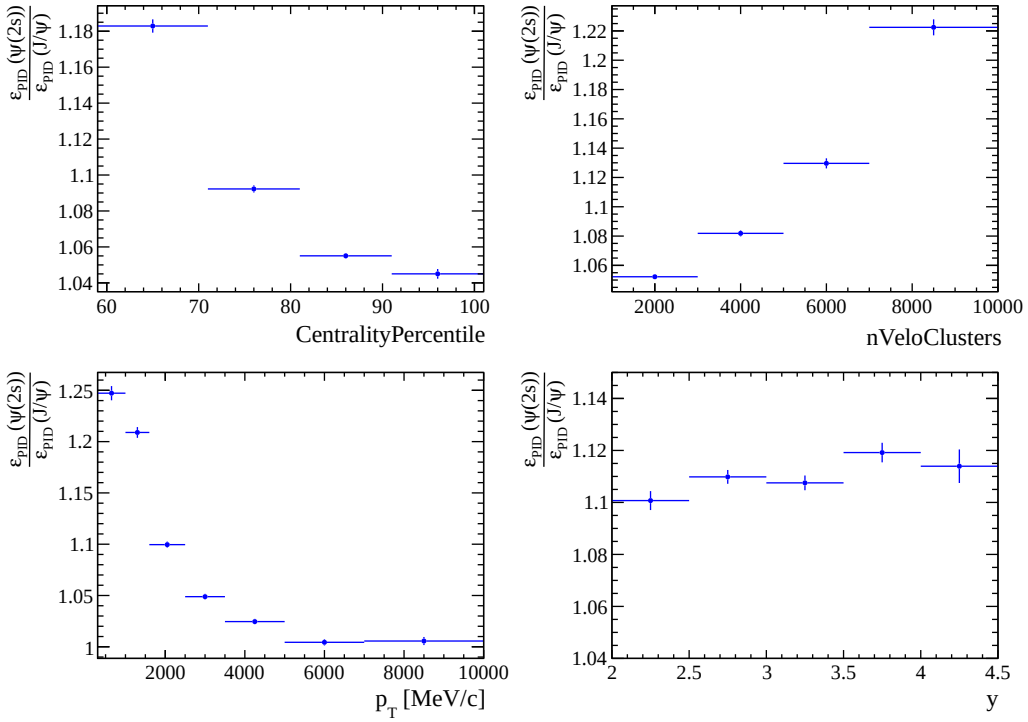


FIGURE 3.26: Particle identification efficiency $\varepsilon_{\text{MuonID}}$ ratio of $\psi(2S)$ over J/ψ as a function of centrality (top left), `nVeloClusters` (top right), p_{T} (bottom left) and y (bottom right).

As shown in Fig. 3.26, the ratio of the $\varepsilon_{\text{MuonID}}$ efficiencies increases with larger values of `nVeloClusters`. This behaviour is attributed to the fact that, for a fixed charmonium transverse momentum, the decay muons from the $\psi(2S)$ have a higher average p_{T} compared to those from the J/ψ, as demonstrated in Fig. A.3 of Appendix A.2. Moreover, the $\varepsilon_{\text{MuonID}}$ efficiency for lower-p_{T} muons exhibits a steeper decline as a function of `nVeloClusters`, as shown in Fig. 3.21.

The efficiency values obtained via the extrapolation method adopted in this analysis have been validated through a cross-check using the Tag&Probe technique on the signal PbPb sample, but only in two intervals of `nVeloClusters` given the poor statistics. The PID selection `ProbNN`$\mu > 0.7$ was tested by applying two different `ProbNN`μ thresholds on the tag muon. Details of this cross-check procedure are provided in Appendix A.3. To allow for a meaningful comparison, the extrapolated PID efficiencies, computed in bins of (p_{T}, `nVeloClusters`) from the pp sample were weighted by the muon p_{T} and `nVeloClusters` distributions observed in the PbPb data. The comparison, shown in Fig. 3.27, demonstrates a reasonable agreement between the two methods, thereby supporting the validity of the extrapolation approach.

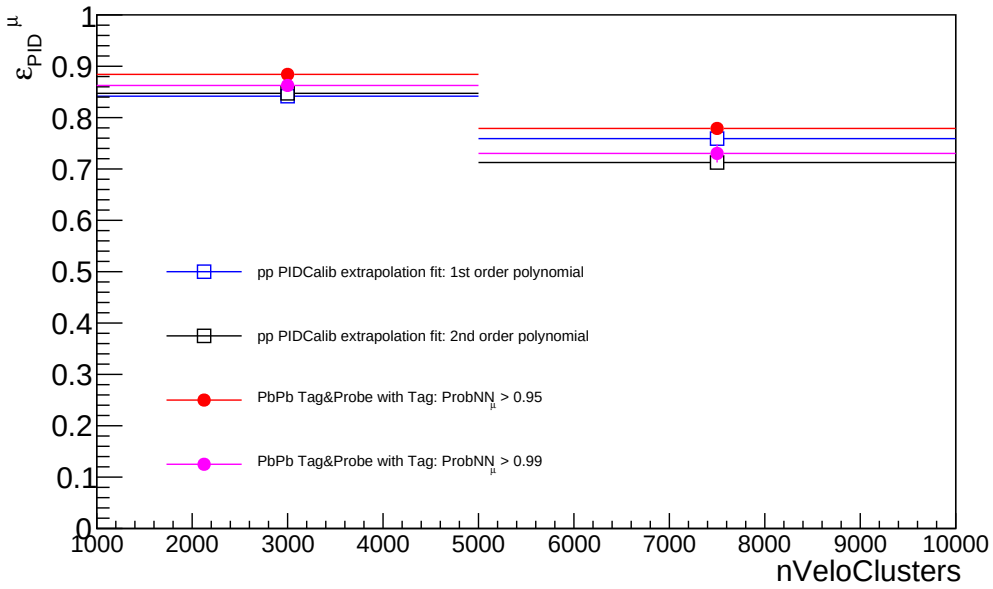


FIGURE 3.27: Efficiency of the `ProbNN`$\mu > 0.7$ requirement computed using the extrapolation from the pp sample (blue open squares for the second-order polynomial extrapolation, black open squares for an alternative first-order polynomial extrapolation), and with the signal PbPb sample using different identification criteria for the tag muon (circles).

3.6.6 Trigger efficiency

The trigger efficiency quantifies the fraction of good events selected by the trigger line used during data-taking. It is estimated using the simulation sample and is defined similarly to the $\varepsilon_{\text{rec\&sel}}$:

$$\varepsilon_{\text{trg}} \equiv \frac{J/\psi\ (\psi(2S))\text{ reconstructed, selected and triggered}}{J/\psi\ (\psi(2S))\text{ reconstructed and selected (with }\mu\text{ PID and without trigger)}}, \tag{3.15}$$

As explained in Sec. 3.2, there are two trigger lines required in this analysis, once for `nVeloClusters` below 6000 and the other for `nVeloClusters` between 6000 and 10 000. As for the other efficiencies estimated using simulation, the trigger efficiency is corrected by the reweighting procedure.

The results are shown in Fig. 3.28 (J/ψ) and Fig. 3.29 ($\psi(2S)$), and summarised in Tab. 3.13 as a function of the centrality.

The efficiency ratios are shown in Fig. 3.30, and exhibit a flat, unitary trend as a function of the centrality. In addition, the inefficiency of the L0 trigger line has been evaluated in simulation and found to be only 0.2% for both J/ψ and $\psi(2S)$. Therefore, it is assumed to be 100%, and its effect cancels out in the ratio.

TABLE 3.13: Trigger efficiency for J/ψ, $\psi(2S)$ and their ratio as a function of centrality. The uncertainty is statistical.

	Centrality			
	$60-70\%$	$70-80\%$	$80-90\%$	$90-100\%$
$\varepsilon(J/\psi)$	$(97.1 \pm 0.06)\%$	$(83.2 \pm 0.11)\%$	$(81.9 \pm 0.12)\%$	$(81.9 \pm 0.23)\%$
$\varepsilon(\psi(2S))$	$(97.1 \pm 0.07)\%$	$(83.8 \pm 0.14)\%$	$(83.0 \pm 0.15)\%$	$(83.2 \pm 0.28)\%$
$\mathcal{R}_{\varepsilon(\psi(2S))/\varepsilon(J/\psi)}$	1.000 ± 0.001	1.007 ± 0.002	1.014 ± 0.002	1.017 ± 0.004

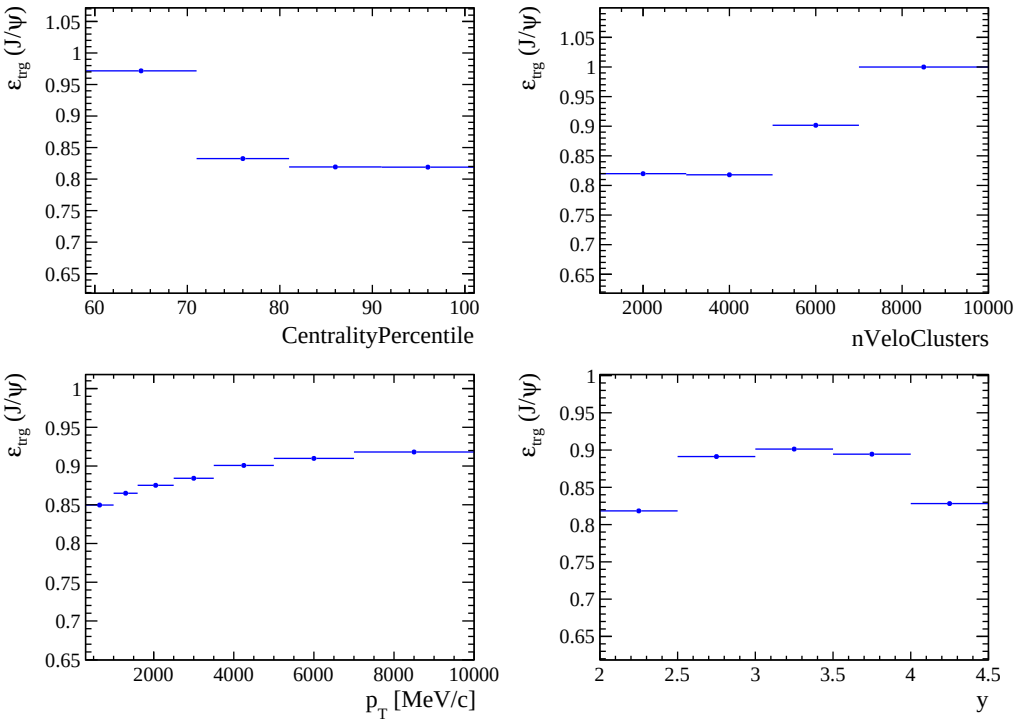


FIGURE 3.28: Trigger efficiency ε_{trg} as a function of centrality (top left), `nVeloClusters` (top right), p_{T} (bottom left) and y (bottom right) for J/ψ.

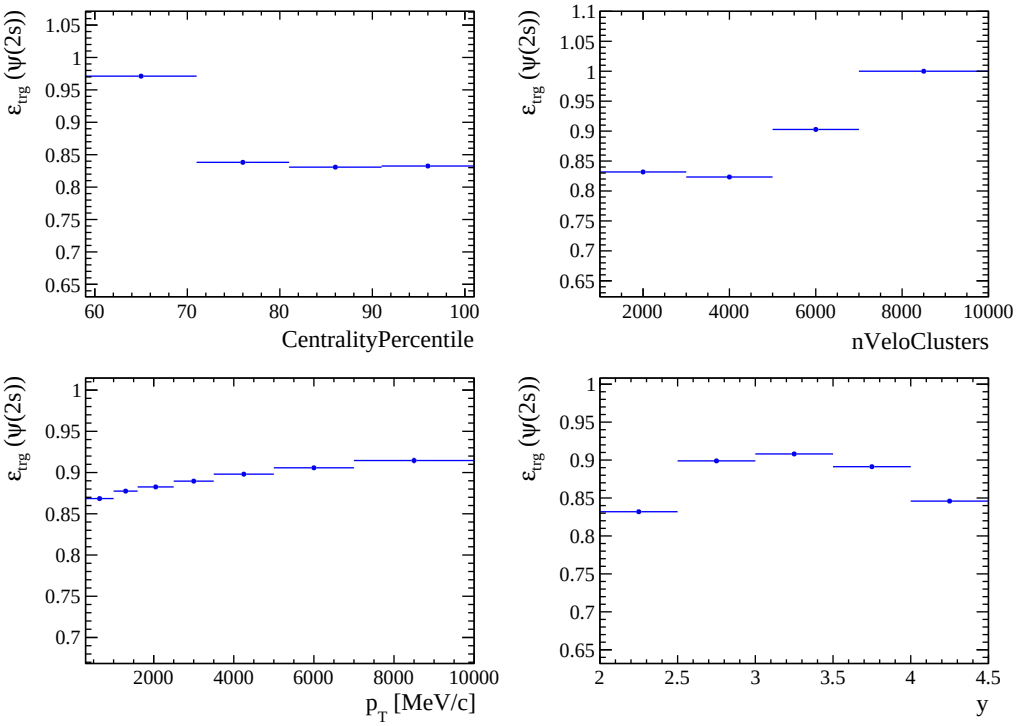


FIGURE 3.29: Trigger efficiency ε_{trg} as a function of centrality (top left), `nVeloClusters` (top right), p_{T} (bottom left) and y (bottom right) for $\psi(2S)$.

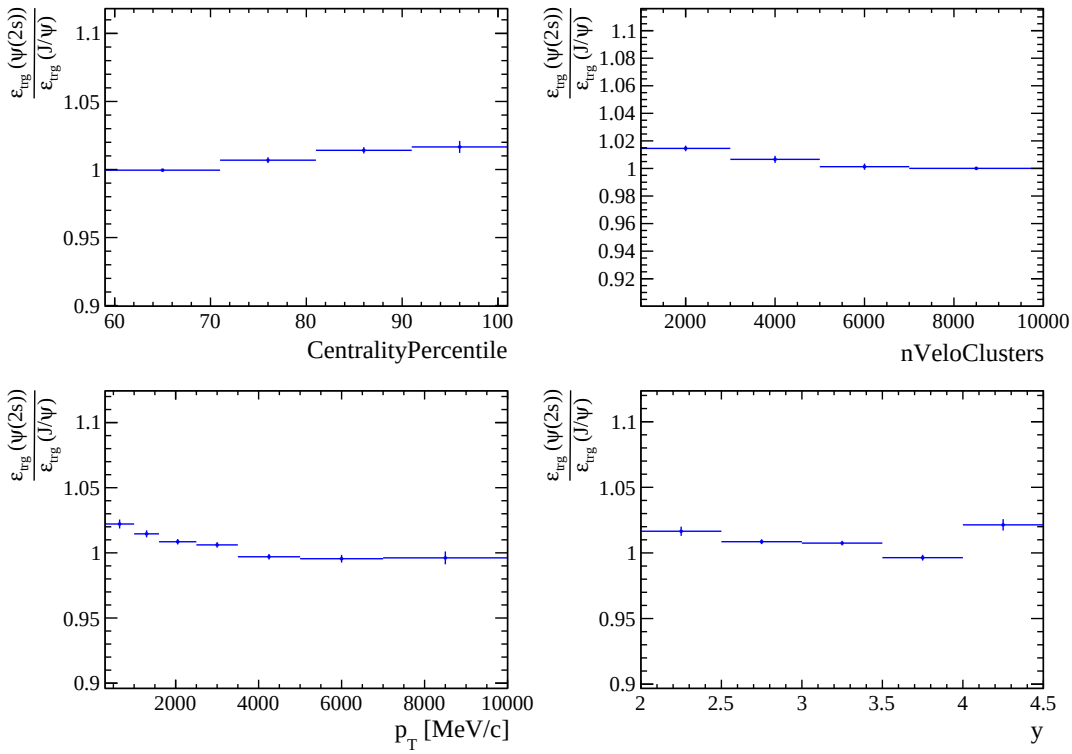


FIGURE 3.30: Trigger efficiency ε_{trg} ratio of $\psi(2S)$ over J/ψ as a function of centrality (top left), `nVeloClusters` (top right), p_{T} (bottom left) and y (bottom right).

3.6.7 Total efficiency

The total efficiency, ε_{tot}, used in the ratio formula (Eq. 3.1), is obtained by multiplying all the individual contributions described above. The resulting values are shown in Fig. 3.31 for the J/ψ and in Fig. 3.32 for the $\psi(2S)$. As usual, the ratio of the total efficiencies is presented in Fig. 3.33, and the numerical values are listed in Table 3.14 as a function of the centrality.

TABLE 3.14: Total efficiency for J/ψ, $\psi(2S)$ and their ratio as a function of centrality. The uncertainty is statistical.

	Centrality			
	$60-70\%$	$70-80\%$	$80-90\%$	$90-100\%$
$\varepsilon(J/\psi)$	$(10.4 \pm 0.05)\%$	$(17.2 \pm 0.06)\%$	$(19.6 \pm 0.07)\%$	$(17.7 \pm 0.11)\%$
$\varepsilon(\psi(2S))$	$(14.4 \pm 0.07)\%$	$(22.4 \pm 0.09)\%$	$(24.9 \pm 0.10)\%$	$(22.2 \pm 0.17)\%$
$\mathcal{R}_{\varepsilon(\psi(2S))/\varepsilon(J/\psi)}$	1.384 ± 0.009	1.297 ± 0.007	1.272 ± 0.007	1.256 ± 0.013

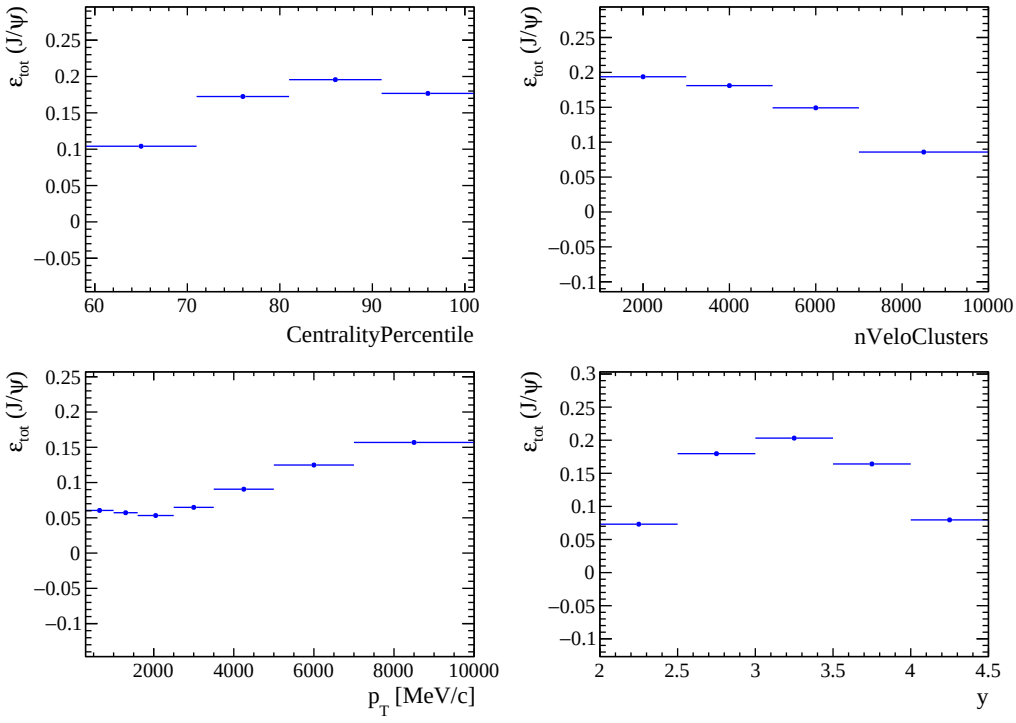


FIGURE 3.31: Total efficiency ε_{tot} as a function of centrality (top left), `nVeloClusters` (top right), p_{T} (bottom left) and y (bottom right) for J/ψ.

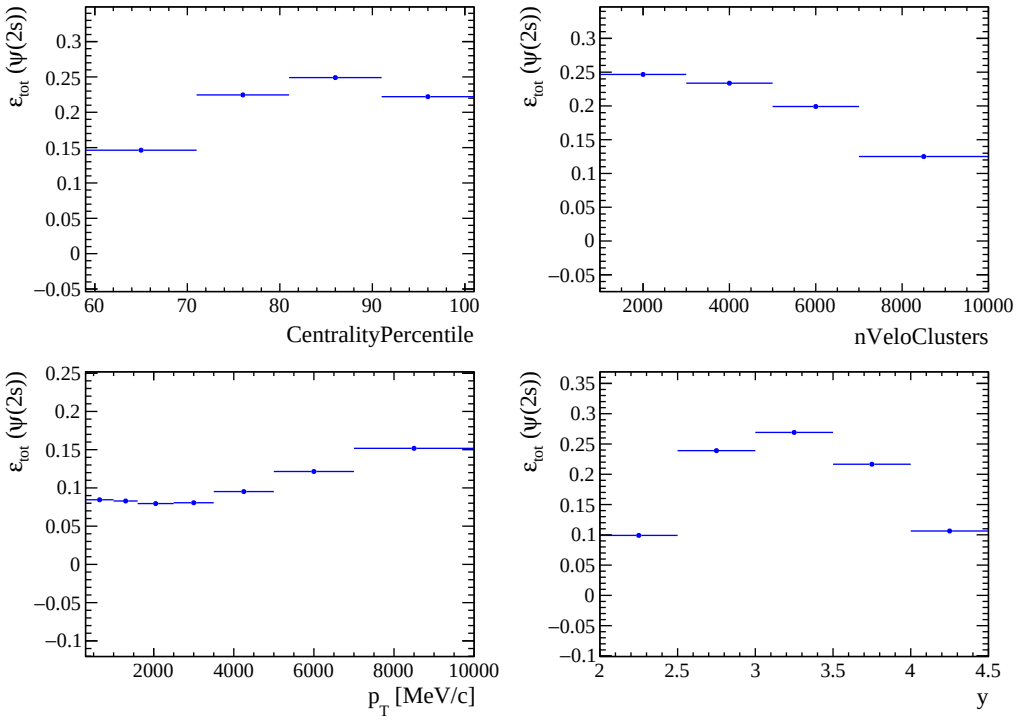


FIGURE 3.32: Total efficiency ε_{tot} as a function of centrality (top left), `nVeloClusters` (top right), p_{T} (bottom left) and y (bottom right) for $\psi(2S)$.

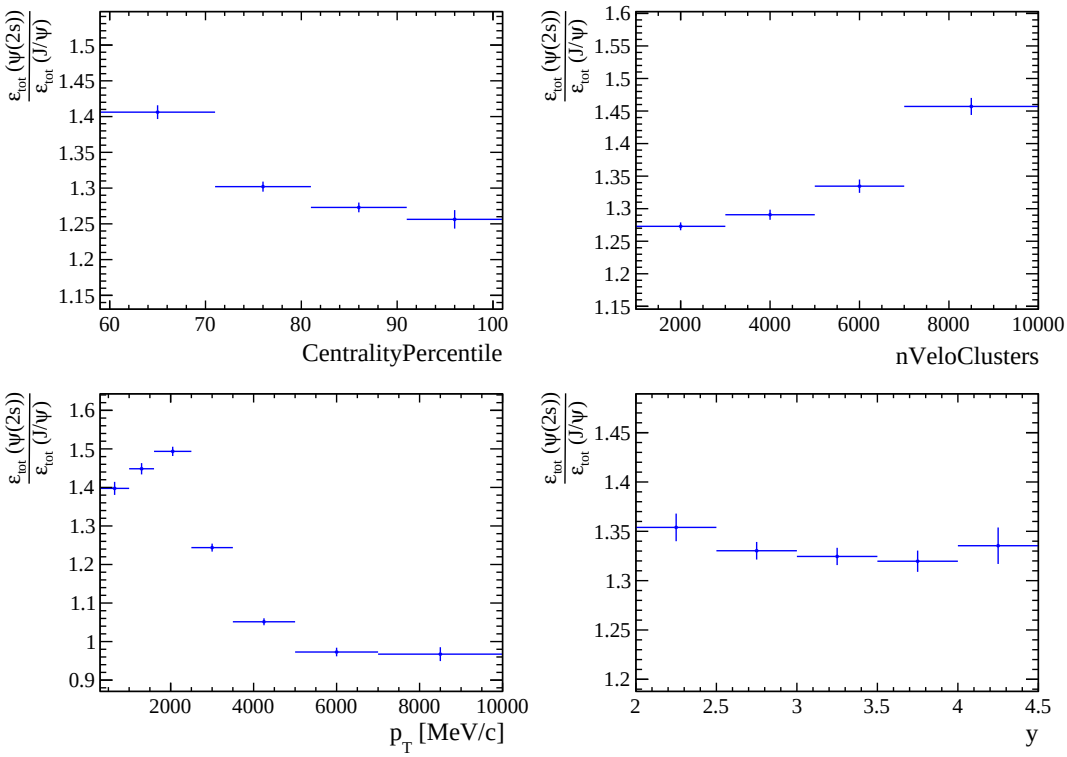


FIGURE 3.33: Total efficiency ε_{trg} ratio of $\psi(2S)$ over J/ψ as a function of centrality (top left), `nVeloClusters` (top right), p_{T} (bottom left) and y (bottom right).

3.7 Systematic uncertainties

The ratio measurement presented in this thesis is affected by several sources of systematic uncertainty. They are described and evaluated in the following sections.

3.7.1 Fit model

One of the main ingredients in the ratio formula (Eq. 3.1) is the number of signal candidates measured for both states. As explained in Sec. 3.5, the yields are extracted by performing an unbinned maximum likelihood fit to the dimuon invariant mass distribution. Therefore, the choice of the functions used to model the signal (see Sec. 3.7.1.1) and background (see Sec. 3.7.1.2) components represents a source of systematic uncertainty, as discussed below.

3.7.1.1 Signal model

In the baseline fit model, the signal is described by a Crystal Ball function for the J/ψ and a Gaussian function for the $\psi(2S)$, with a set of parameters fixed from the fit to simulated data. The uncertainty arising from the signal shape is evaluated through two different contributions:

- The first is estimated by varying the shape parameters that are fixed from simulation. As described in Sec. 3.5, the ratio of the function widths $\sigma_{\psi(2S)}/\sigma_{J/\psi}$ is fixed to the value obtained from simulation. In this study, it is varied within its uncertainty range, *i.e.* $\mu \pm \sigma$. During this variation, the remaining parameters of the signal and background models are kept fixed to reduce statistical fluctuations. The difference in the resulting ratio with respect to the nominal fit is taken as a contribution to the signal model uncertainty. It is negligible being about 0.1% in each interval.

- The second contribution is evaluated by replacing the Crystal Ball function used to model the J/ψ signal with a sum of a Crystal Ball and a Gaussian function. Due to the limited number of $\psi(2S)$ candidates, its model is left unchanged in order to avoid large statistical fluctuations. The difference with respect to the nominal result is taken as an additional contribution to the uncertainty, and results in the leading contribution to the signal model uncertainties around 1-2%. The fit results obtained with this new signal model are shown in App. A.4.

These two contributions are added in quadrature, and the resulting uncertainties are reported in Tab. 3.15.

TABLE 3.15: Systematic uncertainty on the $\psi(2S)/J/\psi$ ratio due to the signal fit model, as a function of centrality.

	Centrality			
	60–70 %	70–80 %	80–90 %	90–100 %
$\mathcal{R}_{\psi(2S)/J/\psi}$	2.2 %	0.6 %	1.4 %	0.5 %

3.7.1.2 Background model

The systematic uncertainty associated with the choice of the background model is evaluated by replacing the nominal exponential function with a second-order Chebyshev polynomial. While studying the impact of the background shape, the signal shape parameters are kept fixed. The fit results obtained with the alternative signal model are shown in App. A.5. The differences in the extracted $\psi(2S)/J/\psi$ yield ratios between the two background models are taken as the systematic uncertainty. The results are summarised in Tab. 3.16.

TABLE 3.16: Systematic uncertainty on the $\psi(2S)/J/\psi$ ratio due to the background fit model, as a function of centrality.

	Centrality			
	60–70 %	70–80 %	80–90 %	90–100 %
$\mathcal{R}_{\psi(2S)/J/\psi}$	3.7 %	0.5 %	5.1 %	6.3 %

3.7.1.3 Same-sign dimuon fit cross-check

The uncertainties listed in Tab. 3.16, particularly in the most peripheral bin, constitute a major contribution to the total systematic uncertainty, as shown in Tab. 3.19, which summarises all systematic sources. To verify that the background model variation provides a sufficiently good estimate of the uncertainty associated with signal yield extraction, a cross-check is performed.

To validate the method, same-sign ($\mu^+\mu^+$ or $\mu^-\mu^-$) dimuon pairs are selected from the dataset, using a different trigger line as explained in Sec. 3.2.1.1, applying the same selection criteria described in Sec. 3.3 but asking for muons of the same charge sign. The combinatorial background present in this distribution is expected to have the same shape as the one affecting the opposite-sign spectrum. An exponential function, as used in the nominal fit, is fitted to the same-sign mass distribution. The results are shown below in Fig. 3.34.

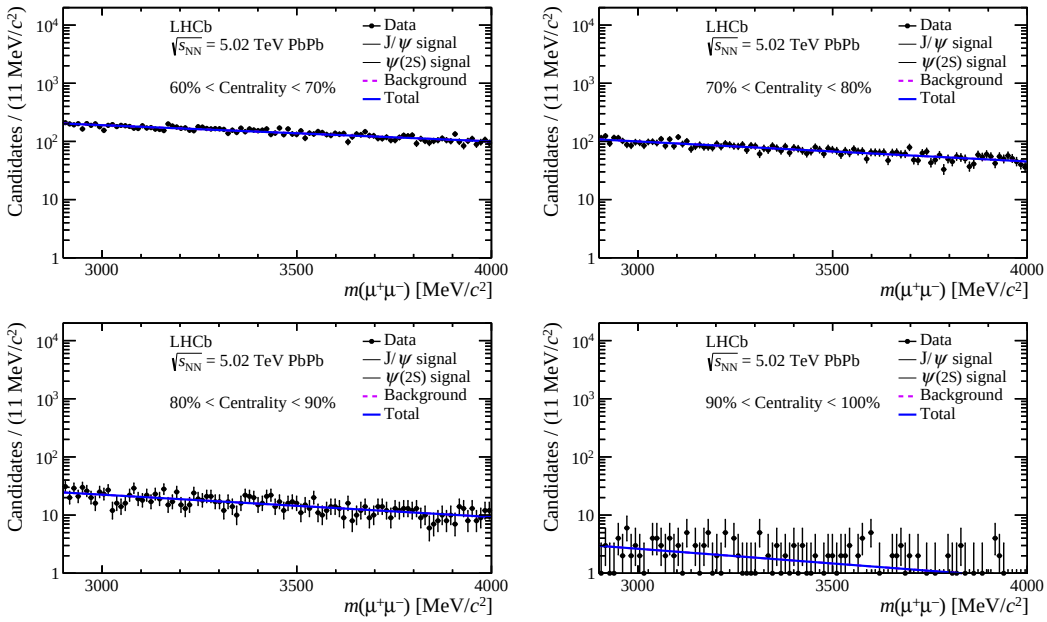


FIGURE 3.34: Same-sign dimuon invariant mass distributions in each centrality interval after selection, overlaid with exponential fit results.

At this point, a fit to the opposite-sign (nominal) invariant mass distribution is repeated, constraining the slope of the exponential background within the uncertainty range extracted from the same-sign fit. The difference in the $\psi(2S)/J/\psi$ ratio obtained with this approach is found to be compatible with the uncertainties listed in Tab. 3.16, within the unit percentage, confirming the validity of the method.

3.7.2 Prompt candidate selection

As discussed in Sec. 3.3.2.1, the selection on `log(IPCHI2)` used to suppress nonprompt background in the signal candidates is not 100% efficient. A residual contamination of approximately 5% is estimated for the J/ψ sample, and about 8% for the $\psi(2S)$ one.

The systematic uncertainty associated with this residual contamination is evaluated by computing the $\psi(2S)/J/\psi$ ratio after varying the yields by $\pm 5\%$ for the J/ψ and $\pm 8\%$ for the $\psi(2S)$, and then taking the difference from the nominal ratio. The resulting uncertainty is found to be 2.8% in each centrality interval.

3.7.3 Efficiency estimation

The second main ingredient in the ratio formula (Eq. 3.1) is the total efficiency associated with the two quarkonium states. Several choices made during the estimation of the different efficiency components, described in Sec. 3.6, represent sources of systematic uncertainty that must be taken into account, as discussed below.

3.7.3.1 MC sample size limitation

First, the finite size of the simulated sample used to determine the efficiencies introduces a source of systematic uncertainty. The relative statistical uncertainties on the total efficiencies are considered, and the resulting uncertainties on the $\psi(2S)/J/\psi$ ratio are listed in Table 3.17.

TABLE 3.17: Systematic uncertainty on the $\psi(2S)/J/\psi$ ratio due to MC sample size, as a function of centrality.

	Centrality			
	60–70 %	70–80 %	80–90 %	90–100 %
$\mathcal{R}_{\psi(2S)/J/\psi}$	0.94%	0.70%	0.68%	1.30%

3.7.3.2 MC reweighting

The systematic uncertainty associated with the simulation reweighting procedure is divided into two contributions:

- The first contribution is evaluated by varying the bin contents of the weight histograms, obtained as described in Sec. 3.6.2. For this purpose, 50 trials are performed. In each trial, a new weight histogram is generated by fluctuating each bin content within its statistical uncertainty ($\pm\ 1\sigma$). The modified histogram is then used to recompute the total efficiency. The resulting 50 efficiency values are stored and fitted with a Gaussian function. The mean (μ) and standard deviation (σ) of the fit are used to estimate the systematic uncertainty. In each centrality bin, this uncertainty is found to be below 0.2% and is therefore considered negligible.

- The second contribution arises from the fact that, in the nominal reweighting procedure, only the J/ψ weights are used for both quarkonium states, as explained in Sec. 3.6.2. This choice is due to the limited statistics of the $\psi(2S)$ sample, which would lead to large fluctuations in the weights. To assess the impact of this approximation, an alternative reweighting is performed in which the J/ψ candidates are further reweighted to match the $\psi(2S)$ distributions in p_{T} and `nVeloClusters`, as shown in Fig. 3.35. The new weights are then used to recompute the ratio. The difference between this result and the one obtained with the nominal weights is found to be approximately 0.5% in each centrality interval, and is taken as the systematic uncertainty associated with the reweighting procedure.

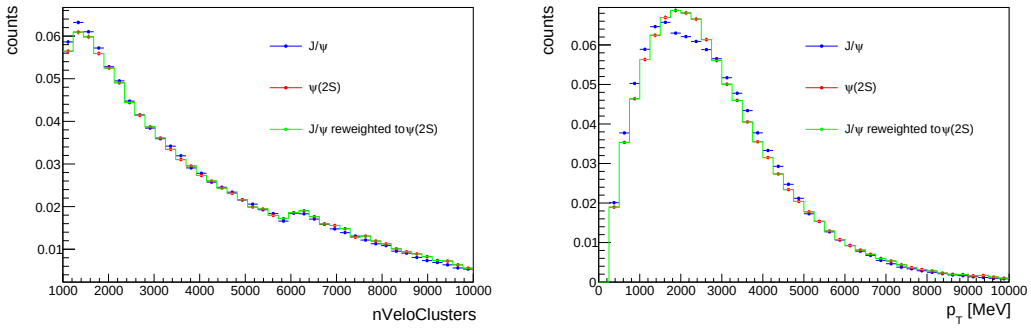


FIGURE 3.35: Comparison of normalised `nVeloClusters` (left) and p_{T} (right) distributions between J/ψ before reweight to match $\psi(2S)$ (blue dots) and after (green line). The distributions are in good agreement after the reweight.

3.7.3.3 MuonID efficiency

As already discussed in Sec. 3.6.5, the method used to estimate the muon identification efficiency required a dedicated treatment which can introduce some systematic uncertainties. In addition to the Tag&Probe cross-check used to validate the method already performed, three sources of systematic uncertainty are considered:

- The first contribution comes from the choice of the binning scheme used in the estimation of the PID tables from the `PidCalib2` package. The nominal (p_{T}, η) binning scheme is varied, and the difference in the efficiency ratio is taken as a systematic uncertainty. This difference is found to be below 0.1% and is therefore considered negligible.

- The second contribution is related to the limited statistics of the *pp* calibration sample used in the PID table estimation. Since this sample is finite, statistical fluctuations in the $\varepsilon^{pp}_{\mathrm{PID}}(p_{\mathrm{T}}, \eta; \texttt{nVeloClusters} < 1000)$ map (see Fig. 3.23) must be taken into account. To estimate their impact, 100 pseudo-experiments are performed where, in each trial, every bin of the PID map is varied randomly within its statistical uncertainty ($\pm\ 1\sigma$). The maximum observed difference in the efficiency ratio (with respect to the nominal value) across the centrality bins is taken as the systematic uncertainty. This contribution is found to be below 0.2% and is thus also considered negligible.

- The third and dominant contribution arises from the choice of the fit function used to extrapolate the muon identification efficiency to large `nVeloClusters`. Since the *pp* calibration sample does not cover the high-occupancy region, an extrapolation is required. In the nominal approach, a second-order polynomial is used. To assess the systematic uncertainty, a first-order polynomial is employed instead. Figure 3.36 shows the resulting $\varepsilon^{\mathrm{extr}}_{\mathrm{PID}}$ obtained with a first-order polynomial fit in the range $0 < \texttt{nVeloClusters} < 5000$ for different p_{T} bins. The differences in the final efficiency ratio with respect to the nominal case are not negligible, and are therefore taken as the systematic uncertainties associated with the MuonID efficiency estimation. These values are summarised in Table 3.18 as a function of centrality.

TABLE 3.18: Systematic uncertainty on the $\psi(2S)/J/\psi$ ratio due to MuonID efficiency estimation, as a function of centrality.

	Centrality			
	60–70 %	70–80 %	80–90 %	90–100 %
$\mathcal{R}_{\psi(2S)/J/\psi}$	2.8%	0.12%	0.25%	0.23%

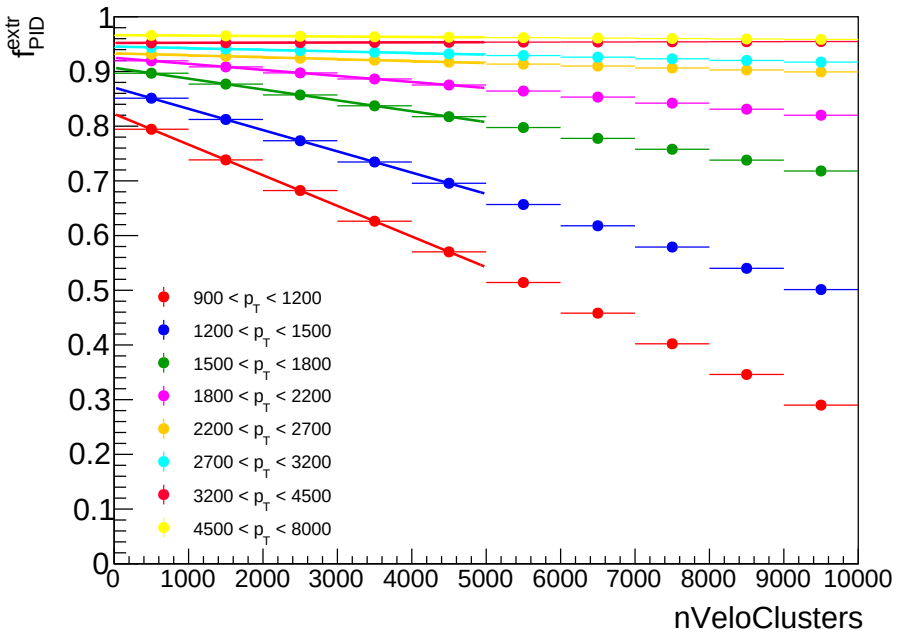


FIGURE 3.36: Muon efficiency from the 2018 pp sample as a function of detector occupancy (up to `nVeloClusters` = 5000) in different p_{T} bins. The fits for the different p_{T} intervals are performed using a first-order polynomial. For `nVeloClusters` > 5000, the efficiency values are extrapolated as explained in the text.

3.7.3.4 Trigger efficiency

The baseline trigger efficiency is estimated using simulation. To evaluate the associated systematic uncertainty, a well-established data-driven method in LHCb is employed, known as the TIS–TOS technique [121]. In this approach, to measure the efficiency the events are selected using triggers that are independent of the signal candidate (*Trigger Independent of Signal*, TIS). In this way, the events are recorded because of other activity in the detector, not because the charmonium candidate fired the trigger. This approach maximises the available statistics and allows an unbiased estimation of the efficiency, defined as the fraction of signal candidates that would have satisfied the specific trigger condition among all those present in the TIS sample.

As in other cases, only the J/ψ sample is large enough to allow for a reliable estimation of this efficiency. This is also the main reason why the nominal efficiency is derived from simulation alone.

In any case, the observed difference between the data-driven efficiency and the simulation-based one is below 0.1% for the J/ψ sample. This validates the use of the simulation-based method and allows the associated systematic uncertainty to be considered negligible.

3.7.4 Summary of systematic uncertanties

This section presents Tab. 3.19, which summarises all the different contributions to the systematic uncertainties affecting the $\psi(2S)/J/\psi$ cross-section ratio, as previously detailed.

As shown, the most significant sources of systematic uncertainty originate from the modelling of the background fit and the treatment of nonprompt contamination. Other contributions, such as those related to efficiency estimation, are generally smaller and in some cases negligible. All these effects are combined in quadrature to obtain the total systematic uncertainty on the final ratio measurement.

TABLE 3.19: Range of the relative systematic uncertainty contributions for the ratio measurement across the four centrality intervals.

Source	Uncertainty
Signal fit model	0.5–2.2 % [Sec. 3.7.1.1]
Background fit model	0.5–6.3 % [Sec. 3.7.1.2]
Nonprompt contamination	2.8 % [Sec. 3.7.2]
Simulation sample size	0.5–1.0 % [Sec. 3.7.3.1]
Weighting procedure	0.5 % [Sec. 3.7.3.2]
PID efficiency extrapolation	0.1–2.8 % [Sec. 3.7.3.3]
Trigger efficiency estimation	< 0.1 % [Sec. 3.7.3.4]

3.8 Results

Using the ratio formula (Eq. 3.1), the signal yields obtained from the fit procedure described in Sec. 3.5, and the efficiencies determined from simulation as discussed in Sec. 3.6, the cross-section ratio of $\psi(2S)$ to J/ψ production is measured as a function of centrality.

The integrated measurement across the four centrality intervals yields:

$$\frac{\sigma(\psi(2S))}{\sigma(J/\psi)} \cdot \frac{\mathcal{B}(\psi(2S) \to \mu^+\mu^-)}{\mathcal{B}(J/\psi \to \mu^+\mu^-)} = 0.022 \pm 0.006 \pm 0.001,$$

where the first uncertainty is statistical and the second systematic.

The results in the individual centrality intervals are reported in Tab. 3.20 and are shown in Figs. 3.37 and 3.38 as a function of the number of participating nucleons, $\langle N_{\text{part}} \rangle$. On the y-axis, the measured observable corresponds to the cross-section ratio $\mathcal{R}(\psi(2S)/J/\psi)$ multiplied by the dimuon branching fractions, according to Eq. 3.1.

TABLE 3.20: Cross-section times branching fraction ratio between $\psi(2S)$ and J/ψ in intervals of centrality, along with the corresponding number of participating nucleons $\langle N_{\rm part}\rangle$. The first uncertainty is statistical and the second systematic.

Centrality (%)	$\langle N_{\rm part}\rangle$	$\frac{\sigma(\psi(2S))}{\sigma(J/\psi)} \cdot \frac{\mathcal{B}(\psi(2S)\to\mu^+\mu^-)}{\mathcal{B}(J/\psi\to\mu^+\mu^-)}$
90–100	2.40–5.50	$0.018 \pm 0.007 \pm 0.001$
80–90	5.50–13.0	$0.020 \pm 0.005 \pm 0.001$
70–80	13.0–26.5	$0.016 \pm 0.006 \pm 0.001$
60–70	26.5–48.0	$0.027 \pm 0.011 \pm 0.001$

Figure 3.37 compares these results with the ALICE measurement [52], which was performed in PbPb collisions at the same centre-of-mass energy and in a similar rapidity and transverse momentum range, but includes both prompt and nonprompt contributions and covers a different centrality region. The two measurements are consistent within uncertainties in the overlapping region and show no significant dependence on $\langle N_{\rm part}\rangle$.

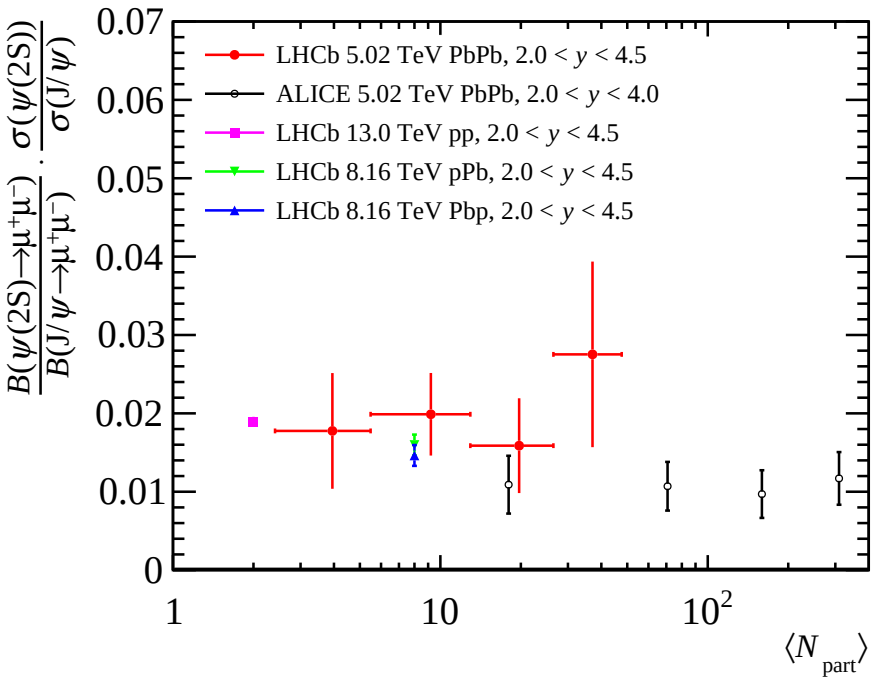


FIGURE 3.37: Cross-section times branching fraction ratio between $\psi(2S)$ and J/ψ as a function of $\langle N_{\rm part}\rangle$ in the $p_{\rm T} > 0.3$ GeV/c region, compared with ALICE PbPb [52], LHCb pp [122], and pPb [123] results. Vertical error bars represent the total uncertainty (statistical and systematic added in quadrature).

Also shown are LHCb results in pp [122] and pPb [123] collisions, which are integrated over the respective kinematic ranges. These measurements are associated with

$\langle N_{\text{part}} \rangle$ values of approximately 2 and 8, respectively, as estimated using the Glauber Monte Carlo model [31], and are in agreement with the PbPb results presented here.

Figure 3.38 compares the measured results to two theoretical predictions. The first is from the Statistical Hadronisation Model (SHMc) [62, 42], which assumes that a fireball in thermal equilibrium is formed near the QGP phase boundary, with charm quarks hadronising at the transition. The second is the TAMU model [41, 124], a transport model based on a non-perturbative hydro-Langevin-RRM approach, which incorporates collisional energy loss and charm-quark recombination in the QGP.

The SHMc model predicts a flat centrality dependence but generally underestimates the measured ratio, while the TAMU model is in better agreement, especially at low to intermediate $\langle N_{\text{part}} \rangle$. A slight tension is observed in the most central bin, where the data lie above both model predictions and the ALICE measurement by approximately 1.5 standard deviations.

It is worth noting that the TAMU model describes inclusive charmonium production, while the SHMc model includes only the prompt component. Moreover, the TAMU prediction is obtained in a slightly narrower rapidity window.

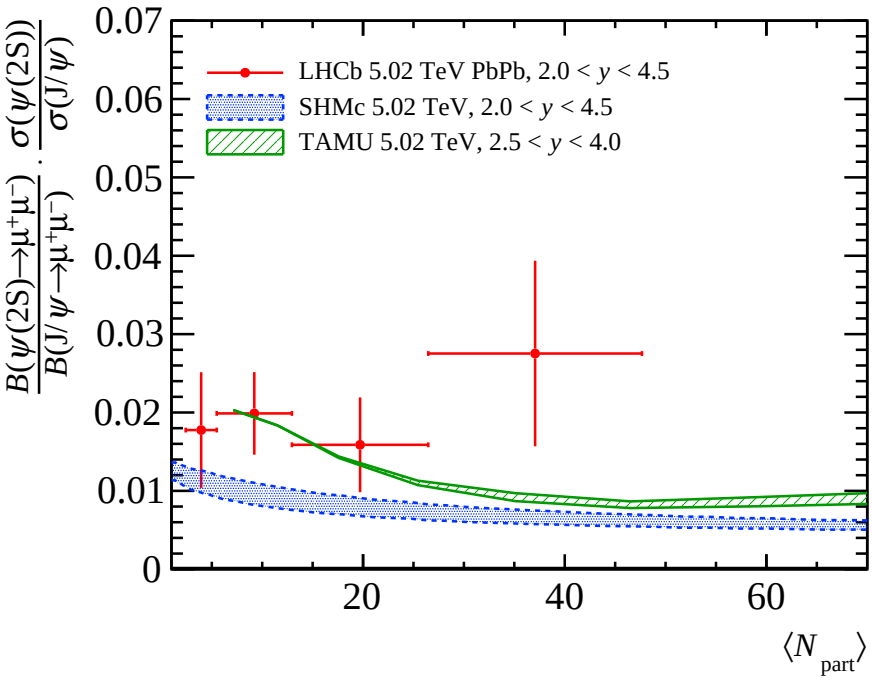


FIGURE 3.38: Cross-section times branching fraction ratio between $\psi(2S)$ and J/ψ as a function of $\langle N_{\text{part}} \rangle$ in the $p_{\text{T}} > 0.3$ GeV/c region, compared with the SHMc [62, 42] and TAMU [41, 124] model predictions. Coloured bands represent model uncertainties. Vertical error bars represent the total uncertainty (statistical and systematic added in quadrature).

This study represents a step forward in understanding quarkonium production in semicentral PbPb collisions.

Looking ahead, improved performance is expected, and already partially demonstrated, as discussed in Sec. 2.3.5, with the upgraded LHCb detector in Run 3 [125]. The increased data sample, enhanced detector efficiencies, and broader centrality coverage provided a high-quality PbPb dataset from the ion run conducted in November 2024. This sample offers excellent prospects for a similar analysis with significantly improved precision.

Work in this direction has already begun, and although still in progress, it is presented in the next chapter of this thesis.

Chapter 4

Measurement of $\psi(2S)/J/\psi$ in PbPb collisions at $\sqrt{s_{\rm NN}} = 5.36$ TeV (Run 3 Analysis)

In this chapter is reported a preliminary study of the $\psi(2S)$ to J/ψ ratio as a function of the event centrality, using the 2024 PbPb collision data collected at $\sqrt{s_{\rm NN}} = 5.36$ TeV by the LHCb detector, during the Run 3 data taking period. The analysis strategy is presented in Sec. 4.1, along with a description of the data sample in Sec. 4.2 and of the selection applied in Sec. 4.3. It follows the explanation of the charmonium yields estimation in Sec. 4.5, then the correction of the raw yields by detector efficiencies is discussed in Sec. 4.6. Finally, the results and outlook are presented in Sec. 4.7, together with a first idea of the systematic uncertainties to be evaluated.

4.1 Analysis strategy

The strategy for the Run 3 analysis follows closely the approach developed for the Run 2 measurement described in Sec. 3.1. The aim is to measure the ratio of the produced $\psi(2S)$ to J/ψ mesons as a function of the event centrality in PbPb collisions collected by the upgraded LHCb detector with the new software trigger system.

Charmonium candidates are reconstructed in the dimuon decay channel, and the signal yields are extracted through unbinned maximum-likelihood fits to the invariant mass distribution of opposite-sign muon pairs. Efficiency corrections, accounting for acceptance, reconstruction, selection and trigger effects, are evaluated using both simulation and data-driven methods adapted to the Run 3 conditions (see Sec. 4.6).

The observable of interest is the ratio

$$\mathcal{R}(\psi(2S)/J/\psi) = \frac{\sigma(\psi(2S))}{\sigma(J/\psi)} \cdot \frac{\mathcal{B}(\psi(2S) \to \mu^+\mu^-)}{\mathcal{B}(J/\psi \to \mu^+\mu^-)} = \frac{N(\psi(2S))}{N(J/\psi)} \cdot \frac{\varepsilon_{\rm tot}(J/\psi)}{\varepsilon_{\rm tot}(\psi(2S))}, \quad (4.1)$$

where N and $\varepsilon_{\rm tot}$ represent the fitted signal yields and total efficiencies, respectively. The ratio is presented in intervals of event centrality, determined from the total

energy deposited in the ECAL, and compared with the previous one already shown in Sec. 3.8.

4.2 Data and simulation samples

This section presents the data and simulation samples used for the Run 3 analysis.

4.2.1 Data and data-taking conditions

The LHCb detector recorded PbPb collisions at $\sqrt{s_{\rm NN}} = 5.36$ TeV during November and December 2024. Although the precise determination of the integrated luminosity is still ongoing at the time of writing, an online estimation indicates a recorded sample of about 450 μb^{-1}, nearly twice that of the previous PbPb dataset. The trigger configuration used to select the events is described below.

4.2.1.1 Trigger selection

The trigger strategy adopted for this analysis is designed to efficiently select hadronic PbPb events. At the first trigger level, events are required to contain at least one reconstructed primary vertex and a minimum energy deposit in the electromagnetic calorimeter of 410 GeV. The second-level trigger operates in *passthrough* mode, accepting all events, as well as the so-called "sprucing" step, equivalent to the Run 2 "stripping" (see Sec. 3.2.1.2).

4.2.2 Simulation

The simulated samples used in this analysis are listed in Table 4.1. The same event generators employed for the Run 2 analysis are used here: Pythia [95] to produce the J/ψ and $\psi(2S)$ mesons, which are then embedded into minimum-bias PbPb events generated with Epos [96] at 5.36 TeV centre-of-mass per nucleon.

Table 4.1: Simulated samples used for the Run 3 analysis.

Decay	Generator	Number of events
$J/\psi \to \mu^+\mu^-$	EPOS/PYTHIA	3217955
$\psi(2S) \to \mu^+\mu^-$	EPOS/PYTHIA	2790908

4.3 Sample selection

Selection criteria are applied to enhance the signal to background ratio. These requirements are grouped into two categories. First, global event requirements (Sec. 4.3.1) are imposed to reject events not relevant for this study. Then, kinematic and PID requirements are applied to increase the purity of the charmonium candidates (Sec. 4.3.2).

Since the two signals are very similar, identical selection criteria are used for both resonances, in data and simulation alike.

4.3.1 Global event selection

A set of global event cuts (GECs) is applied to remove background from electromagnetic processes, which are not part of this analysis. The applied GECs are listed in Table 4.2.

TABLE 4.2: Global event selection (GEC) criteria applied to the data.

Condition	**Selection value**
Photon-production contamination	$p_{\mathrm{T}}(\psi) > 300$ MeV/c
UPC contamination	`eCalTot` > 410 GeV
SMOG contamination	$\lvert z_{\mathrm{PV}}\rvert < 200$ mm
Saturation regime	`eCalTot` < 12.5 TeV

As in the previous analysis, photo-produced ψ mesons are suppressed by requiring $p_{\mathrm{T}} > 300$ MeV/c. Ultra-peripheral collisions, typically characterised by very low detector activity, are rejected by requiring a minimum energy deposit in the ECAL, which is already enforced at the trigger level. In the Run 3 configuration, the SMOG2 gas target (see Sec. 2.3.4) confines beam–gas interactions to a localised region; thus, only a fiducial requirement of $|z_{\mathrm{PV}}| < 200$ mm is applied to select beam–beam interactions around the nominal interaction point. Finally a requirement is set on the maximum numbers of SciFi clusters (`nFTClusters` $< 30\,000$), to avoid detector saturation regime, this corresponds to a maximum energy deposit in the calorimeter of 12.5 TeV.

4.3.2 J/ψ and $\psi(2S)$ candidate selection

The selection of charmonium candidates follows closely the Run 2 strategy. Each muon track is required to have transverse momentum $p_{\mathrm{T}} > 900$ MeV/c, a low probability of being misreconstructed, ensured by the requirement `ProbGhost` < 0.1, together with a good individual track quality, constrained by the track-fit χ^2 per degree of freedom (`CHI2DOF`), which is required to be below three.

A PID requirement of `PID`$\mu > 3$ is applied to ensure that both tracks are genuine muons. This selection is among the most delicate, as it directly impacts the purity of the sample. At the time of writing, the `ProbNN`μ variable, output of a multivariate algorithm using information from all sub-detectors (see Sec. 2.2.6.2), has not yet been calibrated for PbPb collisions, but only for pp [1].

[1] This calibration is actually part of my current work as the person responsible for Real-Time Analysis within the Ion and Fixed-Target working group of the experiment and it is still ongoing.

Thus, for the purpose of obtaining preliminary results, the selection on the PIDμ variable, which is the output of a simpler likelihood-based algorithm relying on hits in the muon chambers, is used here.

The chosen threshold for PIDμ was determined by comparing its distributions in simulation and data sidebands, *i.e.* in invariant-mass regions dominated by combinatorial background ($2900 < m_{\mu^+\mu^-} < 3000$ MeV/c^2 and $3200 < m_{\mu^+\mu^-} < 3400$ MeV/c^2 for the J/ψ sample), as shown in Fig. 4.1. While a value around 4 would maximise purity, a slightly looser selection (PID$\mu > 3$) was adopted to preserve sufficient statistics, particularly for the $\psi(2S)$ sample.

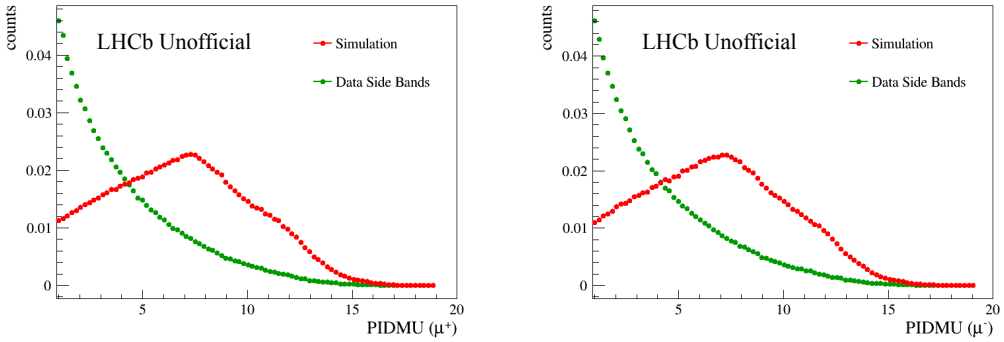


FIGURE 4.1: Distribution of the PIDμ variable for μ^+ (left) and μ^- (right). Red: simulated J/ψ signal; green: J/ψ data in invariant-mass sidebands ($2900 < m_{\mu^+\mu^-} < 3000$ MeV/c^2 and $3200 < m_{\mu^+\mu^-} < 3400$ MeV/c^2).

Finally, the dimuon invariant mass is required to satisfy $2900 < m_{\mu^+\mu^-} < 4000$ MeV/c^2, a range that includes both the J/ψ and $\psi(2S)$ resonances. All selection criteria are summarised in Table 4.3.

TABLE 4.3: Offline selection criteria applied to the dimuon candidates.

Selection variable	**Selection value**
Muon transverse momentum	$p_{\mathrm{T}} > 900$ MeV/c
Track ghost probability	ProbGhost < 0.1
Track χ^2	CHI2DOF < 3
Muon PID requirement	PID$\mu > 3$
Dimuon invariant mass	$2900 < m_{\mu^+\mu^-} < 4000$ MeV/c^2

At the current stage of the analysis no requirement on the impact parameter χ^2 or on the pseudoproper time of the candidates is applied. The separation between prompt and nonprompt components will be introduced in a later stage, using a proper fit to the pseudoproper time distribution rather than a simple selection, as done in the previous analysis. Thus the analysis at the moment measures the inclusive $\psi(2S)/J/\psi$ ratio.

4.4 Centrality determination

In the 2024 PbPb data-taking campaign at $\sqrt{s_{\mathrm{NN}}} = 5.36$ TeV, the centrality determination was performed within the LHCb collaboration, following the same conceptual approach as developed for Run 2 [116] and summarized in Sec. 3.4.

In particular, the total energy deposited in the electromagnetic calorimeter, `eCalTot`, is used as the primary estimator of event activity. This variable is chosen because of its high efficiency and stability in PbPb data, and because it provides a monotonic correlation with the charged-particle multiplicity and, consequently, with N_{part}. The use of `eCalTot` also avoids the need for multiplicity information from the tracking detectors, which may suffer from saturation in the most central collisions.

4.4.1 Methodology

The relation between `eCalTot` and the collision geometry is obtained by fitting the measured distribution of total ECAL energy with a Monte Carlo Glauber model. Here, each collision is characterised by the quantities N_{part}, N_{coll}, and b, generated assuming a Woods–Saxon nuclear density profile and an inelastic nucleon-nucleon cross-section $\sigma_{NN}^{\mathrm{inel}}$. The event activity is simulated by sampling a negative-binomial distribution whose mean multiplicity depends on a linear combination of N_{part} and N_{coll}:

$$N_{\mathrm{anc}} = f_{\mathrm{anc}} N_{\mathrm{part}} + (1 - f_{\mathrm{anc}}) N_{\mathrm{coll}}, \tag{4.2}$$

where f_{anc} represents the relative contribution of soft processes to particle production. The best-fit parameters are found by minimising the χ^2 between data and simulation in the `eCalTot` distribution, excluding the low-activity region dominated by electromagnetic or background events.

For the 2024 PbPb sample, the fit shown in Fig. 4.2 yields $f_{\mathrm{anc}} = 0.869$, with a satisfactory $\chi^2/\mathrm{ndf} = 1.3$, in good agreement with the Run 2 determination.

The resulting Glauber parameters allow to map intervals of `eCalTot` energy to centrality percentiles and to average geometric quantities such as $\langle N_{\mathrm{part}} \rangle$ and $\langle N_{\mathrm{coll}} \rangle$, reported in Tab. 4.4 and shown in Fig. 4.3.

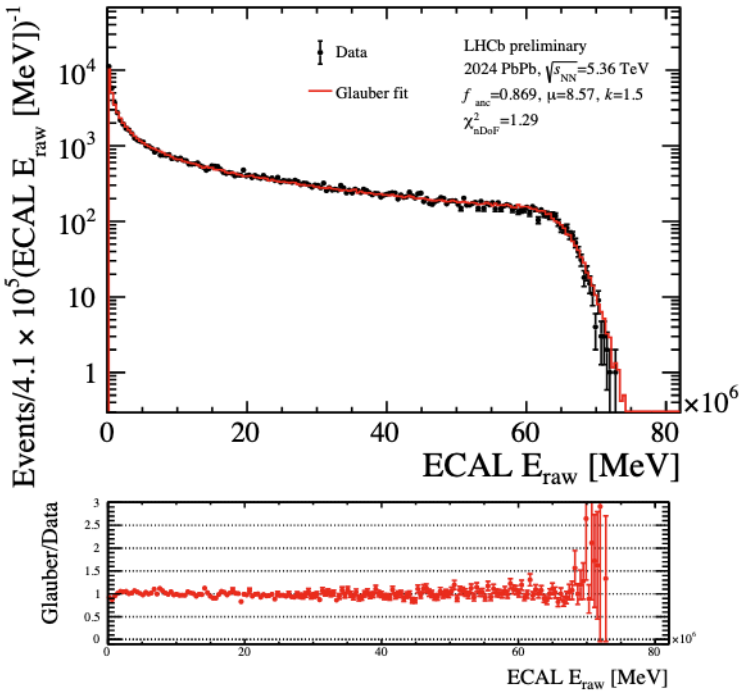


FIGURE 4.2: Top: Glauber MC fit to 2024 PbPb data as a function of ECAL energy. Bottom: data-to-fit ratio.

TABLE 4.4: Centrality classes and corresponding average geometry parameters.

Centrality [%]	E [GeV]	$\langle N_{\text{part}} \rangle$	$\sigma_{N_{\text{part}}}$	$\langle N_{\text{coll}} \rangle$	$\sigma_{N_{\text{coll}}}$
100-95	0.0 – 410.0	3.1	1.4	1.9	1.2
95-90	410.0 – 410.0	0	0	0	0
90-85	410.0 – 820.0	6.8	2.3	5.3	2.3
85-80	820.0 – 1230.0	10.6	2.8	9.1	3.4
80-75	1230.0 – 1640.0	14.3	3.3	13.4	4.5
75-70	1640.0 – 2460.0	19.7	4.3	20.6	6.6
70-65	2460.0 – 3280.0	27	4.9	31.5	9
65-60	3280.0 – 4510.0	35.7	5.9	46.6	12.7
60-55	4510.0 – 6150.0	47.6	7	70.8	17.7
55-50	6150.0 – 8200.0	62.2	8	105.4	23.7
50-44	8200.0 – 10660.0	79.4	9.2	152.7	30.9
44-40	10660.0 – 13530.0	99.1	10.3	214.2	38.6
40-35	13530.0 – 16810.0	120.7	11.4	290.3	46.8
35-30	16810.0 – 20910.0	145.8	12.9	387.1	57.1
30-25	20910.0 – 25420.0	174	13.9	507.2	66.3
25-20	25420.0 – 31160.0	206.4	15.7	657.7	80.2
20-15	31160.0 – 37720.0	244.1	17.1	848.9	93.5
15-10	37720.0 – 45510.0	286.4	18.8	1080.7	110.6
10-5	45510.0 – 54940.0	334.6	20.6	1376.4	134.5
5-0	54940.0 – ∞	385	17.6	1752.6	155.8

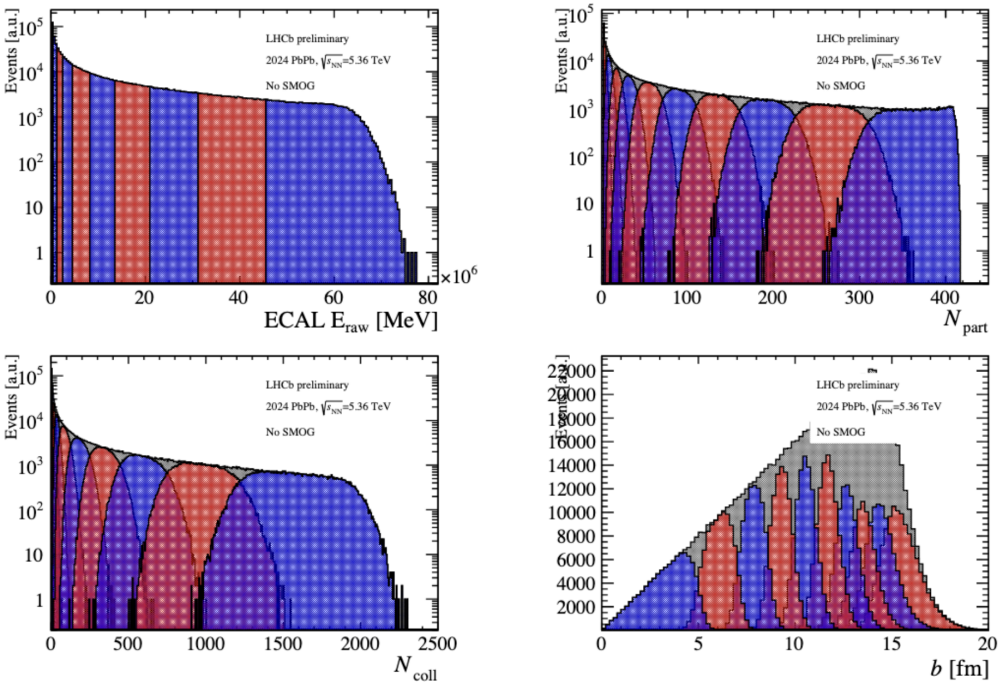


FIGURE 4.3: Top left: classification of events from PbPb data according to the defined centrality classes. Top right: $\langle N_{\text{part}} \rangle$. Bottom left: $\langle N_{\text{coll}} \rangle$. Bottom right: impact parameter distributions.

4.4.2 Centrality classes and current binning

The analysis presented in this thesis focuses on the most central regions accessible given the current GECs. In 2024 data, the selection imposes `eCalTot` < 12.5 TeV, which corresponds to approximately the 40% most central PbPb collisions. The binning scheme adopted for this study is summarised in Table 4.5. It is defined in terms of `eCalTot`, and mapped onto centrality percentiles and average numbers of participating nucleons according to the Glauber calibration.

TABLE 4.5: Binning scheme used for the Run 3 analysis, based on the total ECAL energy. The corresponding centrality and average $\langle N_{\text{part}} \rangle$ values are derived from the Glauber fit.

eCalTot (TeV)	0.410-1.23	1.23-2.46	2.46-4.51	4.51-12.53
Centrality (%)	80-90	70-80	60-70	40-60
$\langle N_{part} \rangle$	3.1-10.6	10.6-19.7	19.7-35.7	35.7-99.1

This binning scheme is preliminary and will be refined once the final centrality calibration, including systematic uncertainties, is completed. Nonetheless, it provides a consistent mapping between detector activity and collision geometry, sufficient for the $\psi(2S)/J/\psi$ measurement presented here.

4.5 Signal yield extraction

This section describes the procedure used to extract the signal yields of the J/ψ and $\psi(2S)$ mesons from the dimuon invariant mass distributions, both in the integrated sample and in intervals of centrality. These yields constitute the inputs to Eq. 3.1 for the evaluation of the cross-section ratio.

The yields are obtained by performing an unbinned extended maximum-likelihood fit to the $\mu^+\mu^-$ invariant mass spectrum. The function used for the fit includes contributions from both signal resonances and the combinatorial background as follows:

$$f(m_{\mu^+\mu^-}) = N_{J/\psi}\, f_{J/\psi}(m_{\mu^+\mu^-}) + N_{\psi(2S)}\, f_{\psi(2S)}(m_{\mu^+\mu^-}) + N_{\text{bkg}}\, f_{\text{bkg}}(m_{\mu^+\mu^-}). \quad (4.3)$$

Similarly to the previous analysis, the J/ψ signal is modelled using a Crystal Ball function, which is also implemented this time to shape the $\psi(2S)$ signal, while the combinatorial background is again described by an exponential function.

To ensure fit stability and reduce correlations among parameters, several constraints are applied identical to the previous measurement:

- The mass difference between the $\psi(2S)$ and J/ψ peaks is fixed to the known PDG value [13]:
$$\mu_{\psi(2S)} - \mu_{J/\psi} = m^{\text{PDG}}_{\psi(2S)} - m^{\text{PDG}}_{J/\psi}.$$
- The width ratio $\sigma_{\psi(2S)}/\sigma_{J/\psi}$ is fixed to the value obtained from fits to simulated signal samples.
- The CB tail parameters (α and n) are also fixed to those extracted from simulation.

The fit to the invariant-mass spectrum integrated over the full dataset is shown in Fig. 4.4, while the corresponding fits in the different centrality intervals are reported in Fig. 4.5. The fitted yields in each interval are summarised in Table 4.6.

TABLE 4.6: Range for the number of the nucleons $\langle N_{\text{part}} \rangle$ and signal yields in each centrality interval, the uncertainties are statistical only.

Centrality (%)	80–90	70–80	60–70	40–60
$\langle N_{\text{part}} \rangle$	3.10–10.6	10.6–19.7	19.7–35.7	35.7–99.1
$N(J/\psi)$	2797 ± 74	3433 ± 73	4825 ± 165	7511 ± 189
$N(\psi(2S))$	43 ± 12	51 ± 22	73 ± 32	84 ± 62

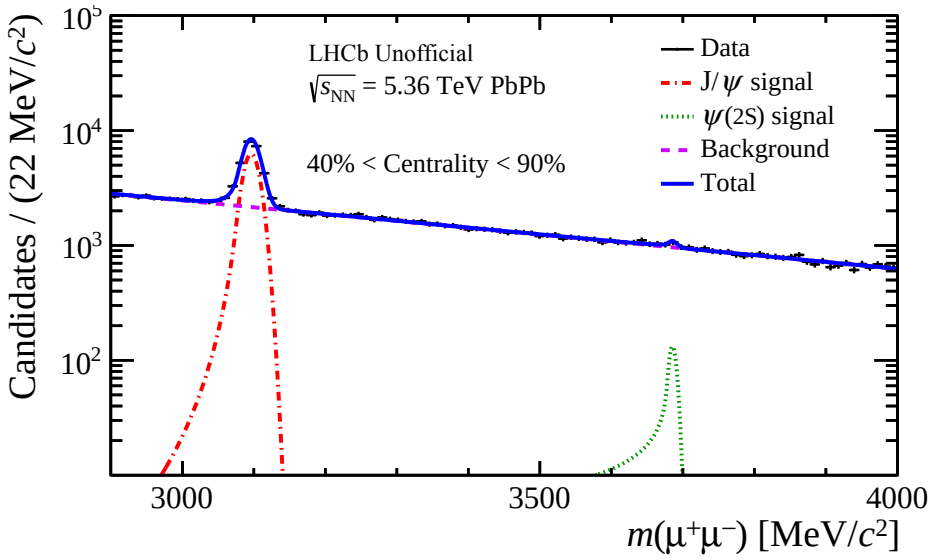


FIGURE 4.4: Dimuon invariant mass distribution for the full dataset after all selection criteria are applied, overlaid with the fit result.

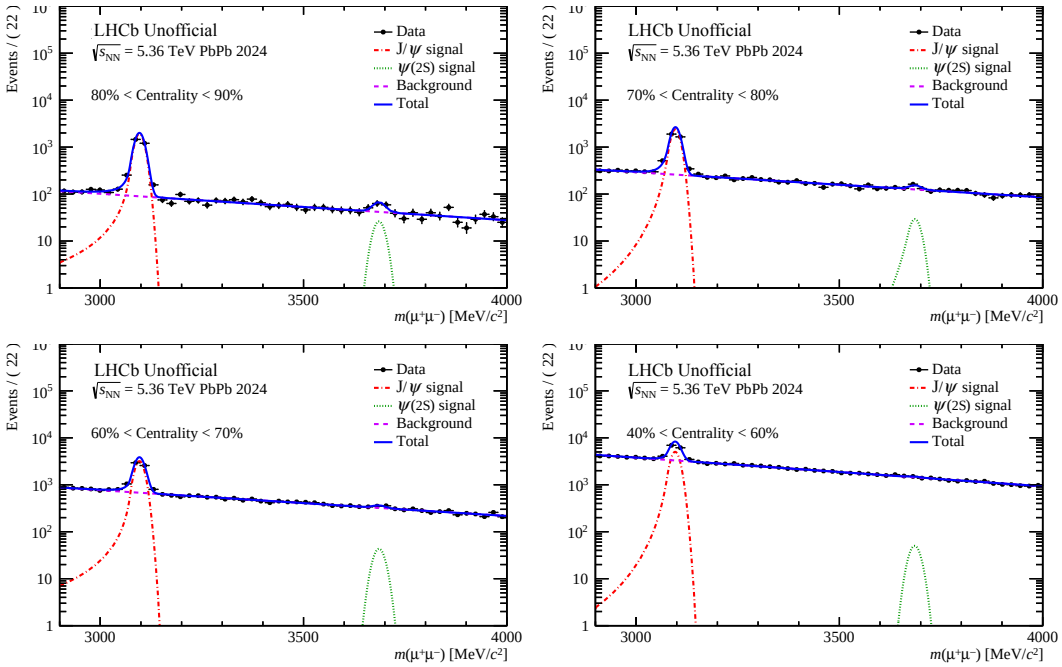


FIGURE 4.5: Dimuon invariant mass distributions in each centrality interval after selection, overlaid with fit results.

The fit successfully describes the J/ψ signal peak, which is clearly visible above the background in all centrality intervals. The $\psi(2S)$ resonance is less pronounced and still partially hidden under the combinatorial background, as expected given its smaller production cross-section and branching fraction to dimuons. It is expected that the retraining of the `ProbNN`μ variable on PbPb collision samples will significantly

improve the muon selection purity and therefore the signal to background ratio in the $\psi(2S)$ fits.

4.6 Efficiencies determination

The raw signal yields of the two charmonium states must be corrected for detector acceptance and efficiency effects. Following Eq. 3.8, the total efficiency ε_{tot} accounts for the geometrical acceptance of the detector, the reconstruction and selection performance, the muon identification, and the trigger response. Compared to the previous analysis, the truth matching efficiency is not explicitly considered here, since it cancels in the $\psi(2S)/J/\psi$ ratio. As in the Run 2 analysis instead, each efficiency component is determined using simulated samples (see Sec. 4.2.2), with data-driven corrections applied to improve the agreement with real data (see Sec. 4.6.1). The only exception is the muon identification efficiency, which is determined by simulation but with data-driven correction factors estimated with the Tag&Probe technique, as described in Sec. 4.6.4.

Efficiencies are evaluated as a function of the variable `eCalTot`, used as a proxy for event centrality (see Sec. 4.4), and are also computed in bins of p_{T} and y to enable further comparison and cross-checks with the Run 2 results. For each component, the absolute efficiencies for the J/ψ and $\psi(2S)$ states, as well as their ratios, are presented through dedicated figures and summary tables. Finally, Sec. 4.6.6 reports the combined total efficiency used in the computation of the cross-section ratio.

4.6.1 MC reweighting

As discussed in Sec. 3.6.2, the simulated samples used to determine the detector efficiencies need to be corrected to better reproduce the distributions observed in data, particularly for key kinematic and event-level quantities. This is achieved through a reweighting procedure that aligns the simulation with real data.

The process starts by statistically separating signal and background contributions in data using the sPlot technique. Reweighting factors are then computed for selected observables by taking the ratio of background-subtracted data to simulation histograms, bin by bin. In this analysis, the weights are derived as functions of p_{T}, y, and event multiplicity, represented by the number of SciFi clusters `nFTClusters`. Compared to the Run 2 analysis, a correction in rapidity has been introduced, since this variable showed larger discrepancies between data and simulation.

Due to the limited statistics available for the $\psi(2S)$ sample, the weights are extracted from the J/ψ sample only and applied to both resonances. This choice is justified by dedicated studies performed in Run 2, where no significant bias was observed when applying the same correction to both charmonium states.

The outcome of the reweighting is illustrated in Fig. 4.6, where the original MC distributions, background-subtracted data, and reweighted MC are compared for the relevant variables. A clear improvement in the data–MC agreement is visible after applying the reweighting procedure. All efficiencies presented in the following sections are computed using these reweighted simulation samples.

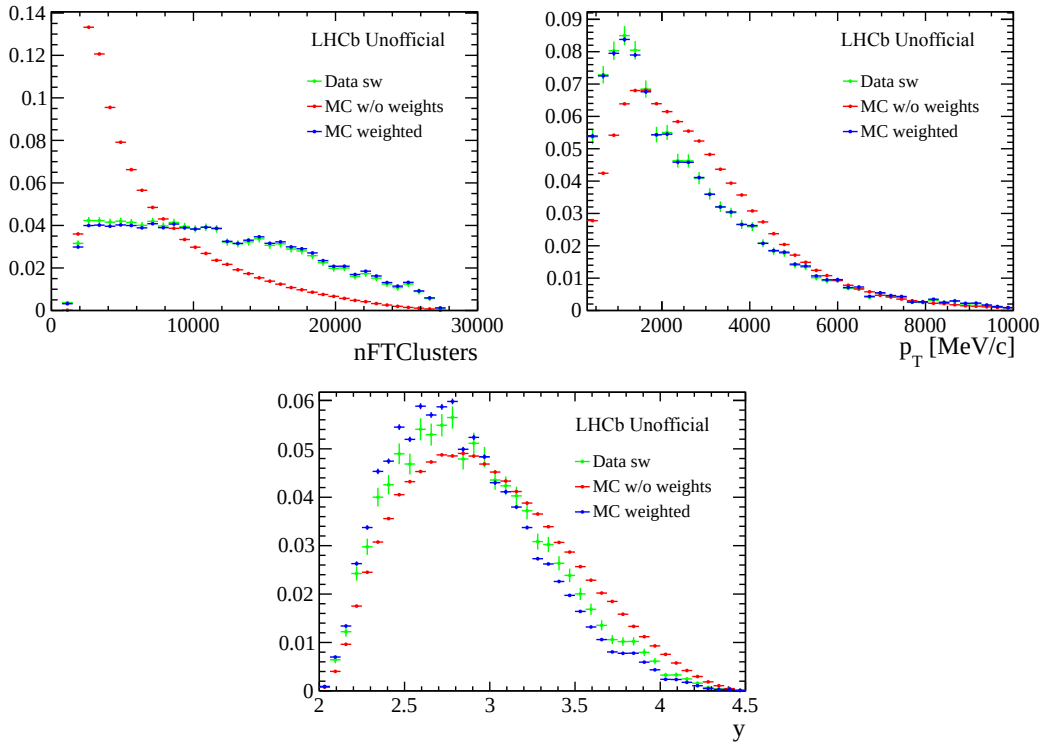


FIGURE 4.6: Comparison of `nFTClusters` (top left), p_{T} (top right), and y (bottom) distributions in background-subtracted data (sWeights), original MC, and reweighted MC for J/ψ. The reweighting significantly improves the agreement between simulation and data.

4.6.2 Acceptance efficiency

The geometrical acceptance of the detector is the first component contributing to the total efficiency. It corresponds to the definition provided in Eq. 3.10, where this efficiency is expressed as the ratio between the number of geometrically accepted decays and the total number of generated J/ψ or $\psi(2S)$ mesons within the fiducial region.

To evaluate this quantity, a generator-level simulation is employed, without imposing any acceptance requirement. Since the purely geometrical trajectories of the decay muons do not depend on the colliding beam species nor on the event multiplicity, the samples are generated in pp collisions. The acceptance efficiency is then evaluated differentially in p_{T} and y, as illustrated in Fig. 4.7 and summarised in Tabs. 4.7 and 4.8.

These distributions are subsequently integrated to obtain a single value used in the centrality-dependent efficiency computation. The resulting integrated acceptance efficiencies are:

$$\varepsilon_{\text{acc}}(J/\psi) = (83.7 \pm 0.1)\%, \qquad \varepsilon_{\text{acc}}(\psi(2S)) = (82.8 \pm 0.1)\%,$$

where the uncertainties are statistical.

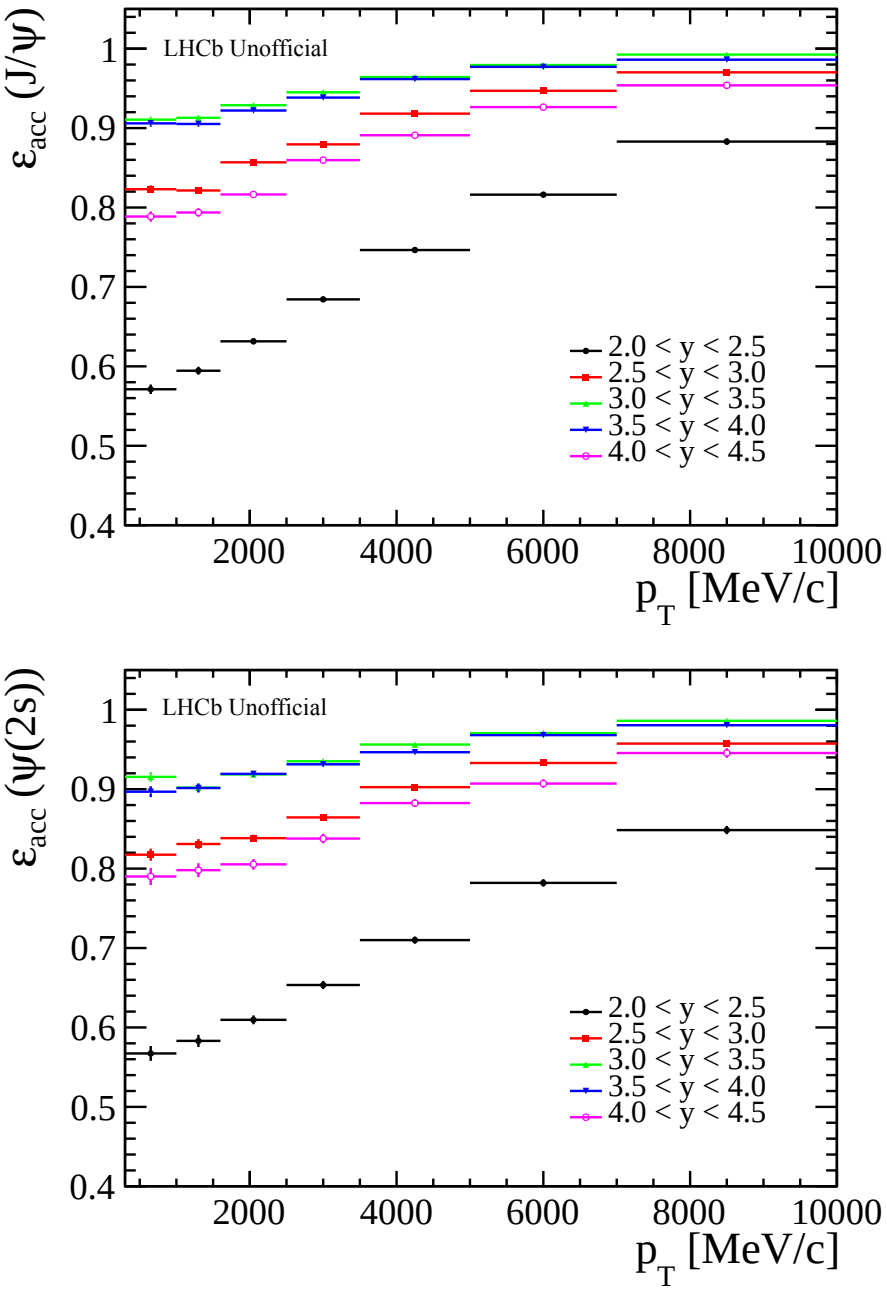


FIGURE 4.7: Geometrical acceptance ε_{acc} calculated using generator-level pp events as a function of p_{T} in bins of y, for J/ψ (top) and $\psi(2S)$ (bottom).

TABLE 4.7: Geometrical acceptance for J/ψ and $\psi(2S)$ as a function of p_{T}.

	p_{T} [GeV/c]						
	0.3−1.0	1.0−1.6	1.6−2.5	2.5−3.5	3.5−5.0	5.0−7.0	7.0−10.0
$\varepsilon(J/\psi)$	76.4%	77.4%	80.2%	83.2%	87.1%	90.1%	94.3%
$\varepsilon(\psi(2S))$	75.9%	76.6%	78.2%	81.1%	84.9%	88.8%	92.3%

TABLE 4.8: Geometrical acceptance for J/ψ and $\psi(2S)$ as a function of y.

	y				
	2.0−2.5	2.5−3.0	3.0−3.5	3.5−4.0	4.0−4.5
$\varepsilon(J/\psi)$	70.9%	88.9%	94.7%	94.1%	85.4%
$\varepsilon(\psi(2S))$	70.6%	88.9%	94.5%	93.8%	85.3%

4.6.3 Reconstruction and selection efficiency

The reconstruction and selection efficiency quantifies the detector's capability to correctly reconstruct the muon tracks and the impact of the selection requirements applied to enhance the signal purity. It is evaluated according to the definition in Eq. 3.11, using the simulated samples described in Sec. 4.2.2, after applying the data-driven reweighting corrections discussed in Sec. 4.6.1.

The resulting efficiencies are shown as a function of `eCalTot`, p_{T}, and y in Fig. 4.8 for the J/ψ and in Fig. 4.9 for the $\psi(2S)$, while their ratio is presented in Fig. 4.10.

The overall behaviour of the individual efficiencies closely follows that observed in the 2018 analysis: it decreases for the most central (highest `eCalTot`) events and towards the edges of the rapidity range, while exhibiting the typical peak around 2–3 GeV in p_{T}, as previously discussed in Sec. 3.6.4.

The absolute values, reported in Table 4.9 as a function of centrality, are generally higher than those obtained in the previous analysis, reflecting the improved performance of the upgraded detector. The ratio between the two states, however, remains consistent with the Run 2 results, confirming the stability of the relative reconstruction and selection efficiencies.

TABLE 4.9: Reconstruction and selection efficiency for J/ψ, $\psi(2S)$, and their ratio, as a function of centrality. The uncertainty is statistical.

	Centrality			
	$40-60\%$	$60-70\%$	$70-80\%$	$80-90\%$
$\varepsilon(J/\psi)$	$(30.7 \pm 0.06)\%$	$(49.2 \pm 0.09)\%$	$(51.6 \pm 0.09)\%$	$(51.9 \pm 0.11)\%$
$\varepsilon(\psi(2S))$	$(38.0 \pm 0.07)\%$	$(61.6 \pm 0.09)\%$	$(64.4 \pm 0.09)\%$	$(64.4 \pm 0.11)\%$
$\mathcal{R}_{\varepsilon(\psi(2S))/\varepsilon(J/\psi)}$	1.238 ± 0.003	1.252 ± 0.003	1.246 ± 0.003	1.239 ± 0.004

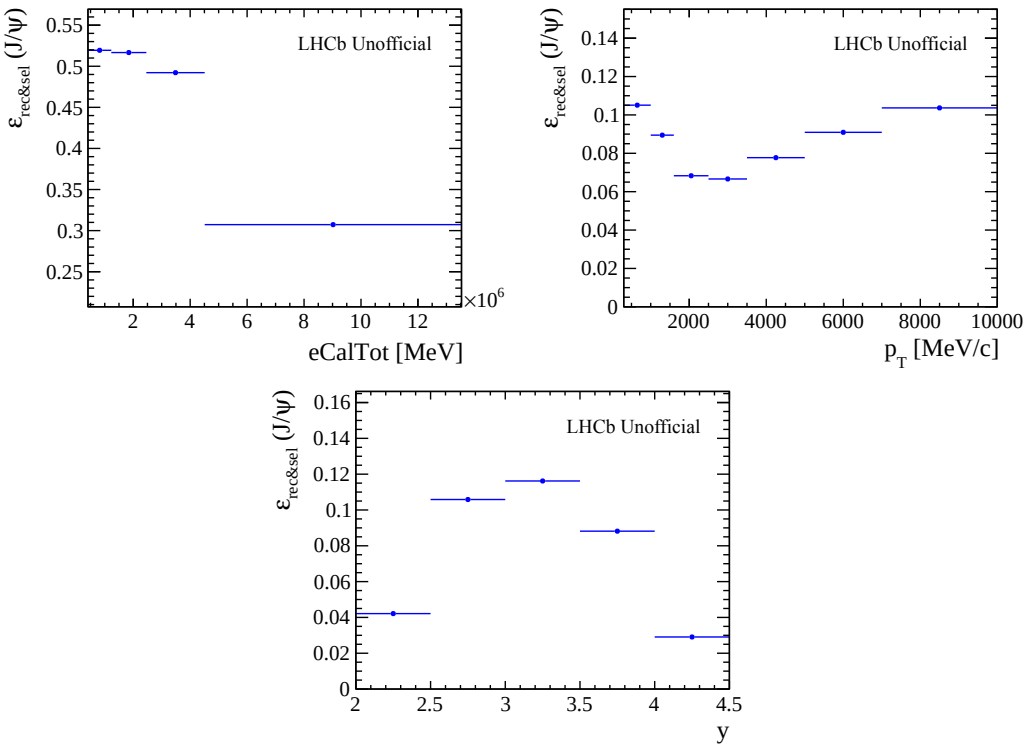


FIGURE 4.8: Reconstruction and selection efficiency $\varepsilon_{\text{rec\&sel}}$ as a function of `eCalTot` (top left), p_{T} (top right), and y (bottom) for the J/ψ.

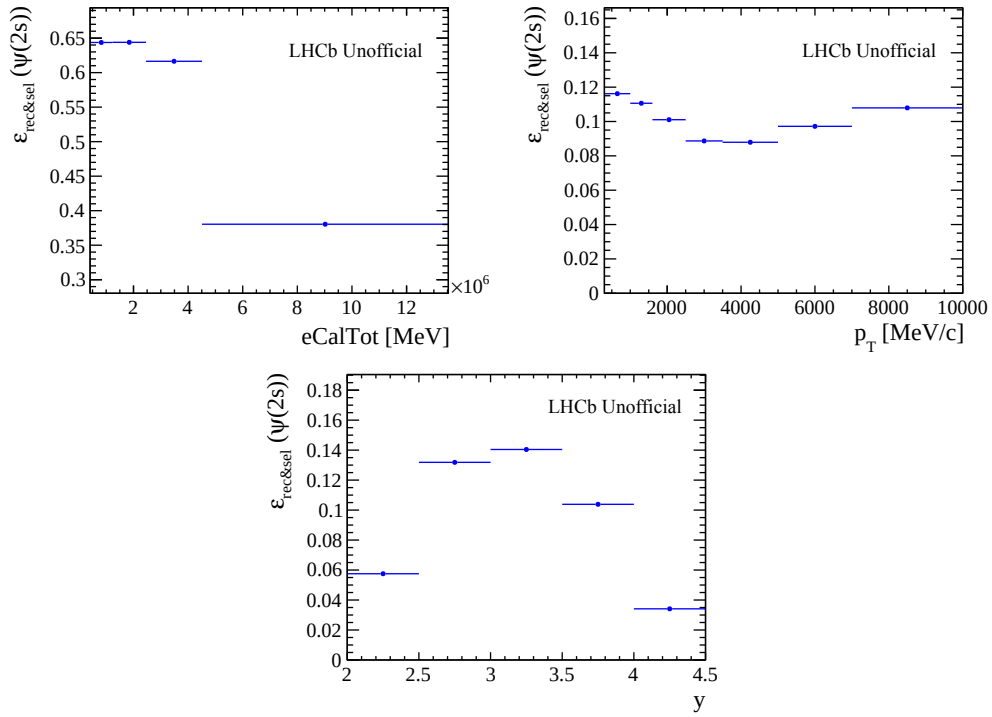


FIGURE 4.9: Reconstruction and selection efficiency $\varepsilon_{\text{rec\&sel}}$ as a function of `eCalTot` (top left), p_{T} (top right), and y (bottom) for the $\psi(2S)$.

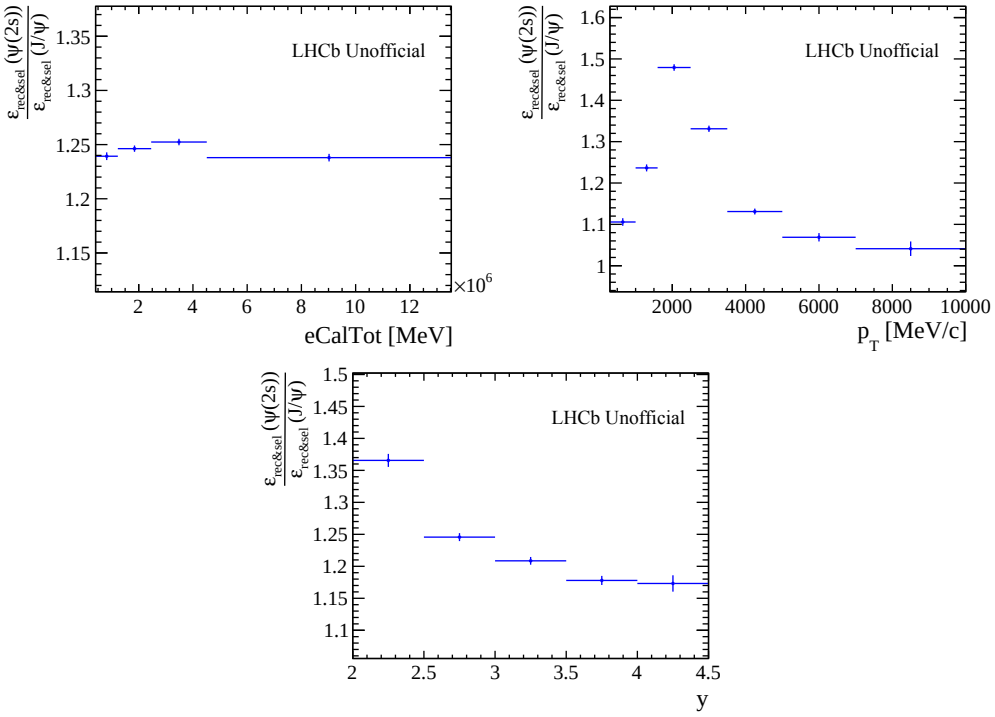


FIGURE 4.10: Ratio of the reconstruction and selection efficiencies $\varepsilon_{\text{rec\&sel}}\ (\psi(2S))/\varepsilon_{\text{rec\&sel}}\ (J/\psi)$ as a function of `eCalTot` (top left), p_{T} (top right), and y (bottom).

4.6.4 Muon identification efficiency

The ability of the particle identification system to correctly identify muon tracks represents one of the most crucial ingredients of this analysis. The efficiency is defined according to Eq. 3.12, but it cannot be directly estimated from simulation, since it is well known that the simulation does not accurately reproduce the response of the PID variables, in particular the PIDμ variable used in this work.

At present, no PIDCalib2 calibration tables are available for PbPb collisions. However, the sample collected in Run 3 is sufficiently large to allow for a dedicated data-driven estimation of the correction weights to be applied to the simulation through the Tag&Probe technique. The weights are defined as:

$$w^{\mu}_{PID} = \frac{N_{J/\psi}(\text{with one tag } \mu \text{ with PID}\mu > 5 \text{ and one probe } \mu \text{ with PID}\mu > 3)}{N_{J/\psi}(\text{with one tag } \mu \text{ with PID}\mu > 5 \text{ and one probe } \mu \text{ without PID applied})}. \tag{4.4}$$

The tight selection applied to the tag muon (PID$\mu > 5$) ensures a clean sample of genuine muons while retaining sufficient statistics, whereas the probe requirement (PID$\mu > 3$) corresponds to the working point used in the analysis, for which the efficiency needs to be determined.

The measurement is performed using the same data sample as the main analysis, applying identical trigger and offline selections, except for the invariant mass window, which is restricted to $3.0 < m_{\mu^+\mu^-} < 3.2$ GeV/c^2 to maximise the fraction of genuine J/ψ decays. The yields entering the numerator and denominator of Eq. 4.4 are extracted via unbinned maximum-likelihood fits to the dimuon invariant-mass distribution, using a Crystal Ball function to model the signal and an exponential for the background. Figure 4.11 shows the fit results for the numerator (left) and denominator (right) in the integrated sample, where the μ^+ is used as the tag muon; consistent results are obtained when swapping the roles of the two muons.

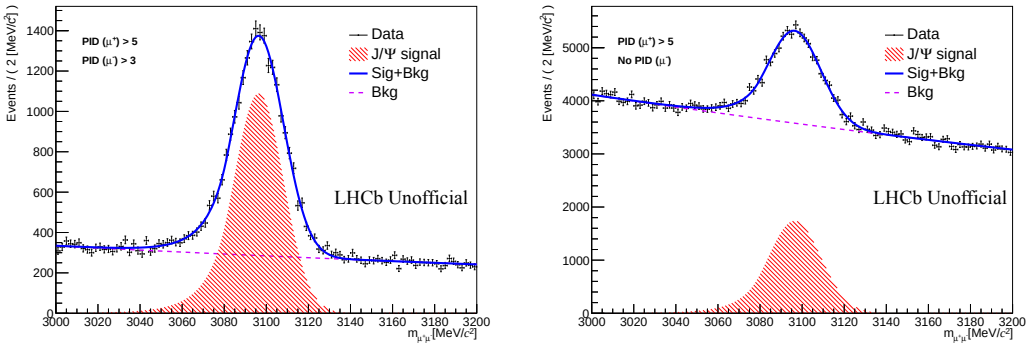


FIGURE 4.11: Dimuon invariant-mass distributions for the numerator (left) and denominator (right) of eq. 4.4, when considering the μ^+ as the tag muon. The fitted signal and background components are overlaid.

The Tag&Probe correction weights are evaluated both single-differentially (as a function of `nFTClusters`, p, p_{T}, and η) and double-differentially, combining pairs of these variables to produce two-dimensional PID efficiency maps, such as `nFTClusters`–p_{T}, `nFTClusters`–η, p–p_{T}, and p–η.

For the purpose of this analysis, the `nFTClusters`–p_{T} map is adopted, shown in Fig. 4.12 for the μ^+ (left) and the μ^- (right) used as probe muon. The invariant mass fits obtained in intervals of `nFTClusters` and p_{T} used to evaluates the tables are reported in App. B.2.

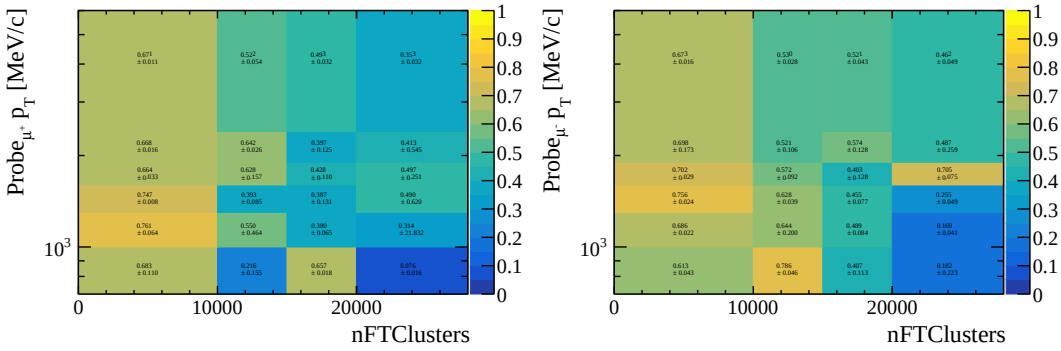


FIGURE 4.12: Muon identification correction weights maps as a function of `nFTClusters` and p_{T}, for the μ^+ (right) and μ^- (left) probe muons.

All other efficiency maps and one-dimensional results are computed in a similar way. Once the recalibration of the multivariate `ProbNN`μ variable on PbPb data is completed, analogous efficiency maps will also be derived for this variable.

Finally, by applying the correction weights obtained from the Tag&Probe tables to the simulated samples, the PID efficiencies are measured for both J/ψ and $\psi(2S)$ candidates. The resulting efficiencies are shown in Fig. 4.13 and Fig. 4.14, while their ratio is presented in Fig. 4.15. The corresponding values, reported as a function of centrality in Table 4.10, are consistent with those obtained in the Run 2 analysis.

TABLE 4.10: Particle identification efficiency for J/ψ, $\psi(2S)$, and their ratio, as a function of centrality. The uncertainty is statistical.

	Centrality			
	$40-60\%$	$60-70\%$	$70-80\%$	$80-90\%$
$\varepsilon(J/\psi)$	$(18.2 \pm 0.05)\%$	$(36.9 \pm 0.11)\%$	$(47.7 \pm 0.13)\%$	$(47.6 \pm 0.15)\%$
$\varepsilon(\psi(2S))$	$(19.1 \pm 0.05)\%$	$(36.0 \pm 0.10)\%$	$(46.3 \pm 0.12)\%$	$(46.3 \pm 0.15)\%$
$\mathcal{R}_{\varepsilon(\psi(2S))/\varepsilon(J/\psi)}$	1.046 ± 0.005	0.976 ± 0.004	0.971 ± 0.004	0.973 ± 0.004

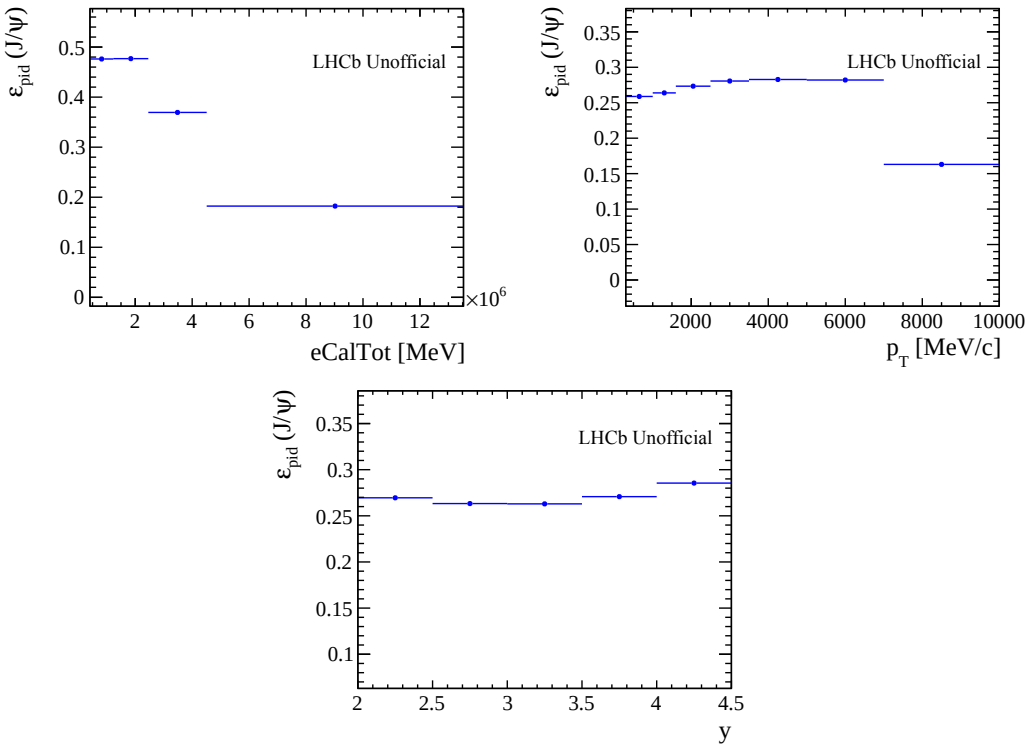


FIGURE 4.13: Particle identification efficiency $\varepsilon_{\text{MuonID}}$ as a function of `eCalTot` (top left), p_{T} (top right) and y (bottom right) for J/ψ.

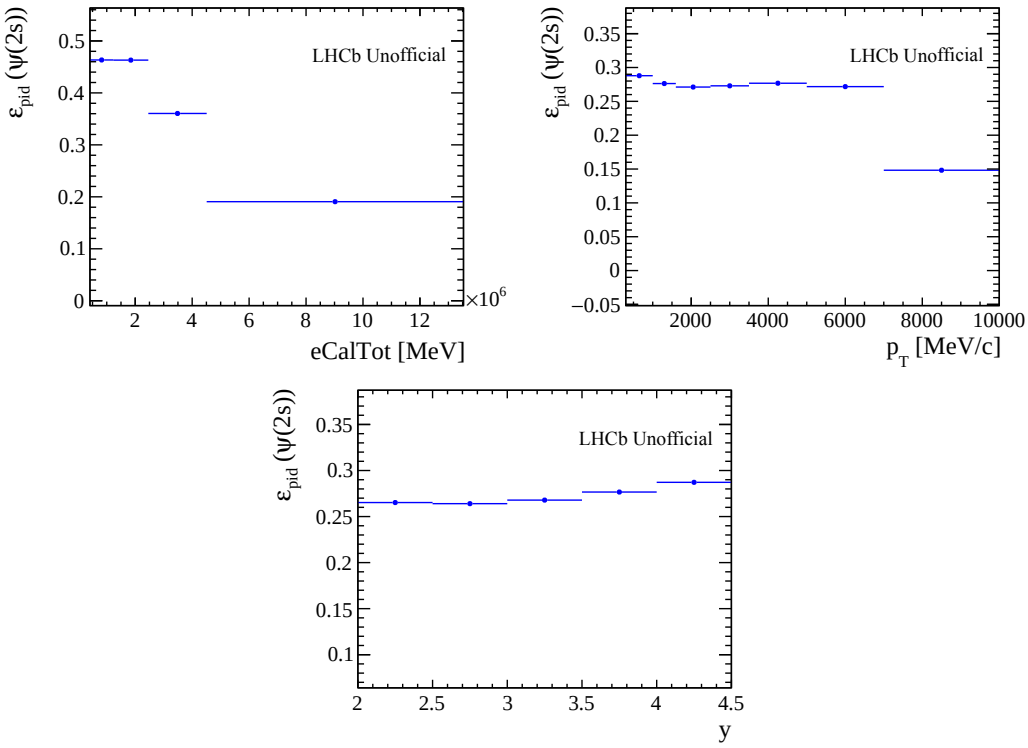


FIGURE 4.14: Particle identification efficiency $\varepsilon_{\text{MuonID}}$ as a function of `eCalTot` (top left), p_{T} (top right) and y (bottom right) for $\psi(2S)$.

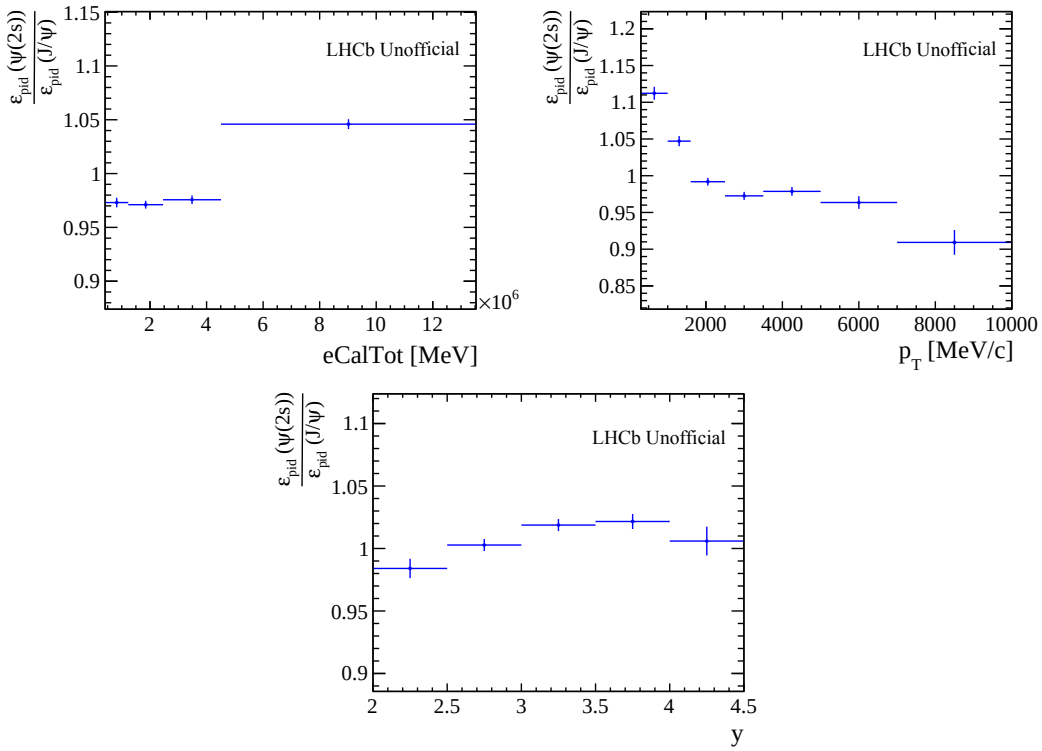


FIGURE 4.15: Particle identification efficiency $\varepsilon_{\text{MuonID}}$ ratio of $\psi(2S)$ over J/ψ as a function of `eCalTot` (top left), p_{T} (top right) and y (bottom right).

4.6.5 Trigger efficiency

The trigger efficiency quantifies the fraction of events that satisfy the trigger requirements with respect to all reconstructed and selected signal candidates, as defined in Eq. 3.15. In this analysis, it is evaluated using the simulated samples described in Sec. 4.2.2.

In the Run 3 configuration, a single HLT1 line is employed to select hadronic PbPb events, requiring at least one reconstructed primary vertex and a minimum energy deposit in the ECAL (see Sec. 4.2.1.1). When applying the full analysis selection, including both global event and offline criteria, all simulated events that satisfy these requirements are found to trigger the same HLT1 line. As a consequence, the trigger efficiency computed according to Eq. 3.15 results in a constant value of unity across all variables considered (`eCalTot`, p_{T}, and y), indicating that no additional inefficiency is introduced by the trigger selection.

For completeness, a cross-check will be performed using the TIS–TOS method, which was employed as a systematic study in the Run 2 analysis explained in Sec. 3.7.3.4. This comparison will allow to verify whether any residual inefficiency or bias exists in the current configuration; if significant differences are observed, their impact will be incorporated as a systematic uncertainty in the final results.

4.6.6 Total efficiency

The total efficiency, ε_{tot}, entering the ratio definition in Eq. 3.1, is obtained as the product of all the individual components discussed in the previous sections. It therefore represents the overall probability for a signal candidate produced in the detector acceptance to be reconstructed, selected, identified, and triggered under the analysis conditions.

The resulting values are shown in Fig. 4.16 for the J/ψ and in Fig. 4.17 for the $\psi(2S)$. The behaviour of the single state efficiency observed is consistent with expectations: a mild decrease towards higher multiplicity (more central events), reflecting the effect of detector occupancy on reconstruction and selection performance. The total efficiencies as a function of centrality are reported in Tab. 4.11 for both J/ψ and $\psi(2S)$, together with their ratio which is presented in Fig. 4.18. The ratio of total efficiencies between the two states is in good agreement with the results obtained in the Run 2 analysis, confirming the stability of the efficiency determination between the two datasets.

TABLE 4.11: Total efficiency for J/ψ, $\psi(2S)$ and their ratio as a function of centrality. The uncertainty is statistical.

	Centrality			
	$40-60\%$	$60-70\%$	$70-80\%$	$80-90\%$
$\varepsilon(J/\psi)$	$(10.4 \pm 0.05)\%$	$(17.2 \pm 0.06)\%$	$(19.6 \pm 0.07)\%$	$(17.7 \pm 0.11)\%$
$\varepsilon(\psi(2S))$	$(14.4 \pm 0.07)\%$	$(22.4 \pm 0.09)\%$	$(24.9 \pm 0.10)\%$	$(22.2 \pm 0.17)\%$
$\mathcal{R}_{\varepsilon(\psi(2S))/\varepsilon(J/\psi)}$	1.384 ± 0.009	1.297 ± 0.007	1.272 ± 0.007	1.256 ± 0.013

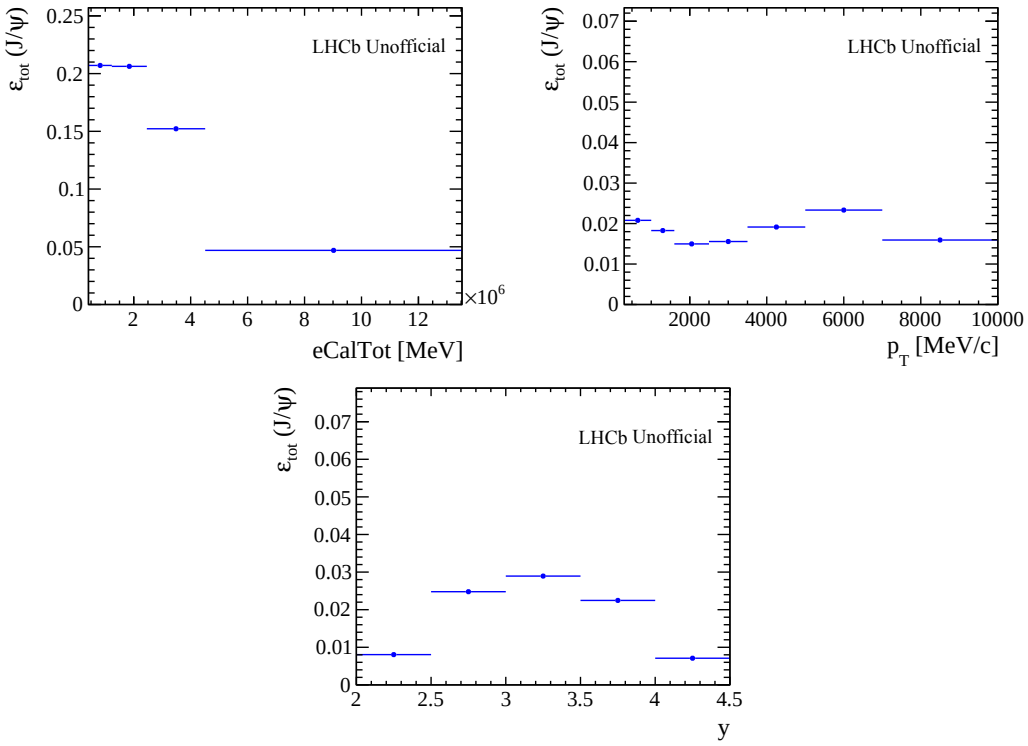


FIGURE 4.16: Total efficiency ε_{tot} as a function of `eCalTot` (top left), p_{T} (top right) and y (bottom) for J/ψ.

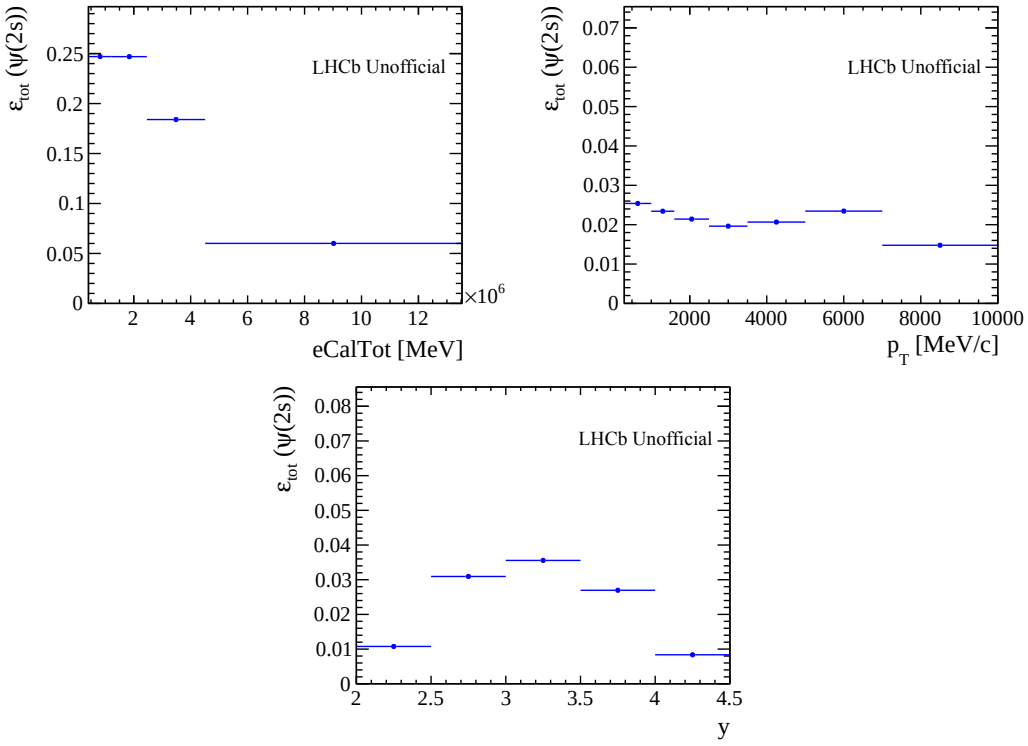


FIGURE 4.17: Total efficiency ε_{tot} as a function of `eCalTot` (top left), p_{T} (top right) and y (bottom) for $\psi(2S)$.

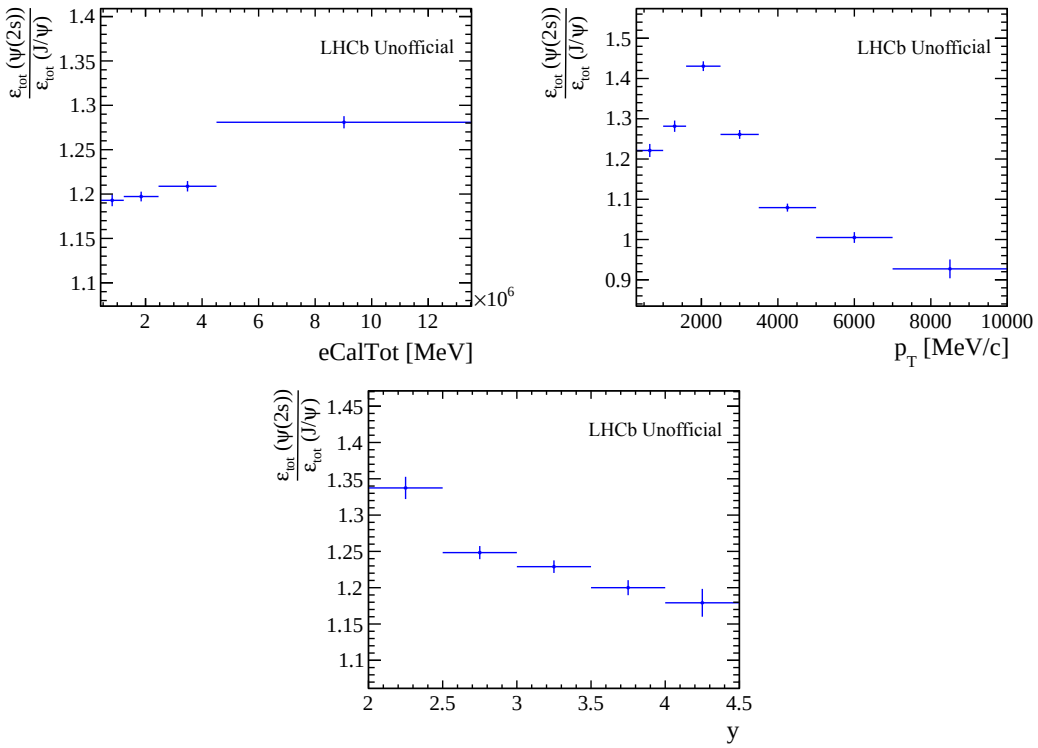


FIGURE 4.18: Total efficiency ε_{trg} ratio of $\psi(2S)$ over J/ψ as a function of `eCalTot` (top left), p_{T} (top right) and y (bottom).

4.7 Preliminary Results

The preliminary results of the measurement of the $\psi(2S)/J/\psi$ cross-section ratio in PbPb collisions at $\sqrt{s_{\text{NN}}} = 5.36$ TeV are presented in this section. The ratio is computed using Eq. 3.1, with the signal yields obtained from the fits described in Sec. 4.5 and the efficiency corrections discussed in Sec. 4.6.

At this stage of the analysis, only statistical uncertainties are included. The evaluation of systematic uncertainties is still ongoing; however, a similar strategy to the one adopted in the Run 2 analysis (see Sec. 3.7) will be followed. The following sources of systematic uncertainty will be considered in the forthcoming evaluation:

- **Signal and background modelling:** the stability of the extracted yields will be tested by varying the signal model (using a Crystal Ball plus Gaussian combination) and by replacing the exponential background with a Chebychev polynomial. In addition, the background description will be cross-checked using same-sign dimuon combinations.

- **Simulation sample size:** the limited statistics of the simulated samples will be propagated as a relative uncertainty on the total efficiencies.

- **MC reweighting:** the impact of the reweighting procedure will be evaluated by fluctuating the weight histograms within their statistical uncertainties and by testing alternative reweighting schemes.
- **MuonID efficiency:** systematic effects will be assessed by varying the binning scheme of the Tag&Probe efficiency tables and by using an alternative configuration in the (`nFTClusters`, η) plane instead of (`nFTClusters`, p_{T}).
- **Trigger efficiency:** the simulation-based trigger efficiency will be cross-checked with the data-driven TIS–TOS method to estimate possible discrepancies.

A full quantification of these effects is ongoing, and the resulting systematic uncertainties will be included in the final version of the measurement, however, based on the Run 2 results, the total systematic contribution is expected to remain at the level of a few percent, and therefore subdominant with respect to the current statistical uncertainty.

The integrated result over the accessible centrality range is:

$$\frac{\sigma(\psi(2S))}{\sigma(J/\psi)} \cdot \frac{\mathcal{B}(\psi(2S) \to \mu^+\mu^-)}{\mathcal{B}(J/\psi \to \mu^+\mu^-)} = 0.012 \pm 0.006,$$

where the uncertainty is purely statistical.

The ratio is also extracted as a function of centrality, expressed through the average number of participating nucleons, $\langle N_{\mathrm{part}} \rangle$, and is shown in Figs. 4.19 and 4.20, with the corresponding numerical values reported in Tab. 4.12.

TABLE 4.12: Cross-section times branching fraction ratio between $\psi(2S)$ and J/ψ in intervals of centrality, along with the corresponding number of participating nucleons $\langle N_{\mathrm{part}} \rangle$. The uncertainty is purely statistical.

Centrality (%)	$\langle N_{\mathrm{part}} \rangle$	$\frac{\sigma(\psi(2S))}{\sigma(J/\psi)} \cdot \frac{\mathcal{B}(\psi(2S) \to \mu^+\mu^-)}{\mathcal{B}(J/\psi \to \mu^+\mu^-)}$
80–90	3.10–10.6	0.015 ± 0.004
70–80	10.6–19.7	0.015 ± 0.006
60–70	19.7–35.7	0.015 ± 0.006
40–60	35.7–99.1	0.011 ± 0.007

Figure 4.19 compares these results with the ALICE measurement [52] at forward rapidity and with our previous LHCb Run 2 result [126]. The new measurement at $\sqrt{s_{NN}} = 5.36$ TeV shows an overall behaviour compatible with the Run 2 result within uncertainties, while exhibiting a better agreement with the ALICE measurement in the region corresponding to the most central, high-multiplicity events.

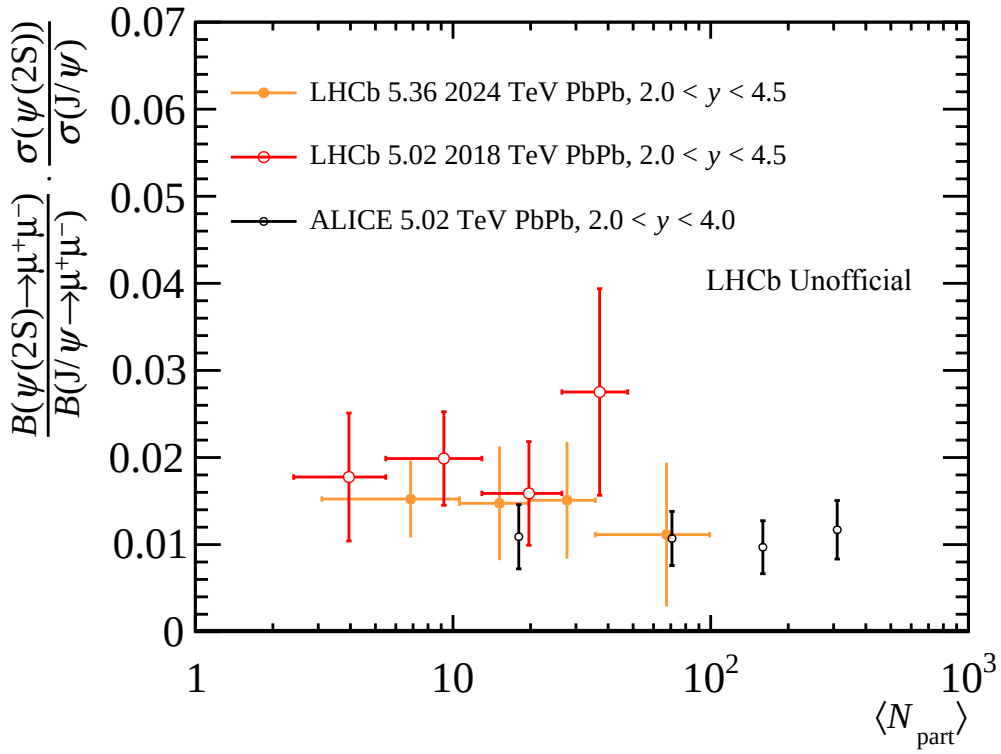


FIGURE 4.19: Cross-section times branching fraction ratio between $\psi(2S)$ and J/ψ as a function of $\langle N_{\text{part}} \rangle$ in the $p_{\text{T}} > 0.3$ GeV/c region, compared with ALICE [52] and LHCb [126] PbPb results. Vertical error bars represent the statistical uncertainties.

A comparison with theoretical models is presented in Fig. 4.20, using the same predictions considered in the Run 2 analysis: the SHMc [62, 42] and the TAMU transport model [41, 124]. Notably, in this case the most central bin shows a very good agreement with the theoretical expectations, improving over the tension observed in the previous measurement.

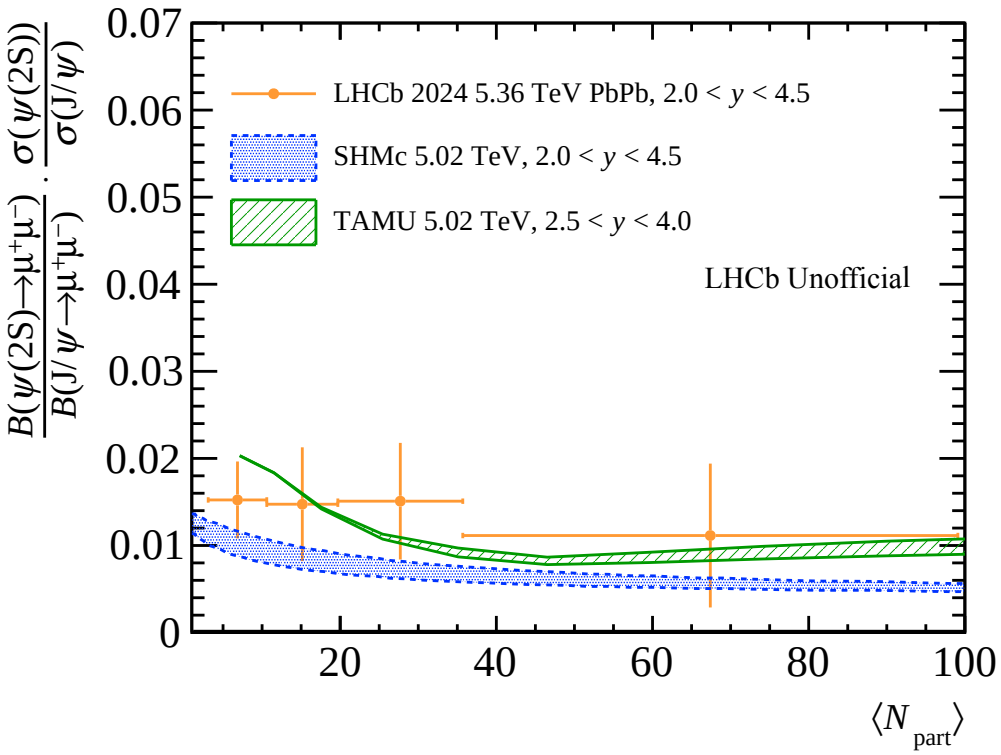


FIGURE 4.20: Cross-section times branching fraction ratio between $\psi(2S)$ and J/ψ as a function of $\langle N_{\text{part}} \rangle$ in the $p_{\text{T}} > 0.3$ GeV/c region, compared with the SHMc [62, 42] and TAMU [41, 124] model predictions. Coloured bands represent model uncertainties. Vertical error bars represent the statistical uncertainties.

Overall, the new measurement confirms the suppression pattern previously observed at $\sqrt{s_{\text{NN}}} = 5.02$ TeV, supporting the interpretation in terms of sequential melting and partial regeneration of charmonium states in the QGP.

The Run 3 results thus strengthen the picture established in Run 2, representing an important step toward a more precise characterisation of quarkonium suppression in the high-density QGP regime. This study constitutes a preliminary step toward a deeper understanding of these phenomena, which will be further investigated by combining this dataset with the PbPb samples to be collected in the 2025 and 2026 ion runs.

Conclusions

This thesis presents a detailed study of charmonium production in heavy-ion collisions with the LHCb detector, focusing on the measurement of the $\psi(2S)/J/\psi$ cross-section ratio in PbPb collisions at $\sqrt{s_{\rm NN}} = 5.02$ and 5.36 TeV. This observable serves as a sensitive probe of the Quark–Gluon Plasma, providing insight into colour screening, sequential quarkonium suppression, and the possible recombination of charm quarks within the deconfined medium created in nucleus–nucleus collisions.

The analysis based on the 2018 PbPb dataset, described in Chapter 3, constitutes the first measurement of the $\psi(2S)/J/\psi$ production ratio at forward rapidity. The results show a clear suppression of the $\psi(2S)$ state relative to the J/ψ, in line with the expected hierarchy of binding energies and consistent with the phenomenon of sequential melting in the QGP. No significant dependence on collision centrality is observed, with the suppression remaining approximately constant across the explored range. When compared to theoretical expectations, the TAMU transport model reproduces the data reasonably well, while the Statistical Hadronisation Model (SHMc) slightly underestimates the observed ratios. These findings highlight the sensitivity of the forward region probed by LHCb to QGP effects and provide an essential complement to midrapidity measurements from other LHC experiments.

The second part of this thesis, presented in Chapter 4, reports on the ongoing analysis of the PbPb dataset collected in 2024 at $\sqrt{s_{\rm NN}} = 5.36$ TeV, the first heavy-ion sample recorded with the fully upgraded LHCb detector in Run 3. Thanks to the improved tracking, trigger, and real-time analysis capabilities, the detector now offers higher efficiency and an extended reach in centrality. The preliminary results show a $\psi(2S)/J/\psi$ ratio consistent with the Run 2 measurement within uncertainties, while expanding the study into a new, more central bin. In this region, the agreement with theoretical models has improved significantly, strengthening the overall interpretation in terms of quarkonium suppression and partial regeneration in the QGP. This new measurement therefore represents an important step forward in mapping the behaviour of charmonium states across a broader centrality range.

In addition to the main heavy-ion analysis, Appendix C presents a complementary study performed during the initial phase of the PhD: the measurement of Λ polarisation in fixed-target pNe collisions at $\sqrt{s_{\rm NN}} = 68.4$ GeV. Published in a peer-reviewed journal, this work provides new input for the study of Transverse-Momentum-Dependent distributions and spin phenomena in the non-perturbative

regime of QCD. Although its physics objectives differ from those of the heavy-ion programme, this analysis illustrates the breadth of the LHCb experiment and the variety of topics explored during this doctoral research.

Together, these studies contribute to a broader understanding of QCD matter across different energy densities and collision systems, from the behaviour of hadrons in fixed-target interactions to the formation of a deconfined Quark–Gluon Plasma in heavy-ion collisions. The results presented in this thesis establish a solid foundation for future high-precision quarkonium measurements with the upgraded detector and represent a significant step toward a more complete characterisation of the QGP and its underlying dynamics. The forthcoming PbPb datasets from Runs 3 and 4, combined with advances in real-time reconstruction and particle identification, will allow for an increasingly detailed characterisation of quarkonium production mechanisms in the extreme conditions created at the LHC.

Appendix A

Run 2 Analysis

A.1 Simulation fit results

As explained in Sec. 3.5 some parameters of the data fit functions used in the analysis are fixed to the parameters of the simulation fit results, shown in Fig. A.1 for J/ψ and Fig. A.2 for $\psi(2S)$ in centrality intervals.

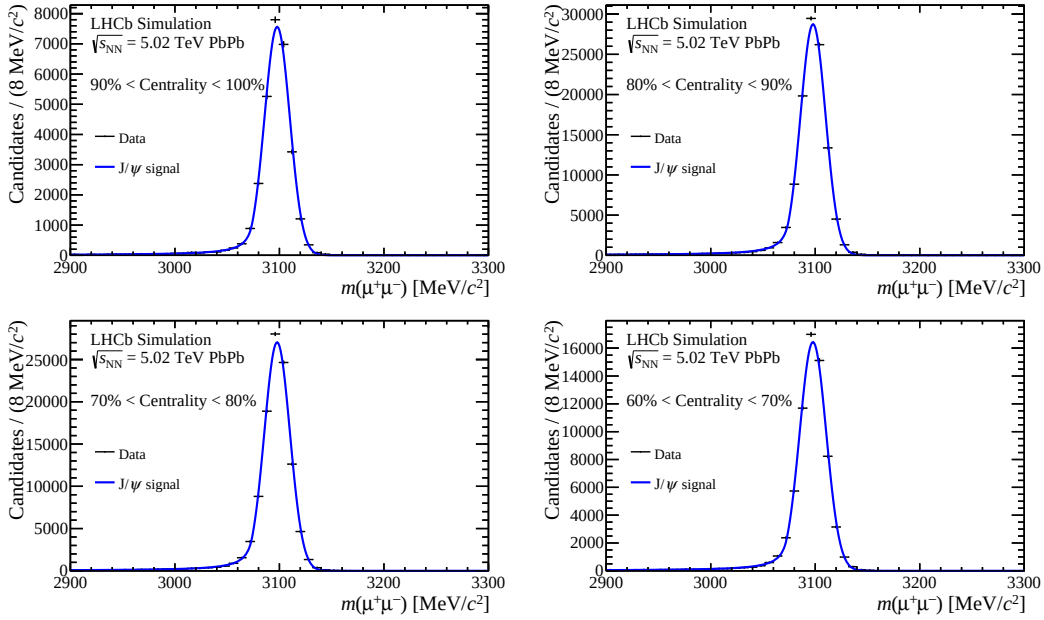


FIGURE A.1: Dimuon simulation invariant mass distributions in each centrality interval after selection for J/ψ, overlaid with fit results.

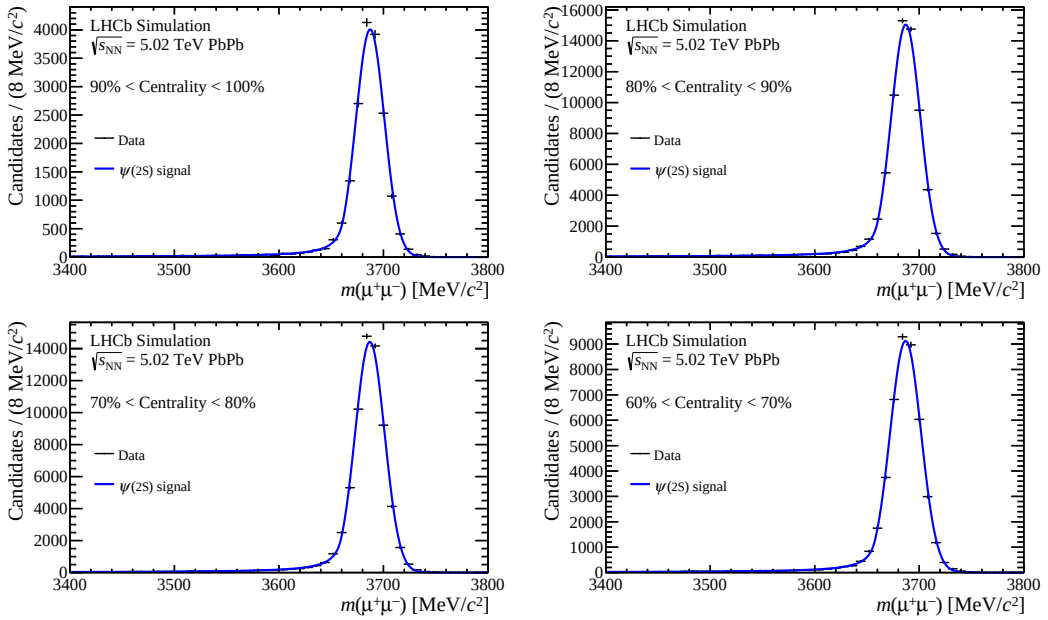


FIGURE A.2: Dimuon simulation invariant mass distributions in each centrality interval after selection for $\psi(2S)$, overlaid with fit results.

A.2 Charmonium–Muon p_{T} Correlation

The plots in Fig. A.3 show the correlation between the transverse momentum of the charmonium state (J/ψ on the left, $\psi(2S)$ on the right) and the corresponding μ^+ transverse momentum. A similar trend is observed for the μ^-. It is evident that the decay muons from the $\psi(2S)$ have, on average, a higher transverse momentum than those from the J/ψ, which has a direct impact on the PID efficiency, especially in high occupancy environments.

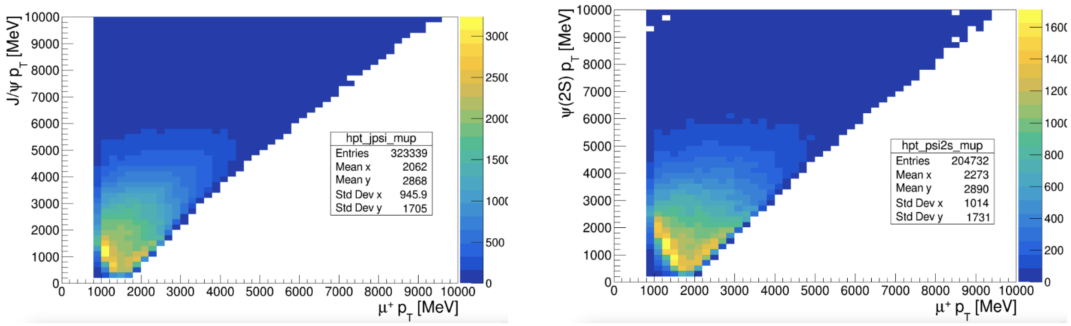


FIGURE A.3: Correlation between charmonium and μ^+ transverse momentum: (left) J/ψ and (right) $\psi(2S)$.

A.3 Tag&Probe PID Efficiency Cross-Check

As discussed in Sec. 3.6.5, the nominal measurement of the muon PID efficiency uses the `PidCalib2` package [120], based on a 2018 *pp* calibration sample. Since the PbPb data sample has a higher track multiplicity, an extrapolation procedure is applied to extend the *pp*-derived efficiency to the `nVeloClusters` range observed in PbPb collisions.

To validate this extrapolation method, given its non-standard nature, the results were cross-checked using a data-driven Tag&Probe technique applied directly to the PbPb signal sample. Due to the limited statistics of the PbPb dataset, the Tag&Probe method cannot be used to determine the PID efficiency in all bins used in the analysis. Nonetheless, it provides an important validation of the extrapolated result.

The `ProbNN`$\mu > 0.7$ PID selection was tested in two `nVeloClusters` intervals (1000–5000 and 5000–10000), using two different tag muon selections: `ProbNN`$\mu >$ 0.95 and `ProbNN`$\mu > 0.99$. The efficiency is computed as:

$$\varepsilon^{\mu}_{\text{PID}} = \frac{N(J/\psi \to \mu^{\text{tag}}\mu^{\text{probe}})\big|_{\text{tag: tight ID, probe: } \texttt{ProbNN}\boldsymbol{\mu} > \mathbf{0.7}}}{N(J/\psi \to \mu^{\text{tag}}\mu^{\text{probe}})\big|_{\text{tag: tight ID, probe: no PID applied}}} \tag{A.1}$$

The number of J/ψ candidates in the numerator and denominator is extracted via an invariant mass fit, using a Crystal Ball function for the signal and an exponential function for the background, consistent with the function used in the main analysis 3.5. Due to limited statistics, this fit is only performed for the J/ψ candidates. All standard selection criteria listed in Tab. 3.4 are applied, and a mass window of $3000 < m_{\mu^+\mu^-} < 3200$ MeV/c^2 is used. Figures A.4 and A.5 show the invariant mass distributions used to extract the yields in the numerator and denominator of Eq. A.1 for tag muon selections `ProbNN`$\mu > 0.95$ and `ProbNN`$\mu > 0.99$, respectively.

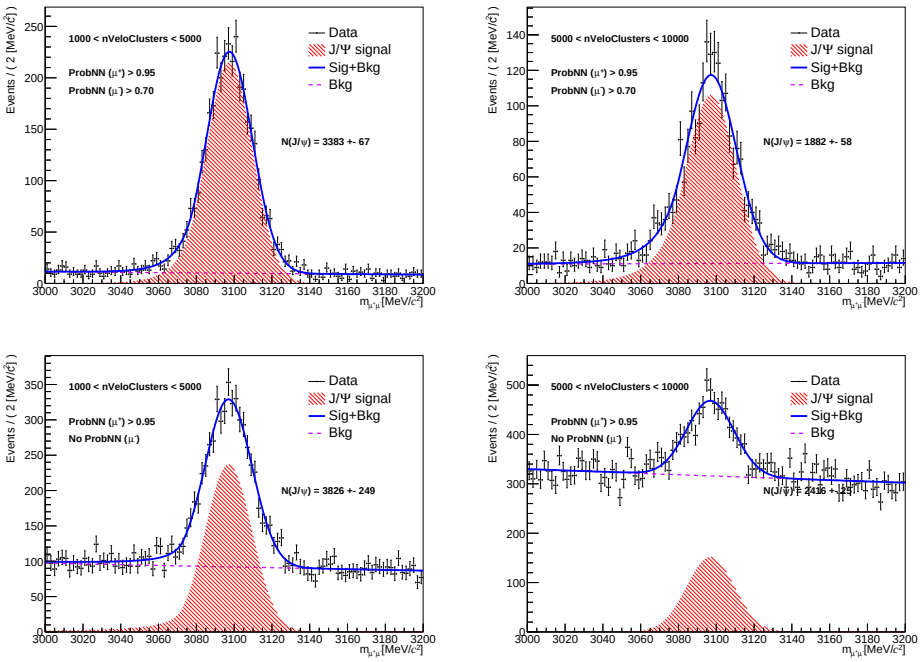


FIGURE A.4: J/ψ invariant mass distributions used in the Tag&Probe cross-check for $\texttt{ProbNN}\mu > 0.95$ tag selection. Top: numerator of Eq. A.1; bottom: denominator. Left: $1000 < \texttt{nVeloClusters} < 5000$; right: $5000 < \texttt{nVeloClusters} < 10000$.

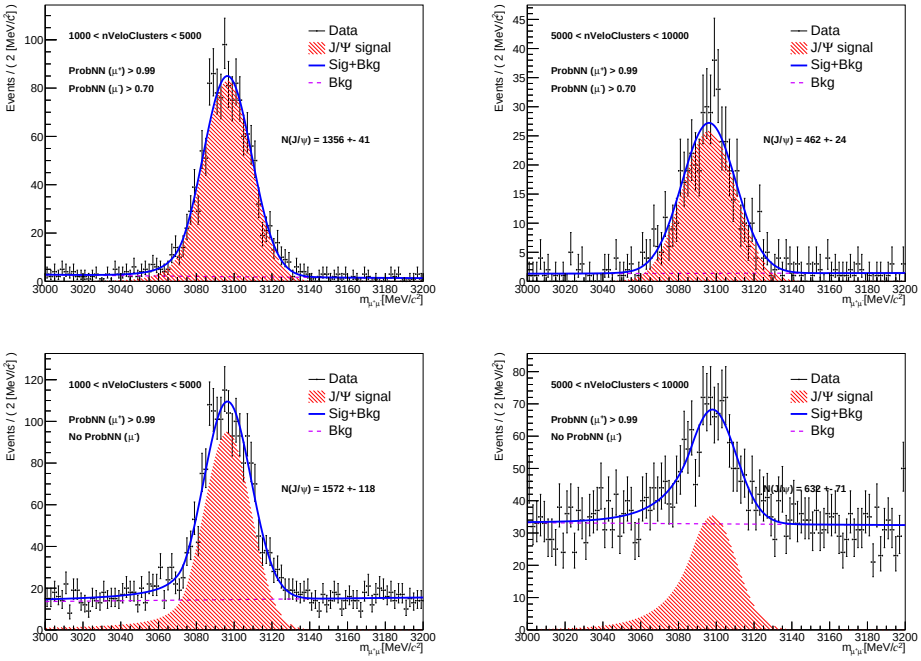


FIGURE A.5: J/ψ invariant mass distributions used in the Tag&Probe cross-check for $\texttt{ProbNN}\mu > 0.99$ tag selection. Top: numerator of Eq. A.1; bottom: denominator. Left: $1000 < \texttt{nVeloClusters} < 5000$; right: $5000 < \texttt{nVeloClusters} < 10000$.

A.4 Alternative signal fit model

As explained in Sec. 3.7.1.1, the leading contribution to the systematic uncertainty arising from the choice of the signal fit function is evaluated by replacing the Crystal Ball function used to model the J/ψ signal with a sum of a Crystal Ball and a Gaussian function. Due to the limited number of $\psi(2S)$ candidates, its model is left unchanged in order to avoid large statistical fluctuations. The fit results are shown below in Fig. A.6 in centrality intervals.

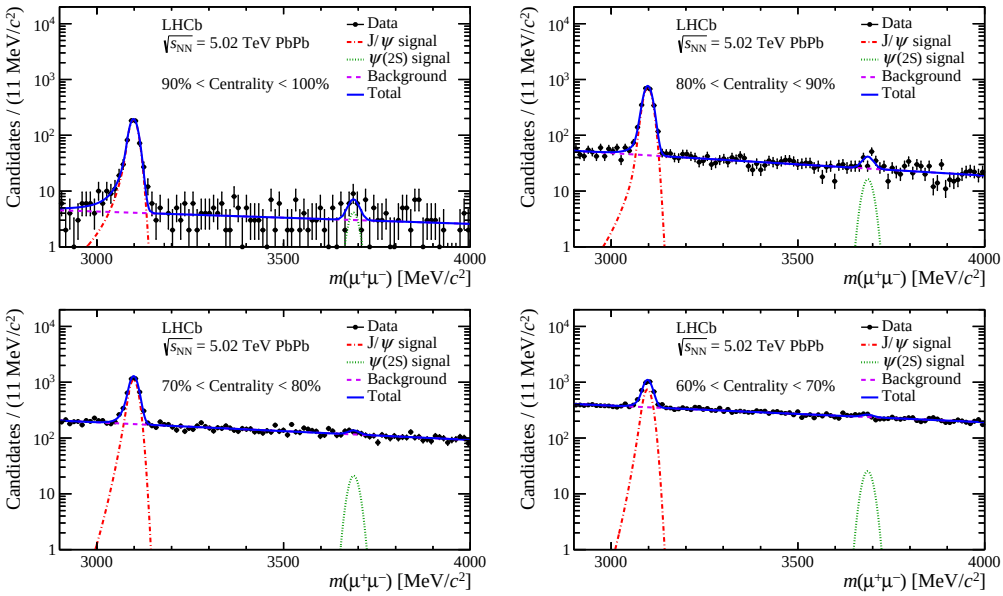


FIGURE A.6: Dimuon simulation invariant mass distributions in each centrality interval after selection with the alternative signal model function, overlaid with fit results.

A.5 Alternative background fit model

As explained in Sec. 3.7.1.2, the systematic uncertainty associated with the choice of the background model is evaluated by replacing the nominal exponential function with a second-order Chebyshev polynomial. While studying the impact of the background shape, the signal shape parameters are kept fixed. The fit results are shown below in Fig. A.7 in centrality intervals.

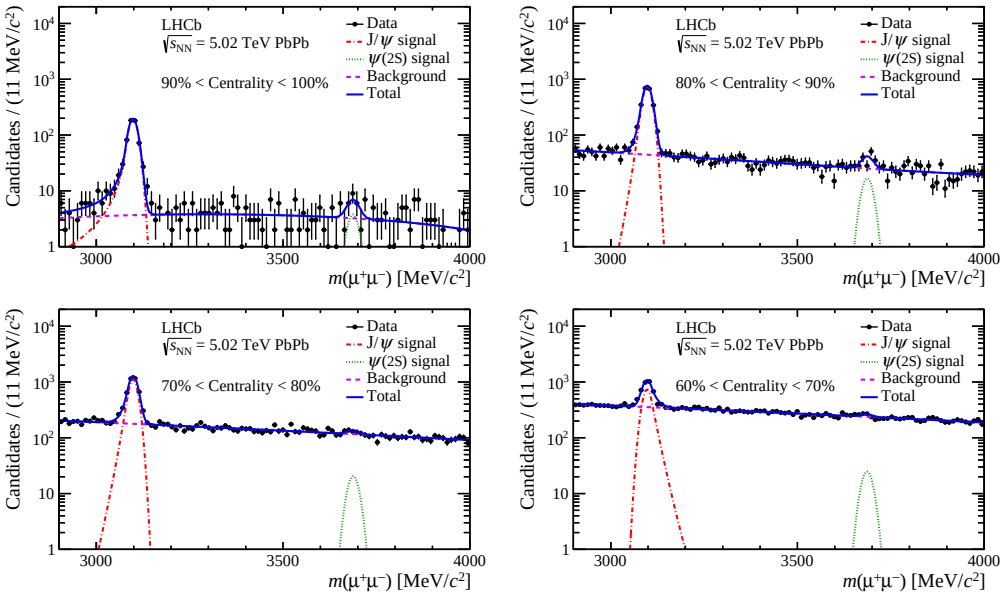


FIGURE A.7: Dimuon simulation invariant mass distributions in each centrality interval after selection with the alternative background model function, overlaid with fit results.

Appendix B

Run 3 Analysis

B.1 Simulation fit results

As explained in Sec. 4.5 some parameters of the data fit functions used in the analysis are fixed to the parameters of the simulation fit results, shown in Fig. B.1 for J/ψ and Fig. A.2 for $\psi(2S)$ in centrality intervals.

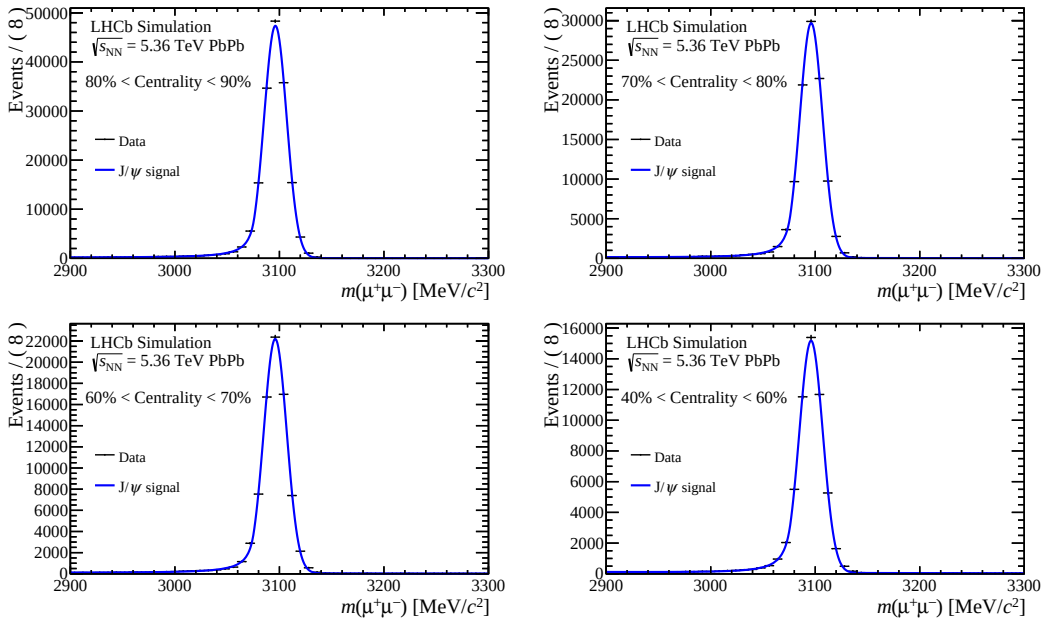


FIGURE B.1: Dimuon simulation invariant mass distributions in each centrality interval after selection for J/ψ, overlaid with fit results.

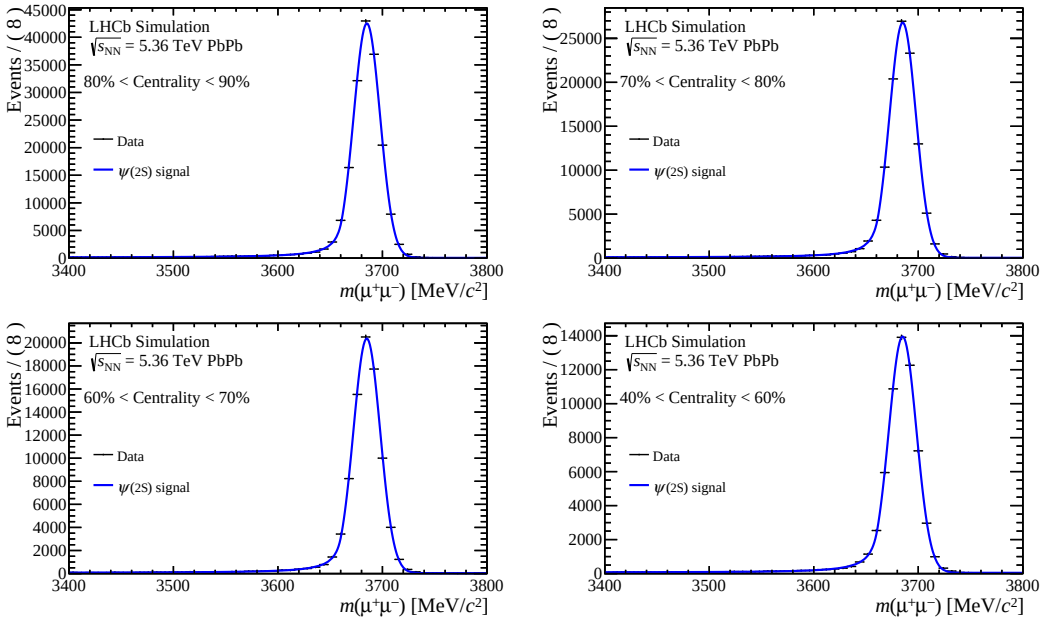


FIGURE B.2: Dimuon simulation invariant mass distributions in each centrality interval after selection for $\psi(2S)$, overlaid with fit results.

B.2 Fit results for the Muon Efficiency with Tag&Probe

As explained in Sec. 4.1 the MuonID efficiency measured through simulation sample needs to be corrected by data-driven correction factors, estimated through the Tag&Probe method. The following figures show the fit results for the numerator (left) and denominator (right) in intervals of `nFTClusters` and p_{T} used to produce the PID tables used in the analysis, shown in Fig. 4.11. In the plots shown the μ^+ is used as the probe muon; consistent results are obtained when swapping the roles of the two muons.

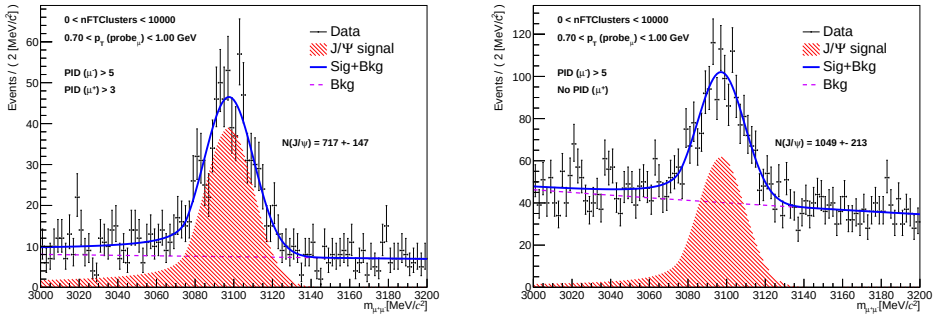


FIGURE B.3: Dimuon invariant-mass distributions for the numerator (left) and denominator (right) of eq. 4.4 for $0 <$ `nFTClusters` $< 10\,000$ and $0.7 < p_{\mathrm{T}} < 1.0$ GeV/c.

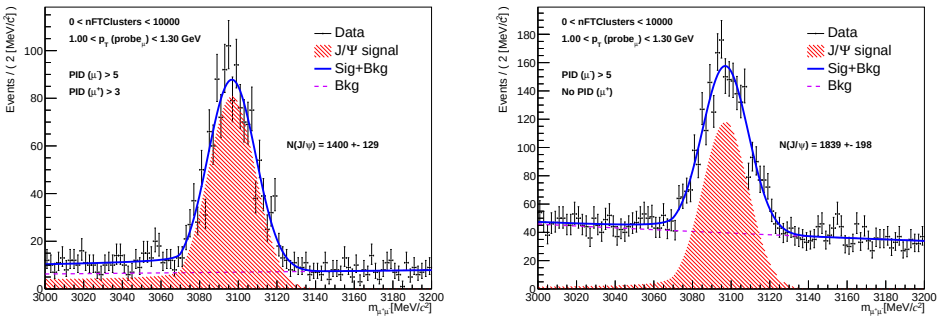


FIGURE B.4: Dimuon invariant-mass distributions for the numerator (left) and denominator (right) of eq. 4.4 for $0 <$ `nFTClusters` $< 10\,000$ and $1.0 < p_{\mathrm{T}} < 1.3$ GeV/c.

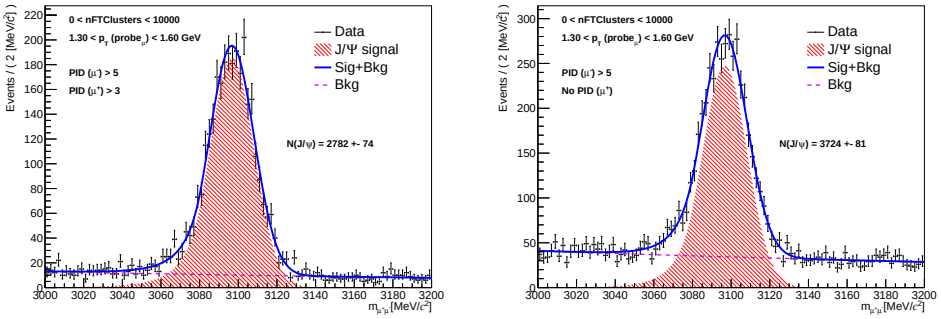


FIGURE B.5: Dimuon invariant-mass distributions for the numerator (left) and denominator (right) of eq. 4.4 for $0 <$ `nFTClusters` $< 10\,000$ and $1.3 < p_{\mathrm{T}} < 1.6$ GeV/c.

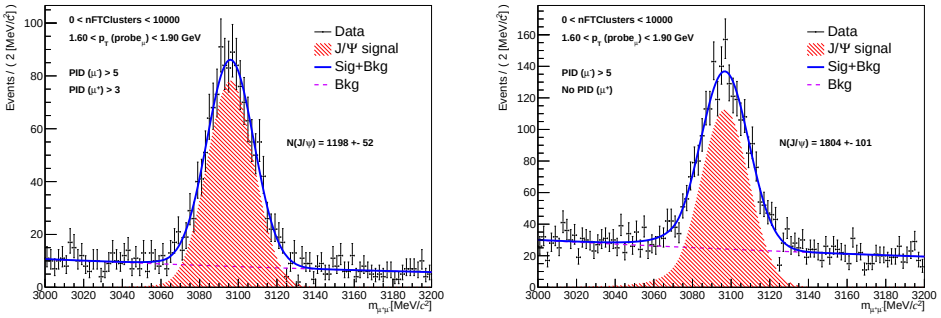


FIGURE B.6: Dimuon invariant-mass distributions for the numerator (left) and denominator (right) of eq. 4.4 for $0 <$ `nFTClusters` $< 10\,000$ and $1.6 < p_{\mathrm{T}} < 1.9$ GeV/c.

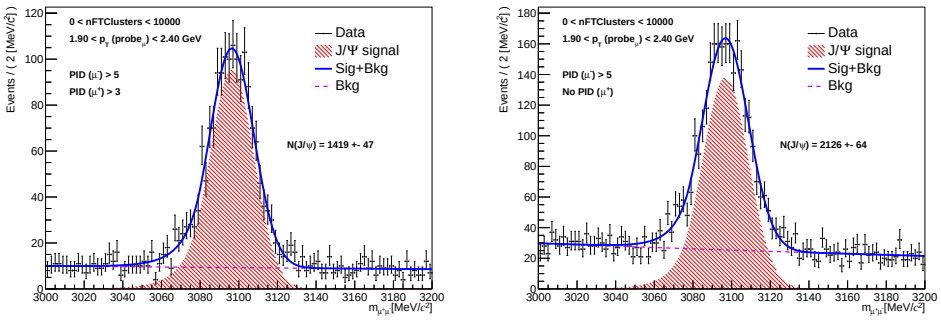


FIGURE B.7: Dimuon invariant-mass distributions for the numerator (left) and denominator (right) of eq. 4.4 for $0 <$ `nFTClusters` $< 10\,000$ and $1.9 < p_{\mathrm{T}} < 2.4$ GeV/c.

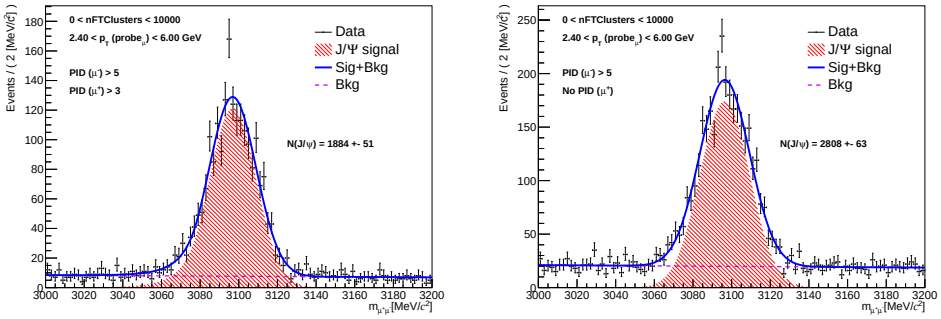


FIGURE B.8: Dimuon invariant-mass distributions for the numerator (left) and denominator (right) of eq. 4.4 for $0 <$ `nFTClusters` $< 10\,000$ and $2.4 < p_{\mathrm{T}} < 6.0$ GeV/c.

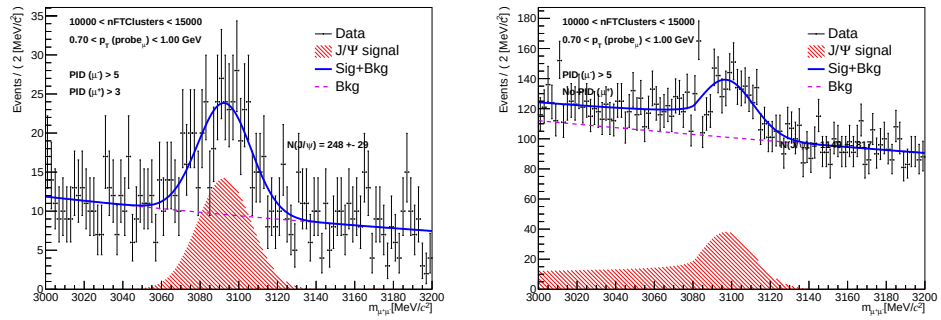


FIGURE B.9: Dimuon invariant-mass distributions for the numerator (left) and denominator (right) of eq. 4.4 for $10\,000 <$ `nFTClusters` $<$ $15\,000$ and $0.7 < p_{\mathrm{T}} < 1.0$ GeV/c.

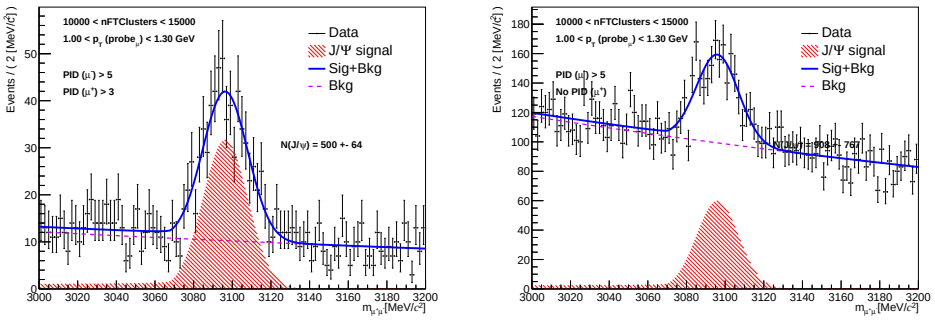


FIGURE B.10: Dimuon invariant-mass distributions for the numerator (left) and denominator (right) of eq. 4.4 for 10 000 $<$ `nFTClusters` $<$ 15 000 and 1.0 $< p_{\mathrm{T}} <$ 1.3 GeV/c.

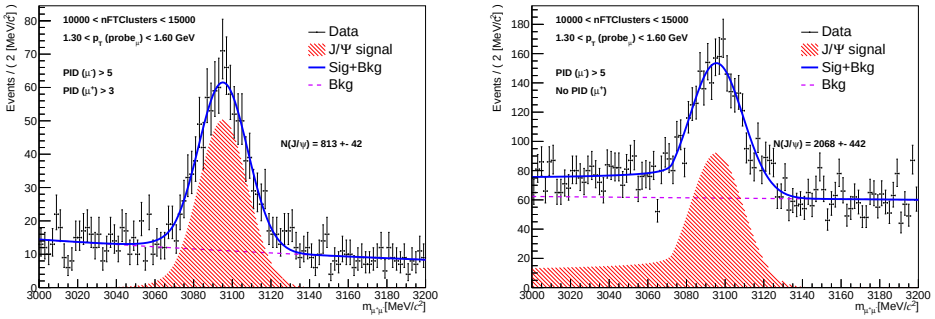


FIGURE B.11: Dimuon invariant-mass distributions for the numerator (left) and denominator (right) of eq. 4.4 for 10 000 $<$ `nFTClusters` $<$ 15 000 and 1.3 $< p_{\mathrm{T}} <$ 1.6 GeV/c.

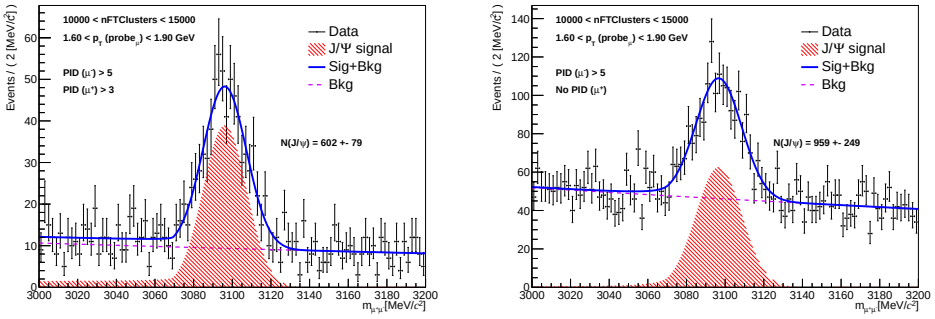


FIGURE B.12: Dimuon invariant-mass distributions for the numerator (left) and denominator (right) of eq. 4.4 for 10 000 $<$ `nFTClusters` $<$ 15 000 and 1.6 $< p_{\mathrm{T}} <$ 1.9 GeV/c.

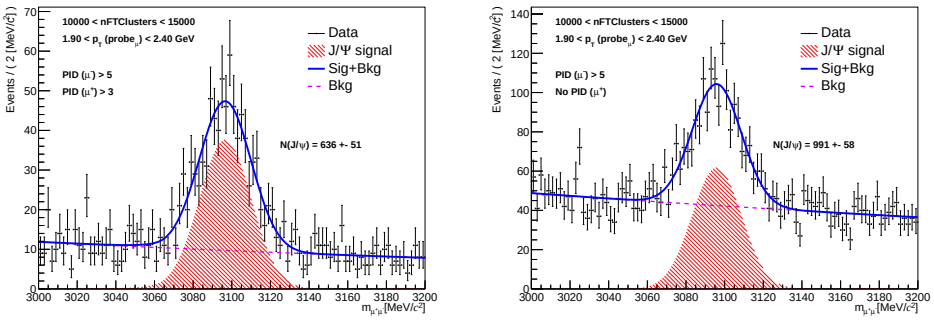


FIGURE B.13: Dimuon invariant-mass distributions for the numerator (left) and denominator (right) of eq. 4.4 for 10 000 $<$ `nFTClusters` $<$ 15 000 and 1.9 $< p_{\mathrm{T}} <$ 2.4 GeV/c.

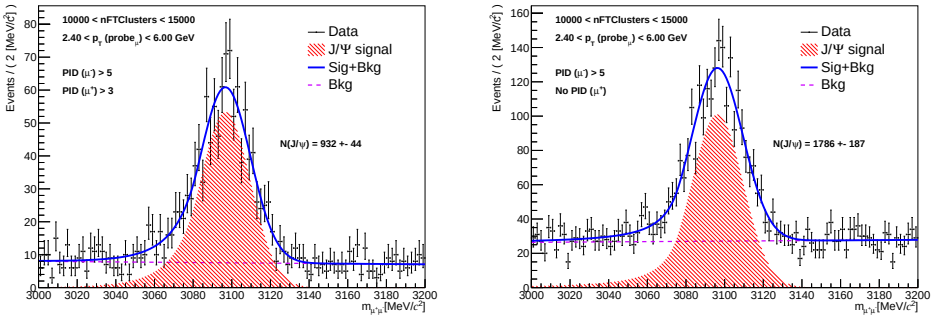


FIGURE B.14: Dimuon invariant-mass distributions for the numerator (left) and denominator (right) of eq. 4.4 for 10 000 $<$ `nFTClusters` $<$ 15 000 and 2.4 $< p_{\mathrm{T}} <$ 6.0 GeV/c.

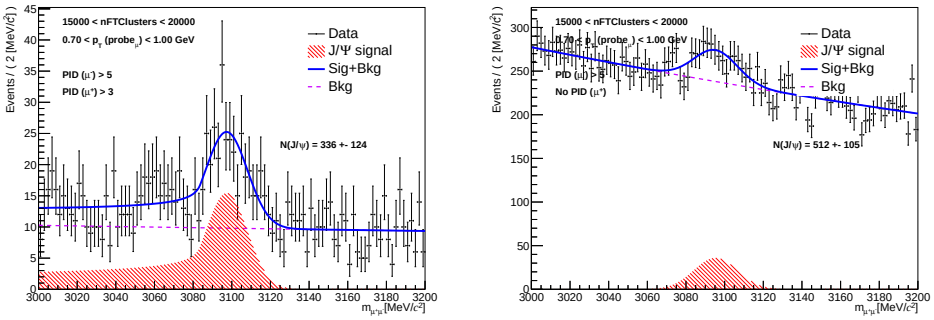


FIGURE B.15: Dimuon invariant-mass distributions for the numerator (left) and denominator (right) of eq. 4.4 for 15 000 $<$ `nFTClusters` $<$ 20 000 and 0.7 $< p_{\mathrm{T}} <$ 1.0 GeV/c.

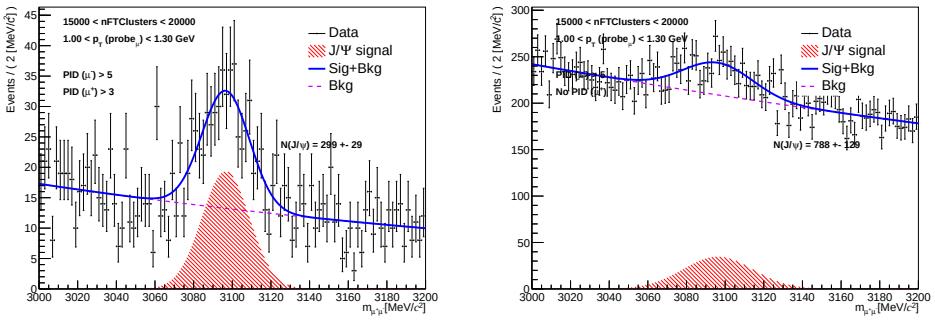


FIGURE B.16: Dimuon invariant-mass distributions for the numerator (left) and denominator (right) of eq. 4.4 for 15 000 $<$ `nFTClusters` $<$ 20 000 and 1.0 $< p_{\mathrm{T}} <$ 1.3 GeV/c.

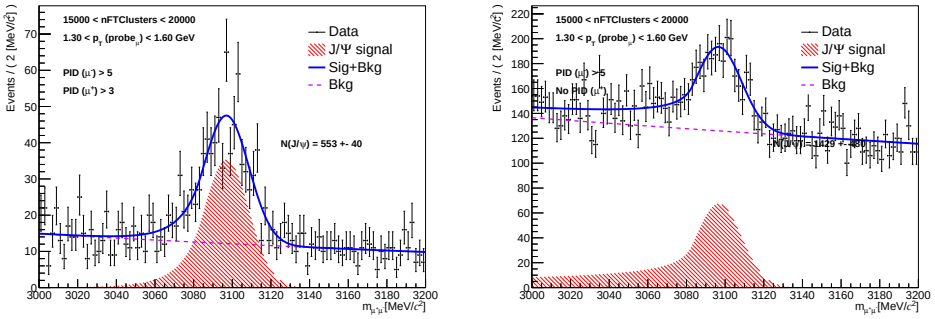


FIGURE B.17: Dimuon invariant-mass distributions for the numerator (left) and denominator (right) of eq. 4.4 for 15 000 $<$ `nFTClusters` $<$ 20 000 and 1.3 $< p_{\mathrm{T}} <$ 1.6 GeV/c.

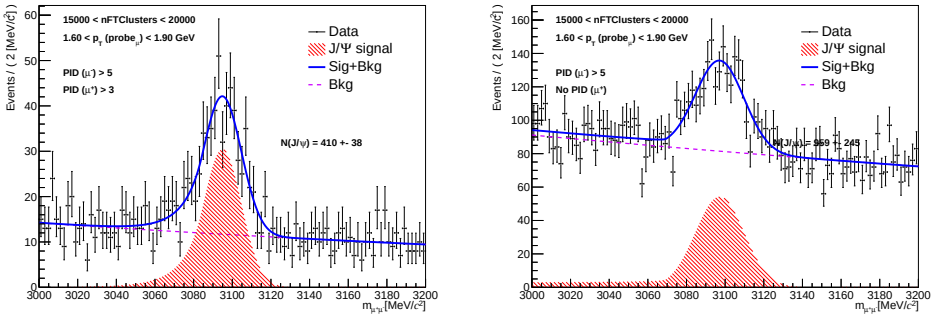


FIGURE B.18: Dimuon invariant-mass distributions for the numerator (left) and denominator (right) of eq. 4.4 for 15 000 $<$ `nFTClusters` $<$ 20 000 and 1.6 $< p_{\mathrm{T}} <$ 1.9 GeV/c.

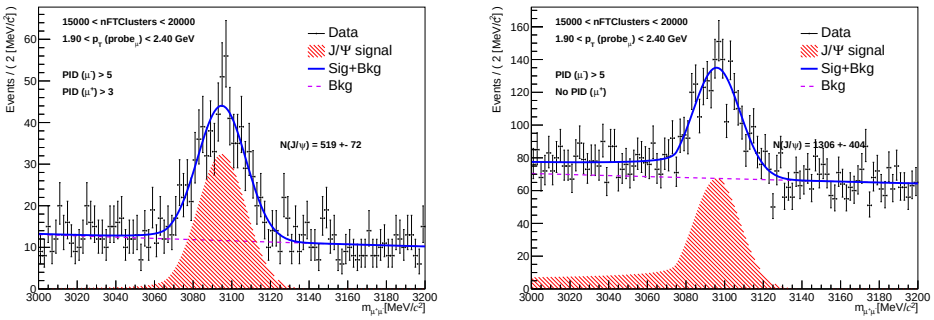


FIGURE B.19: Dimuon invariant-mass distributions for the numerator (left) and denominator (right) of eq. 4.4 for 15 000 $<$ `nFTClusters` $<$ 20 000 and 1.9 $< p_{\mathrm{T}} <$ 2.4 GeV/c.

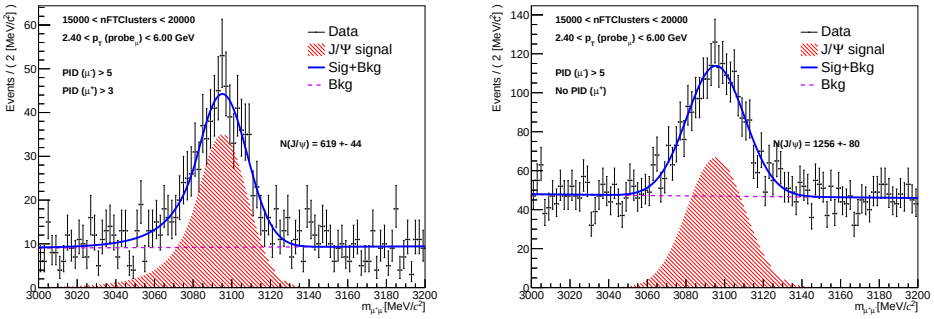


FIGURE B.20: Dimuon invariant-mass distributions for the numerator (left) and denominator (right) of eq. 4.4 for 15 000 $<$ `nFTClusters` $<$ 20 000 and 2.4 $< p_{\mathrm{T}} <$ 6.0 GeV/c.

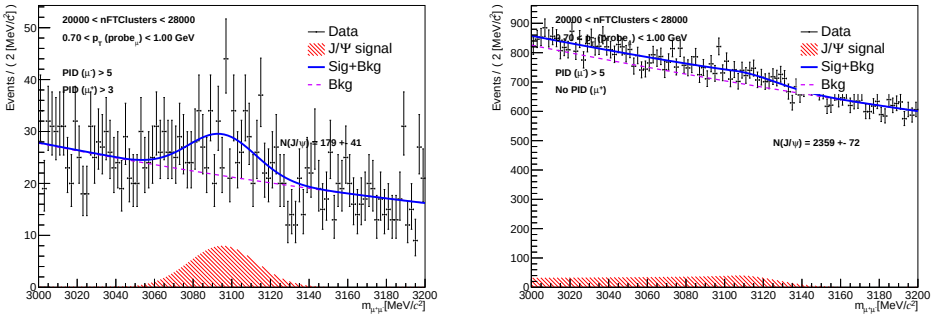


FIGURE B.21: Dimuon invariant-mass distributions for the numerator (left) and denominator (right) of eq. 4.4 for 20 000 $<$ `nFTClusters` $<$ 28 000 and 0.7 $< p_{\mathrm{T}} <$ 1.0 GeV/c.

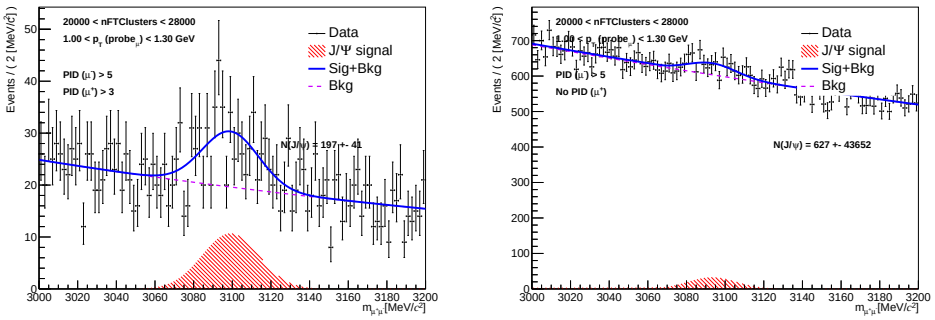


FIGURE B.22: Dimuon invariant-mass distributions for the numerator (left) and denominator (right) of eq. 4.4 for 20 000 $<$ `nFTClusters` $<$ 28 000 and 1.0 $< p_{\mathrm{T}} <$ 1.3 GeV/c.

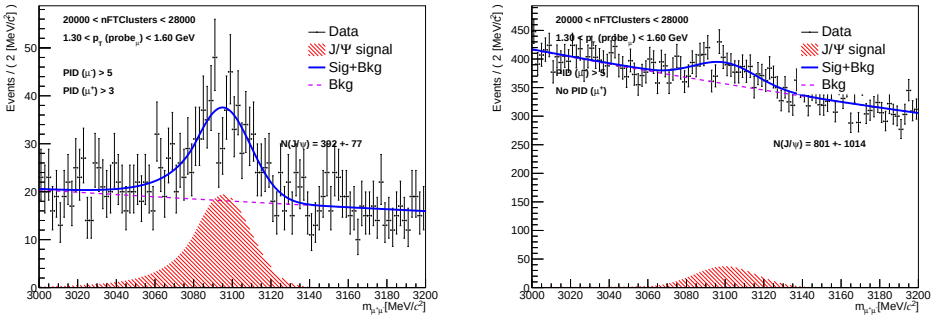


FIGURE B.23: Dimuon invariant-mass distributions for the numerator (left) and denominator (right) of eq. 4.4 for 20 000 $<$ `nFTClusters` $<$ 28 000 and 1.3 $< p_{\mathrm{T}} <$ 1.6 GeV/c.

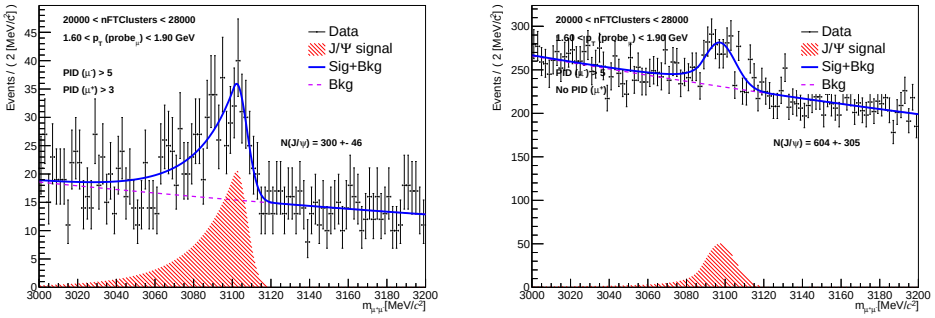


FIGURE B.24: Dimuon invariant-mass distributions for the numerator (left) and denominator (right) of eq. 4.4 for 20 000 $<$ `nFTClusters` $<$ 28 000 and 1.6 $< p_{\mathrm{T}} <$ 1.9 GeV/c.

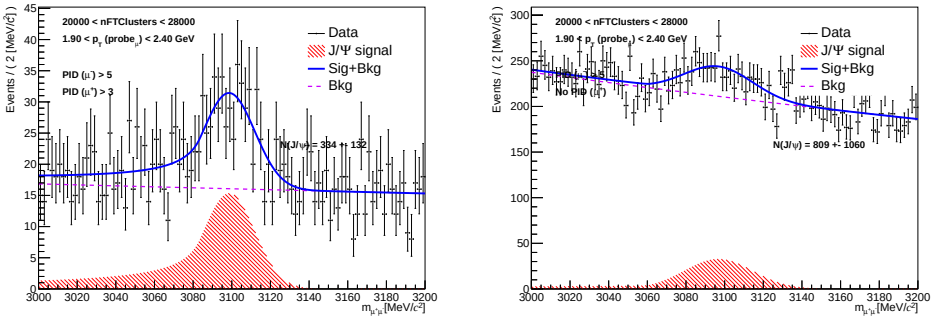


FIGURE B.25: Dimuon invariant-mass distributions for the numerator (left) and denominator (right) of eq. 4.4 for 20 000 $<$ `nFTClusters` $<$ 28 000 and $1.9 < p_{\mathrm{T}} < 2.4$ GeV/c.

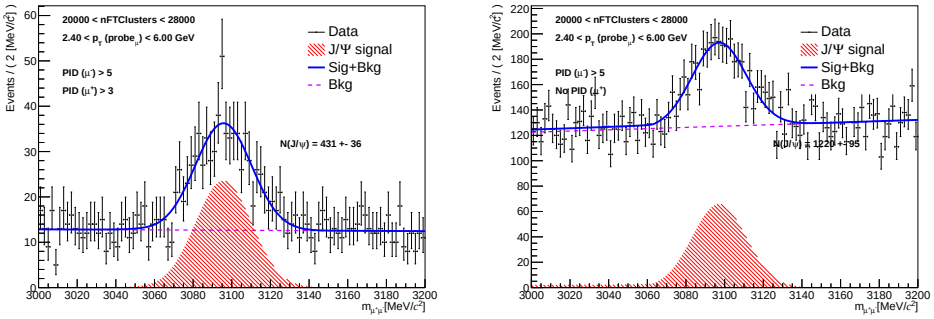


FIGURE B.26: Dimuon invariant-mass distributions for the numerator (left) and denominator (right) of eq. 4.4 for 20 000 $<$ `nFTClusters` $<$ 28 000 and $2.4 < p_{\mathrm{T}} < 6.0$ GeV/c.

Appendix C

Transverse polarization measurement of Λ hyperons in pNe collisions at $\sqrt{s_{\mathrm{NN}}} = 68.4$ GeV

This appendix reports on an independent study conducted during the initial phase of the PhD, concerning the transverse polarization of Λ hyperons in proton–neon (pNe) collisions at $\sqrt{s_{\mathrm{NN}}} = 68.4$ GeV. The analysis exploits data recorded in fixed-target mode using the SMOG system of the LHCb experiment in 2017. The measurement provides insight into spin-dependent effects in hadron production, with particular relevance to the study of transverse-momentum-dependent (TMD) parton distributions and fragmentation mechanisms. Owing to the unique kinematic coverage of the experiment, the results probe an unexplored region in phase space and mark the first observation of Λ polarization in a fixed-target setup at LHC energies. As this was part of my PhD, the corresponding article, published in JHEP, is included below [127].

C.1 Introduction

The spontaneous transverse polarization of Λ hyperons, spin 1/2 baryons with a mass of 1115.683 ± 0.006 MeV/c^2 [13], was first observed in 1976 in unpolarized fixed-target collisions of protons with an energy of 300 GeV and a beryllium target [128]. This result was in contradiction with the expectation that the large number of final states in high-energy particle production would suppress polarization effects and showed that spin effects contribute significantly even at high-energy. A polarizing fragmentation function, denoted by $D_{1T}^{\perp}$, has been proposed in Refs. [7, 8, 9] to account for the polarized production of Λ hyperons. The mechanism involving the $D_{1T}^{\perp}$ function is the same as that used in the framework of the transverse-momentum-dependent unpolarized fragmentation functions (TMDs) to describe the fragmentation of an unpolarized quark into a transversely polarized hadron. The spin and azimuthal asymmetries observed at sufficiently large energy scales cannot be explained by asymmetries at the level of the hard partonic process, instead their origin must lie in soft processes.

By maintaining an explicit dependence on the intrinsic partonic motion, TMDs account for spin and momentum correlations at the soft level, potentially explaining the observed asymmetries. Since these functions arise from soft mechanisms, they are difficult to calculate from first principles. Hence, just as with collinear parton distribution functions and fragmentation functions, one possible approach is to determine them from experimental data. Several attempts were made to describe Λ polarization, both on the theoretical and experimental sides, at different accelerators and center-of-mass energies. Particularly relevant are the measurements from the STAR experiment at RHIC[129] and Belle at KEKB[130]. None of these results led to a fully satisfactory answer, and the mechanism giving rise to Λ polarization is still unclear. In this paper, a measurement of transverse Λ and $\overline{\Lambda}$ polarization is presented, using the LHCb experiment in a fixed-target configuration. The polarization is determined using proton-neon (pNe) data collected in 2017 from collisions at a nucleon-nucleon center-of-mass energy of $\sqrt{s_{\mathrm{NN}}} = 68.4\,\mathrm{GeV}$, generated by a 2.5 TeV proton beam incident on neon nuclei at rest and corresponding to an integrated luminosity of 24.9 nb^{-1}. The hyperons are reconstructed through the decays $\Lambda \to p\pi^-$ and $\overline{\Lambda} \to \bar{p}\pi^+$. The results are obtained as a function of the transverse momentum (p_{T}) of the hyperon, the pseudorapidity (η), the rapidity (y) and the Feynman variable $x_{\mathrm{F}} = \frac{2 \cdot p_{\mathrm{L}}}{\sqrt{s_{\mathrm{NN}}}}$ (where p_{L} is the longitudinal momentum of the particle), as a non trivial dependence of the polarization on these variables has been reported in other publications [131].

C.2 The LHCb detector

The LHCb detector [76, 77] is a single-arm forward spectrometer, designed for the study of particles containing c or b quarks, covering the pseudorapidity range $2 < \eta < 5$. The detector includes: a silicon-strip vertex locator (VELO), three tracking stations of silicon-strip detectors and straw drift tubes, two ring-imaging Cherenkov detectors (RICH) that are able to discriminate between different species of charged hadrons, a calorimeter system consisting of scintillating-pad and preshower detectors, electromagnetic and hadronic calorimeters, and a muon detector composed of alternating layers of iron and multiwire proportional chambers. The System for Measuring the Overlap with Gas (SMOG) [6] enables the injection of gases with a pressure of $\mathcal{O}(10^{-7})$ mbar in the beam pipe section inside the VELO, allowing LHCb to operate as a fixed-target experiment. The SMOG system thus provides a unique opportunity to study proton-nucleus and nucleus-nucleus collisions with various gaseous targets using the LHC beams. In this configuration, the LHCb acceptance extends to the negative rapidity hemisphere, due to the boost induced by the high-energy proton beam, which points to the positive-z direction.

C.3 Data sample and analysis strategy

The pNe sample was taken during the pp data-taking period. Fixed-target events were collected only when a bunch in the beam pointing towards the LHCb detector crossed the interaction region without a corresponding bunch in the beam pointing to the opposite direction. To suppress the remaining pp background, the z-coordinate of the pNe primary vertex (PV) is required to lie in the fiducial region $z_{\rm PV} \in [-200, -100] \cup [100, 150]\,\text{mm}$.[1] Furthermore, events with more than four hits in the VELO stations upstream of the interaction region are rejected. The online event selection is performed by a trigger [121], that requires at least one track reconstructed in the VELO. Since the Λ reconstruction requires two tracks, this trigger condition does not bias the measurement. In the offline selection, the Λ candidates are required to be reconstructed from proton and pion tracks with opposite charge, forming a vertex with a good-quality fit. Protons and pions are required to have a minimum transverse momentum of 100 MeV/c and a minimum momentum of 2 GeV/c. Particle identification (PID) requirements based on the information from the RICH detectors are applied to select protons. Finally, to suppress the contribution of non-prompt Λ hyperons, the impact parameter of the Λ candidate with respect to the PV is required to be less than 1.5 mm, which reduces this contribution to about 5%. Figure C.1 shows the $p\pi^-$ and $\bar{p}\pi^+$ invariant-mass distributions obtained after all the selection criteria have been applied. The distributions are fitted with the convolution of a Cauchy and a Gaussian function to describe the signal shape and a first-order polynomial to model the background.

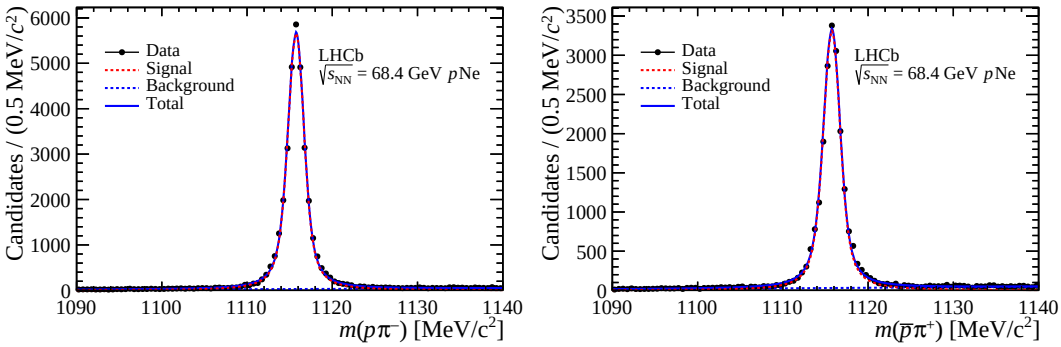


FIGURE C.1: Invariant-mass distributions for (left) Λ and (right) $\overline{\Lambda}$ candidates after all selection requirements are applied. The fit result is overlaid on the data.

The decays $\Lambda \to p\pi^-$ and $\overline{\Lambda} \to \bar{p}\pi^+$ exhibit significant parity violation, resulting in large asymmetries in the angular distribution of their decay particles. In particular,

[1] $z_{\rm PV} = 0$ is the z coordinate of the center of the pp interaction region.

the angular distribution of the proton in the Λ rest frame is given by

$$\frac{dN}{d\cos\theta} = \frac{dN_0}{d\cos\theta}(1 + \alpha P_\Lambda \cos\theta), \tag{C.1}$$

where θ is the angle between the proton momentum and the normal ($\hat{n}$) to the production plane spanned by the beam and the Λ momentum directions as sketched in Fig. C.2, $\frac{dN_0}{d\cos\theta}$ is the decay distribution for unpolarized Λ hyperons, P_Λ is the magnitude of the Λ polarization, and α is the value of the parity-violating decay asymmetry for the channel under study of the Λ hyperon. The magnitude of the polarization is determined from a fit to the angular distribution of the proton in 10 bins of $\cos\theta$.

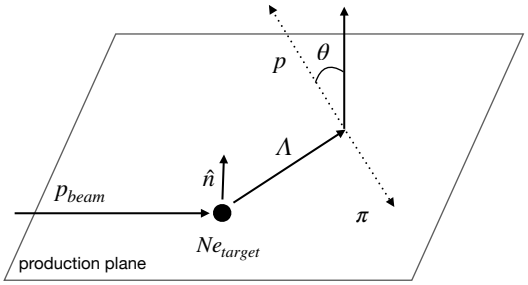


FIGURE C.2: Sketch of the Λ production and decay. The polarization vector $\hat{P}_\Lambda$ is aligned with the normal vector $\hat{n}$ to the Λ production plane; θ is the angle between the momentum of the decay proton and $\hat{n}$ in the Λ rest frame.

C.4 Simulation and efficiencies

Efficiencies are estimated using samples of fully simulated events. The simulated decays are reconstructed and analyzed using the same software tools as those used to process the data. In the simulation, Λ hyperons are generated using PYTHIA [95] with a specific LHCb configuration [132] and with colliding-proton beam momentum equal to the momentum per nucleon of the beam and target in the centre-of-mass frame. The decays of unstable particles are described by EVTGEN [97], in which final-state radiation is generated using PHOTOS [98]. The four-momentum of the Λ decay particles is then embedded into pNe minimum bias events that are generated with the EPOS event generator [96]. The interaction of the generated particles with the detector and its response are implemented using the GEANT4 toolkit [99, 100] as described in Ref. [101].

After reconstruction, the simulated samples are weighted to improve agreement with data. Weights are calculated as the ratio between the normalized data and simulated distributions as a function of $p_{\rm T}$, η and $z_{\rm PV}$ with

$$w(p_{\rm T}, \eta, z_{\rm PV}) = w(p_{\rm T}, \eta) \cdot w(z_{\rm PV}), \tag{C.2}$$

where $w(p_{\mathrm{T}}, \eta)$ is evaluated in 6 intervals of transverse momentum between 300 and 2500 MeV/c and 7 intervals of pseudorapidity between 2 and 5. The weights $w(z_{\mathrm{PV}})$ are evaluated in 6 intervals between -200 and 150 mm, ignoring the region between -100 and 100 mm outside the fiducial region considered in the analysis. Through the weighting procedure, the simulation is corrected on average by 6% as a function of transverse momentum and pseudorapidity, and by 4% as a function of z_{PV}, for both Λ and $\overline{\Lambda}$ hyperons. Accounting for efficiency factors, Eq. C.1 is modified to

$$\frac{dN}{d\cos\theta} = \frac{dN_0}{d\cos\theta}(1 + \alpha P_\Lambda \cos\theta) \times \epsilon(\cos\theta) \times \epsilon_{\mathrm{PID}}, \tag{C.3}$$

where ϵ_{PID} is the particle identification efficiency for the protons, estimated from dedicated calibration data samples and computed as a function of the proton kinematics. The $\epsilon(\cos\theta)$ term is the product of acceptance, reconstruction and selection efficiencies. It is determined using simulation as $\epsilon(\cos\theta) = f_{\mathrm{rec}}(\cos\theta)/f_{\mathrm{gen}}(\cos\theta)$, where f indicates the $\cos\theta$ distribution for generated candidates (f_{gen}), without any detector effect, or for fully reconstructed candidates (f_{rec}), with detector effects included. As the polarization effects are not included in the simulation, the generated $\cos\theta$ distribution is uniform. Since only the shape of the distribution is relevant, the efficiency is proportional to the reconstructed $\cos\theta$ distributions, and the generated one is ignored. To correct the angular distributions in data, in each $\cos\theta$ bin, the normalized number of candidates in the data is divided by the normalized number of candidates in the simulated reconstructed sample.

C.5 Results and systematic uncertainties

The proton angular distributions, after efficiency correction, are shown in Fig. C.3. The function $f(\cos\theta) = A(1 + \alpha P_\Lambda \cos\theta)$ is fitted to the data distributions, where $\alpha = 0.746 \pm 0.007$ for Λ and $\alpha = -0.757 \pm 0.004$ for $\overline{\Lambda}$ are fixed to their world average value [133]. The magnitude of the polarization is given by the free parameter of the fit shown in Fig. C.3.

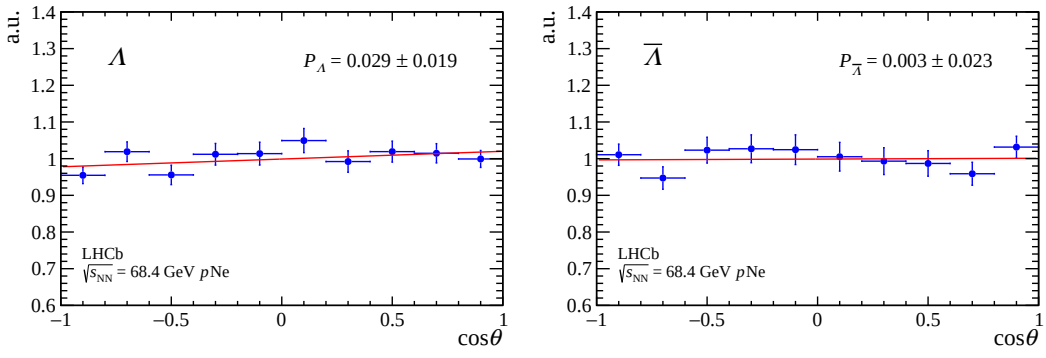


FIGURE C.3: Efficiency-corrected $\cos\theta$ distributions, for (left) Λ and (right) $\overline{\Lambda}$ hyperons. The result of the fit is overlaid (red line).

Several sources of systematic uncertainties are considered. The fit to the invariant-mass distribution is repeated using a double-sided Crystal Ball function [118] instead of the convolution of a Cauchy and a Gaussian function for the signal shape, and a second-order polynomial instead of a first-order one for the background, and the values of the polarization are determined again. The systematic uncertainty is determined as the deviations of these results with respect to those of the default fit. Uncertainties related to the weighting procedure applied to the simulation are taken into consideration by carrying out 100 trials, randomly varying each weight within its uncertainty, calculating new values for the polarization, and taking as systematic uncertainty the largest difference in the polarization values compared to the default one. The choice of the variables used to weight the simulation is also considered; the uncertainty is calculated as the difference between the results obtained by using the track multiplicity and those obtained using the Λ pseudorapidity in the calculation of the weights. The choice of binning for the angular distributions affects the fit results. This is taken into account by repeating the polarization measurements using 5 bins instead of 10 in the angular distribution. Another contribution is associated with the estimation of PID efficiencies. An alternative approach is used, where the particle identification efficiencies are directly estimated from the simulation rather than using dedicated calibration samples. Another systematic uncertainty contribution arises from nonprompt Λ hyperon contamination in the data sample, which is estimated from simulation to account for 5% of the total yield. To estimate an upper limit on the nonprompt contamination, the impact parameter requirement (which retains approximately 50% of the nonprompt signal) is removed, the measurement is repeated and the difference with the baseline value is taken as systematic uncertainty. The systematic uncertainty due to the external parameter α is found to be negligible. The total systematic uncertainty is computed as the sum in quadrature of each contribution shown in Table C.1. The systematic contributions are found to be small and the measurement is dominated by statistical uncertainties. The statistical effect on each systematic contribution is not negligible as reflected in the differences between Λ and $\overline{\Lambda}$ hyperons. The final polarization measurements are

$$P_{\Lambda} = 0.029 \pm 0.018\,(\text{stat}) \pm 0.013\,(\text{syst})\,,$$

$$P_{\overline{\Lambda}} = 0.003 \pm 0.023\,(\text{stat}) \pm 0.014\,(\text{syst})\,.$$

TABLE C.1: Contributions of systematic uncertainties on the polarization measurement for Λ and $\overline{\Lambda}$ hyperons.

Source	Λ	$\overline{\Lambda}$
Signal estimation	0.007	0.001
Background estimation	0.001	0.010
Kinematic weights	0.001	0.001
Multiplicity dependence	0.001	0.004
Binning of $\cos\theta$ distributions	0.007	0.006
PID efficiencies	0.002	0.005
Nonprompt contamination	0.005	0.002

The polarization measurements have also been performed in bins of p_{T}, η, y and x_{F}. The results are shown in Fig. C.4 and listed in Table C.2.

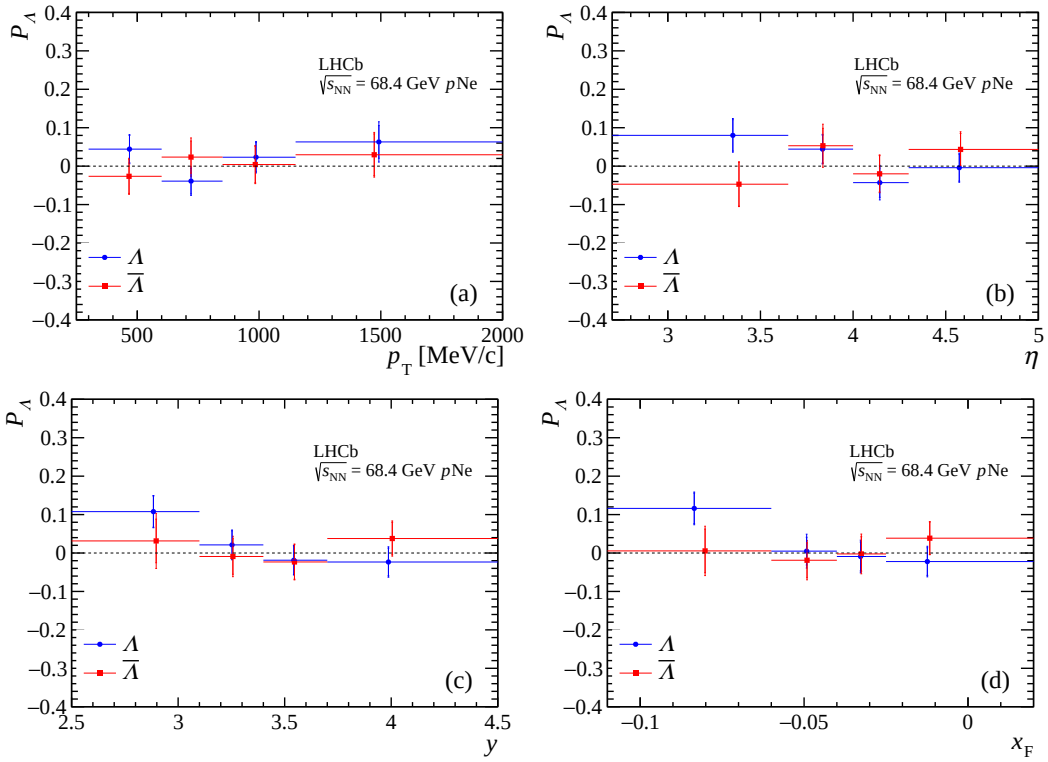


FIGURE C.4: Polarization as a function of (a) p_{T}, (b) η, (c) x_{F} and (d) y. Blue (red) symbols are for Λ ($\overline{\Lambda}$). In each plot the data is integrated over the $0.3 < p_{\mathrm{T}} < 3$ GeV/c and/or $2 < \eta < 5$ kinematic range.

Other experiments with different energies and collision systems have measured the Λ polarization. In its fixed-target configuration, the LHCb experiment covers an energy and kinematic range that is largely unexplored. Figure C.5 compares and shows the agreement between the results of this paper with measurements from other experiments, including ATLAS [134], an experiment at the M2 beam-line at Fermilab

[135], the E799 experiment [136], NA48 [137], and HERA-B [138]. The measurements reported here, and those from HERA-B, cover negative values of x_F, so the results are first transformed using the following symmetry of the transverse polarization $P_\Lambda(-x_F) = -P_\Lambda(x_F)$, and then compared with the other measurements.

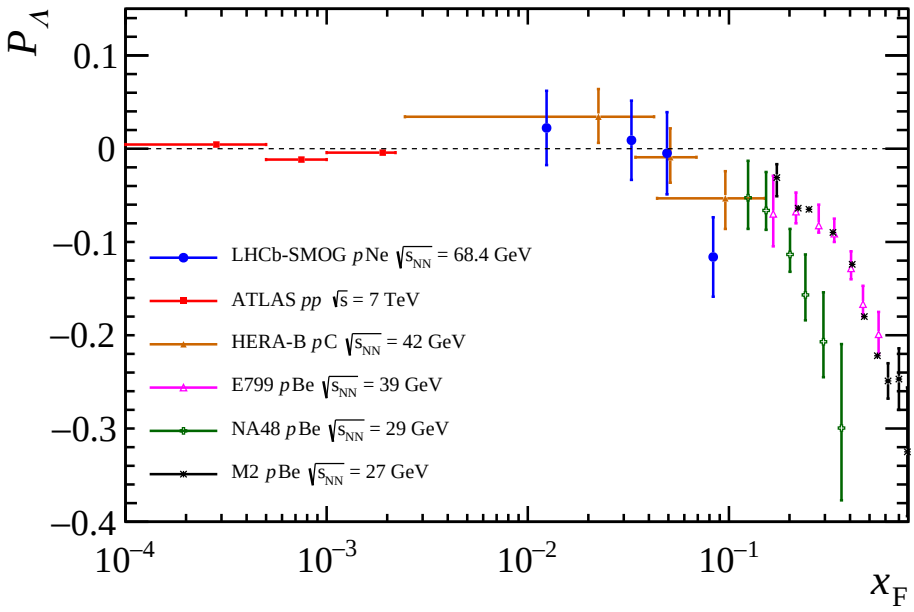


FIGURE C.5: Comparison of polarization as a function of x_F for Λ hyperons obtained in experiments with different energies and with different colliding systems.

TABLE C.2: Polarization in bins of p_{T}, η, x_{F}, and y for Λ and $\overline{\Lambda}$. The first uncertainties are statistical and the second are systematic.

	P_{Λ}	$P_{\overline{\Lambda}}$
p_{T} [MeV/c]		
$[300, 600]$	$0.044 \pm 0.035 \pm 0.013$	$-0.026 \pm 0.044 \pm 0.015$
$[600, 850]$	$-0.039 \pm 0.033 \pm 0.016$	$0.023 \pm 0.042 \pm 0.027$
$[850, 1150]$	$0.023 \pm 0.038 \pm 0.015$	$0.004 \pm 0.047 \pm 0.015$
$[1150, 3000]$	$0.063 \pm 0.042 \pm 0.031$	$0.029 \pm 0.054 \pm 0.021$
η		
$[2.00, 3.65]$	$0.080 \pm 0.040 \pm 0.016$	$-0.047 \pm 0.057 \pm 0.011$
$[3.65, 4.00]$	$0.044 \pm 0.036 \pm 0.012$	$0.053 \pm 0.045 \pm 0.033$
$[4.00, 4.30]$	$-0.043 \pm 0.038 \pm 0.024$	$-0.020 \pm 0.047 \pm 0.014$
$[4.30, 5.00]$	$-0.004 \pm 0.035 \pm 0.014$	$0.043 \pm 0.042 \pm 0.020$
x_{F}		
$[-0.250, -0.060]$	$0.116 \pm 0.040 \pm 0.015$	$0.006 \pm 0.057 \pm 0.030$
$[-0.060, -0.040]$	$0.005 \pm 0.036 \pm 0.025$	$-0.018 \pm 0.045 \pm 0.023$
$[-0.040, -0.025]$	$-0.009 \pm 0.037 \pm 0.020$	$0.002 \pm 0.045 \pm 0.026$
$[-0.025, 0.100]$	$-0.022 \pm 0.036 \pm 0.017$	$0.038 \pm 0.042 \pm 0.008$
y		
$[2.0, 3.1]$	$0.107 \pm 0.040 \pm 0.011$	$0.031 \pm 0.057 \pm 0.044$
$[3.1, 3.4]$	$0.021 \pm 0.036 \pm 0.013$	$-0.009 \pm 0.046 \pm 0.025$
$[3.4, 3.7]$	$-0.019 \pm 0.037 \pm 0.010$	$-0.023 \pm 0.045 \pm 0.013$
$[3.7, 5.0]$	$-0.023 \pm 0.036 \pm 0.016$	$0.038 \pm 0.042 \pm 0.018$

C.6 Conclusions

A measurement of transverse polarization of Λ and $\overline{\Lambda}$ hyperons in pNe collisions at $\sqrt{s_{\mathrm{NN}}} = 68.4\,\mathrm{GeV}$ by the LHCb experiment is presented. This analysis exploits the innovative and unique fixed-target apparatus at LHC. The measurement in a new collision system and region of phase space can provide additional insights on the mechanism of Λ polarization, which can still not be calculated in quantum chromodynamics. The polarization is measured through the decay $\Lambda \to p\pi^-$ and its charge conjugate, and is studied both as integrated values and in different bins of four kinematic variables: p_{T}, η, x_{F}, and y.

The integrated results are

$$P_{\Lambda} = 0.029 \pm 0.018\,(\mathrm{stat}) \pm 0.013\,(\mathrm{syst})\,,$$

$$P_{\overline{\Lambda}} = 0.003 \pm 0.023\,(\mathrm{stat}) \pm 0.014\,(\mathrm{syst})\,.$$

The polarization values obtained in this analysis are compatible with previous measurements, in particular with the HERA-B results which cover a similar x_{F} interval.

The agreement is noteworthy considering the different experiments and colliding systems.

The LHCb fixed-target program has become particularly active since the installation of the SMOG2 system, which increases data luminosity by more than two orders of magnitude compared to the SMOG system used in this analysis. With the new data, we expect to explore different target species and improve our reach into the lower negative regions of x_{F} which have been poorly explored so far.

Bibliography

[1] David Griffiths. *Introduction to Elementary Particles*. 2nd. Wiley-VCH, 2008 (pages xi, 1).

[2] Edward V. Shuryak. "Quantum Chromodynamics and the theory of superdense matter". In: *Phys. Rept.* 61 (1980), pp. 71–158. DOI: 10.1016/0370-1573(80)90105-2 (page xi).

[3] Wit Busza, Krishna Rajagopal, and Wilke van der Schee. "Heavy Ion Collisions: The Big Picture, and the Big Questions". In: *Ann. Rev. Nucl. Part. Sci.* 68 (2018), pp. 339–376. DOI: 10.1146/annurev-nucl-101917-020852. arXiv: 1802.04801 [hep-ph] (page xi).

[4] T. Matsui and H. Satz. "J/ψ suppression by quark-gluon plasma formation". In: *Phys. Lett.* B178 (1986), pp. 416–422. DOI: 10.1016/0370-2693(86)91404-8 (pages xi, 16).

[5] Peter Braun-Munzinger and Johanna Stachel. "The quest for the quark-gluon plasma". In: *Nature* 448 (2007), pp. 302–309. DOI: 10.1038/nature06080 (pages xi, 17).

[6] R. Aaij et al. "Precision luminosity measurements at LHCb". In: *JINST* 9 (2014), P12005. DOI: 10.1088/1748-0221/9/12/P12005. arXiv: 1410.0149 [hep-ex] (pages xii, 42, 158).

[7] D. Boer et al. "Spin asymmetries in jet-hyperon production at LHC". In: *Phys. Lett.* B659.1 (2008), pp. 127–136. ISSN: 0370-2693. DOI: https://doi.org/10.1016/j.physletb.2007.10.059. URL: https://www.sciencedirect.com/science/article/pii/S0370269307012993 (pages xii, 157).

[8] Daniel Boer. "Transverse Lambda polarization at LHC". In: (2009). arXiv: 0907.1610 [hep-ph] (pages xii, 157).

[9] P.J Mulders and R.D Tangerman. "The complete tree-level result up to order 1/Q for polarized deep-inelastic leptoproduction". In: *Nuclear Physics* B461.1–2 (Feb. 1996), 197–237. ISSN: 0550-3213. DOI: 10.1016/0550-3213(95)00632-x. URL: http://dx.doi.org/10.1016/0550-3213(95)00632-X (pages xii, 157).

[10] Joey Huston, Klaus Rabbertz, and Giulia Zanderighi. "Quantum Chromodynamics". In: (Dec. 2023). arXiv: 2312.14015 [hep-ph] (page 4).

[11] Robert D. Pisarski and Frank Wilczek. "Remarks on the chiral phase transition in chromodynamics". In: *Phys. Rev.* D29 (1984), pp. 338–341. DOI: 10.1103/PhysRevD.29.338 (page 5).

[12] Kenji Fukushima and Tetsuo Hatsuda. "The phase diagram of dense QCD". In: *Rept. Prog. Phys.* 74 (2011), p. 014001. DOI: 10.1088/0034-4885/74/1/014001. arXiv: 1005.4814 [hep-ph] (page 5).

[13] S. Navas et al. "Review of particle physics". In: *Phys. Rev.* D110.8 (2024), p. 030001. DOI: 10.1103/PhysRevD.110.030001 (pages 6, 7, 68, 78, 120, 157).

[14] R. Baier and R. Ruckl. "Hadronic Production of J/ψ and Υ: Transverse Momentum Distributions". In: *Phys. Lett.* B102 (1981), pp. 364–370. DOI: 10.1016/0370-2693(81)90636-5 (page 6).

[15] P. Cho and A. K. Leibovich. "Color-octet quarkonia production". In: *Phys. Rev.* D53 (1996), pp. 150–162. DOI: 10.1103/PhysRevD.53.150 (page 7).

[16] P. Cho and A. K. Leibovich. "Color-octet quarkonia production. II." In: *Phys. Rev.* D53 (1996), pp. 6203–6217. DOI: 10.1103/PhysRevD.53.6203 (page 7).

[17] G. T. Bodwin, E. Braaten, and G. P. Lepage. "Rigorous QCD analysis of inclusive annihilation and production of heavy quarkonium". In: *Phys. Rev.* D51 (1995), pp. 1125–1171. DOI: 10.1103/PhysRevD.51.1125 (page 7).

[18] N. Brambilla et al. "Heavy Quarkonium: Progress, Puzzles, and Opportunities". In: *Eur. Phys. J. C* 71 (2011), p. 1534. DOI: 10.1140/epjc/s10052-010-1534-9. arXiv: 1010.5827 [hep-ph] (page 7).

[19] R. Aaij et al. "Measurement of J/ψ production in pp collisions at $\sqrt{s} = 7$ TeV". In: *Eur. Phys. J. C* 71 (2011), p. 1645. DOI: 10.1140/epjc/s10052-011-1645-y. arXiv: 1103.0423 [hep-ex] (page 8).

[20] R Aaij et al. "Measurement of $\psi(2S)$ meson production in pp collisions at $\sqrt{s}$=7 TeV". In: *Eur. Phys. J. C* 72 (2012). [Erratum: Eur.Phys.J.C 80, 49 (2020)], p. 2100. DOI: 10.1140/epjc/s10052-012-2100-4. arXiv: 1204.1258 [hep-ex] (page 8).

[21] Tapan K. Nayak. "Probing the QCD phase structure using event-by-event fluctuations". In: *J. Phys. Conf. Ser.* 1602.1 (2020). Ed. by Rene Bellwied et al., p. 012003. DOI: 10.1088/1742-6596/1602/1/012003. arXiv: 2008.04643 [nucl-ex] (page 9).

[22] A. Bazavov et al. "Equation of state in (2+1)-flavor QCD". In: *Phys. Rev.* D90 (2014), p. 094503. DOI: 10.1103/PhysRevD.90.094503. arXiv: 1407.6387 [hep-lat] (page 8).

[23] A. Bazavov et al. "Chiral crossover in QCD at zero and non-zero chemical potentials". In: *Phys. Lett. B* 795 (2019), pp. 15–21. DOI: 10.1016/j.physletb.2019.05.013. arXiv: 1812.08235 [hep-lat] (pages 8, 12).

[24] Mikhail A. Stephanov. "QCD Phase Diagram and the Critical Point". In: *Prog. Theor. Phys. Suppl.* 153 (2004). Ed. by Berndt Muller and C. I. Tan, pp. 139–156. DOI: 10.1143/PTPS.153.139. arXiv: hep-ph/0402115 (page 8).

[25] Paolo Parotto et al. "QCD equation of state matched to lattice data and exhibiting a critical point singularity". In: *Phys. Rev.* C101.3 (2020), p. 034901. DOI: 10.1103/PhysRevC.101.034901. arXiv: 1805.05249 [hep-ph] (page 8).

[26] Kari J. Eskola et al. "EPPS16: Nuclear parton distributions with LHC data". In: *Eur. Phys. J.* C77.3 (2017), p. 163. DOI: 10.1140/epjc/s10052-017-4725-9. arXiv: 1612.05741 [hep-ph] (page 10).

[27] K. Kovarik et al. "nCTEQ15 - Global analysis of nuclear parton distributions with uncertainties in the CTEQ framework". In: *Phys. Rev.* D93.8 (2016), p. 085037. DOI: 10.1103/PhysRevD.93.085037. arXiv: 1509.00792 [hep-ph] (page 10).

[28] F. D. Aaron et al. "A Precision Measurement of the Inclusive ep Scattering Cross Section at HERA". In: *Eur. Phys. J.* C64 (2009), pp. 561–587. DOI: 10.1140/epjc/s10052-009-1169-x. arXiv: 0904.3513 [hep-ex] (pages 10, 11).

[29] Francois Arleo and Stephane Peigne. "Heavy-quarkonium suppression in p-A collisions from parton energy loss in cold QCD matter". In: *JHEP* 03 (2013), p. 122. DOI: 10.1007/JHEP03(2013)122. arXiv: 1212.0434 [hep-ph] (page 11).

[30] J. D. Bjorken. "Highly Relativistic Nucleus-Nucleus Collisions: The Central Rapidity Region". In: *Phys. Rev.* D27 (1983), pp. 140–151. DOI: 10.1103/PhysRevD.27.140 (page 11).

[31] C. Loizides, J. Nagle, and P. Steinberg. "Improved version of the PHOBOS Glauber Monte Carlo". In: *SoftwareX* 1-2 (2015), pp. 13–18. DOI: 10.1016/j.softx.2015.05.001. arXiv: 1408.2549 [nucl-ex] (pages 14, 110).

[32] Jorge Casalderrey-Solana and Carlos A. Salgado. "Introductory lectures on jet quenching in heavy ion collisions". In: *Acta Phys. Polon. B* 38 (2007). Ed. by Michal Praszalowicz, Marek Kutschera, and Edward Malec, pp. 3731–3794. arXiv: 0712.3443 [hep-ph] (page 15).

[33] Johann Rafelski and Berndt Muller. "Strangeness Production in the Quark - Gluon Plasma". In: *Phys. Rev. Lett.* 48 (1982). [Erratum: Phys.Rev.Lett. 56, 2334 (1986)], p. 1066. DOI: 10.1103/PhysRevLett.48.1066 (page 15).

[34] R. Rapp, D. Blaschke, and P. Crochet. "Charmonium and bottomonium production in heavy-ion collisions". In: *Prog. Part. Nucl. Phys.* 65 (2010), pp. 209–266. DOI: 10.1016/j.ppnp.2010.07.002. arXiv: 0807.2470 [hep-ph] (page 16).

[35] M. C. Abreu et al. "J/ψ and Drell-Yan cross-sections in PbPb interactions at 158 GeV/c per nucleon". In: *Phys. Lett.* B410 (1997), pp. 327–336. DOI: 10.1016/S0370-2693(97)00914-3 (page 16).

[36] B. Alessandro et al. "A new measurement of J/ψ suppression in Pb-Pb collisions at 158 GeV per nucleon". In: *Eur. Phys. J.* C39 (2005), pp. 335–345. DOI: 10.1140/epjc/s2004-02107-9. arXiv: hep-ex/0412036 (page 16).

[37] E. G. Ferreiro. "Charmonium dissociation and recombination at LHC: Revisiting comovers". In: *Phys. Lett. B* 731 (2014), pp. 57–63. DOI: 10.1016/j.physletb.2014.02.011. arXiv: 1210.3209 [hep-ph] (pages 16, 18, 19, 22, 24).

[38] P. Braun-Munzinger and J. Stachel. "(Non)thermal aspects of charmonium production and a new look at J/ψ suppression". In: *Phys. Lett.* B490 (2000), pp. 196–202. DOI: 10.1016/S0370-2693(00)00991-6. arXiv: nucl-th/0007059 (page 17).

[39] Robert L. Thews, Martin Schroedter, and Johann Rafelski. "Enhanced J/ψ production in deconfined quark matter". In: *Phys. Rev.* C63 (2001), p. 054905. DOI: 10.1103/PhysRevC.63.054905. arXiv: hep-ph/0007323 (page 17).

[40] Xingbo Zhao and Ralf Rapp. "Medium Modifications and Production of Charmonia at LHC". In: *Nucl. Phys.* A859 (2011), pp. 114–125. DOI: 10.1016/j.nuclphysa.2011.05.001 (page 17).

[41] Xiaojian Du, Ralf Rapp, and Min He. "Color Screening and Regeneration of Bottomonia in High-Energy Heavy-Ion Collisions". In: *Phys. Rev.* C96.5 (2017), p. 054901. DOI: 10.1103/PhysRevC.96.054901 (pages 17, 22, 110, 136, 137).

[42] Anton Andronic et al. "Decoding the phase structure of QCD via particle production at high energy". In: *Nature* 561 (2018), pp. 321–330. DOI: 10.1038/s41586-018-0491-6 (pages 17, 110, 136, 137).

[43] Elena G. Ferreiro. "Excited charmonium suppression in proton–nucleus collisions as a consequence of comovers". In: *Phys. Lett.* B749 (2015), pp. 98–103. DOI: 10.1016/j.physletb.2015.07.066 (page 18).

[44] Betty Bezverkhny Abelev et al. "Measurement of quarkonium production at forward rapidity in pp collisions at $\sqrt{s} = 7$ TeV". In: *Eur. Phys. J.* C74.8 (2014), p. 2974. DOI: 10.1140/epjc/s10052-014-2974-4. arXiv: 1403.3648 [nucl-ex] (page 19).

[45] Roel Aaij et al. "Measurement of forward J/ψ production cross-sections in pp collisions at $\sqrt{s} = 13$ TeV". In: *JHEP* 10 (2015). [Erratum: JHEP 05, 063 (2017)], p. 172. DOI: 10.1007/JHEP10(2015)172. arXiv: 1509.00771 [hep-ex] (pages 19, 90).

[46] A. et al. [PHENIX Collaboration] Adare. "J/ψ production versus transverse momentum and rapidity in $p+p$ collisions at $\sqrt{s}$ = 200 GeV". In: *Phys. Rev.* D82 (2010), p. 012001. DOI: 10.1103/PhysRevD.82.012001 (page 19).

[47] Roel Aaij et al. "Multiplicity dependence of $\sigma_{(2S)}/\sigma_{J/}$ in pp collisions at $\sqrt{s}$ = 13 TeV". In: *JHEP* 05 (2024), p. 243. DOI: 10.1007/JHEP05(2024)243. arXiv: 2312.15201 [hep-ex] (page 19).

[48] Albert M Sirunyan et al. "Measurement of prompt ψ(2S) production cross sections in proton-lead and proton-proton collisions at $\sqrt{s_{\mathrm{NN}}}$ = 5.02 TeV". In: *Phys. Lett. B* 790 (2019), pp. 509–532. DOI: 10.1016/j.physletb.2019.01.058. arXiv: 1805.02248 [hep-ex] (page 20).

[49] Morad Aaboud et al. "Measurement of quarkonium production in proton–lead and proton–proton collisions at 5.02 TeV with the ATLAS detector". In: *Eur. Phys. J. C* 78.3 (2018), p. 171. DOI: 10.1140/epjc/s10052-018-5624-4. arXiv: 1709.03089 [nucl-ex] (page 20).

[50] Betty Bezverkhny Abelev et al. "Suppression of ψ(2S) production in p-Pb collisions at $\sqrt{s_{\mathrm{NN}}}$ = 5.02 TeV". In: *JHEP* 12 (2014), p. 073. DOI: 10.1007/JHEP12(2014)073. arXiv: 1405.3796 [nucl-ex] (page 20).

[51] Roel Aaij et al. "Measurement of $\psi(2S)$ to J/ψ cross-section ratio as function of multiplicity in pPb collisions at$\sqrt{s_{NN}}$ = 8.16 TeV". In: (June 2025). arXiv: 2506.08624 [nucl-ex] (page 20).

[52] Shreyasi Acharya et al. "ψ(2S) Suppression in Pb-Pb Collisions at the LHC". In: *Phys. Rev. Lett.* 132.4 (2024), p. 042301. DOI: 10.1103/PhysRevLett.132.042301. arXiv: 2210.08893 [nucl-ex] (pages 20, 22, 23, 109, 136).

[53] A. Adare et al. "Cold Nuclear Matter Effects on J/ψ Yields as a Function of Rapidity and Nuclear Geometry in Deuteron-Gold Collisions at $\sqrt{s_{NN}}$ = 200 GeV". In: *Phys. Rev. Lett.* 107 (2011), p. 142301. DOI: 10.1103/PhysRevLett.107.142301. arXiv: 1010.1246 [nucl-ex] (page 20).

[54] Jaroslav Adam et al. "J/ψ suppression at forward rapidity in Pb-Pb collisions at $\sqrt{s_{\mathrm{NN}}}$ = 5.02 TeV". In: *Phys. Lett.* B766 (2017), pp. 212–224. DOI: 10.1016/j.physletb.2016.12.064. arXiv: 1606.08197 [nucl-ex] (page 21).

[55] Morad Aaboud et al. "Prompt and non-prompt J/ψ and ψ(2S) suppression at high transverse momentum in 5.02 TeV Pb+Pb collisions with the ATLAS experiment". In: *Eur. Phys. J. C* 78.9 (2018), p. 762. DOI: 10.1140/epjc/s10052-018-6219-9. arXiv: 1805.04077 [nucl-ex] (page 21).

[56] Serguei Chatrchyan et al. "Suppression of Non-Prompt J/ψ, Prompt J/ψ, and Y(1S) in PbPb Collisions at $\sqrt{s_{NN}}$ = 2.76 TeV". In: *JHEP* 05 (2012), p. 063. DOI: 10.1007/JHEP05(2012)063. arXiv: 1201.5069 [nucl-ex] (page 21).

[57] L. Adamczyk et al. "J/ψ production at high transverse momenta in $p+p$ and Au+Au collisions at $\sqrt{s_{NN}} = 200$ GeV". In: *Phys. Lett.* B722 (2013), pp. 55–62. DOI: 10.1016/j.physletb.2013.04.010. arXiv: 1208.2736 [nucl-ex] (page 21).

[58] A. Adare et al. "J/ψ Production vs Centrality, Transverse Momentum, and Rapidity in Au+Au Collisions at $\sqrt{s_{NN}} = 200$ GeV". In: *Phys. Rev. Lett.* 98 (2007), p. 232301. DOI: 10.1103/PhysRevLett.98.232301. arXiv: nucl-ex/0611020 (page 21).

[59] Helmut Satz. "Colour deconfinement and quarkonium binding". In: *J. Phys.* G32 (2006), R25. DOI: 10.1088/0954-3899/32/3/R01. arXiv: hep-ph/0512217 (page 22).

[60] Jaroslav Adam et al. "Direct photon production in Pb-Pb collisions at $\sqrt{s_{NN}} = 2.76$ TeV". In: *Phys. Lett.* B754 (2016), pp. 235–248. DOI: 10.1016/j.physletb.2016.01.020. arXiv: 1509.07324 [nucl-ex] (page 22).

[61] B. Alessandro et al. "psi-prime production in Pb-Pb collisions at 158-GeV/nucleon". In: *Eur. Phys. J.* C49 (2007), pp. 559–567. DOI: 10.1140/epjc/s10052-006-0153-y. arXiv: nucl-ex/0612013 (page 22).

[62] Anton Andronic et al. "Transverse momentum distributions of charmonium states with the statistical hadronization model". In: *Phys. Lett. B* 797 (2019), p. 134836. DOI: 10.1016/j.physletb.2019.134836. arXiv: 1901.09200 [nucl-th] (pages 22, 110, 136, 137).

[63] Albert M Sirunyan et al. "Relative Modification of Prompt ψ(2S) and J/ψ Yields from pp to PbPb Collisions at $\sqrt{s_{NN}} = 5.02$ TeV". In: *Phys. Rev. Lett.* 118.16 (2017), p. 162301. DOI: 10.1103/PhysRevLett.118.162301. arXiv: 1611.01438 [nucl-ex] (pages 23, 24).

[64] A. Adare et al. "Measurement of the relative yields of $\psi(2S)$ to $\psi(1S)$ mesons produced at forward and backward rapidity in p+p, p+Al, p+Au, and ^{3}He+Au collisions at $\sqrt{s_{NN}} = 200$ GeV". In: *Phys. Rev.* C95.3 (2017), p. 034904. DOI: 10.1103/PhysRevC.95.034904. arXiv: 1609.06550 [nucl-ex] (pages 24, 25).

[65] Xiaojian Du and Ralf Rapp. "In-Medium Charmonium Production in Proton-Nucleus Collisions". In: *Nucl. Phys. A* 943 (2015), pp. 147–158. DOI: 10.1016/j.nuclphysa.2015.09.006 (page 24).

[66] A. Augusto Alves Jr. et al. "The LHCb Detector at the LHC". In: *JINST* 3 (2008), S08005. DOI: 10.1088/1748-0221/3/08/S08005 (pages 27, 30).

[67] Emilie Maurice. "Fixed-target physics at LHCb". In: *5th Large Hadron Collider Physics Conference*. Aug. 2017. arXiv: 1708.05184 [hep-ex] (page 27).

[68] "LHC Machine". In: *JINST* 3 (2008). Ed. by Lyndon Evans and Philip Bryant, S08001. DOI: 10.1088/1748-0221/3/08/S08001 (page 27).

[69] G. Apollinari et al. "High Luminosity Large Hadron Collider HL-LHC". In: *CERN Yellow Rep.* 5 (2015). Ed. by G Apollinari et al., pp. 1–19. DOI: 10.5170/CERN-2015-005.1. arXiv: 1705.08830 [physics.acc-ph] (page 28).

[70] Esma Mobs. "The CERN accelerator complex. Complexe des accélérateurs du CERN". In: *OPEN-PHO-ACCEL-2016-009* (2016). General Photo. URL: https://cds.cern.ch/record/2197559 (page 29).

[71] R. Bailey and Paul Collier. *Standard Filling Schemes for Various LHC Operation Modes*. fr. Institution: CERN-LHC-Project-Note-323 Number: LHC-PROJECT-NOTE-323. Sept. 2003. URL: https://cds.cern.ch/record/691782 (page 29).

[72] G. Arduini et al. "LHC Upgrades in preparation of Run 3". In: *JINST* 19.05 (2024), P05061. DOI: 10.1088/1748-0221/19/05/P05061 (page 30).

[73] G. Aad et al. "The ATLAS Experiment at the CERN Large Hadron Collider". In: *JINST* 3 (2008), S08003. DOI: 10.1088/1748-0221/3/08/S08003 (page 30).

[74] S. Chatrchyan et al. "The CMS Experiment at the CERN LHC". In: *JINST* 3 (2008), S08004. DOI: 10.1088/1748-0221/3/08/S08004 (page 30).

[75] K. Aamodt et al. "The ALICE experiment at the CERN LHC". In: *JINST* 3 (2008), S08002. DOI: 10.1088/1748-0221/3/08/S08002 (page 30).

[76] A. A. Alves Jr. et al. "The LHCb detector at the LHC". In: *JINST* 3.LHCb-DP-2008-001 (2008), S08005. DOI: 10.1088/1748-0221/3/08/S08005 (pages 31, 33, 35, 39, 42, 158).

[77] R. Aaij et al. "LHCb detector performance". In: *Int. J. Mod. Phys.* A30 (2015), p. 1530022. DOI: 10.1142/S0217751X15300227. arXiv: 1412.6352 [hep-ex] (pages 31, 158).

[78] I. Belyaev et al. "The history of LHCb". In: *Eur. Phys. J. H* 46.1 (2021), p. 3. DOI: 10.1140/epjh/s13129-021-00002-z. arXiv: 2101.05331 [physics.hist-ph] (pages 31, 32).

[79] R. Aaij et al. "Performance of the LHCb Vertex Locator". In: *JINST* 9 (2014), P09007. DOI: 10.1088/1748-0221/9/09/P09007. arXiv: 1405.7808 [physics.ins-det] (page 34).

[80] J. Gassner, M. Needham, and O. Steinkamp. "Layout and Expected Performance of the LHCb TT Station". In: (Apr. 2004) (page 36).

[81] M. Adinolfi et al. "Performance of the LHCb RICH detector at the LHC". In: *Eur. Phys. J.* C73 (2013), p. 2431. DOI: 10.1140/epjc/s10052-013-2431-9. arXiv: 1211.6759 [physics.ins-det] (page 38).

[82] Carlos Abellán Beteta et al. "Calibration and performance of the LHCb calorimeters in Run 1 and 2 at the LHC". In: (Aug. 2020). arXiv: 2008.11556 [physics.ins-det] (page 40).

[83] Albert Bursche et al. "Physics opportunities with the fixed-target program of the LHCb experiment using an unpolarized gas target". In: (2018) (pages 43, 44).

[84] "LHCb SMOG Upgrade". In: (). DOI: 10.17181/CERN.SAQC.EOWH (page 43).

[85] Roel Aaij et al. "Design and performance of the LHCb trigger and full real-time reconstruction in Run 2 of the LHC". In: *JINST* 14.04 (2019), P04013. DOI: 10.1088/1748-0221/14/04/P04013. arXiv: 1812.10790 [hep-ex] (pages 45, 47).

[86] Wouter D. Hulsbergen. "Decay chain fitting with a Kalman filter". In: *Nucl. Instrum. Meth. A* 552 (2005), pp. 566–575. DOI: 10.1016/j.nima.2005.06.078. arXiv: physics/0503191 (page 46).

[87] Denis Derkach, Mikhail Hushchyn, and Nikita Kazeev. "Machine Learning based Global Particle Identification Algorithms at the LHCb Experiment". In: *EPJ Web Conf.* 214 (2019). Ed. by A. Forti et al., p. 06011. DOI: 10.1051/epjconf/201921406011 (pages 48, 49).

[88] F. Archilli et al. "Performance of the Muon Identification at LHCb". In: *JINST* 8 (2013), P10020. DOI: 10.1088/1748-0221/8/10/P10020. arXiv: 1306.0249 [physics.ins-det] (page 48).

[89] G. Barrand et al. "GAUDI - A software architecture and framework for building HEP data processing applications". In: *Comput. Phys. Commun.* 140 (2001), pp. 45–55. DOI: 10.1016/S0010-4655(01)00254-5 (page 49).

[90] *The GAUSS Project*. URL: http://lhcbdoc.web.cern.ch/lhcbdoc/gauss/ (page 49).

[91] *The BOOLE Project*. URL: http://lhcbdoc.web.cern.ch/lhcbdoc/boole/ (pages 49, 50).

[92] *The BRUNEL Project*. URL: http://lhcbdoc.web.cern.ch/lhcbdoc/brunel/ (page 50).

[93] *The DAVINCI Project*. URL: http://lhcbdoc.web.cern.ch/lhcbdoc/davinci/ (page 50).

[94] *The LHCb data flow — LHCb Starterkit Lessons documentation*. URL: https://lhcb.github.io/starterkit-lessons/first-analysis-steps/dataflow.html (page 50).

[95] Torbjörn Sjöstrand, Stephen Mrenna, and Peter" Skands. "A brief introduction to PYTHIA 8.1". In: *Comput. Phys. Commun.* 178 (2008), pp. 852–867. DOI: 10.1016/j.cpc.2008.01.036. arXiv: 0710.3820 [hep-ph] (pages 50, 69, 114, 160).

[96] T. Pierog et al. "EPOS LHC: Test of collective hadronization with data measured at the CERN Large Hadron Collider". In: *Phys. Rev.* C92.3 (Sept. 2015), p. 034906. ISSN: 1089-490X. DOI: 10.1103/physrevc.92.034906. URL: http://dx.doi.org/10.1103/PhysRevC.92.034906 (pages 50, 69, 114, 160).

[97] D. J. Lange. "The EvtGen particle decay simulation package". In: *Nucl. Instrum. Meth.* A462 (2001), pp. 152–155. DOI: 10.1016/S0168-9002(01)00089-4 (pages 50, 160).

[98] P. Golonka and Z. Was. "PHOTOS Monte Carlo: a precision tool for QED correctionsin Z and W decays". In: *Eur. Phys. J.* C45.1 (2006), pp. 97–107. DOI: 10.1140/epjc/s2005-02396-4. URL: https://doi.org/10.1140%2Fepjc%2Fs2005-02396-4 (pages 50, 160).

[99] S. Agostinelli et al. "Geant4: A simulation toolkit". In: *Nucl. Instrum. Meth.* A506 (2003), p. 250. DOI: 10.1016/S0168-9002(03)01368-8 (pages 51, 160).

[100] John Allison et al. "Geant4 developments and applications". In: *IEEE Trans.Nucl.Sci.* 53 (2006), p. 270. DOI: 10.1109/TNS.2006.869826 (pages 51, 160).

[101] M Clemencic et al. "The LHCb simulation application, Gauss: Design, evolution and experience". In: *J. Phys. Conf. Ser.* 331 (2011), p. 032023. DOI: 10.1088/1742-6596/331/3/032023 (pages 51, 160).

[102] "LHCb Trigger and Online Upgrade Technical Design Report". In: (May 2014) (pages 53, 61, 62).

[103] Roel Aaij et al. "The LHCb Upgrade I". In: *JINST* 19.05 (2024), P05065. DOI: 10.1088/1748-0221/19/05/P05065. arXiv: 2305.10515 [hep-ex] (page 54).

[104] I. Bediaga. "LHCb VELO Upgrade Technical Design Report". In: (Nov. 2013) (pages 54, 55).

[105] *SIMATIC WinCC Open Architecture Version 3.18 Documentation.* https://www.winccoa.com/documentation/WinCCOA/3.18/en_US/index.html (page 56).

[106] "LHCb Tracker Upgrade Technical Design Report". In: (Feb. 2014) (pages 58, 59).

[107] "LHCb PID Upgrade Technical Design Report". In: (Nov. 2013) (page 60).

[108] Roel Aaij et al. "Allen: A high level trigger on GPUs for LHCb". In: *Comput. Softw. Big Sci.* 4.1 (2020), p. 7. DOI: 10.1007/s41781-020-00039-7. arXiv: 1912.09161 [physics.ins-det] (pages 61, 62).

[109] Renato Quagliani. "Novel real-time alignment and calibration of LHCb detector for Run II and tracking for the upgrade." In: *J. Phys. Conf. Ser.* 762.1 (2016). Ed. by Luis Salinas and Claudio Torres, p. 012046. DOI: 10.1088/1742-6596/762/1/012046 (page 62).

[110] O. Boente Garcia et al. "High-density gas target at the LHCb experiment". In: *Phys. Rev. Accel. Beams* 27.11 (2024), p. 111001. DOI: 10.1103/PhysRevAccelBeams.27.111001. arXiv: 2407.14200 [physics.ins-det] (page 63).

[111] Noemi Caraban Gonzalez. "SMOG2 installation in the LHCb cavern". In: (2020). General Photo. URL: https://cds.cern.ch/record/2727007 (page 63).

[112] " First invariant mass spectra and performance figures of the 2023 ion run ". In: (2023). URL: https://cds.cern.ch/record/2883088 (pages 64, 65).

[113] Roel Aaij et al. "Precision luminosity measurements at LHCb". In: *JINST* 9.12 (2014), P12005. DOI: 10.1088/1748-0221/9/12/P12005. arXiv: 1410.0149 [hep-ex] (page 68).

[114] Felipe A. Garcia et al. "A centrality tuple tool for LHCb". In: (2020) (page 68).

[115] Roel Aaij et al. "Prompt and nonprompt ψ(2S) production in pPb collisions at $\sqrt{s_{\rm NN}}$ = 8.16 TeV". In: *JHEP* 04 (2024), p. 111. DOI: 10.1007/JHEP04(2024)111. arXiv: 2401.11342 [hep-ex] (page 72).

[116] Roel Aaij et al. "Centrality determination in heavy-ion collisions with the LHCb detector". In: *JINST* 17.05 (2022), P05009. DOI: 10.1088/1748-0221/17/05/P05009. arXiv: 2111.01607 [nucl-ex] (pages 74, 117).

[117] B. et al. Abelev. "Centrality determination of Pb-Pb collisions at $\sqrt{s_{NN}} = 2.76$ TeV with ALICE". In: *Phys. Rev.* C88 (4 2013), p. 044909. DOI: 10.1103/PhysRevC.88.044909. URL: https://link.aps.org/doi/10.1103/PhysRevC.88.044909 (page 75).

[118] Tomasz Skwarnicki. "A study of the radiative cascade transitions between the Upsilon-prime and Upsilon resonances". DESY-F31-86-02. PhD thesis. Institute of Nuclear Physics, Krakow, 1986 (pages 78, 162).

[119] Muriel Pivk and Francois R. Le Diberder. "sPlot: A statistical tool to unfold data distributions". In: *Nucl. Instrum. Meth.* A555 (2005), pp. 356–369. DOI: 10.1016/j.nima.2005.08.106. arXiv: physics/0402083 [physics.data-an] (page 84).

[120] Lucio Anderlini et al. *The PIDCalib package*. 2016. URL: http://cds.cern.ch/record/2202412 (pages 90, 143).

[121] R. Aaij et al. "The LHCb trigger and its performance in 2011". In: *JINST* 8 (2013), P04022. DOI: 10.1088/1748-0221/8/04/P04022. arXiv: 1211.3055 [hep-ex] (pages 107, 159).

[122] R. Aaij et al. "Multiplicity dependence of $\sigma_{\psi(2S)}/\sigma_{J/\psi}$ in pp collisions at $\sqrt{s}$ = 13 TeV". In: *JHEP* 05 (2024), p. 243. DOI: 10.1007/JHEP05(2024)243. arXiv: 2312.15201 [hep-ex] (page 109).

[123] R. Aaij et al. "Prompt and nonprompt $\psi(2S)$ production in pPb collisions at $\sqrt{s_{NN}} = 8.16$ TeV". In: *JHEP* 04 (2024), p. 111. DOI: 10.1007/JHEP04(2024)111. arXiv: 2401.11342 [hep-ex] (page 109).

[124] Biaogang Wu and Ralf Rapp. "Charmonium transport in heavy-ion collisions at the LHC". In: *Universe* 10.6 (2024), p. 244. DOI: 10.3390/universe10060244. arXiv: 2404.09881 [nucl-th] (pages 110, 136, 137).

[125] Roel Aaij et al. "The LHCb Upgrade I". In: *JINST* 19 (2024), P05065. DOI: 10.1088/1748-0221/19/05/P05065. arXiv: 2305.10515 [hep-ex] (page 111).

[126] Roel Aaij et al. "Measurement of the ψ(2S) to J/ψ cross-section ratio as a function of centrality in PbPb collisions at $\sqrt{s_{NN}} = 5.02$ TeV". In: *JHEP* 07 (2025), p. 235. DOI: 10.1007/JHEP07(2025)235. arXiv: 2411.05669 [nucl-ex] (page 136).

[127] R. Aaij et al. "Transverse polarization measurement of Λ hyperons in pNe collisions at $\sqrt{s_{NN}} = 68.4$ GeV with the LHCb detector". In: *JHEP* 09 (2024), p. 082. DOI: 10.1007/JHEP09(2024)082. arXiv: 2405.11324 [hep-ex] (page 157).

[128] G. Bunce et al. "Λ^0 hyperon polarization in inclusive production by 300-GeV protons on beryllium". In: *Phys. Rev. Lett.* 36 (19 1976), pp. 1113–1116. DOI: 10.1103/PhysRevLett.36.1113. URL: https://link.aps.org/doi/10.1103/PhysRevLett.36.1113 (page 157).

[129] Taoya Gao. "Measurement of transverse polarization of $\Lambda/\bar{\Lambda}$ within jet in pp collisions at STAR". In: (2024). arXiv: 2402.01168 [hep-ex] (page 158).

[130] Y. Guan et al. "Observation of transverse $\Lambda/\bar{\Lambda}$ hyperon polarization in e^+e^- annihilation at Belle ". In: *Physical Review Letters* 122.4 (Jan. 2019), p. 042001. ISSN: 1079-7114. DOI: 10.1103/physrevlett.122.042001. arXiv: 1808.05000. URL: http://dx.doi.org/10.1103/PhysRevLett.122.042001 (page 158).

[131] A. Airapetian, N. Akopov, and Z. Akopov. "Transverse polarization of Λ hyperons from quasireal photoproduction on nuclei". In: *Phys. Rev.* D90.7 (2014), p. 072007. DOI: 10.1103/physrevd.90.072007. URL: https://doi.org/10.1103%2Fphysrevd.90.072007 (page 158).

[132] I. Belyaev et al. "Handling of the generation of primary events in Gauss, the LHCb simulation framework". In: *J. Phys. Conf. Ser.* 331 (2011), p. 032047. DOI: 10.1088/1742-6596/331/3/032047 (page 160).

[133] R. L. Workman et al. "Review of particle physics". In: *Prog. Theor. Exp. Phys.* 2022.8 (2022), p. 083C01. DOI: 10.1093/ptep/ptac097 (page 161).

[134] Georges Aad et al. "Measurement of the transverse polarization of Λ and $\bar{\Lambda}$ hyperons produced in proton-proton collisions at $\sqrt{s} = 7$ TeV using the ATLAS detector". In: *Phys. Rev.* D91.3 (2015), p. 032004. DOI: 10.1103/PhysRevD.91.032004. arXiv: 1412.1692 [hep-ex] (page 163).

[135] B. Lundberg et al. "Polarization in inclusive Λ and $\overline{\Lambda}$ production at large p_T". In: *Phys. Rev.* D40 (11 1989), pp. 3557–3567. DOI: 10.1103/PhysRevD.40.3557. URL: https://link.aps.org/doi/10.1103/PhysRevD.40.3557 (page 164).

[136] E.J. Ramberg et al. "Polarization of Λ and $\overline{\Lambda}$ produced by 800-GeV protons". In: *Phys. Lett.* B338.2 (1994), pp. 403–408. ISSN: 0370-2693. DOI: https://doi.org/10.1016/0370-2693(94)91397-8. URL: https://www.sciencedirect.com/science/article/pii/0370269394913978 (page 164).

[137] A. Tkachev. "A measurement of the transverse polarization of Λ hyperons produced in inelastic pN-reactions at 450 GeV proton energy". In: *Nucl. Phys. B Proc. Suppl.* 75 (1999). Ed. by Calvin S. Kalman et al., pp. 45–47. DOI: 10.1016/S0920-5632(99)00321-7 (page 164).

[138] I. Abt et al. "Polarization of Λ and $\overline{\Lambda}$ in 920-GeV fixed-target proton-nucleus collisions". In: *Phys. Lett.* B638 (2006), pp. 415–421. DOI: 10.1016/j.physletb.2006.05.040. arXiv: hep-ex/0603047 (page 164).

List of Figures

1.1 Elementary particles of the Standard Model, with their mass, charge and spin. 2
1.2 Summary of different measurements of the running constant of the strong interaction as a function of the energy scale Q [10]. 4
1.3 Feynman diagrams of the main $c\bar{c}$ production mechanisms at Leading Order (LO): quark annihilation (left) and gluon fusion (right). 6
1.4 Phase diagram of the hadronic matter [21]. 9
1.5 Schematic behaviour of the nPDFs effects as a function of Bjorken-x for a fixed Q^2. 10
1.6 Evolution of the gluon, sea quark, and valence quark distributions at $Q^2 = 10$ GeV$^2/c^2$ [28]. 11
1.7 Space-time evolution of a heavy-ion collision with QGP formation. . . 12
1.8 Illustration of a heavy-ion collision, showing (top) the impact parameter b, the separation of spectators and participants, and (bottom) the classification of collisions by centrality in the transverse plane. The colliding beams travel along the z axis, perpendicular to the plane of the figure. 13
1.9 Schematic illustration of the almond-shaped overlap region in a non-central heavy-ion collision. 15
1.10 Low energies: the only $c\bar{c}$ pair created (red dots) is screened by QGP and the single (anti)-charm, paired with any other quark, hadronises into a D meson (purple circles). High energies: many $c\bar{c}$ pairs produced, at hadronisation c and $\bar{c}$ quarks from different original pairs may combine to form a charmonium (yellow stars) [5] 17
1.11 Normalised production ratio of $\psi(2S)$ over J/ψ measured by LHCb as a function of the multiplicity of the event [47]. Prompt (red circles) contribution show a decreasing trend with respect to the nonpront (blue circles) one, in agreement with the co-mover model [37], which could be QGP-like behaviour in small systems. 19
1.12 Production ratio of $\psi(2S)/J/\psi$ measured by LHCb as a function of the multiplicity of the event. Red circles: pp, blue circles: pPb, green circles: Pbp, similar shape as ALICE PbPb results (red band) [52]. . . 20

1.13 Inclusive J/ψ R_{AA} at mid-rapidity measured by ALICE [54], as a function of the number of participating nucleons integrated over p_{T} (left), and as a function of p_{T} for central collisions (right). 21
1.14 Representation of the binding energies of different quarkonia states compiled using the known values [59], compared to the peak QGP temperature estimated from thermal photon yields [60]. 22
1.15 Ratio of the $\psi(2S)$ to J/ψ inclusive production cross-section as a function of the number of participating nuclei, measured by ALICE [52] . . 23
1.16 Double ratio of the $\psi(2S)$ to J/ψ prompt production cross-section as a function of the transverse momentum in two rapidity intervals, measured by CMS [63] 24
1.17 Double ratio of the $\psi(2S)$ to J/ψ production cross-section as a function of the rapidity in different collision systems, measured by PHENIX [64] 25

2.1 The CERN accelerator complex [70]. 29
2.2 Pseudo-rapidity coverage of the main experiments at LHC, with the main subdetectors details. 31
2.3 Side view of the LHCb detector in its Run 2 configuration [78]. The positive x axis is entering the page towards the centre of the LHC ring. 32
2.4 Perspective view of the LHCb dipole magnet (units in mm) (left). Magnetic field along z axis (right) [76]. 33
2.5 Cross section in the (x, z) plane of the VELO silicon sensors, at $y = 0$, with the detector in the fully closed position. The beams travel along the z axis perpendicular to the page. The front face of the first modules is illustrated in both the closed and open positions. The two pile-up veto stations are located upstream of the VELO sensors [76]. 35
2.6 Sketch illustrating the $r\phi$ geometry of the VELO sensors [76]. 35
2.7 Layout of the four detection layers of the TT station in the xy plane [80]. 36
2.8 Layout of a T station in the xy plane. 37
2.9 Reconstructed Cherenkov angle as a function of track momentum in the C_4F_{10} radiator [81]. 38
2.10 Layout of the RICH1 (left) and RICH2 (right) detectors [76]. 39
2.11 Layout of the calorimeter system [82]. 40
2.12 Side (left) and front (right) view of the muon system [76]. The beam moves in the z direction. 42
2.13 Zoom of the Vertex Locator region, showing the spatial extension of the internal gas target provided by the SMOG device, highlighted in dark purple [83]. The light purple square indicates the SMOG upgrade, SMOG2 [84] (discussed is Sec. 2.3.4). 43
2.14 The SMOG gas feed system [83]. 44
2.15 Overview of the LHCb trigger system [85]. 45

2.16 Sketch of the different types of tracks within LHCb. [85]. 47
2.17 Illustration of the detector response for different particle types in LHCb. [87]. 48
2.18 Illustration of the data processing flow in LHCb [94]. 50
2.19 Number of VELO clusters as a function of the energy deposit in ECAL for Run 2 PbPb collisions recorded by LHCb. 52
2.20 Number of Long tracks as a function of the VELO tracks for Run 2 PbPb collisions recorded by LHCb. 52
2.21 Layout of the upgraded LHCb detector [103]. 54
2.22 Layout of the upgraded VELO. Top: schematic cross section at y = 0, together with illustrations of the z-extent of the luminous region and the nominal LHCb acceptance. Bottom: schematic layout in the (x, y) plane (left: VELO closed, right: VELO fully open) [104]. 55
2.23 Detail of a VELO module (left) and the correspondent temperature sensors in the expert control panel (right). 56
2.24 Picture of the setting alarm panel for the NTC sensors. 57
2.25 Picture of the setting alarm panel for the PT100 sensors. 57
2.26 Picture of the monitoring alarm panel for the NTC sensors. 58
2.27 Picture of the monitoring alarm panel for the PT100 sensors. 58
2.28 Layout of the four stations composing the UT detector [106]. 59
2.29 Layout of the SciFi detector. 60
2.30 Overview of the LHCb trigger system in Run 3 [109]. 62
2.31 Picture of the SMOG2 cell (left) and gas feed system (right) [111]. . . 63
2.32 Correlation between the total energy collected in the ECAL and the number of clusters in the SciFi tracker for PbPb collision events [112]. 64
2.33 Correlation between the total energy collected in the ECAL and the number of clusters in the VELO for PbPb events. The main population correspond to PbPb collisions, while the smaller population spanning at lower VELO clusters values corresponds to PbAr collisions collected simultaneously thanks to SMOG2. [112]. 65
2.34 Distribution of the total energy collected in the ECAL for PbPb collision events divided in event activity classes, highlighting the lower centrality classes reachable in Run 3 [112]. 65

3.1 $\rho = \sqrt{x_{PV}^2 + y_{PV}^2}$ against $|z_{PV}|$ distribution before the selection criteria (left plot) and after (right plot). 71
3.2 `nVeloClusters` against ECAL deposit energy before the selection criteria (left plot) and after (right plot). 71
3.3 J/ψ pseudoproper time distribution after the selection criteria without the `log(IPCHI2)` requirement (left), with the full selection (right). Fit model overlaid. 73

3.4 $\psi(2S)$ pseudoproper time distribution after the selection criteria without the `log(IPCHI2)` requirement (left), with the full selection (right), with muon p_{T} greater than 900 MeV/c. Fit model overlaid. 73
3.5 $\psi(2S)$ pseudoproper time distribution after the selection criteria without the `log(IPCHI2)` requirement (left), with the full selection (right), with muon p_{T} greater than 700 MeV/c. Fit model overlaid. 74
3.6 Distributions of N_{part}, N_{coll}, and N_{anc} from a Glauber MC simulation of 1M PbPb collisions at $\sqrt{s_{\mathrm{NN}}} = 5.02$ TeV. A value of $f = 0.751$ was used. 75
3.7 Top: Glauber MC fit to 2018 PbPb data as a function of ECAL energy. Bottom: data-to-fit ratio. Right: zoom at low energy values. 76
3.8 Top left: classification of events from PbPb data according to the defined centrality classes. Top right: impact parameter distributions. Bottom: $\langle N_{\mathrm{coll}} \rangle$ and $\langle N_{\mathrm{part}} \rangle$ quantities for the corresponding centrality classes. 77
3.9 Dimuon invariant mass distribution for the full dataset after all selection criteria are applied, overlaid with the fit result. 79
3.10 Dimuon invariant mass distributions in each centrality interval after selection, overlaid with fit results. 79
3.11 Truth matching efficiency $\varepsilon_{\mathrm{MCTruth}}$ as a function of centrality (top left), `nVeloClusters` (top right), p_{T} (bottom left) and y (bottom right) for J/ψ. 82
3.12 Truth matching efficiency $\varepsilon_{\mathrm{MCTruth}}$ as a function of centrality (top left), `nVeloClusters` (top right), p_{T} (bottom left) and y (bottom right) for $\psi(2S)$. 83
3.13 Truth matching efficiency $\varepsilon_{\mathrm{MCTruth}}$ ratio of $\psi(2S)$ over J/ψ as a function of centrality (top left), `nVeloClusters` (top right), p_{T} (bottom left) and y (bottom right). 83
3.14 Comparison of normalised `nVeloClusters` (left) and p_{T} (right) distributions between J/ψ and $\psi(2S)$ simulation. The distributions are in good agreement. 85
3.15 Comparison of `nVeloClusters` (left) and p_{T} (right) distributions in background-subtracted data (sWeights), original MC, and reweighted MC for J/ψ. The reweighting significantly improves the agreement between simulation and data. 85
3.16 Geometrical acceptance $\varepsilon_{\mathrm{acc}}$ calculated using generator-level pp events as a function of p_{T} in bins of y, for J/ψ (top) and $\psi(2S)$ (bottom). . . 87
3.17 Reconstruction and selection efficiency $\varepsilon_{\mathrm{rec\&sel}}$ as a function of centrality (top left), `nVeloClusters` (top right), p_{T} (bottom left), and y (bottom right) for the J/ψ. 88

3.18 Reconstruction and selection efficiency $\varepsilon_{\text{rec\&sel}}$ as a function of centrality (top left), `nVeloClusters` (top right), p_{T} (bottom left), and y (bottom right) for the $\psi(2S)$. 89
3.19 Ratio of the reconstruction and selection efficiencies $\varepsilon_{\text{rec\&sel}}\,(\psi(2S))/\varepsilon_{\text{rec\&sel}}\,(J/\psi)$ as a function of centrality (top left), `nVeloClusters` (top right), p_{T} (bottom left), and y (bottom right). 89
3.20 Muon efficiency from pp 2018 sample versus occupancy in different η bins. 92
3.21 Muon efficiency from pp 2018 sample versus occupancy (up to `nVeloClusters` = 5000) in different bins of p_{T} indidcated in MeV/c. The fits are performed using a second-order polynomial function. The efficiency values for `nVeloClusters` > 5000 are obtained through the extrapolation explained in the text. 92
3.22 $f_{\text{PID}}^{\text{extr}}$ results in bins of p_{T} and `nVeloClusters`. 93
3.23 $\varepsilon_{\text{PID}}^{pp}$ $(p_{\text{T}}, \eta;$ `nVeloClusters` $< 1000)$ results. 93
3.24 Particle identification efficiency $\varepsilon_{\text{MuonID}}$ as a function of centrality (top left), `nVeloClusters` (top right), p_{T} (bottom left) and y (bottom right) for J/ψ. 94
3.25 Particle identification efficiency $\varepsilon_{\text{MuonID}}$ as a function of centrality (top left), `nVeloClusters` (top right), p_{T} (bottom left) and y (bottom right) for $\psi(2S)$. 95
3.26 Particle identification efficiency $\varepsilon_{\text{MuonID}}$ ratio of $\psi(2S)$ over J/ψ as a function of centrality (top left), `nVeloClusters` (top right), p_{T} (bottom left) and y (bottom right). 95
3.27 Efficiency of the `ProbNN`$\mu > 0.7$ requirement computed using the extrapolation from the pp sample (blue open squares for the second-order polynomial extrapolation, black open squares for an alternative first-order polynomial extrapolation), and with the signal PbPb sample using different identification criteria for the tag muon (circles). 96
3.28 Trigger efficiency ε_{trg} as a function of centrality (top left), `nVeloClusters` (top right), p_{T} (bottom left) and y (bottom right) for J/ψ. 98
3.29 Trigger efficiency ε_{trg} as a function of centrality (top left), `nVeloClusters` (top right), p_{T} (bottom left) and y (bottom right) for $\psi(2S)$. 98
3.30 Trigger efficiency ε_{trg} ratio of $\psi(2S)$ over J/ψ as a function of centrality (top left), `nVeloClusters` (top right), p_{T} (bottom left) and y (bottom right). 99
3.31 Total efficiency ε_{tot} as a function of centrality (top left), `nVeloClusters` (top right), p_{T} (bottom left) and y (bottom right) for J/ψ. 100
3.32 Total efficiency ε_{tot} as a function of centrality (top left), `nVeloClusters` (top right), p_{T} (bottom left) and y (bottom right) for $\psi(2S)$. 100

3.33 Total efficiency ε_{trg} ratio of $\psi(2S)$ over J/ψ as a function of centrality (top left), `nVeloClusters` (top right), p_{T} (bottom left) and y (bottom right). 101
3.34 Same-sign dimuon invariant mass distributions in each centrality interval after selection, overlaid with exponential fit results. 103
3.35 Comparison of normalised `nVeloClusters` (left) and p_{T} (right) distributions between J/ψ before reweight to match $\psi(2S)$ (blue dots) and after (green line). The distributions are in good agreement after the reweight. 105
3.36 Muon efficiency from the 2018 pp sample as a function of detector occupancy (up to `nVeloClusters` = 5000) in different p_{T} bins. The fits for the different p_{T} intervals are performed using a first-order polynomial. For `nVeloClusters` > 5000, the efficiency values are extrapolated as explained in the text. 107
3.37 Cross-section times branching fraction ratio between $\psi(2S)$ and J/ψ as a function of $\langle N_{\text{part}} \rangle$ in the $p_{\text{T}} > 0.3$ GeV/c region, compared with ALICE PbPb [52], LHCb pp [122], and pPb [123] results. Vertical error bars represent the total uncertainty (statistical and systematic added in quadrature). 109
3.38 Cross-section times branching fraction ratio between $\psi(2S)$ and J/ψ as a function of $\langle N_{\text{part}} \rangle$ in the $p_{\text{T}} > 0.3$ GeV/c region, compared with the SHMc [62, 42] and TAMU [41, 124] model predictions. Coloured bands represent model uncertainties. Vertical error bars represent the total uncertainty (statistical and systematic added in quadrature). 110

4.1 Distribution of the `PID`μ variable for μ^+ (left) and μ^- (right). Red: simulated J/ψ signal; green: J/ψ data in invariant-mass sidebands ($2900 < m_{\mu^+\mu^-} < 3000$ MeV/c^2 and $3200 < m_{\mu^+\mu^-} < 3400$ MeV/c^2). . 116
4.2 Top: Glauber MC fit to 2024 PbPb data as a function of ECAL energy. Bottom: data-to-fit ratio. 118
4.3 Top left: classification of events from PbPb data according to the defined centrality classes. Top right: $\langle N_{\text{part}} \rangle$. Bottom left: $\langle N_{\text{coll}} \rangle$. Bottom right: impact parameter distributions. 119
4.4 Dimuon invariant mass distribution for the full dataset after all selection criteria are applied, overlaid with the fit result. 121
4.5 Dimuon invariant mass distributions in each centrality interval after selection, overlaid with fit results. 121
4.6 Comparison of `nFTClusters` (top left), p_{T} (top right), and y (bottom) distributions in background-subtracted data (sWeights), original MC, and reweighted MC for J/ψ. The reweighting significantly improves the agreement between simulation and data. 123

4.7 Geometrical acceptance ε_{acc} calculated using generator-level pp events as a function of p_{T} in bins of y, for J/ψ (top) and $\psi(2S)$ (bottom). . . 124
4.8 Reconstruction and selection efficiency $\varepsilon_{\text{rec\&sel}}$ as a function of `eCalTot` (top left), p_{T} (top right), and y (bottom) for the J/ψ. 126
4.9 Reconstruction and selection efficiency $\varepsilon_{\text{rec\&sel}}$ as a function of `eCalTot` (top left), p_{T} (top right), and y (bottom) for the $\psi(2S)$. 127
4.10 Ratio of the reconstruction and selection efficiencies $\varepsilon_{\text{rec\&sel}}$ $(\psi(2S))/\varepsilon_{\text{rec\&sel}}$ (J/ψ) as a function of `eCalTot` (top left), p_{T} (top right), and y (bottom).127
4.11 Dimuon invariant-mass distributions for the numerator (left) and denominator (right) of eq. 4.4, when considering the μ^+ as the tag muon. The fitted signal and background components are overlaid. 128
4.12 Muon identification correction weights maps as a function of `nFTClusters` and p_{T}, for the μ^+ (right) and μ^- (left) probe muons. 129
4.13 Particle identification efficiency $\varepsilon_{\text{MuonID}}$ as a function of `eCalTot` (top left), p_{T} (top right) and y (bottom right) for J/ψ. 130
4.14 Particle identification efficiency $\varepsilon_{\text{MuonID}}$ as a function of `eCalTot` (top left), p_{T} (top right) and y (bottom right) for $\psi(2S)$. 130
4.15 Particle identification efficiency $\varepsilon_{\text{MuonID}}$ ratio of $\psi(2S)$ over J/ψ as a function of `eCalTot` (top left), p_{T} (top right) and y (bottom right). . . 131
4.16 Total efficiency ε_{tot} as a function of `eCalTot` (top left), p_{T} (top right) and y (bottom) for J/ψ. 133
4.17 Total efficiency ε_{tot} as a function of `eCalTot` (top left), p_{T} (top right) and y (bottom) for $\psi(2S)$. 133
4.18 Total efficiency ε_{trg} ratio of $\psi(2S)$ over J/ψ as a function of `eCalTot` (top left), p_{T} (top right) and y (bottom). 134
4.19 Cross-section times branching fraction ratio between $\psi(2S)$ and J/ψ as a function of $\langle N_{\text{part}} \rangle$ in the $p_{\text{T}} > 0.3$ GeV/c region, compared with ALICE [52] and LHCb [126] PbPb results. Vertical error bars represent the statistical uncertainties. 136
4.20 Cross-section times branching fraction ratio between $\psi(2S)$ and J/ψ as a function of $\langle N_{\text{part}} \rangle$ in the $p_{\text{T}} > 0.3$ GeV/c region, compared with the SHMc [62, 42] and TAMU [41, 124] model predictions. Coloured bands represent model uncertainties. Vertical error bars represent the statistical uncertainties. 137

A.1 Dimuon simulation invariant mass distributions in each centrality interval after selection for J/ψ, overlaid with fit results. 141
A.2 Dimuon simulation invariant mass distributions in each centrality interval after selection for $\psi(2S)$, overlaid with fit results. 142
A.3 Correlation between charmonium and μ^+ transverse momentum: (left) J/ψ and (right) $\psi(2S)$. 142

A.4 J/ψ invariant mass distributions used in the Tag&Probe cross-check for `ProbNN`$\mu > 0.95$ tag selection. Top: numerator of Eq. A.1; bottom: denominator. Left: $1000 <$ `nVeloClusters` < 5000; right: $5000 <$ `nVeloClusters` < 10000. 144
A.5 J/ψ invariant mass distributions used in the Tag&Probe cross-check for `ProbNN`$\mu > 0.99$ tag selection. Top: numerator of Eq. A.1; bottom: denominator. Left: $1000 <$ `nVeloClusters` < 5000; right: $5000 <$ `nVeloClusters` < 10000. 144
A.6 Dimuon simulation invariant mass distributions in each centrality interval after selection with the alternative signal model function, overlaid with fit results. 145
A.7 Dimuon simulation invariant mass distributions in each centrality interval after selection with the alternative background model function, overlaid with fit results. 146

B.1 Dimuon simulation invariant mass distributions in each centrality interval after selection for J/ψ, overlaid with fit results. 147
B.2 Dimuon simulation invariant mass distributions in each centrality interval after selection for $\psi(2S)$, overlaid with fit results. 148
B.3 Dimuon invariant-mass distributions for the numerator (left) and denominator (right) of eq. 4.4 for $0 <$ `nFTClusters` $< 10\,000$ and $0.7 < p_{\mathrm{T}} < 1.0$ GeV/c. 148
B.4 Dimuon invariant-mass distributions for the numerator (left) and denominator (right) of eq. 4.4 for $0 <$ `nFTClusters` $< 10\,000$ and $1.0 < p_{\mathrm{T}} < 1.3$ GeV/c. 149
B.5 Dimuon invariant-mass distributions for the numerator (left) and denominator (right) of eq. 4.4 for $0 <$ `nFTClusters` $< 10\,000$ and $1.3 < p_{\mathrm{T}} < 1.6$ GeV/c. 149
B.6 Dimuon invariant-mass distributions for the numerator (left) and denominator (right) of eq. 4.4 for $0 <$ `nFTClusters` $< 10\,000$ and $1.6 < p_{\mathrm{T}} < 1.9$ GeV/c. 149
B.7 Dimuon invariant-mass distributions for the numerator (left) and denominator (right) of eq. 4.4 for $0 <$ `nFTClusters` $< 10\,000$ and $1.9 < p_{\mathrm{T}} < 2.4$ GeV/c. 150
B.8 Dimuon invariant-mass distributions for the numerator (left) and denominator (right) of eq. 4.4 for $0 <$ `nFTClusters` $< 10\,000$ and $2.4 < p_{\mathrm{T}} < 6.0$ GeV/c. 150
B.9 Dimuon invariant-mass distributions for the numerator (left) and denominator (right) of eq. 4.4 for $10\,000 <$ `nFTClusters` $< 15\,000$ and $0.7 < p_{\mathrm{T}} < 1.0$ GeV/c. 150

B.10 Dimuon invariant-mass distributions for the numerator (left) and denominator (right) of eq. 4.4 for 10 000 < `nFTClusters` < 15 000 and $1.0 < p_{\mathrm{T}} < 1.3$ GeV/c. 151
B.11 Dimuon invariant-mass distributions for the numerator (left) and denominator (right) of eq. 4.4 for 10 000 < `nFTClusters` < 15 000 and $1.3 < p_{\mathrm{T}} < 1.6$ GeV/c. 151
B.12 Dimuon invariant-mass distributions for the numerator (left) and denominator (right) of eq. 4.4 for 10 000 < `nFTClusters` < 15 000 and $1.6 < p_{\mathrm{T}} < 1.9$ GeV/c. 151
B.13 Dimuon invariant-mass distributions for the numerator (left) and denominator (right) of eq. 4.4 for 10 000 < `nFTClusters` < 15 000 and $1.9 < p_{\mathrm{T}} < 2.4$ GeV/c. 152
B.14 Dimuon invariant-mass distributions for the numerator (left) and denominator (right) of eq. 4.4 for 10 000 < `nFTClusters` < 15 000 and $2.4 < p_{\mathrm{T}} < 6.0$ GeV/c. 152
B.15 Dimuon invariant-mass distributions for the numerator (left) and denominator (right) of eq. 4.4 for 15 000 < `nFTClusters` < 20 000 and $0.7 < p_{\mathrm{T}} < 1.0$ GeV/c. 152
B.16 Dimuon invariant-mass distributions for the numerator (left) and denominator (right) of eq. 4.4 for 15 000 < `nFTClusters` < 20 000 and $1.0 < p_{\mathrm{T}} < 1.3$ GeV/c. 153
B.17 Dimuon invariant-mass distributions for the numerator (left) and denominator (right) of eq. 4.4 for 15 000 < `nFTClusters` < 20 000 and $1.3 < p_{\mathrm{T}} < 1.6$ GeV/c. 153
B.18 Dimuon invariant-mass distributions for the numerator (left) and denominator (right) of eq. 4.4 for 15 000 < `nFTClusters` < 20 000 and $1.6 < p_{\mathrm{T}} < 1.9$ GeV/c. 153
B.19 Dimuon invariant-mass distributions for the numerator (left) and denominator (right) of eq. 4.4 for 15 000 < `nFTClusters` < 20 000 and $1.9 < p_{\mathrm{T}} < 2.4$ GeV/c. 154
B.20 Dimuon invariant-mass distributions for the numerator (left) and denominator (right) of eq. 4.4 for 15 000 < `nFTClusters` < 20 000 and $2.4 < p_{\mathrm{T}} < 6.0$ GeV/c. 154
B.21 Dimuon invariant-mass distributions for the numerator (left) and denominator (right) of eq. 4.4 for 20 000 < `nFTClusters` < 28 000 and $0.7 < p_{\mathrm{T}} < 1.0$ GeV/c. 154
B.22 Dimuon invariant-mass distributions for the numerator (left) and denominator (right) of eq. 4.4 for 20 000 < `nFTClusters` < 28 000 and $1.0 < p_{\mathrm{T}} < 1.3$ GeV/c. 155

B.23 Dimuon invariant-mass distributions for the numerator (left) and denominator (right) of eq. 4.4 for 20 000 < `nFTClusters` < 28 000 and $1.3 < p_{\mathrm{T}} < 1.6$ GeV/c. 155
B.24 Dimuon invariant-mass distributions for the numerator (left) and denominator (right) of eq. 4.4 for 20 000 < `nFTClusters` < 28 000 and $1.6 < p_{\mathrm{T}} < 1.9$ GeV/c. 155
B.25 Dimuon invariant-mass distributions for the numerator (left) and denominator (right) of eq. 4.4 for 20 000 < `nFTClusters` < 28 000 and $1.9 < p_{\mathrm{T}} < 2.4$ GeV/c. 156
B.26 Dimuon invariant-mass distributions for the numerator (left) and denominator (right) of eq. 4.4 for 20 000 < `nFTClusters` < 28 000 and $2.4 < p_{\mathrm{T}} < 6.0$ GeV/c. 156

C.1 Invariant-mass distributions for (left) Λ and (right) $\overline{\Lambda}$ candidates after all selection requirements are applied. The fit result is overlaid on the data. 159
C.2 Sketch of the Λ production and decay. The polarization vector $\hat{P}_{\Lambda}$ is aligned with the normal vector $\hat{n}$ to the Λ production plane; θ is the angle between the momentum of the decay proton and $\hat{n}$ in the Λ rest frame. 160
C.3 Efficiency-corrected $\cos\theta$ distributions, for (left) Λ and (right) $\overline{\Lambda}$ hyperons. The result of the fit is overlaid (red line). 161
C.4 Polarization as a function of (a) p_{T}, (b) η, (c) x_{F} and (d) y. Blue (red) symbols are for Λ ($\overline{\Lambda}$). In each plot the data is integrated over the $0.3 < p_{\mathrm{T}} < 3$ GeV/c and/or $2 < \eta < 5$ kinematic range. 163
C.5 Comparison of polarization as a function of x_{F} for Λ hyperons obtained in experiments with different energies and with different colliding systems. 164

List of Tables

1.1 Main quarkonium states with their quantum numbers and masses [13]. 6

2.1 Summary of the main LHC running periods and corresponding collision systems and energies. 28
2.2 Muon stations required to trigger the `IsMuon` decision in different momentum ranges. 49

3.1 Selection criteria for the stripping line used. 69
3.2 Simulation samples used for the analysis. 69
3.3 GEC criteria applied to the event. 70
3.4 Offline selection criteria applied to the dimuon candidates. 72
3.5 Centrality classes and corresponding average geometry parameters. Uncertainties are the RMS of each distribution. 76
3.6 Centrality and corresponding $\langle N_{part} \rangle$ bins used in this analysis. 77
3.7 Range for the number of participating nucleons $\langle N_{\rm part} \rangle$ and signal yields in each centrality interval, the uncertainties are statistical only. 80
3.8 Truth matching efficiency for J/ψ, $\psi(2S)$, and their ratio, as a function of centrality. The uncertainty is negligible. 82
3.9 Geometrical acceptance for J/ψ and $\psi(2S)$ as a function of $p_{\rm T}$. 86
3.10 Geometrical acceptance for J/ψ and $\psi(2S)$ as a function of y. 86
3.11 Reconstruction and selection efficiency for J/ψ, $\psi(2S)$, and their ratio, as a function of centrality. The uncertainty is statistical. 90
3.12 Particle identification efficiency for J/ψ, $\psi(2S)$, and their ratio, centrality. The uncertainty is statistical. 94
3.13 Trigger efficiency for J/ψ, $\psi(2S)$ and their ratio as a function of centrality. The uncertainty is statistical. 97
3.14 Total efficiency for J/ψ, $\psi(2S)$ and their ratio as a function of centrality. The uncertainty is statistical. 99
3.15 Systematic uncertainty on the $\psi(2S)/J/\psi$ ratio due to the signal fit model, as a function of centrality. 102
3.16 Systematic uncertainty on the $\psi(2S)/J/\psi$ ratio due to the background fit model, as a function of centrality. 103
3.17 Systematic uncertainty on the $\psi(2S)/J/\psi$ ratio due to MC sample size, as a function of centrality. 104

3.18 Systematic uncertainty on the $\psi(2S)/J/\psi$ ratio due to MuonID efficiency estimation, as a function of centrality. 106
3.19 Range of the relative systematic uncertainty contributions for the ratio measurement across the four centrality intervals. 108
3.20 Cross-section times branching fraction ratio between $\psi(2S)$ and J/ψ in intervals of centrality, along with the corresponding number of participating nucleons $\langle N_{\text{part}} \rangle$. The first uncertainty is statistical and the second systematic. 109

4.1 Simulated samples used for the Run 3 analysis. 114
4.2 Global event selection (GEC) criteria applied to the data. 115
4.3 Offline selection criteria applied to the dimuon candidates. 116
4.4 Centrality classes and corresponding average geometry parameters. . . 118
4.5 Binning scheme used for the Run 3 analysis, based on the total ECAL energy. The corresponding centrality and average $\langle N_{\text{part}} \rangle$ values are derived from the Glauber fit. 119
4.6 Range for the number of the nucleons $\langle N_{\text{part}} \rangle$ and signal yields in each centrality interval, the uncertainties are statistical only. 120
4.7 Geometrical acceptance for J/ψ and $\psi(2S)$ as a function of p_{T}. 125
4.8 Geometrical acceptance for J/ψ and $\psi(2S)$ as a function of y. 125
4.9 Reconstruction and selection efficiency for J/ψ, $\psi(2S)$, and their ratio, as a function of centrality. The uncertainty is statistical. 126
4.10 Particle identification efficiency for J/ψ, $\psi(2S)$, and their ratio, as a function of centrality. The uncertainty is statistical. 129
4.11 Total efficiency for J/ψ, $\psi(2S)$ and their ratio as a function of centrality. The uncertainty is statistical. 132
4.12 Cross-section times branching fraction ratio between $\psi(2S)$ and J/ψ in intervals of centrality, along with the corresponding number of participating nucleons $\langle N_{\text{part}} \rangle$. The uncertainty is purely statistical. 135

C.1 Contributions of systematic uncertainties on the polarization measurement for Λ and $\overline{\Lambda}$ hyperons. 163
C.2 Polarization in bins of p_{T}, η, x_{F}, and y for Λ and $\overline{\Lambda}$. The first uncertainties are statistical and the second are systematic. 165